TAMPEREEN TEKNILLINEN YLIOPISTO
TAMPERE UNIVERSITY OF TECHNOLOGY

Janne Koivumäki

Stability-Guaranteed Nonlinear Model-Based Control of Hydraulic Robotic Manipulators

Julkaisu 1446 • Publication 1446

Tampere 2016

Tampereen teknillinen yliopisto. Julkaisu 1446
Tampere University of Technology. Publication 1446

Janne Koivumäki

Stability-Guaranteed Nonlinear Model-Based Control of Hydraulic Robotic Manipulators

Thesis for the degree of Doctor of Science in Technology to be presented with due permission for public examination and criticism in Konetalo Building, Auditorium K1702, at Tampere University of Technology, on the 2nd of December 2016, at 12 noon.

Tampereen teknillinen yliopisto - Tampere University of Technology
Tampere 2016

Pre-Examiners

Dr. Wen-Hong Zhu
Robot Automation Engineer, Canadian Space Agency
Canada

Prof. Guangjun Liu
Canada Research Chair in Control Systems and Robotics
Department of Aerospace Engineering
Ryerson University
Canada

Opponents

Dr. Wen-Hong Zhu
Robot Automation Engineer, Canadian Space Agency
Canada

Dr. Marcus Rösth
R&D Manager Control Systems, HIAB
Sweden

Custos

Prof. Jouni Mattila
Department of Intelligent hydraulics and Automation
Tampere University of Technology
Finland

ISBN 978-952-15-3868-1 (printed)
ISBN 978-952-15-3894-0 (PDF)
ISSN 1459-2045

Abstract

Robotics technology is booming and it is projected to dominate in the coming decade. Although robotics has already made a considerable impact on many aspects of modern life, advanced robotics is still in its infancy. However, applications of robots are increasing all the time, and their structures are becoming more complex. This increasing complexity creates new challenges in control design, and with the advent of more advanced and more demanding operations, new solutions for controlling robots are needed.

Hydraulic actuators can benefit robotic systems because, compared to electric actuators, they can produce significant forces and torques for their size. Thus, typical operations with hydraulic robotic systems are contact tasks in which heavy objects are handled or in which forces are generated on the environment (e.g., excavation). However, in contact tasks, the control system stability (which is the primary requirement for all control systems) has drawn considerable attention since the installation of the first industrial robots, and numerous reasons for unstable responses have been identified. One of the most significant reasons for instability is that a robot's nonlinear dynamics are not considered rigorously. However, rigorously addressing robot dynamics is one of the fundamental challenges in highly nonlinear hydraulic robotic systems, and this issue has also slowed the spread of their closed-loop control solutions. To address the highly nonlinear dynamics of hydraulic robotic systems, nonlinear model-based (NMB) control methods can be used. However, a stability-guaranteed NMB control design for hydraulic robotic systems has remained an open problem in contact tasks.

This thesis studies a high-performance NMB control method for hydraulic robotic manipulators and provides a rigorous solution for the above open problem. In this thesis, a novel subsystem-dynamics-based virtual decomposition control (VDC) approach is used as an underlying control design framework. The unique features of VDC enable the system's control design and stability analysis at the subsystem level, without imposing additional approximations. This thesis also studies another fundamental challenge of the lack of energy efficiency in hydraulic systems and a force-sensorless contact force estimation for hydraulic robotic manipulators. For energy-efficient control of hydraulic systems, the control design principles of VDC are extended from robotic systems to a broader group of dynamic systems.

This compendium thesis is composed of four publications and one unpublished manuscript. The publications extend the state of the art in the control of hydraulic robotic manipulators in free-space motion and in constrained motion. To provide a possibility for reducing energy consumption, the unpublished manuscript proposes an adaptive and NMB controller for variable displacement axial piston pumps (VDAPPs), whose dynamic behaviour is highly nonlinear in the fourth order, for the first time without using any linearization or order reduction. All control designs in this thesis are stability-guaranteed NMB controls.

Preface

This study was carried out from 2013 to 2016 at the Department of Intelligent Hydraulics and Automation (IHA) at Tampere University of Technology (TUT). This study was partly funded by the Academy of Finland under the project "Cooperative heavy-duty hydraulic manipulators for sustainable subsea infrastructure installation and dismantling" (Grant No. 286553), and by EUROfusion Ph.D. student funding.

I would like to express my deepest gratitude to my supervisor Prof. Jouni Mattila. It has been my absolute privilege to prepare this thesis under your supervision.

I wish to thank the preliminary examiners Dr. Wen-Hong Zhu and Prof. Guangjun Liu for the evaluation of this thesis and their reassuring comments. It was the greatest privilege to have you for this important part of the thesis.

Special thanks go to Dr. Janne Honkakorpi, who at the beginning helped me in the experiments with the dSpace real-time control system and electronics, and to IHA laboratory personnel Markku, Seppo, Ari, and Jonathan, who helped me with the experimental installations.

I want to thank the personnel at IHA and, especially, all my colleagues in room K2442B during 2011 – 2016. It has been a pleasure to work with you! I am also grateful to my friends Markku and Juha. Thank you for your friendship and understanding that I have been only occasionally available during the last years.

I want to thank my parents Irmeli and Kalevi and my siblings Nina and Jarkko for their support, love, and understanding. During this process, these people have seen (and probably also felt) the entire spectrum of the state of my mind and behaviour.

Finally, the greatest thanks goes to my beloved wife Maratee. You were the main source of motivation for this thesis.

Genova, November 2016.

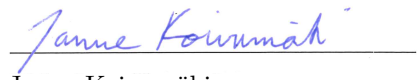

Janne Koivumäki

Contents

Acronyms

AI	artificial intelligence
ARC	adaptive robust control
DCARC	desired compensation adaptive robust control
DOF	degrees of freedom
IHA	Department of Intelligent Hydraulics and Automation
LS	load sensing
NMB	nonlinear model-based
RP	research problem
SOG	simple oriented graph
TUT	Tampere University of Technology
VCP	virtual cutting point
VDAPP	variable displacement axial piston pump
VDC	virtual decomposition control
VDP	variable displacement pump
VPF	virtual power flow

Nomenclature

Latin alphabet

$\{\mathbf{A}\}$	rigid body coordinate frame
a_e	parameter to adjust the variable impedance control
b_e	parameter to adjust the variable impedance control
$\mathbf{C_A}({}^\mathbf{A}\omega)$	Coriolis and centripetal matrix of rigid body expressed in frame $\{\mathbf{A}\}$
$\mathbf{D}_\mathrm{d}$	diagonal positive-definite desired damping matrix
$\mathbf{D}_\mathrm{d}(\boldsymbol{e}_\chi)$	diagonal positive-definite desired variable damping matrix
$\overline{\mathrm{D}}_\mathrm{d}$	upper bound desired variable damping
$\underline{\mathrm{D}}_\mathrm{d}$	lower bound desired variable damping
$\mathbf{e}_\chi$	Cartesian space position tracking error vector
${}^\mathbf{A}F$	force/moment vector in frame $\{\mathbf{A}\}$
${}^\mathbf{A}F^*$	net force/moment vector in frame $\{\mathbf{A}\}$
${}^\mathbf{A}F_\mathrm{r}$	required force/moment vector in frame $\{\mathbf{A}\}$
${}^\mathbf{A}F_\mathrm{r}^*$	required net force/moment vector in frame $\{\mathbf{A}\}$
${}^\mathbf{A}\mathbf{f}$	three-dimensional force vector expressed in frame $\{\mathbf{A}\}$
${}^\mathbf{G}\boldsymbol{f}$	Cartesian space contact force vector
${}^\mathbf{G}\boldsymbol{f}_\mathrm{d}$	desired Cartesian space contact force vector
$f_\mathrm{e}(e_\chi)$	Cartesian position error dependent function
${}^\mathbf{G}\tilde{f}$	filtered force
$\mathbf{G_A}$	gravity vector of rigid body expressed in frame $\{\mathbf{A}\}$
$\mathbf{K_A}$	symmetric positive-definite matrix characterizing velocity feedback control
$\mathbf{K}_\mathrm{d}$	diagonal positive-definite desired stiffness matrix
$\mathbf{K}_\mathrm{d}(\boldsymbol{e}_\chi)$	diagonal positive-definite desired variable stiffness matrix
$\overline{\mathrm{K}}_\mathrm{d}$	upper bound desired variable stiffness
$\underline{\mathrm{K}}_\mathrm{d}$	lower bound desired variable stiffness
$\mathbf{M_A}$	mass matrix of rigid body expressed in frame $\{\mathbf{A}\}$
${}^\mathbf{A}\mathbf{m}$	three-dimensional moment vector expressed in frame $\{\mathbf{A}\}$
$\mathbf{N}_\mathrm{c}$	mapping matrix $\mathbb{R}^2 \to \mathbb{R}^6$
$\mathbf{N}_\mathrm{x}$, $\mathbf{N}_\mathrm{y}$	mapping matrix $\mathbb{R} \to \mathbb{R}^2$
$\mathbf{P}$	block-diagonal positive-definite matrix
$\mathcal{P}(\cdot)$	projection function
$p_\mathbf{A}$	virtual power flow at frame $\{\mathbf{A}\}$
$\mathbf{Q}$	block-diagonal positive-definite matrix
$\dot{\boldsymbol{q}}_\mathrm{r}$	required joint velocity vector
${}^\mathbf{A}\mathbf{R_B}$	rotation matrix
${}^\mathbf{A}\mathbf{U_B}$	force/moment transformation matrix
${}^\mathbf{A}V$	linear/angular velocity vector of frame $\{\mathbf{A}\}$
${}^\mathbf{A}V_\mathrm{r}$	required linear/angular velocity vector of frame $\{\mathbf{A}\}$
${}^\mathbf{A}\mathbf{v}$	three-dimensional linear velocity vector of frame $\{\mathbf{A}\}$
$\mathbf{Y_A}$	regressor matrix of rigid body expressed in frame $\{\mathbf{A}\}$

Greek alphabet

ν, ξ	a non-negative accompanying function
$\boldsymbol{\Lambda}_f$	diagonal positive-definite matrix characterizing Cartesian position control
$\boldsymbol{\Lambda}_\chi$	diagonal positive-definite matrix characterizing Cartesian force control
$\boldsymbol{\theta}$	parameter vector
$\widehat{\boldsymbol{\theta}}$	estimate of parameter vector $\boldsymbol{\theta}$
$\overline{\theta}_i$	upper bound for parameter estimate $\widehat{\theta}_i$
$\underline{\theta}_i$	lower bound for parameter estimate $\widehat{\theta}_i$
κ	kappa-function for parameter adaptation
ρ_{fs}	unifying performance indicator for free-space motion control
ρ_{hmf}	unifying performance indicator for hybrid motion/force control
ρ_{imp}	unifying performance indicator for impedance control
ρ_{p}	unifying performance indicator for discharge pressure dynamics
ρ_i	parameter update gain for parameter estimate $\widehat{\theta}_i$
$\dot{\boldsymbol{\chi}}$	Cartesian space velocity vector
$\dot{\boldsymbol{\chi}}_{\mathrm{d}}$	desired Cartesian space velocity vector
$\dot{\boldsymbol{\chi}}_{\mathrm{r}}$	required Cartesian space velocity vector
${}^{\mathbf{A}}\boldsymbol{\omega}$	three-dimensional angular velocity vector of frame $\{\mathbf{A}\}$

List of Publications

This compendium thesis is based on the following four publications, **P.I**–**P.IV** (and one unpublished manuscript, **P.V**, shown in the next chapter):

P.I Janne Koivumäki and Jouni Mattila, "High Performance Non-Linear Motion/Force Controller Design for Redundant Hydraulic Construction Crane Automation," *Automation in Construction*, vol. 51, pp. 59–77, Jan. 2015.

P.II Janne Koivumäki and Jouni Mattila, "Stability-Guaranteed Force-Sensorless Contact Force/Motion Control of Heavy-Duty Hydraulic Manipulators," *IEEE Transactions on Robotics*, vol. 31, no. 4, pp. 918–935, June 2015.

P.III Janne Koivumäki and Jouni Mattila, "Stability-Guaranteed Impedance Control of Hydraulic Robotic Manipulators," *IEEE Transactions on Mechatronics*, 2016. [Accepted]

P.IV Janne Koivumäki and Jouni Mattila, "Stability-Guaranteed Multiple Cartesian Degrees of Freedom Variable Impedance Control of Hydraulic Manipulators," in *Proc. FPNI Ph.D. Symposium on Fluid Power*, Florianopolis, Brazil, Oct. 2016.

In all publications **P.I**–**P.IV**, the author of this thesis was responsible for writing the papers, developing the theories, designing the controllers, and conducting the experiments. Professor Jouni Mattila guided the author with ideas about the developed methods, reviewed the papers, and made corrections and suggestions.

Publication **P.I** proposes a state-of-the-art free-space motion tracking controller for hydraulic robotic manipulators. The controller designed in this paper serves as a baseline controller on which the contact controllers in publications **P.II**–**P.IV** are built. The state-of-the-art Cartesian position tracking performance in this paper constitutes a vital property later in publication **P.IV** where the position-tracking error data are used to detect the contact.

Publication **P.II** proposes for the first time a hybrid motion/force control for hydraulic robotic manipulators with a rigorous stability proof. In this paper, a novel force-sensorless contact force estimation method is also developed for the highly nonlinear hydraulic robotic manipulators. The estimation method is used later in publications **P.III** and **P.IV**. The experimental results demonstrate state-of-the-art control performance with the proposed controller.

Publication **P.III** proposes a novel non-switching impedance control method for hydraulic robotic manipulators. This paper implements an impedance control using the VDC framework. The rigorous stability proof for a hydraulic manipulator is provided for the

first time to cover both free-space motion and constrained motion. The experimental results demonstrate state-of-the-art control performance.

Publication **P.IV** extends the proposed impedance control method (from publication **P.III**) to a novel variable impedance control method and introduces for the first time variable impedance control with hydraulic manipulators. The proposed method is developed especially to improve Cartesian free-space position control accuracy in force-sensorless contact force control with hydraulic manipulators.

Unpublished Manuscript

In addition to publications **P.I**–**P.IV**, this compendium thesis is based on the following unpublished manuscript **P.V**:

P.V Janne Koivumäki and Jouni Mattila. "Adaptive and Nonlinear Control of Discharge Pressure for Variable Displacement Axial Piston Pumps," 2016. [Submitted]

In unpublished manuscript **P.V**, the author was responsible for writing the paper, developing the theory, designing the controller, and conducting the experiments. Professor Jouni Mattila guided the author with ideas about the developed method, reviewed the paper, and made corrections and suggestions.

Unpublished manuscript **P.V** proposes for the first time without using any linearization or order reduction an adaptive and NMB discharge pressure control design for VDAPPs, the dynamic behaviour of which is highly nonlinear and can be described by a fourth-order differential equation. A rigorous stability proof, with an asymptotic convergence, is proved for the entire system. To reach these objectives, a novel control design method (which is extended from VDC) is developed. The experimental results demonstrate state-of-the-art control performance with the proposed controller. This paper is currently under review.

1 Introduction

"*We think about how the thing moves as an ongoing process, not a series of static points in time. The key ingredient is to let the system be dynamic*"

– Marc Raibert, Boston Dynamics

Robotics is the science and technology of robots, i.e., the study of machines that can replace human beings in the execution of tasks, including both physical activity and decision making [1]. The modern meaning of the word *robot* comes from the Slavic word *robota*, meaning forced labor or slavery, and it was introduced by Czech writer Karel Čapek in 1920 in his play *R.U.R.* (*Rossum's Universal Robots*). The Robotics Institute of America (RIA) has given the following widely cited definition of robots: "*A robot is a reprogrammable multifunctional manipulator designed to move material, parts, tools, or specialized devices through variable programmed motions for the performance of a variety of tasks.*" *Robotic manipulators* are kinematically composed of links connected by joints to form a kinematic chain [2]. The robot *end-effector* is the part mounted on the last link to do the required job of the robot [2]. *Advanced robotics* usually refers to the science studying robots with marked characteristics of autonomy, the applications of which are conceived to solve operation problems in hostile environments or to execute service missions [1].

Robots have made—and are still making—a considerable impact on many aspects of modern life, from industrial manufacturing to healthcare, transportation, and exploration of the sea and deep space [3]. Currently, robotics technology is booming; it is projected to dominate during the coming decade, and substantial growth is expected for the robotic market [4]. Indeed, advanced humanoid robots [5–9], quadruped robots [6, 10], surgeon robots [11], and walking excavators [12, 13] are already here. Robotics is an interdisciplinary branch of science, involving such areas as *mechanics*, *electric*, *electronics*, *automatic control*, *material science*, *computer science*, *mathematics*, and *information theory* [1, 2, 14].

The structure of a basic robotic system is illustrated in Fig. 1.1. The robot's capability for action is provided by a *mechanical structure* (see block 3 in Fig. 1.1). The mechanical structure creates a movable skeleton for the robotic system composed of a sequence of *links* connected with *joints*. Links in the system can be rigid or flexible. In this thesis, the system is considered to be composed of rigid links only. The joints can be unactuated or actuated with a specific actuator. Comprehensive studies on actuator technologies for robotics can be found in [3, 15, 16]. A robot's structural design focuses on the number of joints, physical size, payload capacity, and movement requirements of the end-effector [3].

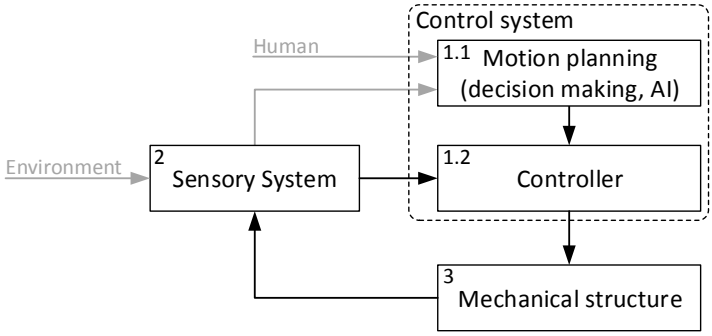

Figure 1.1: Illustration of a common structure of a robotic system.

The robot structure has two basic topologies: *serial robot* (open-loop chain) and *parallel robot* (closed-loop chain) [1–3]. In this thesis, the focus is on serial robotic manipulators.

In most cases with robotics, a complete real-world model is not available, and perfect models of mechanical systems are never realistic. Consequently, a *sensory system* (block 2 in Fig. 1.1) is used to compensate for this lack of complete information; its role is to provide information for a *control system* about the states of the mechanical structure (with proprioceptive sensors) and, if necessary, the status of the environment (with extroceptive sensors) [1, 3]. Thus, the *sensory system* can provide a method of perception for the robotic system. Detailed information on sensors used in robotics can be found in [3].

The uppermost layer in a robotic system is the *control system*. As Fig. 1.1 shows, this layer is divided into *motion planning* (high-level control in block 1.1) and the *controller* (low-level control in block 1.2). The aim of motion planning is to generate the reference inputs (trajectories) for the controller. Depending on the technical level of the robotic system (and the level of autonomy), motion planning can consist of methods ranging from simple trajectory planning to artificial intelligence (AI), which is one of the original goals of robotics. In addition, methods that unify the trajectory planning and tracking tasks in one (for dynamic catch, grasp, and carry maneuvers) have been proposed [17]. In advanced operations, such as decision making, sensory system data may be needed, e.g., to detect obstacles in the environment. In addition, the human operator may be responsible for generating the output of this layer, e.g., in robotic tele-operation. Recent advances, such as deep learning [18, 19] (which is a new area of machine learning with the objective of moving closer to advanced AI), have provided promising results. In addition, companies like Google and many leading automotive companies have made significant investments in developing advanced decision making and AI algorithms, e.g., to realize driverless robotic cars [20–23].

The controller (block 1.2 in Fig. 1.1) is responsible for executing the planned trajectories of motion planning. In [1], the control of a robotic manipulator is specified as the problem of determining the generalized forces/torques to be developed by the joint actuators so that execution of the commanded task is guaranteed while satisfying given transient and steady-state requirements. In addition to the execution of specified tasks in free space, the specified tasks can also be the execution of specified motions and contact forces for a manipulator whose end-effector is constrained by the environment.

The main focus in this thesis is to extend the state of the art in closed-loop control of hydraulic robotic manipulators. Thus, this thesis addresses the control design in block 1.2 in Fig. 1.1.

1.1 General Challenges in Closed-Loop Controlled Robotic Systems

The applications of robots are increasing all the time, and robotic structures are becoming more complex [2]. For advanced robotic systems, such as those introduced in [5–13], the number of actuators, i.e., the number of degrees of freedom (DOF) of motion, can easily be more than thirty, making their kinematic structures and dynamic behaviour very complex. With articulated robotic systems, the associated multibody dynamics is nonlinear by nature, thus complicating the system control design [1]. In addition, the dynamic behaviour of the system actuators can be highly nonlinear (depending on the utilized actuators), making the control design task even more multifaceted.

If impeded by significant nonlinearities in the system dynamics, traditional linear (or linearized) control methods are typically inadequate for high-performance control of robotic systems. This is because these methods can provide tolerable control performance only at a narrow range (at small signal magnitudes) in the nonlinear operational space and become unstable at a larger range. To address the highly nonlinear dynamic behaviour of robotic systems, nonlinear model-based (NMB) control methods can be used. In contrast to linear control methods, NMB control methods (where the specific feedforward control term is used for system nonlinearities) can theoretically provide "infinite" control bandwidth in the entire nonlinear operational space, as long as proper feedforward control is designed [24].

In NMB control, the system control design is based on the system dynamic model. As introduced in many books on robotics [1–3, 25, 26], for robotic systems the control designs are based on the complete dynamic models of robots using the *Lagrange method*. However, as discussed in [24, 27], with these Lagrange-based control methods the complexity (computational burden) of robot dynamics is proportional to the fourth power of the number of DOF of motion. Thus, it is very difficult, if not impossible, to implement the complete-dynamics-based control on a single computer [24] for advanced robotic systems like [5–13], where the number of DOF of motion can easily be more than thirty.

In (complex) robotic systems, a great number of different parameters can exist in the dynamic model of the system. What is more, large uncertainty can exist in the parameter values, and some parameters can vary in time. Adaptive control is a mechanism for adjusting these parameters online based on signals in closed-loop systems [3]; the original goal is to control plants with unknown parameters [28]. As the structures of robotic systems are becoming increasingly complex, as projected in [2], the number of individual system parameters and the level of overall parameter uncertainty are increasing. However, addressing parameter uncertainties with adaptive control would further complicate the design of control systems and require more computation power, which might already be a problem as shown in the previous paragraph.

The backstepping method [28] is the best-known and most widely used NMB control method, and it has become a powerful tool in the adaptive control area for nonlinear systems [29]. This method provides tools for designing adaptive control systems with rigorously addressed system stability and error convergence, and it provides the possibility of including a broad class of nonlinearities in the control system design. However, recently various researchers have become aware of the inherent problem of the "explosion of complexity" in backstepping design methods [29–32]. This problem originates from the fact that the computational complexity increases with the system order due to the necessity to perform repeated differentiations of the nonlinear functions [29, 32].

Most likely, based on the above reasons, very simple low-level controls are still used in complex robotic systems (see, e.g., Section 4.6 in [9]). Thus far the main interest, e.g., with the humanoid robots, has been balancing during locomotion and recovering from a fall. Because of this, precision control (addressing the system's full dynamic behaviour) has long been overlooked (as witnessed by [9]), and the motions of these systems are still quite clumsy. However, as technology moves toward more advanced, human-like behaviours and motions, it is evident that more sophisticated control solutions are needed.

This thesis examines a novel subsystem-dynamics-based control design method, the virtual decomposition control (VDC) approach [24, 33], for hydraulic robotic manipulators. This method has been proven to provide state-of-the-art closed-loop control with electric manipulators (see [34–39]) and to overcome the computational burden of Lagrange methods (see [24, 39]) while still realizing full-dynamics-based control without additional approximations.

1.2 Special Challenges in Closed-Loop Controlled Hydraulic Robotic Systems

Hydraulic actuators are advantageous for robotic systems because (compared to electric actuators) they can produce significant forces and torques for their size and they are robust. However, compared to an electric actuator (where the relation between the actuator control input, i.e., electric current, and the actuator output, i.e., torque, can be approximately linear), high-performance (force) control of a hydraulic actuator is truly challenging [40]. This is because the actuator (with nonlinear dynamic behaviour) is controlled indirectly with an electro-hydraulic valve (with nonlinear dynamic characteristics). In addition, these systems may be subjected to non-smooth and discontinuous nonlinearities due to actuator friction, hysteresis, control input saturation, directional change in valve opening, or valve under/overlap; typically, there are also many model and parameter uncertainties [41–43]. The control design of hydraulic robotic systems is further complicated by the nonlinear nature of the associated multibody dynamics. Thus, it is quite evident that traditional linear control methods are inadequate for high-performance closed-loop control of hydraulic robotic systems, and it can be argued that NMB control methods are the best option to control these highly nonlinear systems.

Based on the large power-to-weight ratio, hydraulic (robotic) manipulators are typically built to operate heavy objects (e.g., logs) or to exert large forces on the physical environment (e.g., excavation). For advanced hydraulic robotic systems, such as those introduced in [6–10, 12, 13], it is evident that free-space motion control alone is inadequate for the completion of different tasks (e.g., legged locomotion or manipulation of the environment), and the robotic system must be capable of controlling its interaction forces with the surrounding environment. However, despite considerable research in recent decades, closed-loop control of physical interaction is still a challenging research issue, and contact control applications are insignificant in comparison to free-space robot applications [44]. One of the most critical factors inhibiting the widespread use of contact control applications has been the control system stability problems [44].

In contact tasks, control system stability (the primary requirement for all control systems [28]) has drawn considerable attention since the installation of the first industrial robots. Numerous reasons for unstable responses have been identified (see [45–50]), and one of the most significant reasons is that contact dynamics between the robotic system and the environment can be drastic while the nonlinear dynamics of a robot are not

considered rigorously [47, 51]. Thus, in contact tasks with highly nonlinear hydraulic robotic systems, the demand for NMB control is even stronger (compared to free-space motion control tasks or contact tasks with electric manipulators) to rigorously address the system's highly nonlinear dynamic behaviour. However, stability-guaranteed NMB control of hydraulic robotic manipulators has been a significant design challenge when only free-space motions are considered (see the discussion in [52]). Evidently, with the addition of constrained motions, the design of stability-guaranteed NMB control is an even more multifaceted challenge. In fact, a stability-guaranteed NMB control design for hydraulic robotic systems has remained an open problem in constrained motion tasks. Based on these challenges, the hydraulic robotic manipulators are still almost entirely controlled with operator-based open-loop controls (e.g., with joysticks) without any automated functionality.

In this thesis, publications P.I through P.IV extend the state of the art in the closed-loop control of hydraulic robotic manipulators, covering free-space motion control and different types of constrained motion controls.

1.3 Force-Sensorless Contact Force Estimation

Contact force control requires force feedback. The conventional method of performing robot force control requires a six-DOF force/moment sensor, which is placed at the end-effector. As shown by the research of Stolt et al. [53, 54], force-sensorless contact force control has received significant interest in recent years. In [53], force-sensorless contact force sensing was realized for a redundant electronic seven-joint robotic arm by estimating the contact forces from the measured joint torques and position errors. In [54], a machine-learning-based classifier was proposed to detect contact force transients in robotic assembly tasks. The paper [53] received the Best Automation Paper Award at ICRA 2012, and the paper [54] was a finalist for the Best Automation Paper Award at ICRA 2015.

In contact tasks with hydraulic robotic manipulators, the use of a conventional six-DOF force/moment sensor can be very problematic. Built using either strain-gauge technology or optics, this sensor is usually sensitive to shocks and overloading, a situation that frequently occurs in hydraulic operations. Moreover, in many heavy-duty tasks (e.g., excavation and logging) use of this fragile six-DOF force/moment sensor at the end-effector is not even practically possible due to the nature of contact tasks. This motivates the development of new advanced solutions for hydraulic robotic manipulators to eliminate the use of force sensors at the end-effector. However, it is evident that the highly nonlinear nature of hydraulic manipulators (compared to electric manipulators) makes the realization of force-sensorless contact force estimation a challenging task.

In this thesis, publication P.II proposes a novel method for force-sensorless contact force estimation for hydraulic robotic manipulators.

1.4 Hydraulics and Energy Efficiency

Along with the robotics technology, energy efficiency is another high-impact topic. Today, strict administrative regulations surround energy issues for industry. For instance, the new European Union (EU) directive for energy efficiency [55], effective since October 2012, demands that EU countries reduce energy consumption at a rate of 1.5% per year.

Similar targets have been set, for example, by the 12th Chinese Five-Year Plan [56], which mandated that energy use should be reduced by 16% before 2016.

It is well-known that conventional hydraulic systems are not energy efficient. In most conventional hydraulic systems, a constant amount of fluid is discharged into the system (using a constant displacement pump) regardless of the actual system demands. An excessive amount of fluid is then discharged back to the reservoir through a pressure relief valve, which simultaneously determines a constant supply pressure level for the system. Thus, a significant amount of energy is typically wasted across the pressure relief valve.

In many industrial systems, especially in stationary applications, energy efficiency can be a secondary design objective compared to other performance requirements. However, the situation becomes different in mobile (off-highway) machines where energy source(s) must be carried on board in limited space. What makes energy efficiency challenging, especially in advanced robotic systems, is that it cannot be achieved at the expense of lower control performance. Currently, only servo hydraulic control can provide the required control performance for robotic systems in terms of control accuracy and response time. However, the very nature of servovalve control is dissipative as the control principle of servovalves is accomplished by dissipating power via valve meter-in and meter-out throttling losses to heat energy [57]. In some studies, e.g., [58] and [59], pump displacement control[1] is proposed as an alternative to servovalve control. Although actuators with pump displacement control can provide better energy efficiency, their dynamic response is typically much slower compared to that of servovalves [57]. In pump displacement control studies (e.g., [58] and [59]), there is a lack of attention to the tracking performance, which is essential in robotics.

One solution to improving the energy-efficiency of the system without control performance deterioration may be the combination of servovalve control and pump displacement control. In this solution, the servovalve between the system pump and the actuator is responsible for high-performance control accuracy, whereas the system pump is responsible for providing the fluid flow rate to meet the demands of the actuator in an energy-efficient manner. The hydraulic power P transferred into the system is a product of the pump flow rate Q_p and the discharge pressure p_s ($P = Q_\mathrm{p} p_\mathrm{s}$).

Variable displacement pumps (VDPs) are devices that enable one to regulate the hydraulic power delivered to the system. Among VDPs, variable displacement axial piston pumps (VDAPPs) are the best-known and most widely used VDPs, and during the past decades, these pumps have attracted significant research interest (see [60 – 67]). The amount of fluid discharged into the system per revolution of the VDAPP's input shaft can be adjusted by varying the pump's swash plate angle, which is done by driving a swash-plate-mounted control piston through a specific control valve. In these systems, the discharge pressure is a build-up function of the system resistance to the discharged fluid flow, and the pressure relief valve is used only as a safety valve (not to define the system discharge pressure level). Thus, from the control point of view, optimized energy consumption can be achieved if the discharge pressure remains a bit higher than the required load pressure.

The load sensing (LS) systems (see [68 – 72] for traditional LS systems and [73 – 75] for electric LS systems) are built on this idea, and they are considered to be one of the key technologies for improving the energy efficiency of hydraulic systems. However, in LS systems the load dynamics and the pump dynamics become heavily coupled through a

[1] In this method, a variable displacement pump (VDP) is used to set the pump displacement to meet the demands of the actuator without using the load control valve between the pump and the actuator.

specific LS mechanism. Consequently, LS systems are well known for their oscillatory or even unstable behaviour (see [68, 69, 71]), which is caused by the highly complex nature of pressure dynamics and the interaction between the LS mechanism and the load.

An alternative method for controlling LS systems is to design a discharge pressure controller with the electro-hydraulically controlled VDAPP. In this method, the control objective is to make a system's discharge pressure track a prespecified desired discharge pressure trajectory. However, the design for such a pressure tracking controller is not straightforward. The mapping between the discharge pressure and the control valve input is very complex, governed by a highly nonlinear fourth-order differential equation, making the control design task extremely challenging. This difficulty in control design has prevented many previous researchers from adopting full-model-based nonlinear control, forcing them to use either linearization or model-reduction methods at the expense of control performance.

Other solutions for controlling the hydraulic power supply exist. One feasible solution is to use a constant displacement pump with an angular velocity controlled (electric) motor [76]. Although this solution can substantially simplify the system dynamics and control, the control of the input shaft angular velocity can lead to conservative and large servomotor sizing, which might not always be feasible. In addition, with this method, the dynamic response would be at least four times slower compared to the responses of the VDP [76].

One recent and very promising method for hydraulic power supply control is digital hydraulic pumps [77–81]. This method has shown a substantial potential for reduced system energy consumption.

In this thesis, paper P.V proposes a novel solution for discharging pressure control with an electro-hydraulically controlled VDAPP.

1.5 Misconceptions in Hydraulics

Hydraulics is widely considered a noisy, messy, and environmentally unfriendly technology. This is not completely true. The poor environmental image of hydraulics originates from oil leaks. However, leak-free component designs and fittings have been readily available for years [84]. Moreover, oil leaks typically originate from insufficient installations, lack of maintenance, and use of inappropriate components. Fig. 1.2(a) and Fig. 1.2(b) show examples of clean high-tech commercial hydraulic manipulators developed for underwater manipulation and nuclear decommissioning, respectively. As these images show, the structure of these systems is compact, with body-integrated hydraulic power transmission.

(a) Schilling ORION [82] for underwater manipulation

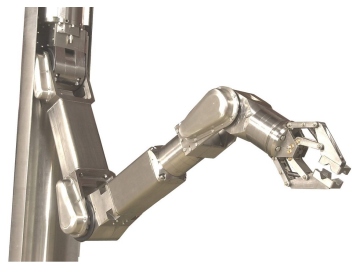

(b) Cybernetix's MAESTRO [83] for nuclear decommissioning

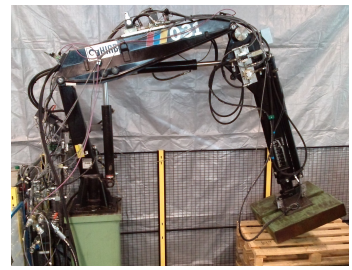

(c) HIAB031 for academic research purposes

Figure 1.2: Hydraulically actuated robotic manipulators

In contrast, Fig. 1.2(c) shows a hydraulic manipulator used in academic research (the system in this figure is used as an experimental platform in this thesis). This system contains a variety of research installations, making the system look messy. Unfortunately, academic systems like this may misleadingly promote a picture of messy hydraulics.

With hydraulic systems, it is evident that all noise cannot be totally eliminated. However, a number of products and techniques exist to bring the noise down to an acceptable level [85]. In December 2015, the US military shelved Boston Dynamics' (Google's) hydraulically actuated BigDog due to its noisy operation [86]. However, the main reason was not the hydraulics; instead, it was the noise of the petrol-powered engine. The company then created a much quieter, still hydraulically actuated, electric-powered alternative called Spot. Studies on the reduction of noise in hydraulic systems can be found in [85, 87].

1.6 Motivation and Research Problem

Hydraulic actuation can benefit robotic systems with its superior power-to-weight ratio. As discussed in Sections 1.1–1.3, fundamental challenges are found in complex hydraulic robotic systems: 1) The dynamic behaviour of hydraulic systems is highly nonlinear, making force control, especially in constrained motions, a truly challenging task, 2) traditional hydraulic systems are not energy efficient, and 3) when moving toward complex hydraulic robotic systems (even with hyper-DOF of motion), high-performance control in real time becomes a substantial challenge with the commonly used Lagrange-based control design methods. These three fundamental challenges together with the megatrends of robotics and energy efficiency provided the main motivation for this study *to improve the state of the art in the control of hydraulic robotic manipulators and to close the gap between the performances of hydraulic and electric manipulators.*

Beyond the academic robotic systems, hydraulic "robotic" manipulators have been widely used in various heavy-duty working machines (e.g., in construction, forestry, mining, and agricultural machines) for decades. Finland already has a substantial strategic industrial sector for manufacturing hydraulic high-tech heavy-duty working machines (e.g., companies like Ponsse, Sandvik [formerly Tamrock] and Cargotec). Therefore, innovative solutions that provide increased levels of automation, safety, and energy efficiency would strengthen the competitiveness and protect the leading position of Finland's mobile machine manufacturing industry. This provided an additional source of motivation for the research in this study (in papers **P.I**–**P.V**) *to develop methods that are beneficial for and applicable to industrial hydraulic machines, as well as for advanced (academic) hydraulic robotic systems.*

In view of Sections 1.1–1.3, the research problem (RP) addressed in this thesis involves the design of NMB controller(s) for hydraulic robotic manipulators with the following features:

1. **High performance**: The developed controller(s) should be capable of 1) rigorously addressing the highly nonlinear dynamic behaviour of the entire system and 2) realizing the state-of-the-art control performance;
2. **Adaptive control**: The developed controller(s) should be capable of addressing a wide variety of system parameter uncertainties in hydraulic robotic systems;
3. **Stability-guaranteed**: A rigorous stability proof should be provided for the developed NMB controller(s);

4. **Real-time applicable**: The developed controller(s) should be computationally deterministic and applicable to real-time control. The computational burden of Lagrange-based control methods (see Section 1.1) should be avoided to provide the possibility (in future studies) of extending the proposed methods to complex robotic systems in which the number of DOF of motion can easily exceed thirty;
5. **Modularity**: The developed controller(s) should be composed of elementary modular "subsystems" similar to the "subsystems" of a real robotic system, such that changes to the original system affect only the respective local control equations associated with this subsystem, while the other control equations associated with the rest of the system remain unchanged. Once designed, the ensemble, e.g., a hydraulic manipulator with its control, should be able to be "plugged" into another system, without redesigning the control for the entire system. The controller architecture should allow the replacement of the actuators, e.g., from hydraulic to electric, without substantial controller redesign;
6. **Force estimation**: A practical solution for force-sensorless contact force control should be provided, because the typically six-DOF force/moment sensors (at the system end-effector) are sensitive to shocks and overloading, a situation that frequently occurs in hydraulic operations; and
7. **Experimentally verified**: The developed controller(s) should be practically implemented and experimentally verified.

Further, in view of Section 1.4, the RP addressed in this thesis involves the design of an NMB controller for the VDAPP with the following feature:

8. **Energy efficiency**: An advanced control for the VDAPP should be designed that provides the possibility of reducing energy consumption. The designed controller should meet the features defined in items 1 through 4 and 7.

1.7 Restrictions

There are no major restrictions in the utilized control design framework. This is because the VDC principles can be applied to robotic systems without restrictions on the target systems and without foreseeable boundaries to virtually decompose subsystems into sub-subsystems [24]. In addition, the control design principles of VDC are extended in this thesis from robotic systems to a broader group of dynamic systems. This thesis uses the assumption of a rigid body, meaning that all the links in the studied robotic system are assumed to be rigid. However, control of flexible link robots is incorporated into the VDC framework (see [24, Chapter 13]).

High-performance control requires high-performance hardware. The controller architectures proposed in this thesis are no exception and require high-frequency and low-latency hardware. Thus, high-end hardware components (e.g., control valves, pressure sensors, incremental encoders, and a real-time control system) are needed. In addition, the time derivatives (e.g., velocities and first-order pressure dynamics) of the system states exist in the control designs. It is well-known that, especially with a high sampling rate, approximation methods for the derivative (e.g., backward difference) often lead to noisy differentiated signals. Thus, more advanced approximation methods can be needed with high-resolution sensors.

Using digitalized position measurements to estimate acceleration is difficult and sometimes impractical. If only the angular encoders are available, the contact force can be estimated using the cylinder pressures and removing the gravitational forces (see publication **P.II** for more details). This was the case in the proposed contact force estimation method in publication **P.II**. However, this scheme works only for slow motions with negligible accelerations and velocities. If inertia, Coriolis, and centripetal forces must be considered, one practical method for estimating the accelerations and velocities of the system's links can be found in [88]. Improving the contact force estimation accuracy is left to future studies.

If cylinder pressure sensors are used in the contact force estimation instead of cylinder rod loadcell sensors, the piston friction, which totals about $1-2$ kN, then comes into play. Fortunately, due to the studied hydraulic manipulator's special geometry (see Fig. 1.2(c)), the piston's friction forces reflected to the end-effector are scaled down by an order of magnitude (10 times, for example) that depends on the manipulator's configuration. Therefore, if force control accuracy within 200 N is considered acceptable, there is no need to implement loadcell sensors. These sensors are necessary only when higher force control precision is required.

In unpublished manuscript **P.V**, which concerns discharging pressure control with the electro-hydraulically controlled VDAPP, a constant orifice was used as the system load. In robotic systems this is generally not the case because actively controlled orifices (control orifices in the valves) are used to control the system load. Thus, with the proposed method in unpublished manuscript **P.V**, more detailed experiments with varying system loads are still needed to verify the method's feasibility in reducing energy consumption for hydraulic robotic systems.

1.8 Contributions

The scientific contributions of this thesis are as follows:

C1 An experimentally verified, stability-guaranteed, state-of-the-art free-space position tracking controller is proposed for hydraulic robotic manipulators;

C2 An experimentally verified, stability-guaranteed NMB controller is proposed for the first time for hydraulic robotic manipulators performing contact tasks (with hybrid motion/force control); the state-of-the-art Cartesian force and motion tracking performance is demonstrated;

C3 A novel force-sensorless contact force estimation method is proposed for hydraulic robotic manipulators;

C4 A novel, stability-guaranteed impedance control method is designed using the framework of VDC;

C5 A special connection between the proposed impedance control parameters and the targeted impedance is discovered, making stability-guaranteed hydraulic robot impedance control possible;

C6 An experimentally verified, stability-guaranteed NMB controller is proposed for hydraulic robotic manipulators for the first time covering both free-space motion and constrained motion; this contribution is made with the proposed novel impedance control method, and the state-of-the-art impedance control performance is demonstrated;

C7 A variable impedance control is proposed for the first time for hydraulic robotic manipulators; the proposed method is stability-guaranteed and experimentally verified;

C8 A novel, rigorous NMB control design method is proposed by extending the control design principles of VDC from robotic systems to a broader group of dynamic systems; this is done by generalizing the concept of virtual power flows (VPFs) in VDC to new terminologies such as *stabilizing terms* and *stability preventing terms*, that can have units beyond the original power units;

C9 Using the proposed NMB control design method (in **C8**), an experimentally verified, stability-guaranteed, adaptive NMB controller is proposed for VDAPPs (whose dynamics are highly nonlinear and can be described by a fourth-order equation) for the first time without using any linearization or order reduction.

1.9 Outline of the Thesis

This compendium thesis is composed of four publications **P.I**–**P.IV** and one unpublished manuscript **P.V**. These papers are attached.

This thesis is divided into six chapters. The content of the remaining chapters is summarized below.

Chapter 2 reviews the state of the art in the field of control of serial-chain hydraulic robotic manipulators and discharge pressure control with electro-hydraulically controlled VDAPPs.

Chapter 3 introduces first the mathematical preliminaries needed in the VDC control design. Then, based on the VDC approach, the designed Cartesian free-space and constrained motion control methods for hydraulic robotic manipulators are provided. Finally, the extendability of the VDC principles beyond robotic systems is briefly discussed.

Chapter 4 presents the experimental results of this thesis, including the free-space position tracking performance, hybrid motion/force control performance, impedance control performance, and variable impedance control performance for the hydraulic robotic manipulator. The discharge pressure tracking performance with the electro-hydraulically controlled VDAPP, using the proposed novel control design method, is also shown.

Chapter 5 discusses how all the RPs are addressed and summarizes the results in Chapter 4.

Chapter 6 concludes this thesis and provides a discussion of future work.

2 Review of the State of the Art

This chapter reviews the state of the art in the field of control of serial-chain hydraulic robotic manipulators and electro-hydraulically controlled VDAPPs. In this thesis, a manipulator is considered a serial manipulator if it has only one chain of links from the base to the end-effector, as shown in Fig. 1.2. Before the hydraulic robotic manipulators are described, the most significant research on the control of single-DOF electro-hydraulic systems is first briefly introduced in Section 2.1. Then, Section 2.2 shows the state of the art in free-space motion control of hydraulic serial manipulators. Methods for constrained motion control with hydraulic serial-chain manipulators are introduced in Section 2.3. Section 2.4 shows the methods for discharge pressure control with electro-hydraulically controlled VDAPPs. Finally, a summary of the state-of-the-art methods in Sections 2.2 – 2.4 is given in Section 2.5.

2.1 Single-Degree-of-Freedom Electro-Hydraulic Servosystems

As introduced in Section 1.2, high-performance force control of electro-hydraulic servosystems with only a single-DOF is challenging because of their highly nonlinear dynamic behaviour. Edge [42] presented a survey of control of electro-hydraulic servosystems, covering the early days from the 1970s to 1996. In [89], Edge extended the survey in [42] to cover 1997 – 2003.

High-performance NMB control of electro-hydraulic servosystems, with rigorously proven stability, has been well studied in recent decades. In one pioneering single-DOF study, Alleyne et al. [90, 91] proposed Lyapunov-based control algorithms with parameter adaptation for force tracking control of an electro-hydraulic actuator. Sohl and Bobrow [92] also proposed a Lyapunov-based nonlinear position tracking controller. Sirouspor and Salcudean [93] proposed nonlinear control for hydraulic servosystems based on the backstepping design strategy, incorporating parameter adaptation to deal with uncertainties in hydraulic model parameters. Niksefat et al. [94, 95] proposed stable control for an electro-hydraulic actuator for contact tasks. In their work, a Lyapunov-based controller was designed to cover both free-space and constrained motions. Bu and Yao proposed adaptive robust control (ARC) [43] and desired compensation adaptive robust control (DCARC) [96] for electro-hydraulic servosystems. Guan and Pan [97] proposed adaptive sliding mode control for electro-hydraulic systems with nonlinear unknown parameters. In addition, they proposed ARC of a single-rod electro-hydraulic actuator with unknown nonlinear parameters [98]. Nakkarat and Kuntanapreeda [99] proposed observer-based backstepping force control of an electro-hydraulic actuator. Most recently, Kim et al. [100] proposed flatness-based nonlinear control for position tracking for electro-hydraulic systems. In addition, the same authors (Won et al. [101]) proposed high-gain disturbance observer-based backstepping control without tracking error constraint. Both [100] and [101] showed very

accurate position tracking (error < 0.4 mm) for the hydraulic cylinder when driving a single-DOF boom.

2.2 Hydraulic Serial Manipulators in Free-Space Motion

Various free-space control strategies have been proposed for hydraulic manipulators, e.g., feedback linearization and linear quadratic optimal control [102], computed-torque and variable-structure multi-variable control [103], decentralized adaptive control [104], fuzzy control [105], adaptive model-based actuator control and linear perturbation adaptive control algorithms [106], sliding mode control [107–109], sliding mode control with active disturbance rejection [110], computed-torque control [111], observer-based ARC [112], DCARC [96], model-based control [113], two-DOF control with parallel feedforward compensators [114], time-delay control [115], model reference adaptive control [107, 116], robust position control based on sliding-mode control [117], feedforward Cartesian control [118], adaptive backstepping control [119], VDC [120–122], proportional integral derivative (PID) structures with feed-forward components [123], and model predictive control [124].

In addition, preliminary solutions for decreasing the energy consumption of hydraulic manipulators, using separate-meter-in-separate-meter-out control [125], have been proposed in [111, 122, 126].

Bech et al. [107] and Bonchis et al. [116] evaluated different control strategies with a hydraulic robotic manipulator. In [107], different linear and nonlinear controllers were evaluated, demonstrating that all nonlinear controllers gave better performance than the best linear controller. In [116], ten different control strategies were evaluated, with similar observations as [107].

As discussed in Section 1.2, stability is the primary requirement for all control systems [28]. However, one design challenge related to NMB control of hydraulic manipulators has been the lack of stability proofs for the proposed control laws [52]. Only a few of the control approaches provide guaranteed stability for hydraulic manipulators in free-space motion. These approaches are based on backstepping [96, 112, 119], sliding mode control [107, 117] ([117] with simulation results only), model reference adaptive control with velocity measurement [107], and the L_2 and L_∞ stability and VDC approach [120–122]. For serial-chain hydraulic robotic manipulators, the studies [107, 120, 121] show the state of the art in free-space motion control[1].

In addition to serial-chain hydraulic robotic manipulators, some Lyapunov-based stability-guaranteed NMB control designs have been proposed for parallel-chain hydraulic robotic manipulators (Stewart-Gough Platforms) in [52, 127–131]. Sirouspour and Salcudean [52] showed state-of-the-art parallel-chain hydraulic robotic manipulators in free-space motion control.

2.3 Hydraulic Serial Manipulators in Constrained Motion

The basic approaches for robotic force control can be roughly divided into methods that originate from hybrid position/force control by Raibert [132] or impedance control by Hogan [133]. In hybrid position/force control, the task space is divided into two

[1] Different control methods were evaluated using the unifying performance indicator, discussed in more detail in Section 4.1.

orthogonal non-conflicting subspaces, where end-effector motions are controlled in the subspace where there are natural constraints on the contact forces, whereas the end-effector forces are controlled in the subspace where there are natural constraints on the motions. In impedance control, end-effector motion and force trajectories are not tracked directly, but control is established by defining a dynamic relation between the end-effector positions and the interaction forces. Historical overviews of robot force control can be found in [44, 51, 134, 135].

Different force control methods with electrically driven manipulators have been extensively studied [132, 133, 136–140]. Compared to electric manipulators, one advantage of hydraulic manipulators is their ability to generate significantly larger forces with respect to their size without concern about overloading. Consequently, typical tasks with hydraulic manipulators are tasks in which heavy objects (e.g., logs) are handled or tasks in which forces need to be exerted on the physical environment (e.g., excavation). Therefore, it is surprising that only a few studies exist regarding closed-loop constrained motion (contact force) control of hydraulic robotic manipulators.

Ostoja-Starzewski and Skibniewski made one of the early attempts at contact control with hydraulic manipulators [141]. In their study, the master-slave force-feedback method for hydraulic manipulators was proposed; however, no experimental data or detailed control designs were given.

Dunnigan, Lane, Clegg, et al. proposed hybrid position/force control [142], adaptive hybrid position/force control [143], and self-tuning position and force control [144] for an underwater hydraulic manipulator. In [143], variable structure control and multivariable self-tuning adaptive control were used for the manipulator. No stability proofs for the proposed controller designs were given.

Heinrich et al. [145] implemented impedance control with nonlinear proportional-integral (NPI) joint control for a hydraulic manipulator. A rigorous stability proof of the proposed controller design was not given.

Ha et al. [146, 147] proposed impedance control for a hydraulically actuated robotic excavator. They designed a robust sliding mode controller, incorporating a fuzzy tuning approach, for an excavator using generalized excavator dynamics. A discontinuous observer was developed for estimating the piston displacement velocity and disturbance, including load force and friction. Asymptotic convergence for the impedance error (considering the manipulator equation of motion, sliding function, and the target impedance law) was provided. However, the stability of the electro-hydraulic control (in Section 4.3 in [147]) and observer-based disturbance estimation (in Section 4.2 in [147]) was not discussed. The validity of the proposed method was experimentally verified with a three-DOF hydraulic backhoe manipulator.

Tafazoli et al. [148] (see also their related studies in [149–151]) proposed impedance control for a teleoperated mini-excavator based on a simple proportional-derivative (PD) controller. The stability proof for the simple PD impedance controller was provided, but it was limited to the single-DOF hydraulic cylinder acting on the environment.

Itoh et al. [152] proposed a minimal controller synthesis (MCS) algorithm for adaptive impedance control of hydraulic manipulators. The stability of the proposed method was provided based on the hyperstability theorem. Experiments with a two-DOF hydraulic robot, with an end-effector-attached force sensor, illustrated the validity of the proposed method.

A major step forward from the existing solutions was taken by Zeng and Sepehri [153], who proposed nonlinear tracking control with internal force control for multiple hydraulic manipulators handling a rigid object. Their control design was based on backstepping, and the stability of the entire system was proven. However, the stability analysis was limited to situations in which a connection to the held object was already established. The experiments were carried out with two single-axis electro-hydraulic actuators, which were connected to the common object with spring mechanisms [154], thus preventing unilateral constraint.

Boaventura, Semini et al. [155 – 157] proposed active impedance control for lightweight hydraulic legs in their quadruped HyQ robot. In their control designs, feedback linearization was used to linearize the relation between the control input and the controlled variable. As an interesting contribution in [155], the concept of Z-width, i.e., the achievable range of impedance to keep the system passive, was extended to hydraulic legged robots for the first time.

Based on the author's best knowledge, variable impedance control has not been studied and tested with hydraulic manipulators. Research on variable impedance control methods with electrical manipulators can be found in [158 – 165].

2.4 Hydraulic Power Supply Systems

As discussed in Section 1.4, LS systems are considered one of the key technologies for improving the energy efficiency of hydraulic systems. However, these systems are well-known for their oscillatory or even unstable behaviour. An alternative method for controlling LS systems is to design a discharge pressure controller with an electro-hydraulically controlled VDAPP, where the control objective is to make a system's discharge pressure track a prespecified desired discharge pressure trajectory.

Research on reducing the VDAPP's fourth-order dynamics to the second order can be found in [61, 62, 65]. Lin and Akers presented in [166] one of the early works on electro-hydraulically controlled VDAPPs, employing a linear control method. More linear and reduced order control strategies for electro-hydraulically controlled VDAPPs can be found in [58, 167, 168].

A significant step forward was taken in [169], in which Kemmetmüller et al. proposed a model-based nonlinear control strategy with a load estimator. Based on singular perturbation theory, reduced order dynamic models, e.g., neglecting the second-order swash plate motion model, were used in the controller design. The stability of the controller design with load estimation was provided. The results of this study showed a significant improvement in the discharge pressure control performance compared to the linear controllers.

Guo and Wei [170] proposed an ARC design, where parameter adaptation was incorporated for three system parameters. As a disadvantage, a swivel torque was approximated with a reduced order polynomial function, and the controller performance was evaluated with simulations only.

Wei et al. [171] proposed a nonlinear discharge pressure control for a VDAPP with a disturbance observer for the varying load. Sliding mode control was used to compensate load flow estimation error. The system used a simplified second-order dynamic model. The stability of the whole system was proved using Lyapunov theory.

Both state-of-the-art studies [169] and [171] applied in their experiments a narrow discharge pressure range (with range of $\leqslant 60$ bars).

2.5 Summary

NMB control methods have been shown to provide the most accurate control performance with highly nonlinear hydraulic robotic manipulators in [107] and [116] (this is also demonstrated in this thesis in Section 4.1 in Tables 4.1 and 4.2). However, stability-guaranteed NMB control design for hydraulic robotic manipulators faces a formidable challenge regarding free-space motions alone, and only a few NMB control approaches have provided guaranteed stability for hydraulic manipulators in free-space motion.

As shown in Section 2.1, some stability-guaranteed NMB control methods for contact tasks with a single-DOF electro-hydraulic servosystem exist. However, stability-guaranteed NMB control for hydraulic robotic manipulators has remained an open problem in constrained motion control (in contact tasks).

The current methods for the discharge pressure control of VDAPPs use linearization and/or reduced order methods, without accommodating parametric uncertain dynamics and without extensively covering a VDAPP's highly nonlinear operation space. Thus, full-model-based tracking control of VDAPPs incorporating parametric uncertainty remains an open problem.

3 Overall Control Concept

As introduced in many books on robotics [1, 2, 25, 26, 172], common solutions for modeling the dynamics equations of motion of robots are the *Lagrange method* and the *Newton-Euler method*. The Lagrange method is based on a system's kinetic and potential energies and provides a description of the relationship between joint actuator torques and the motion of the structure [1]. The Newton-Euler method is based on a balance of all the forces acting on the generic link of the robot and leads to a set of equations whose structure allows a recursive type of solution (a forward recursion is performed for propagating link velocities and accelerations, and then a backward recursion is performed for the propagating forces) [1]. Thus, the Newton-Euler method can be said to be a "force balance" approach to dynamics, whereas the Lagrange method is an "energy-based" approach to dynamics [26]. Of these two methods, the Newton-Euler method is more fundamental [2] and computationally more efficient as it exploits the typical open structure of the manipulator kinematic chain [1]. However, the Lagrange method is considered conceptually simpler and more systematic [1]. In books on the control of robots (e.g., in [1 – 3, 25, 26]), the control designs are based on the complete dynamic models of robots using the Lagrange method. However, as discussed in [24, 27], with these Lagrange-based control methods the complexity (computational burden) of robot dynamics is proportional to the fourth power of the number of DOF of motion. Thus, it is very difficult, if not impossible, to implement the complete-dynamics-based control on a single computer for advanced robotic systems, such as [5 – 13], where the number of DOF of motion can easily exceed thirty [24].

Motivated by the results of Newton-Euler method studies [27, 173, 174], the VDC [24, 33] approach is the first rigorous control method to take full advantage of the Newton-Euler method without imposing additional approximations in the control design. The VDC approach is developed especially for controlling complex robotic systems. It can be applied to these systems without restrictions on target systems, and its unique subsystem-dynamics-based control design philosophy brings a certain type of modularity for the first time to control systems. A number of significant state-of-the-art control performance improvements have already been reported with electrically-driven robots (see [34 – 39]) and hydraulically-driven robots (see [120 – 122]). As one of the most impressive achievements, in [36], two force-controlled electric industrial manipulators rigidly held a raw egg while in motion. Furthermore, in [39], the best control performance ever measured, in view of the performance indicator ρ_{fs}, defined later in equation (4.1), was achieved for electric-driven harmonic drives, the dynamic behaviour of which is highly nonlinear.

In addition to the superior control performance, VDC enables an NMB control design with many attractive special features, including the following: 1) The control computations are proportional to the number of subsystems (not to the fourth power of the number of DOF of motion) and can be performed even by locally embedded hardware/software with

an ultrahigh sampling rate; see [39], 2) the subsystem dynamics remain relatively simple with fixed dynamic structures invariant to the target system, 3) changing the control (or dynamics) of one subsystem does not affect the control equations within the rest of the system, 4) parameter uncertainties in the subsystem dynamics can be addressed with a parameter adaptation, and 5) system stability analysis can be addressed at the subsystem level, without imposing additional approximations, using the unique features of VDC, *VPF*, and *virtual stability*.

This chapter shows a control design framework used for the studied hydraulic robotic manipulator. First, Section 3.1 provides the most essential mathematical foundations needed in control system design. Then, Section 3.2 describes the fundamentals of the control design procedure with VDC. The same hydraulic robotic manipulator described in publications **P.I**–**P.IV** is used as an illustrative example. Note that Section 3.2 introduces the basis of the VDC design procedure, whereas detailed control designs can be found in publications **P.I**–**P.IV**. In Section 3.3, the different Cartesian space control strategies proposed in publications **P.I**–**P.IV** (free-space motion control, hybrid motion/force control, impedance control, variable impedance control) are summed up. Section 3.4 shows a diagram for the designed control systems, consisting of the VDC design and the Cartesian control concepts. Section 3.5 provides a rigorous stability proof for the entire system with the proposed control strategies. Finally, Section 3.6 discusses the proposed novel NMB control design method (in unpublished manuscript **P.V**), extending the control design principles of VDC from robotic systems to a broader group of dynamic systems.

3.1 Mathematical Preliminaries

3.1.1 Linear/Angular Velocity Vectors and Force/Moment Vectors

Consider an orthogonal, three-dimensional coordinate system $\{\mathbf{A}\}$ (called frame $\{\mathbf{A}\}$ for simplicity) attached to the rigid body. Let the linear/angular velocity vector of frame $\{\mathbf{A}\}$ be written as ${}^{\mathbf{A}}V = [{}^{\mathbf{A}}\mathbf{v} \;\; {}^{\mathbf{A}}\boldsymbol{\omega}]^T$, where ${}^{\mathbf{A}}\mathbf{v} \in \mathbb{R}^3$ and ${}^{\mathbf{A}}\boldsymbol{\omega} \in \mathbb{R}^3$ are the linear and angular velocity vectors of frame $\{\mathbf{A}\}$. Similarly, let the force/moment vector in frame $\{\mathbf{A}\}$ be written as ${}^{\mathbf{A}}F = [{}^{\mathbf{A}}\mathbf{f} \;\; {}^{\mathbf{A}}\mathbf{m}]^T$, where ${}^{\mathbf{A}}\mathbf{f} \in \mathbb{R}^3$ and ${}^{\mathbf{A}}\mathbf{m} \in \mathbb{R}^3$ are the force and moment vectors applied to the origin of frame $\{\mathbf{A}\}$, expressed in frame $\{\mathbf{A}\}$. Then, consider two given frames, denoted as $\{\mathbf{A}\}$ and $\{\mathbf{B}\}$, fixed to a common rigid body. The following relations hold

$$ {}^{\mathbf{B}}V = {}^{\mathbf{A}}\mathbf{U}_{\mathbf{B}}^{T}\,{}^{\mathbf{A}}V \tag{3.1} $$

$$ {}^{\mathbf{A}}F = {}^{\mathbf{A}}\mathbf{U}_{\mathbf{B}}\,{}^{\mathbf{B}}F \tag{3.2} $$

where ${}^{\mathbf{A}}\mathbf{U}_{\mathbf{B}} \in \mathbb{R}^{6\times 6}$ denotes a force/moment transformation matrix that transforms the force/moment vector measured and expressed in frame $\{\mathbf{B}\}$ to the same force/moment vector measured and expressed in frame $\{\mathbf{A}\}$.

3.1.2 Parameter Adaptation

The following projection function $\mathcal{P}(\cdot)$ can be used for parameter adaptation, if only the first-order time derivative $\dot{\mathcal{P}}(\cdot)$ is needed in the control design.

Definition 1 ([24, 35]) *A projection function $\mathcal{P}(s(t), k, a(t), b(t), t) \in \mathbb{R}$ is a differentiable scalar function defined for $t \geqslant 0$ such that its time derivative is governed by*

$$ \dot{\mathcal{P}} = ks(t)\kappa \tag{3.3} $$

with

$$\kappa = \begin{cases} 0, & \text{if } \mathcal{P} \leqslant a(t) \text{ and } s(t) \leqslant 0 \\ 0, & \text{if } \mathcal{P} \geqslant b(t) \text{ and } s(t) \geqslant 0 \\ 1, & \text{otherwise} \end{cases}$$

where $s(t) \in \mathbb{R}$ *is a scalar variable,* $k > 0$ *is a constant and* $a(t) \leqslant b(t)$ *holds.*

The following projection function $\mathcal{P}_2(\cdot)$ can be used for parameter adaptation, if the second-order time derivative $\ddot{\mathcal{P}}_2(\cdot)$ is needed in the control design.

Definition 2 ([24, 34, 35]) *A projection function* $\mathcal{P}_2(s(t), k, a(t), b(t), d, t) \in \mathbb{R}$ *is a second-order differentiable scalar function defined for* $t \geqslant 0$ *such that its time derivative is governed by*

$$\dot{\mathcal{P}}_2 = k\left(s(t) + d\kappa_2\right) \tag{3.4}$$

with

$$\kappa_2 = \begin{cases} a(t) - \mathcal{P}_2, & \text{if } \mathcal{P}_2 \leqslant a(t) \\ b(t) - \mathcal{P}_2, & \text{if } \mathcal{P}_2 \geqslant b(t) \\ 0, & \text{otherwise} \end{cases}$$

where $s(t) \in \mathbb{R}$ *is a scalar variable,* $k > 0$ *and* $d > 0$ *are two constants, and* $a(t) \leqslant b(t)$ *holds.*

3.1.3 Virtual Cutting Points and a Simple Oriented Graph

In the VDC approach, the original system is virtually decomposed into subsystems by placing conceptual *virtual cutting points* (VCPs). A *cutting point* forms a virtual cutting surface on which three-dimensional force vectors and three-dimensional moment vectors can be exerted from one part to another. The VCP is defined as shown in Definition 3.

Definition 3 ([24]) *A cutting point is a directed separation interface that conceptually cuts through a rigid body. At the cutting point, two parts resulting from the virtual cut maintain equal positions and orientations. The cutting point is interpreted as a driving cutting point by one part and is simultaneously interpreted as a driven cutting point by another part. A force vector* $\mathbf{f} \in \mathbb{R}^3$ *and a moment vector* $\mathbf{m} \in \mathbb{R}^3$ *are exerted from one part to which the cutting point is interpreted as a driving cutting point to the other part to which the cutting point is interpreted as a driven cutting point.*

After the original system is virtually decomposed into subsystems by placing VCPs, the system can be represented by a simple oriented graph. A simple oriented graph is defined, as shown in Definition 4.

Definition 4 ([24]) *A graph consists of nodes and edges. A directed graph is a graph in which all edges have directions. An oriented graph is a directed graph in which each edge has a unique direction. A simple oriented graph (SOG) is an oriented graph in which no loop is formed.*

3.1.4 L_2 and L_∞ Stability

The Lebesgue space is defined as shown in Definition 5.

Definition 5 ([24]) *Lebesgue space, denoted as L_p with p being a positive integer, contains all Lebesgue measurable and integrable functions $f(t)$ subject to*

$$\|f\|_p = \lim_{T\to\infty} \left[\int_0^T |f(t)|^p d\tau\right]^{\frac{1}{p}} < +\infty. \tag{3.5}$$

Two particular cases are considered:

a) *A Lebesgue measurable function $f(t)$ belongs to L_2 if and only if $\lim_{T\to\infty} \int_0^T |f(t)|^2 dt < +\infty$.*

b) *A Lebesgue measurable function $f(t)$ belongs to L_∞ if and only if $\max_{t\in[0,\infty)} |f(t)| < +\infty$.*

Lemma 1 (Lemma 2.3 in [24]) provides that a system is stable with its affiliated vector $\mathbf{x}(t)$ being a function in L_∞ and its affiliated vector $\mathbf{y}(t)$ being a function in L_2.

Lemma 1 ([24]) *Consider a non-negative differentiable function $\xi(t)$ defined as*

$$\xi(t) \geqslant \frac{1}{2}\mathbf{x}(t)^T \mathbf{P}\mathbf{x}(t) \tag{3.6}$$

with $\mathbf{x}(t) \in \mathbb{R}^n$, $n \geqslant 1$ and $\mathbf{P} \in \mathbb{R}^{n\times n}$ being a symmetric positive-definite matrix. If the time derivative of $\xi(t)$ is Lebesgue integrable and governed by

$$\dot{\xi}(t) \leqslant -\mathbf{y}(t)^T \mathbf{Q}\mathbf{y}(t) - s(t) \tag{3.7}$$

where $\mathbf{y}(t) \in \mathbb{R}^m$, $m \geqslant 1$ and $\mathbf{Q} \in \mathbb{R}^{m\times m}$ being a symmetric positive-definite matrix and $s(t)$ is subject to

$$\int_0^\infty s(t)dt \geqslant -\gamma_0 \tag{3.8}$$

with $0 \leqslant \gamma_0 < \infty$, then it follows that $\xi(t) \in L_\infty$, $\mathbf{x}(t) \in L_\infty$ and $\mathbf{y}(t) \in L_2$ hold.

If *asymptotic stability* is demanded for the control system, then the well-known Barbalat's lemma is typically used [175]. The following Lemma 2 provides a simple alternative to the Barbalat's lemma and asymptotic convergence for error signal $e(t)$.

Lemma 2 ([176]) *If $e(t) \in L_2$ and $\dot{e}(t) \in L_\infty$, then $\lim_{t\to\infty} e(t) = 0$.*

Remark 1 *As a distinction to Lyapunov approaches, Lemma 1 allows different appearances of variables in the non-negative function itself and in its time-derivative. Thus, in relation to Lyapunov approaches, Lemma 1 provides a more flexible tool for control system design. When all error signals are first proven to belong to L_2 and L_∞ in the sense of Lemma 1, then asymptotic stability can be proven with Lemma 2, if the time-derivatives of all error signals belong to L_∞.*

3.1.5 Virtual Stability

The unique feature of the VDC approach is the introduction of a scalar term, namely, the *virtual power flow* (VPF); see Definition 6. VPFs uniquely define the dynamic interactions among the subsystems and play an important role in the definition of *virtual stability*, which is defined in Definition 7.

Definition 6 ([24]) *The VPF with respect to frame $\{\boldsymbol{A}\}$ can be defined as the inner product of the linear/angular velocity vector error and the force/moment vector error as*

$$p_{\mathbf{A}} = ({}^{\mathbf{A}}V_r - {}^{\mathbf{A}}V)^T({}^{\mathbf{A}}F_r - {}^{\mathbf{A}}F) \tag{3.9}$$

where ${}^{\mathbf{A}}V_r \in \mathbb{R}^6$ and ${}^{\mathbf{A}}F_r \in \mathbb{R}^6$ represent the required vectors of ${}^{\mathbf{A}}V \in \mathbb{R}^6$ and ${}^{\mathbf{A}}F \in \mathbb{R}^6$, respectively.

Definition 7 ([24]) *A subsystem with a driven VCP to which frame $\{\mathbf{A}\}$ is attached and a driving VCP to which frame $\{\mathbf{C}\}$ is attached is said to be virtually stable with its affiliated vector $\mathbf{x}(t)$ being a virtual function in L_∞ and its affiliated vector $\mathbf{y}(t)$ being a virtual function in L_2, if and only if there exists a non-negative accompanying function*

$$\nu(t) \geqslant \frac{1}{2}\mathbf{x}(t)^T\mathbf{P}\mathbf{x}(t) \tag{3.10}$$

such that

$$\dot{\nu}(t) \leqslant -\mathbf{y}(t)^T\mathbf{Q}\mathbf{y}(t) + p_{\mathbf{A}} - p_{\mathbf{C}} - s(t) \tag{3.11}$$

holds, subject to

$$\int_0^\infty s(t)dt \geqslant -\gamma_s \tag{3.12}$$

with $0 \leqslant \gamma_s < \infty$, where $\mathbf{P}$ and $\mathbf{Q}$ are two block-diagonal positive-definite matrices, and $p_{\mathbf{A}}$ and $p_{\mathbf{C}}$ denote the VPFs (by Definition 6) at frames $\{\mathbf{A}\}$ and $\{\mathbf{C}\}$, respectively.

Finally, when every subsystem is virtually stable in the sense of Definition 7, the following theorem ensures that the L_2 and L_∞ stability of the entire complex robot can be guaranteed.

Theorem 1 ([24]) *Consider a complex robot that is virtually decomposed into subsystems and is represented by a simple oriented graph in Definition 4. If every subsystem is virtually stable in the sense of Definition 7, then all virtual functions in L_2 are functions in L_2 and all virtual functions in L_∞ are functions in L_∞.*

3.2 Virtual Decomposition Control

This section introduces the designed control systems using the VDC approach as the underlying control design framework. The hydraulic manipulator, used in publications **P.I**–**P.IV**, is shown in Fig. 3.1(a). As this figure illustrates, the manipulator is actuated by two hydraulic cylinders.[1] Thus, two *closed-chain* structures exist in the system. Although a two-DOF system is studied, the methods developed in publications **P.I**–**P.IV** are easily extendable to systems with any number of actuators. This is due to the modular nature of the subsystem-dynamics-based control of VDC.

[1] In publication **P.I**, a redundant telescopic actuator, which can be seen in Fig. 3.1(a), was enabled.

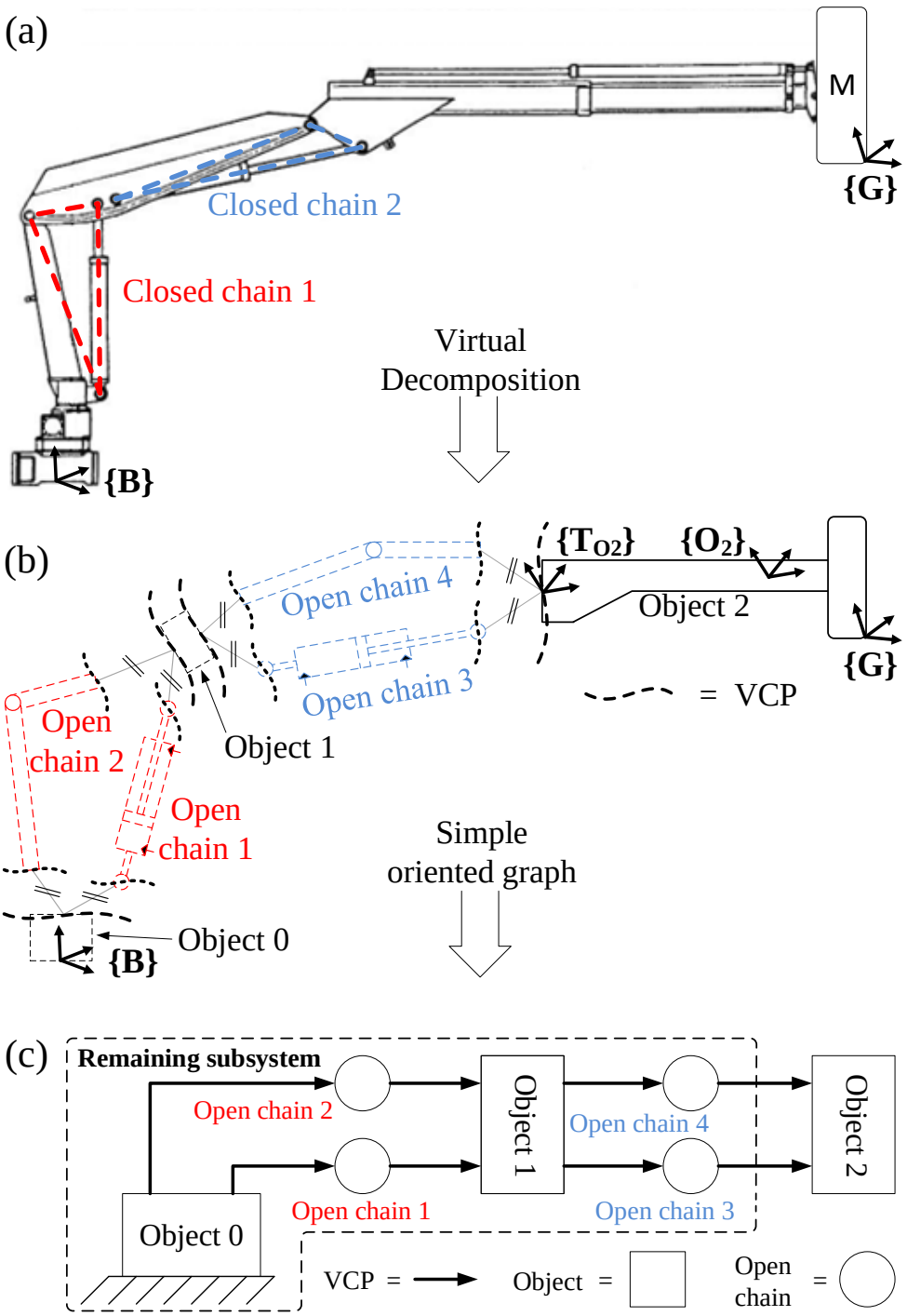

Figure 3.1: The studied system. Subfigure (a) shows the original two-DOF hydraulic manipulator. Subfigure (b) shows a virtual decomposition of the system. Note the parallelism (//) in the VCPs. Subfigure (c) shows a simple oriented graph of the virtually decomposed system.

The first step in the VDC approach is to virtually decompose the original system into subsystems (i.e., *objects* and *open chains*) by placing conceptual virtual cutting points (VCPs) (see Definition 3). In this process, the original system is first virtually decomposed into *object* and *closed chain* structures. Then, existing *closed chain* structures are further decomposed into *open chain* structures, so that only *object* and *open chain* structures exist in the system. The virtually decomposed manipulator is shown in Fig. 3.1(b). Note the corresponding colors between the *closed chain* and its decomposed *open chains* in Fig. 3.1. After the virtual decomposition, the fixed body frames are attached to the decomposed subsystems to describe the motion and force specifications. The frame attachment is described in detail in publications **P.I**–**P.II**.

Next, the decomposed subsystems are represented by a SOG that imposes dynamic interactions among the subsystems. In a SOG, each subsystem corresponds to a node, and each VCP corresponds to a directed edge whose direction defines the force reference direction. Nodes that have pointing-away edges only are called *source nodes*, and nodes that have pointing-to edges only are called *sink nodes*. No loop can be formed in the VCP reference directions [24]. The SOG for the manipulator is shown in Fig. 3.1(c). The subsystems inside the dashed line in Fig. 3.1(c) are considered as one subsystem; the corresponding lines can be seen in Fig. 3.1(b).

After virtual decomposition and the SOG presentation, the kinematics of the subsystems can be computed by propagating along the direction of the VCP flow in the SOG, starting from the *source node* (Object 0) toward the *sink node* (Object 2). Then, using the kinematics, the dynamics of the subsystems can be computed by propagating along the opposite directions of the SOG, starting from the *sink node* (Object 2) toward the *source node* (Object 0). Finally, subsystem-dynamics-based control design can be performed, followed by the stability analysis based on the concept of *virtual stability*.

As discussed earlier, changing the control (or dynamics) of one subsystem does not affect the control equations within the rest of the system. This enables the advantageous property that once the control is designed for all subsystems, e.g., for the different contact control strategies, only the control design for the environment-interacting subsystem (Object 2) needs to be redesigned. Thus, only the control design for Object 2 is studied in detail in this chapter. Control designs for the remaining subsystems, shown as dashed lines in Fig. 3.1(b), can be found in publications **P.I** and **P.II**.

3.2.1 Object 2 – Kinematics

Fig. 3.2 shows Object 2, to which frame $\{\mathbf{O}_2\}$ is fixed to describe the force and motion specifications. Frame $\{\mathbf{T}_{O2}\}$ exists at the driven VCP of Object 2, and frame $\{\mathbf{G}\}$ is the end-effector target frame where the contact occurs. Frame $\{\mathbf{G}\}$ is aligned with respect to the system base frame $\{\mathbf{B}\}$.

The linear/angular velocity vector ${}^{\mathbf{G}}V \in \mathbb{R}^6$ in frame $\{\mathbf{G}\}$ can be written as

$$ {}^{\mathbf{G}}V = \mathbf{N}_{\mathrm{c}}\dot{\boldsymbol{\chi}} \tag{3.13} $$

where $\dot{\boldsymbol{\chi}} \in \mathbb{R}^2$ is the Cartesian velocity vector, and the mapping matrix $\mathbf{N}_{\mathrm{c}}$ can be written as

$$ \mathbf{N}_{\mathrm{c}} = \begin{bmatrix} 1 & 0 & 0 & 0 & 0 & 0 \\ 0 & 1 & 0 & 0 & 0 & 0 \end{bmatrix}^T. $$

The following relations hold for Object 2:

$$\begin{aligned} {}^{\mathbf{O}_2}V &= {}^{\mathbf{G}}\mathbf{U}_{\mathbf{O}_2}^{T}\,{}^{\mathbf{G}}V \\ &= {}^{\mathbf{T}_{O2}}\mathbf{U}_{\mathbf{O}_2}^{T}\,{}^{\mathbf{T}_{O2}}V. \end{aligned} \tag{3.14}$$

3.2.2 Object 2 – Dynamics

The end-effector force/moment vector in frame $\{\mathbf{G}\}$ can be written as

$${}^{\mathbf{G}}F = \mathbf{N}_{\mathrm{c}}\,{}^{\mathbf{G}}\boldsymbol{f} \tag{3.15}$$

where ${}^{\mathbf{G}}\boldsymbol{f} \in \mathbb{R}^2$ is a Cartesian contact force vector (exerted by the manipulator on the environment). Note that in free-space motions, ${}^{\mathbf{G}}\boldsymbol{f} = [0\ 0]^T$ holds.

The net force/moment vector ${}^{\mathbf{O}_2}F^* \in \mathbb{R}^6$ of Object 2, expressed in frame $\{\mathbf{O}_2\}$, can be written in view of [24] as

$$\mathbf{M}_{\mathbf{O}_2}\frac{d}{dt}({}^{\mathbf{O}_2}V) + \mathbf{C}_{\mathbf{O}_2}({}^{\mathbf{O}_2}\omega)\,{}^{\mathbf{O}_2}V + \mathbf{G}_{\mathbf{O}_2} = {}^{\mathbf{O}_2}F^* \tag{3.16}$$

where $\mathbf{M}_{\mathbf{O}_2} \in \mathbb{R}^{6\times 6}$ denotes the mass matrix, $\mathbf{C}_{\mathbf{O}_2}({}^{\mathbf{O}_2}\omega) \in \mathbb{R}^{6\times 6}$ denotes the matrix of Coriolis and centrifugal terms, and $\mathbf{G}_{\mathbf{O}_2} \in \mathbb{R}^6$ denotes the gravity terms.

On the other hand, the net force/moment vector (i.e., force resultant equation) for Object 2 can be written as

$${}^{\mathbf{O}_2}F^* = {}^{\mathbf{O}_2}\mathbf{U}_{\mathbf{T}_{O2}}\,{}^{\mathbf{T}_{O2}}F - {}^{\mathbf{O}_2}\mathbf{U}_{\mathbf{G}}\,{}^{\mathbf{G}}F. \tag{3.17}$$

3.2.3 Object 2 – Control

This section addresses the VDC-based rigid body control of Object 2. Similar to (3.13), the required linear/angular velocity vector in the end-effector target frame $\{\mathbf{G}\}$ can be written as

$${}^{\mathbf{G}}V_{\mathrm{r}} = \mathbf{N}_{\mathrm{c}}\dot{\boldsymbol{\chi}}_{\mathrm{r}} \tag{3.18}$$

where $\dot{\boldsymbol{\chi}}_{\mathrm{r}} \in \mathbb{R}^2$ is the required Cartesian space velocity (design) vector specified later in Section 3.3.

In view of (3.14), the required velocity transformations in Object 2 can be written as

$$\begin{aligned} {}^{\mathbf{O}_2}V_{\mathrm{r}} &= {}^{\mathbf{G}}\mathbf{U}_{\mathbf{O}_2}^{T}\,{}^{\mathbf{G}}V_{\mathrm{r}} \\ &= {}^{\mathbf{T}_{O2}}\mathbf{U}_{\mathbf{O}_2}^{T}\,{}^{\mathbf{T}_{O2}}V_{\mathrm{r}}. \end{aligned} \tag{3.19}$$

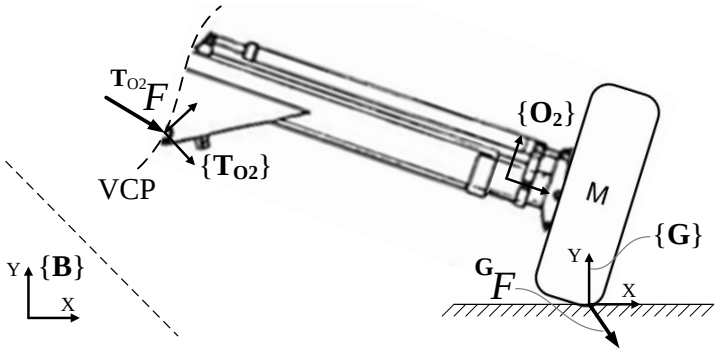

Figure 3.2: Object 2 in the constrained motion.

Similar to (3.15), the required force/moment vector in the end-effector target frame $\{\mathbf{G}\}$ can be obtained as

$$^{\mathbf{G}}F_{\mathrm{r}} = \mathbf{N}_{\mathrm{c}}{}^{\mathbf{G}}\boldsymbol{f}_{\mathrm{d}} \tag{3.20}$$

where $^{\mathbf{G}}\boldsymbol{f}_{\mathrm{d}} \in \mathbb{R}^2$ is the desired Cartesian contact force vector.

Then, in view of [24], the required net force/moment vector for Object 2 can be written as

$$^{\mathbf{O}_2}F_{\mathrm{r}}^{*} = \mathbf{Y}_{\mathbf{O}_2}\widehat{\boldsymbol{\theta}}_{\mathbf{O}_2} + \mathbf{K}_{\mathbf{O}_2}(^{\mathbf{O}_2}V_{\mathrm{r}} - {}^{\mathbf{O}_2}V) \tag{3.21}$$

with

$$\mathbf{Y}_{\mathbf{O}_2}\boldsymbol{\theta}_{\mathbf{O}_2} = \mathbf{M}_{\mathbf{O}_2}\frac{d}{dt}(^{\mathbf{O}_2}V_{\mathrm{r}}) + \mathbf{C}_{\mathbf{O}_2}(^{\mathbf{O}_2}\omega)^{\mathbf{O}_2}V_{\mathrm{r}} + \mathbf{G}_{\mathbf{O}_2} \tag{3.22}$$

where regressor matrix $\mathbf{Y}_{\mathbf{O}_2} \in \mathbb{R}^{6\times 13}$ and parameter vector $\boldsymbol{\theta}_{\mathbf{O}_2} \in \mathbb{R}^{13}$ can be solved as shown in [24, in Appendix A]. Moreover, in (3.21), $\widehat{\boldsymbol{\theta}}_{\mathbf{O}_2}$ denotes the estimate of $\boldsymbol{\theta}_{\mathbf{O}_2}$, and $\mathbf{K}_{\mathbf{O}_2}$ is a symmetric positive-definite matrix characterizing the velocity feedback control.

The estimated parameter vector $\widehat{\boldsymbol{\theta}}_{\mathbf{O}_2}$ in (3.21) needs to be updated. Define

$$\mathbf{s}_{\mathbf{O}_2} = \mathbf{Y}_{\mathbf{O}_2}^{T}(^{\mathbf{O}_2}V_{\mathrm{r}} - {}^{\mathbf{O}_2}V). \tag{3.23}$$

Then, (3.3) can be used to update the ith element of $\widehat{\boldsymbol{\theta}}_{\mathbf{O}_2}$ as

$$\widehat{\theta}_{\mathbf{O}_2 i} = \mathcal{P}(\mathrm{s}_{\mathbf{O}_2 i}, \rho_{\mathbf{O}_2 i}, \underline{\theta}_{\mathbf{O}_2 i}, \overline{\theta}_{\mathbf{O}_2 i}, t), \forall i \in \{1, 2, ..., 13\} \tag{3.24}$$

where $\widehat{\theta}_{\mathbf{O}_2 i}$ denotes the ith element of $\widehat{\boldsymbol{\theta}}_{\mathbf{O}_2}$, $\mathrm{s}_{\mathbf{O}_2 i}$ denotes the ith element of $\mathbf{s}_{\mathbf{O}_2}$, $\rho_{\mathbf{O}_2 i} > 0$ is the update gain, and $\underline{\theta}_{\mathbf{O}_2 i}$ and $\overline{\theta}_{\mathbf{O}_2 i}$ denote the lower bound and the upper bound of $\theta_{\mathbf{O}_2 i}$, respectively.

In relation to (3.17), the required force resultant equation can be written as

$$^{\mathbf{O}_2}F_{\mathrm{r}}^{*} = {}^{\mathbf{O}_2}\mathbf{U}_{\mathbf{T}_{\mathrm{O2}}}{}^{\mathbf{T}_{\mathrm{O2}}}F_{\mathrm{r}} - {}^{\mathbf{O}_2}\mathbf{U}_{\mathbf{G}}{}^{\mathbf{G}}F_{\mathrm{r}}. \tag{3.25}$$

Finally, the following Lemma 3 is used to prove the *virtual stability* of Object 2.

Lemma 3 *Consider Object 2, described by* (3.14), (3.16), *and* (3.17), *combined with its control equations* (3.19), (3.21), *and* (3.25) *and with the parameter adaptation* (3.23) *and* (3.24). *Let the non-negative accompanying function* $\nu_{\mathbf{O}_2}$ *be*

$$\nu_{\mathbf{O}_2} = \frac{1}{2}(^{\mathbf{O}_2}V_r - {}^{\mathbf{O}_2}V)^T\mathbf{M}_{\mathbf{O}_2}(^{\mathbf{O}_2}V_r - {}^{\mathbf{O}_2}V) + \frac{1}{2}\sum_{i=1}^{13}\frac{(\theta_{\mathbf{O}_2 i} - \widehat{\theta}_{\mathbf{O}_2 i})^2}{\rho_{\mathbf{O}_2 i}} \tag{3.26}$$

Then, the time derivative of (3.26) *can be expressed by*

$$\dot{\nu}_{\mathbf{O}_2} \leqslant -(^{\mathbf{O}_2}V_r - {}^{\mathbf{O}_2}V)^T\mathbf{K}_{\mathbf{O}_2}(^{\mathbf{O}_2}V_r - {}^{\mathbf{O}_2}V) + p_{\mathbf{T}_{O2}} - p_{\mathbf{G}} \tag{3.27}$$

where $p_{\mathbf{T}_{O2}}$ *is the VPF by Definition 6 at the driven VCP of Object 2, and* $p_{\mathbf{G}}$ *characterizes the VPF between the end-effector and the environment.*

Proof. See Appendix B in Publication **P.II**. ■

Remark 2 *Note that Object 2 has only one VCP (see Fig. 3.2), but two VPFs exist in* (3.27). *The VPF* $p_{\mathbf{T}_{O2}}$ *is located at the VCP in Object 2. Thus, for the virtual stability of Object 2, a solution (which satisfies Definition 7) must be found for the VPF* $p_{\mathbf{G}}$ *in* (3.27). *This solution is addressed in Section 3.5.*

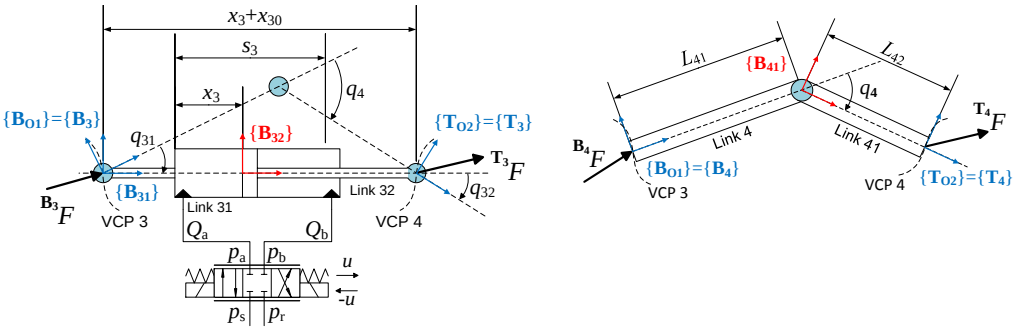

(a) Actuated Open chain 3. **(b)** Unactuated Open chain 4.

Figure 3.3: Decomposed open chains (Open chain 3 and Open chain 4) in Closed chain 2.

3.2.4 Closed Chain 2 – Kinematics, Dynamics, and Control

This section briefly describes the procedure for the kinematics, dynamics, and control of Closed chain 2. The same procedure can be used for Closed chain 1 in Fig. 3.1.

Consider Closed chain 2, which is decomposed to actuated Open chain 3 and unactuated Open chain 4 (see Fig. 3.3). Similar to Object 2, the kinematics of Open chain 3 and Open chain 4 can be computed along the direction of the VCP flow in the SOG. Note that the linear/angular velocity vector ${}^{\mathbf{B}_{O1}}V$ in the driven VCP of Closed chain 2 is known (from the kinematics of Object 0, Open chains 1 and 2, and Object 1), and joint angle q_4 and joint velocity $\dot{q}_4$ can be measured.

Then, the dynamics of the rigid links in Open chain 3 and in Open chain 4 can be computed along the opposite direction of the VCP flow in the SOG. The force/moment vector ${}^{\mathbf{T}_{O2}}F$ in the driving VCP of Closed chain 2 can be computed from (3.17). Also, the load distribution factors (between Open chain 3 and Open chain 4) at the driving VCP of Closed chain 2 and the internal force vector (only Open chain 3 can generate forces) must be solved due to the existence of the closed-chain structure. Then, the dynamics of the hydraulic actuator is addressed. The detailed control design for the system closed-chain structures are addressed in publications **P.I** and **P.II**.

3.3 The Cartesian Space Control Concepts

In the framework of VDC, the concept of a required velocity is used to serve as a reference trajectory for a system, and the control objective is to make the controlled actual velocities track the required velocities. The general format of the required velocity includes the desired velocity (which usually serves as the reference trajectory for the system) and one or more terms that are related to control errors [24]. The concept of required velocity can be implemented for the system in the actuator space or in the Cartesian space. In this thesis, the Cartesian space implementation is considered. Publication **P.I** shows how this method can be implemented in the actuator space.

As discussed earlier, changing the control (or dynamics) of one subsystem does not affect the control equations within the rest of the system. Thus, for the different control concepts (free-space motion control and constrained motion controls), only the control for the environment-interacting subsystem, i.e., Object 2, needs to be redesigned. The possibilities for addressing the control of Object 2 are $\dot{\boldsymbol{\chi}}_{\mathrm{r}}$ in (3.18) and ${}^{\mathbf{G}}\boldsymbol{f}_{\mathrm{d}}$ in (3.20).

Then, the control objective is to design such Cartesian space contact control for $\dot{\boldsymbol{\chi}}_{\mathrm{r}}$ (and for ${}^{\mathbf{G}}\boldsymbol{f}_{\mathrm{d}}$), which 1) realizes the control action (free-space motion control, hybrid motion/force control, impedance control, etc.) in demand and 2) qualifies Object 2 as *virtually stable* in the sense of Definition 7.

Next, in Sections 3.3.1 – 3.3.4, the control concepts for the manipulator's free-space motion control, hybrid motion/force control, impedance control, and variable impedance control are shown, respectively.

3.3.1 Free-Space Motion Control

In view of [24], the expression for the required Cartesian velocity vector $\dot{\boldsymbol{\chi}}_{\mathrm{r}} \in \mathbb{R}^2$ for the manipulator[2] can be written for free-space motions as

$$\dot{\boldsymbol{\chi}}_{\mathrm{r}} = \dot{\boldsymbol{\chi}}_{\mathrm{d}} + \boldsymbol{\Lambda}_{\chi}(\boldsymbol{\chi}_{\mathrm{d}} - \boldsymbol{\chi}) \tag{3.28}$$

$${}^{\mathbf{G}}\boldsymbol{f}_{\mathrm{d}} = [0\ 0]^T \tag{3.29}$$

where $\boldsymbol{\Lambda}_{\chi} \in \mathbb{R}^{2\times 2}$ is a diagonal positive-definite matrix characterizing Cartesian position control. Note that in the free-space motion, ${}^{\mathbf{G}}\boldsymbol{f} = [0\ 0]^T$ in (3.15) holds.

3.3.2 Hybrid Motion/Force Control

The following hybrid motion/force control from [24] is designed in publication **P.II** in Section IV.B.4:

$$\dot{\boldsymbol{\chi}}_{\mathrm{r}} = \mathbf{N}_{\mathrm{x}}[\dot{\chi}_{\mathrm{d}x} + \lambda_{\chi}(\chi_{\mathrm{d}x} - \chi_x)] + \mathbf{N}_{\mathrm{y}}\lambda_f({}^{\mathbf{G}}\tilde{f}_{\mathrm{d}y} - {}^{\mathbf{G}}\tilde{f}_y) \tag{3.30}$$

$${}^{\mathbf{G}}\boldsymbol{f}_{\mathrm{d}} = \mathbf{N}_{\mathrm{x}}{}^{\mathbf{G}}\widehat{f}_x + \mathbf{N}_{\mathrm{y}}{}^{\mathbf{G}}f_{\mathrm{d}y} \tag{3.31}$$

where $\mathbf{N}_{\mathrm{x}} = [1\ 0]^T$ and $\mathbf{N}_{\mathrm{y}} = [0\ 1]^T$ are mapping matrices, and ${}^{\mathbf{G}}\tilde{f}_{\mathrm{d}y}$ and ${}^{\mathbf{G}}\tilde{f}_y$ are filtered vectors of ${}^{\mathbf{G}}f_{\mathrm{d}y}$ and ${}^{\mathbf{G}}f_y$, respectively, defined as

$${}^{\mathbf{G}}\dot{\tilde{f}}_{\mathrm{d}y} = -c_f{}^{\mathbf{G}}\tilde{f}_{\mathrm{d}y} + c_f{}^{\mathbf{G}}f_{\mathrm{d}y} \tag{3.32}$$

$${}^{\mathbf{G}}\dot{\tilde{f}}_y = -c_f{}^{\mathbf{G}}\tilde{f}_y + c_f{}^{\mathbf{G}}f_y \tag{3.33}$$

with $c_f > 0$ being a gain. In addition, estimated force ${}^{\mathbf{G}}\widehat{f}_x$ can be written as

$${}^{\mathbf{G}}\widehat{f}_x = \mathbf{Y}_s\widehat{\boldsymbol{\theta}}_s \tag{3.34}$$

which implies that the independent (friction) force coordinate in the motion configuration space can be expressed in linear parametrization form with $\boldsymbol{\theta}_s$ being a parameter vector [24]. Then, by defining

$$\mathbf{s}_s = \mathbf{Y}_s^T[\dot{\chi}_{\mathrm{d}x} - \dot{\chi}_x + \lambda_{\chi}(\chi_{\mathrm{d}x} - \chi_x)] \tag{3.35}$$

the γth element of $\widehat{\boldsymbol{\theta}}_s$ is updated by using the $\mathcal{P}$ function defined by (3.3) as

$$\widehat{\theta}_{s\gamma} = \mathcal{P}(s_{s\gamma}, \rho_{s\gamma}, \underline{\theta}_{s\gamma}, \overline{\theta}_{s\gamma}, t) \tag{3.36}$$

where $\widehat{\theta}_{s\gamma}$ denotes the γth element of $\widehat{\boldsymbol{\theta}}_s$, $s_{s\gamma}$ denotes the γth element of $\mathbf{s}_s$, $\rho_{s\gamma} > 0$ is an update gain, $\underline{\theta}_{s\gamma}$ denotes the lower bound of $\theta_{s\gamma}$ and $\overline{\theta}_{s\gamma}$ denotes the upper bound of $\theta_{s\gamma}$.

[2] As shown in section 3.3.6 in [24] and in publication **P.I**, in addition to the Cartesian space control, the required velocity can also be implemented in the actuator space. If the actuator space approach is used, then the desired joint space vectors $\dot{\boldsymbol{q}}_{\mathrm{d}}$ and $\boldsymbol{q}_{\mathrm{d}}$ (desired joint velocities and desired joint positions) are solved from the desired Cartesian space vectors $\dot{\boldsymbol{\chi}}_{\mathrm{d}}$ and $\boldsymbol{\chi}_{\mathrm{d}}$ with inverse kinematics. Then, the required velocity control can be implemented in the actuator space as $\dot{\boldsymbol{q}}_{\mathrm{r}} = \dot{\boldsymbol{q}}_{\mathrm{d}} + \boldsymbol{\lambda}_q(\boldsymbol{q}_{\mathrm{d}} - \boldsymbol{q})$.

3.3.3 Impedance Control

The following novel impedance control method is proposed in publication **P.III** in Section IV.B.2:

$$\dot{\boldsymbol{\chi}}_{\mathrm{r}} = \dot{\boldsymbol{\chi}}_{\mathrm{d}} + \boldsymbol{\Lambda}_{\chi}(\boldsymbol{\chi}_{\mathrm{d}} - \boldsymbol{\chi}) + \boldsymbol{\Lambda}_{f}({}^{\mathbf{G}}\boldsymbol{f}_{\mathrm{d}} - {}^{\mathbf{G}}\boldsymbol{f}) \tag{3.37}$$

$${}^{\mathbf{G}}\boldsymbol{f}_{\mathrm{d}} = [0\ 0]^{T} \tag{3.38}$$

where $\boldsymbol{\Lambda}_{\chi} \in \mathbb{R}^{2\times 2}$ and $\boldsymbol{\Lambda}_{f} \in \mathbb{R}^{2\times 2}$ are two diagonal positive-definite matrices characterizing the Cartesian position and force control, which are defined according to Condition 1.

Condition 1 *The diagonal positive-definite matrices $\boldsymbol{\Lambda}_{f}$ and $\boldsymbol{\Lambda}_{\chi}$ are defined as*

$$\boldsymbol{\Lambda}_{f} = \mathbf{D}_{\mathrm{d}}^{-1} \tag{3.39}$$

$$\boldsymbol{\Lambda}_{\chi} = \mathbf{K}_{\mathrm{d}}\mathbf{D}_{\mathrm{d}}^{-1}. \tag{3.40}$$

In Condition 1, $\mathbf{D}_{\mathrm{d}} \in \mathbb{R}^{2\times 2}$ and $\mathbf{K}_{\mathrm{d}} \in \mathbb{R}^{2\times 2}$ are diagonal positive-definite matrices characterizing the system target impedance behaviour; the desired damping and the desired stiffness, respectively. The diagonal positive-definite property of $\mathbf{D}_{\mathrm{d}}$ ensures that $\mathbf{D}_{\mathrm{d}}^{-1}$ exists.

3.3.4 Variable Impedance Control

The following novel variable impedance control method is proposed for multiple Cartesian DOF in publication **P.IV**.

Let the Cartesian position tracking error $\boldsymbol{e}_{\chi} \in \mathbb{R}^{2}$ be defined as

$$\boldsymbol{e}_{\chi} = \boldsymbol{\chi}_{\mathrm{d}} - \boldsymbol{\chi} = \begin{bmatrix} \chi_{\mathrm{d}x} - \chi_{x} \\ \chi_{\mathrm{d}y} - \chi_{y} \end{bmatrix} = \begin{bmatrix} e_{\chi x} \\ e_{\chi y} \end{bmatrix} \tag{3.41}$$

Then, the proposed variable impedance law is written as

$$\dot{\boldsymbol{\chi}}_{\mathrm{r}} = \dot{\boldsymbol{\chi}}_{\mathrm{d}} + \boldsymbol{\Lambda}_{\chi}(\boldsymbol{e}_{\chi})\boldsymbol{e}_{\chi} + \boldsymbol{\Lambda}_{f}(\boldsymbol{e}_{\chi})({}^{\mathbf{G}}\boldsymbol{f}_{\mathrm{d}} - {}^{\mathbf{G}}\boldsymbol{f}) \tag{3.42}$$

$${}^{\mathbf{G}}\boldsymbol{f}_{\mathrm{d}} = [0\ 0]^{T} \tag{3.43}$$

and the following Condition 2 is imposed for the variable diagonal positive-definite matrices $\boldsymbol{\Lambda}_{\chi}(\boldsymbol{e}_{\chi})$ and $\boldsymbol{\Lambda}_{f}(\boldsymbol{e}_{\chi})$.

Condition 2 *The diagonal positive-definite matrices $\boldsymbol{\Lambda}_{f}(\boldsymbol{e}_{\chi})$ and $\boldsymbol{\Lambda}_{\chi}(\boldsymbol{e}_{\chi})$ are defined as*

$$\boldsymbol{\Lambda}_{f}(\boldsymbol{e}_{\chi}) = \mathrm{diag}\left(\Lambda_{f}(e_{\chi x}), \Lambda_{f}(e_{\chi y})\right) = \mathbf{D}_{\mathrm{d}}^{-1}(\boldsymbol{e}_{\chi}) \tag{3.44}$$

$$\boldsymbol{\Lambda}_{\chi}(\boldsymbol{e}_{\chi}) = \mathrm{diag}\left(\Lambda_{\chi}(e_{\chi x}), \Lambda_{\chi}(e_{\chi y})\right) = \mathbf{K}_{\mathrm{d}}(\boldsymbol{e}_{\chi})\mathbf{D}_{\mathrm{d}}^{-1}(\boldsymbol{e}_{\chi}). \tag{3.45}$$

In Condition 2, $\mathbf{D}_{\mathrm{d}}(\boldsymbol{e}_{\chi})$ and $\mathbf{K}_{\mathrm{d}}(\boldsymbol{e}_{\chi})$ are diagonal positive-definite matrices characterizing the desired variable damping and the desired variable stiffness. The diagonal positive-definite property of $\mathbf{D}_{\mathrm{d}}(\boldsymbol{e}_{\chi})$ ensures that $\mathbf{D}_{\mathrm{d}}^{-1}(\boldsymbol{e}_{\chi})$ exists in Condition 2. Matrices $\mathbf{D}_{\mathrm{d}}(\boldsymbol{e}_{\chi})$ and $\mathbf{K}_{\mathrm{d}}(\boldsymbol{e}_{\chi})$ are written as

$$\mathbf{D}_{\mathrm{d}}(\boldsymbol{e}_{\chi}) = \begin{bmatrix} \overline{\mathrm{D}}_{\mathrm{d}x} - (\overline{\mathrm{D}}_{\mathrm{d}x} - \underline{\mathrm{D}}_{\mathrm{d}x})f_{\mathrm{e}}(e_{\chi x}) & 0 \\ 0 & \overline{\mathrm{D}}_{\mathrm{d}y} - (\overline{\mathrm{D}}_{\mathrm{d}y} - \underline{\mathrm{D}}_{\mathrm{d}y})f_{\mathrm{e}}(e_{\chi y}) \end{bmatrix} \tag{3.46}$$

and

$$\mathbf{K}_{\mathrm{d}}(\boldsymbol{e}_{\chi}) = \begin{bmatrix} \overline{\mathrm{K}}_{\mathrm{d}x} - (\overline{\mathrm{K}}_{\mathrm{d}x} - \underline{\mathrm{K}}_{\mathrm{d}x}) f_{\mathrm{e}}(e_{\chi x}) & 0 \\ 0 & \overline{\mathrm{K}}_{\mathrm{d}y} - (\overline{\mathrm{K}}_{\mathrm{d}y} - \underline{\mathrm{K}}_{\mathrm{d}y}) f_{\mathrm{e}}(e_{\chi y}) \end{bmatrix} \tag{3.47}$$

where $\overline{\mathrm{D}}_{\mathrm{d}x}$ and $\overline{\mathrm{D}}_{\mathrm{d}y}$ denote the upper bounds of $\mathbf{D}_{\mathrm{d}}(\boldsymbol{e}_{\chi})$; $\underline{\mathrm{D}}_{\mathrm{d}x}$ and $\underline{\mathrm{D}}_{\mathrm{d}y}$ denote the lower bounds of $\mathbf{D}_{\mathrm{d}}(\boldsymbol{e}_{\chi})$; $\overline{\mathrm{K}}_{\mathrm{d}x}$ and $\overline{\mathrm{K}}_{\mathrm{d}y}$ denote the upper bounds of $\mathbf{K}_{\mathrm{d}}(\boldsymbol{e}_{\chi})$; $\underline{\mathrm{K}}_{\mathrm{d}x}$ and $\underline{\mathrm{K}}_{\mathrm{d}y}$ denote the lower bounds of $\mathbf{K}_{\mathrm{d}}(\boldsymbol{e}_{\chi})$; and $\overline{\mathrm{D}}_{\mathrm{d}x} \geqslant \underline{\mathrm{D}}_{\mathrm{d}x} > 0$, $\overline{\mathrm{D}}_{\mathrm{d}y} \geqslant \underline{\mathrm{D}}_{\mathrm{d}y} > 0$, $\overline{\mathrm{K}}_{\mathrm{d}x} \geqslant \underline{\mathrm{K}}_{\mathrm{d}x} > 0$ and $\overline{\mathrm{K}}_{\mathrm{d}y} \geqslant \underline{\mathrm{K}}_{\mathrm{d}y} > 0$ hold. Furthermore, the Cartesian position error dependent (a continuously differentiable) function $f_{\mathrm{e}}(e_{\chi})$ in (3.46) and (3.47) can be written as

$$f_{\mathrm{e}}(e_{\chi}) = \begin{bmatrix} - \left(\frac{e_{\chi}}{a_{\mathrm{e}}}\right)^{b_{\mathrm{e}}} \\ 1 - e \end{bmatrix} \tag{3.48}$$

where $a_{\mathrm{e}} > 0$, and $b_{\mathrm{e}} = 2n,\ n \in \mathbb{N}^{+}$, hold. The behaviour of the function $f_{\mathrm{e}}(e_{\chi})$ with respect to its argument e_{χ} is shown in Fig. 3.4.

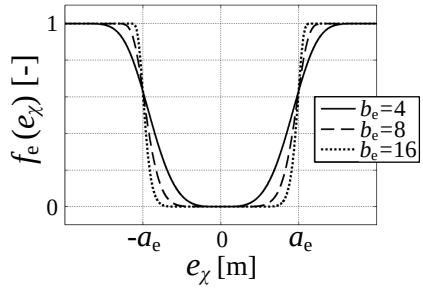

Figure 3.4: The behaviour of the function $f_{\mathrm{e}}(e_{\chi})$ with respect to its argument e_{χ}.

Remark 3 *With $a_{\mathrm{e}} > 0$ and $b_{\mathrm{e}} = 2n,\ n \in \mathbb{N}^{+}$, $f_e(e_{\chi}, \boldsymbol{\theta}_{\mathrm{e}})$ converges $0 \to 1$ as $|e_{\chi}| \to \infty$. The region where f_e stays close to zero can be adjusted with a_{e} and b_{e}. The rate at which f_e converges $0 \to 1$ (and $1 \to 0$) can be adjusted with b_{e}. Note that the function in* (3.48) *is continuously differentiable. An accurate free-space position tracking performance (demonstrated in publication **P.I**) is an important part of the functionality of $f_e(e_{\chi}, \boldsymbol{\theta}_{\mathrm{e}})$ in* (3.48)*. This is because the constrained motion (contact) is detected from the Cartesian position tracking error e_{χ} with* (3.48) *when $|e_{\chi}| > a_{\mathrm{e}}$ (see Fig. 3.4).*

The following conditions 3 and 4 are imposed for the variable damping $\mathbf{D}_{\mathrm{d}}(\boldsymbol{e}_{\chi})$ and for the variable stiffness $\mathbf{K}_{\mathrm{d}}(\boldsymbol{e}_{\chi})$ in (3.46) and (3.47).

Condition 3 *Along a certain Cartesian space axis, the upper bound $\overline{\mathrm{D}}_{\mathrm{d}}$ and the lower bound $\underline{\mathrm{D}}_{\mathrm{d}}$ for the desired variable damping $\mathrm{D}_{\mathrm{d}}(e_{\chi})$ and the upper bound $\overline{\mathrm{K}}_{\mathrm{d}}$ and the lower bound $\underline{\mathrm{K}}_{\mathrm{d}}$ for the desired variable stiffness $\mathrm{K}_{\mathrm{d}}(e_{\chi})$ must be selected within the dynamic range of achievable impedances of the system.*

Condition 4 *The rates of change of the variable damping $\mathbf{D}_d(\boldsymbol{e}_{\chi})$ and the variable stiffness $\mathbf{K}_d(\boldsymbol{e}_{\chi})$ profiles should not yield to unstable system behaviour.*

Condition 3 imposes that the variable impedance bounds must be selected within the dynamic range of achievable impedances. This can be illustrated by the so called Z-width

(see Fig. 3.5), which defines the combination of stiffness and damping that can be passively achieved by a certain mechanism. One method for defining the Z-width for hydraulic articulated systems is shown in [155].

As addressed in [177] and [178], impedance control makes the closed-loop system passive and therefore passive (and stable) in interactions with passive environments when constant gains are used. However, as addressed in [179], when the impedance parameters are varied over time, system instability can occur. For Condition 4, a method for defining the stability constraints for the variable stiffness and damping profiles is studied in [179].

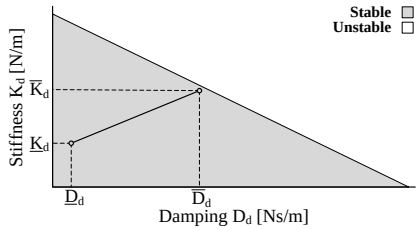

Figure 3.5: The dynamic range of achievable virtual impedances, i.e., the Z-width.

3.4 A Diagram of the Proposed Controller

A diagram of the proposed control design is shown in Fig. 3.6. Using one of the proposed Cartesian space control laws in Section 3.3, the required Cartesian space velocity vector can be obtained. Then, the required joint velocity vector $\dot{\boldsymbol{q}}_\mathrm{r}$, needed in VDC-based control of Open chains 1–4, is solved from $\dot{\boldsymbol{\chi}}_\mathrm{r}$ using the manipulator's Jacobian matrix. The rigid body control for Object 2 is addressed in Section 3.2.3. The detailed structure of the remaining subsystem (see Fig. 3.1) inside the VDC block can be found in publication **P.II**. The output $\boldsymbol{u}_\mathrm{c}$ of the VDC block is the control signal for the hydraulic valves, which control the hydraulic cylinders. The motion dynamics of the manipulator is produced by the output force $\boldsymbol{f}_\mathrm{p}$ of the hydraulic cylinders. See publication **P.II** for more details.

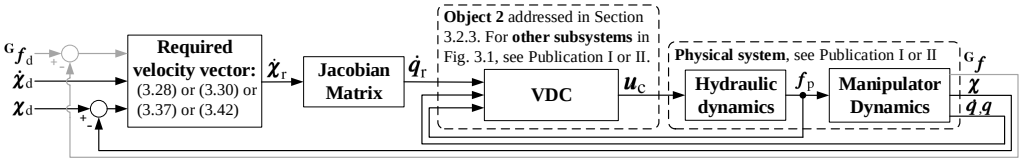

Figure 3.6: Diagram of the designed controls for the hydraulic manipulator.

3.5 Stability Analysis

The conceptual VPFs (see Definition 6) are a unique feature of VDC, and they are used to address the dynamic interaction between subsystems. The *virtual stability* (see Definition 7) of every subsystem ensures that, at every placed VCP, a negative VPF (at the driving VCP of the subsystem) is connected to its corresponding positive VPF (at the driven VCP of the adjacent subsystem). Thus, VPFs act as "stability connectors" between subsystems; eventually, the VPFs cancel each other out at every VCP [24]. Finally, as addressed in Theorem 1, the *virtual stability* of every subsystem ensures the L_2 and L_∞ stability (see Lemma 1) of the entire system.

As can be seen in Fig. 3.2, only one VCP ($p_{\mathbf{T}_{O2}}$; see (3.27)) is specified for Object 2. However, in (3.27), there also exists another VPF $p_{\mathbf{G}}$ (characterizing the dynamic interaction between the manipulator and the environment), which has no "stabilizing counterpart". Consequently, it is the control designer's obligation to ensure that such control is designed for Object 2 that it qualifies as *virtually stable* in the sense of Definition 7.

Next, in Section 3.5.1, the VPF $p_{\mathbf{G}}$ between the manipulator and the environment is analyzed using Definitions 6 and 7, eventually leading to the stabilizing solution for $p_{\mathbf{G}}$ and the *virtual stability* of Object 2 with all the proposed Cartesian control methods in Section 3.3. Finally, the stability of the entire system is proven in Section 3.5.2.

3.5.1 Virtual Stability of Object 2

Using the Cartesian free-space control in Section 3.3.1, the hybrid motion/force control in Section 3.3.2, the impedance control in Section 3.3.3, or the variable impedance control in Section 3.3.4, the following Lemma 4 can be derived for $p_{\mathbf{G}}$ in (3.27) in Lemma 3.

Lemma 4 *With all the proposed Cartesian control methods in Section 3.3,*

$$\int_0^t p_{\mathbf{G}}(\tau)d\tau \geqslant -\gamma_{\mathbf{G}} \tag{3.49}$$

holds with $0 \leqslant \gamma_{\mathbf{G}} < \infty$ *for* $p_{\mathbf{G}}$ *in* (3.27) *in Lemma 3.*

Proof. In view of Definition 6, VPF $p_{\mathbf{G}}$ in Lemma 3 can be written as $p_{\mathbf{G}} = ({}^{\mathbf{G}}V_{\mathrm{r}} - {}^{\mathbf{G}}V)^T({}^{\mathbf{G}}F_{\mathrm{r}} - {}^{\mathbf{G}}F)$. In free-space motions, ${}^{\mathbf{G}}F = \mathbf{0}$ holds (no external forces are imposed on the end-effector), ${}^{\mathbf{G}}F_{\mathrm{r}} = \mathbf{0}$ can be designed, and thus, $p_{\mathbf{G}} = 0 \rightarrow \int_0^t p_{\mathbf{G}}(\tau)d\tau = 0$ holds. In constrained motion control, (3.49) in Lemma 4 can be proven 1) for the hybrid motion/force control as shown in Appendix A in publication **P.II**, 2) for the proposed impedance control as shown in Appendix C in publication **P.III**, and 3) for the proposed variable impedance control as shown in Lemma 4 in publication **P.IV**. ■

Using Lemma 3 and Lemma 4, the following Theorem 2 ensures that Object 2 qualifies as *virtually stable* in the sense of Definition 7.

Theorem 2 *Let* (3.49) *in Lemma 4 hold for the VPF* $p_{\mathbf{G}}$ *in Lemma 3. Then, consider the fact that Object 2 has one driven VCP associated with frame* $\{\mathbf{T}_{O2}\}$*. Consequently, using* (3.26)*,* (3.27)*, and* (3.49)*, Object 2 qualifies as virtually stable in the sense of Definition 7.*

Proof. The proof can be obtained as outlined in Theorem 2. ■

3.5.2 Stability of the Entire System

As can be seen in publications **P.I** and **P.II**, the non-negative accompanying function and its time derivative for the remaining subsystem, shown with dashed lines in Fig. 3.1, can be written as

$$\nu_{\mathbf{R}} \geqslant 0 \tag{3.50}$$

$$\dot{\nu}_{\mathbf{R}} \leqslant -p_{\mathbf{T}_{O2}} \tag{3.51}$$

where $p_{\mathbf{T}_{O2}}$ is the VPF at the driving VCP of this subsystem.

Theorem 3 guarantees the stability of the entire system, in view of Lemma 1.

Theorem 3 *Consider Object 2, shown in Fig. 3.2 and described by Lemma 3. Furthermore, let the remaining subsystem be addressed with* (3.50) *and* (3.51)*. Then, in view of* (3.26) *and* (3.50)*, the non-negative accompanying function ν_{tot} for the entire manipulator can be chosen as*

$$\begin{aligned}\nu_{tot} &= \nu_{\mathbf{R}} + \nu_{\mathbf{O}_2} \\ &\geqslant \frac{1}{2}({}^{\mathbf{O}_2}V_r - {}^{\mathbf{O}_2}V)^T \mathbf{M}_{\mathbf{O}_2}({}^{\mathbf{O}_2}V_r - {}^{\mathbf{O}_2}V) + \frac{1}{2}\sum_{i=1}^{13} \frac{(\theta_{\mathbf{O}_2 i} - \widehat{\theta}_{\mathbf{O}_2 i})^2}{\rho_{\mathbf{O}_2 i}}. \end{aligned} \tag{3.52}$$

Then, in view of (3.27) *and* (3.51)*, the time derivative of* (3.52) *can be written as*

$$\begin{aligned}\dot{\nu}_{tot} &\leqslant -({}^{\mathbf{O}_2}V_r - {}^{\mathbf{O}_2}V)^T \mathbf{K}_{\mathbf{O}_2}({}^{\mathbf{O}_2}V_r - {}^{\mathbf{O}_2}V) - p_{\mathbf{T}_{O2}} + p_{\mathbf{T}_{O2}} - p_{\mathbf{G}} \\ &= -({}^{\mathbf{O}_2}V_r - {}^{\mathbf{O}_2}V)^T \mathbf{K}_{\mathbf{O}_2}({}^{\mathbf{O}_2}V_r - {}^{\mathbf{O}_2}V) - p_{\mathbf{G}} \end{aligned} \tag{3.53}$$

where, in view of Lemma 4,

$$\int_0^t p_{\mathbf{G}}(\tau)d\tau \geqslant -\gamma_{\mathbf{G}} \tag{3.54}$$

holds with $0 \leqslant \gamma_{\mathbf{G}} < \infty$, which guarantees the stability of the entire system in view of Lemma 1.

3.6 Extending the VDC Principles Beyond Robotic Systems

The VDC approach is developed especially for controlling complex robotic systems [24, 33]. In the book *Virtual Decomposition Control - Towards Hyper Degrees of Freedom Robots* [24], it is shown that this novel approach can also be applied to, for instance, electrical circuits in terms of the duality between mechanical and electrical systems. As shown in Sections 3.1.5 and 3.5, unique VPFs define the dynamic interaction among subsystems and play a vital role in proving the L_2 and L_∞ stability of the entire system. When VDC principles are applied beyond robotic systems, the cross-couplings among subsystems in some cases cannot be necessarily described in the form of VPFs; thus, alternative methods must be provided to address the dynamic interactions among the subsystems. This is the case in unpublished manuscript **P.V**, where a novel controller design method (originating from VDC) was developed for controlling the discharge pressure of a VDAPP.

In the system in unpublished manuscript **P.V**, three coupled subsystems are identified (see Fig. 3.7). The first subsystem encompasses the volume of the pump's discharge line and can be described with a first-order fluid continuity differential equation. The second subsystem is the pump itself and can be described with a second-order swash plate motion differential equation. The third subsystem is the volume of the control piston and can be described with a first-order fluid continuity differential equation. Thus, the dynamic behaviour of the entire system can be described by a highly nonlinear fourth-order differential equation.

As demonstrated in unpublished manuscript **P.V**, a *stability-preventing term* (created by local subsystem control) can appear in the time derivative of the non-negative accompanying function of the nth subsystem. Thus, a specific *stabilizing term* is designed for the

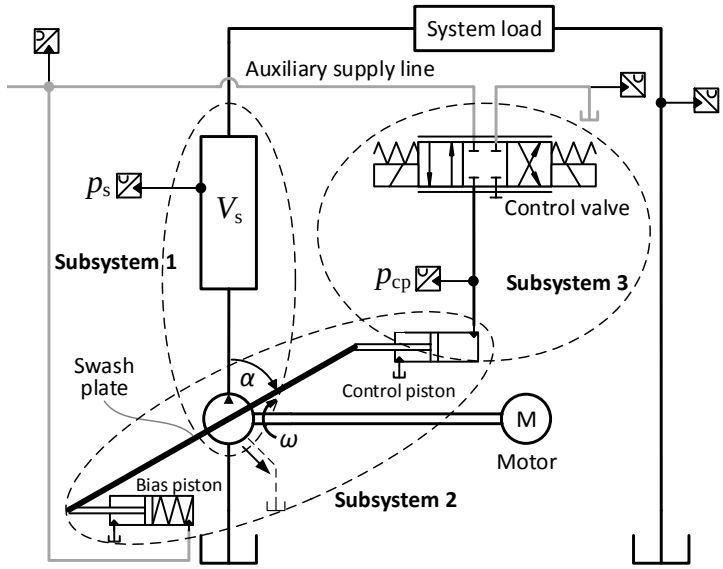

Figure 3.7: A diagram for a discharge pressure controlling VDAPP with the identified subsystems.

time derivative of the non-negative accompanying function of the subsequent $(n+1)$th subsystem. The stabilizing term is designed by placing a specific stabilizing feedback in the control law of the $(n+1)$th subsystem. As Theorems 1 and 2 in unpublished manuscript **P.V** show, the stability of the entire system is obtained (in the sense of Lemma 1), as these designed stabilizing terms eventually cancel out all the stability-preventing terms. Similar to VDC, stability is rigorously based on Lemma 1. Then, if all error signals are first proved to belong to L_2 and L_∞, then asymptotic stability can be proved with Lemma 2 if the time derivatives of all error signals belong to L_∞.

Similar to VDC, the proposed method allows an independent control design of the individual subsystems as long as the "stability connectors" (*stability-preventing terms* and *stabilizing terms*) are properly handled. This allows flexibility in the control system design. In contrast, the well-known backstepping control design framework imposes restrictions on the forms a system must take for the procedure to follow. In unpublished manuscript **P.V**, the proposed method enabled adaptive and NMB control for the VDAPP, for the first time without employing any linearization or order reduction, while rigorously guaranteeing the stability of the entire system. The existing nonlinear control methods for the discharge pressure controlling VDAPP (see [169–171]) employ linearization and/or order reduction, without extensively accommodating parametric uncertain dynamics.

4 Experimental Results

This section presents the main experimental results in publications **P.I**–**P.IV** and in unpublished manuscript **P.V**. These papers are attached. **The scientific contributions C1–C9 (the main theoretical results) of this thesis are listed in Section 1.8**. Fig. 4.1 shows the interconnection between the publications. The publications and unpublished manuscript are listed in chronological order from top to bottom.

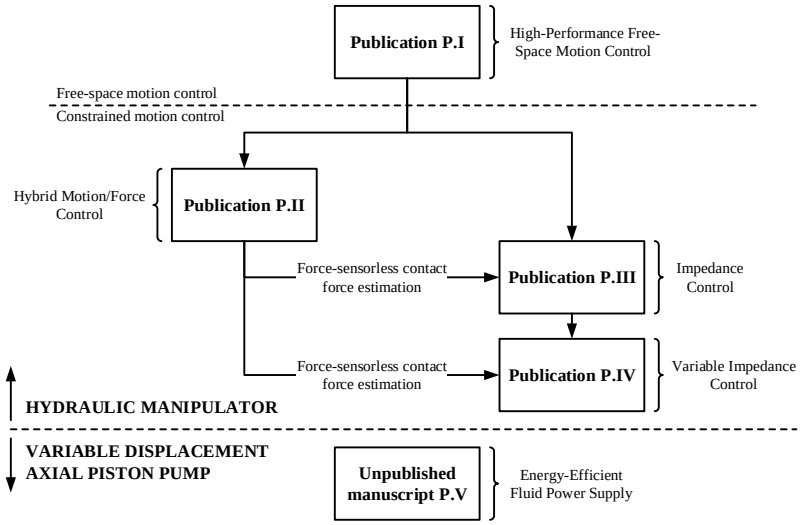

Figure 4.1: Publications **P.I**–**P.IV** and unpublished manuscript **P.V**.

The hydraulic manipulator used in publications **P.I**–**P.IV** is shown in Fig. 4.2. This manipulator operates in the Cartesian X-Y plane and can be actuated with three hydraulic cylinders: Cylinder 1 for lift, Cylinder 2 for tilt, and Cylinder 3 to operate the telescopic boom. In publications **P.II**–**P.IV**, Cylinder 3 was disabled. A detailed description of the system hardware components is given in publications **P.I**–**P.III**. Although a planar two-DOF Cartesian space system was studied in publications **P.I**–**P.IV**, the developed methods are easily extendable to systems with any number of actuators.

In publication **P.I**, the objective was to design the state-of-the-art free-space motion control for a hydraulic robotic manipulator by rigorously addressing the nonlinear dynamic behaviour of the system. The controller developed in publication **P.I** provided a baseline controller to be extended to contact control in publications **P.II**–**P.IV**.

In publication **P.II**, the objective was to design for the first time a hybrid motion/force controller for hydraulic robotic manipulators with rigorously addressed system stability. In addition, a novel force-sensorless contact force estimation method was developed in

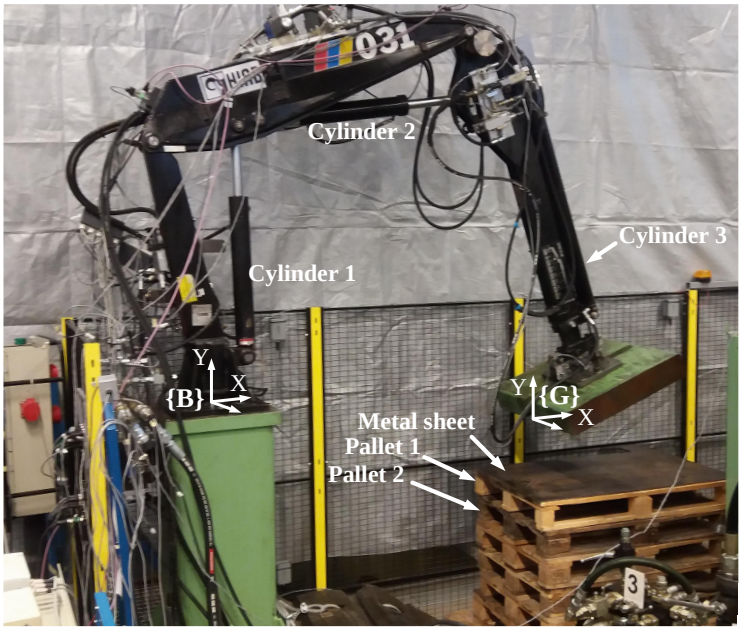

Figure 4.2: Experiment set-up. For the environmental interaction, a set of wooden pallets and a metal sheet were used in the constrained motion control experiments. Frame {**G**} is the end-effector target frame where the contact occurs, and it is aligned with respect to the system base frame {**B**} (whose Y-axis is aligned with respect to gravity).

this paper. This provides a practical solution for contact control with hydraulic systems without using the six-DOF force/moment sensor (attached to the end-effector) that is typically sensitive to shocks and overloading, a situation that frequently occurs in hydraulic operations. The developed force-sensorless contact force estimation method was also used in the subsequent publications **P.III** and **P.IV**.

In publication **P.III**, a novel impedance control method was developed. In this paper, the objective was to incorporate the impedance control method in the framework of VDC and provide for the first time a rigorous stability proof for a hydraulic manipulator covering both free-space motions and constrained motions.

As demonstrated in publication **P.III**, the greater the driven velocity, the worse the contact force estimation in free-space motions (i.e., estimated contact force ${}^{\mathbf{G}}\boldsymbol{f}_{\mathrm{d}} \neq \mathbf{0}$; see Fig. 5 in publication **P.III**). Thus, if an accurate (but fragile) six-dimensional force/moment sensor at the end-effector cannot be used, it follows that 1) an accurate contact force estimation is very hard to achieve due to the highly nonlinear dynamic behavior of the hydraulic manipulators, and 2) with the impedance control, contact force estimation errors impair the accuracy of free-space position tracking.

In publication **P.IV**, a novel variable impedance control method was developed. The proposed method was developed especially to improve the Cartesian free-space position control accuracy in force-sensorless contact force control with hydraulic manipulators. With the proposed method, the manipulator can be made stiff in free-space motions (enabling accurate free-space position tracking) and compliant along the axis of the constrained motion when coming into contact with the environment. The results of publication **P.I** provided a rigorous foundation for publication **P.IV** because the proposed variable impedance control law relies rigorously on high-performance Cartesian position tracking accuracy.

In unpublished manuscript **P.V**, an adaptive and NMB discharge pressure control design was proposed for the first time for VDAPPs (the dynamic behaviour of which is highly nonlinear and can be described with a fourth-order differential equation) without using any linearization or order reduction. The control objective was to make a system's discharge pressure track a prespecified desired discharge pressure trajectory, which would enable the possibility of optimizing energy consumption. A rigorous stability proof, with asymptotic convergence, is given for the entire system. As discussed in Section 3.6, this paper also demonstrates the extendability of VDC beyond robotic systems.

Next, Sections 4.1–4.5 present the main experimental results in papers **P.I**–**P.IV** and in unpublished manuscript **P.V**.

4.1 Free-Space Motion Control Performance (Publication P.I)

In free-space motion control of manipulators, the most important factor is typically the control accuracy of the manipulator end-effector. To evaluate the control performance of the proposed free-space motion controller, a parallelogram point-to-point trajectory (having length of 1 m along the Cartesian X-axis and height of 2 m along the Cartesian Y-axis) was used as the test trajectory (see Fig. 12 in publication **P.I**). This test trajectory was driven with three Cartesian velocities (fast-, medium-, and slow-velocity trajectories). Term t_f in Fig. 4.3 denotes the transition time between two points in the driven point-to-point test trajectory.

Fig. 4.3 shows the Cartesian position tracking errors with the driven test trajectories. As this figure shows, the Cartesian position tracking errors remain very small in relation to the size of the system workspace (with the telescopic boom, the manipulator has a reach of more than 4 m on the Cartesian X-axis) for all the driven trajectories. The maximum Cartesian position tracking errors in Fig. 4.3 are 5.20 mm, 4.60 mm, and 4.67 mm, with the fast-, medium-, and slow-velocity trajectories, respectively, whereas the maximum Cartesian velocities were 1.05 m/s, 0.53 m/s, and 0.26 m/s, respectively. Note that the shape of the Cartesian position tracking error curves remains almost unchanged in spite of the driven velocity. This clearly shows that the proposed controller is able to cope with

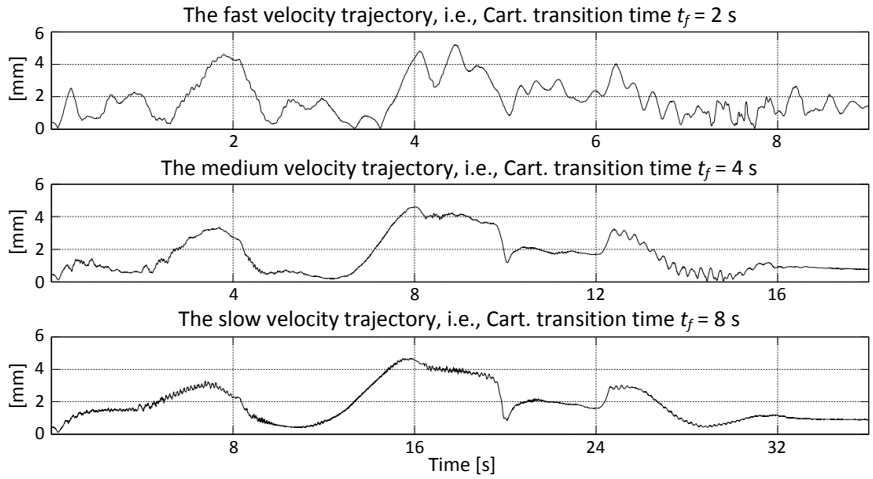

Figure 4.3: The Cartesian position tracking errors with the fast-, medium-, and slow-velocity trajectories.

the highly nonlinear dynamic behaviour of the hydraulic system; these tracking errors mainly originate from static error sources, e.g., parameter uncertainties. The parameter adaptation was disabled in publication **P.I**.

The cornerstone of all scientific research is an objective evaluation of the results. As recently addressed in [180], it is difficult to find good examples of replicable and measurable scientific research in robotics and automation. This makes an objective evaluation and benchmarking of the state of the art in a given field very challenging. When dealing with pure engineering applications, experimental proofs of the effectiveness of the proposed solutions are needed, and the results should be compared, in terms of the chosen performance criteria, to existing methods in the same field. In addition, objective and unifying performance evaluations would also speed up the technology transfer between academia and industry, as well as promote the most advanced practices in a given field. For these purposes, a unifying performance indicator ρ_{fs} was used in the studies conducted by Zhu (e.g., in [38] and [120]). To objectively evaluate the control performances in the literature for free-space control of hydraulic manipulators (see section 2.2), this unifying performance indicator, which uses the ratio of the maximum position tracking error with respect to the maximum velocity, is defined as

$$\rho_{\text{fs}} = \frac{\max(|\mathbf{x}_{des} - \mathbf{x}|)}{\max(|\dot{\mathbf{x}}|)} \tag{4.1}$$

where $\mathbf{x}_{des}$ is the desired position vector and $\mathbf{x}$ is the measured position vector. Using ρ_{fs}, the position control accuracies of the different systems can be unified by scaling them with the driven velocity, making it possible to compare systems of different sizes. With ρ_{fs}, the smaller the value, the better the performance.

Table 4.1 shows the *actuator space* performance indicators for state-of-the-art studies on hydraulic manipulators where sufficient data are available. Note that in this table, two single-DOF studies[1] ([100] and [101] from Section 2.1) are included due to the lack of data for n-DOF hydraulic manipulators. The first column in Table 4.1 shows the study and its reference. The second column shows the performance indicator ρ_{fs} value. The third column shows the number of driven actuators. The last column shows if the control design is stability-guaranteed NMB control. The performance indicators are given *for the best actuator*, if the results for more than one actuator are given.

In free-space motion control of manipulators, the major interest should be in the end-effector positioning accuracy[2]. Table 4.2 shows the performance indicators in the *Cartesian space* for studies with appropriately documented data. Note that in Table 4.2 one study used the parallel-chain Stewart-Gough platform (Sirouspour 2001 [52]), which is not fully comparable to the other studies with a serial-chain structure. The first column in Table 4.2 shows the study and its reference. The second column shows the performance indicator ρ_{fs} value. The third column shows the number of driven actuators. The last column shows whether the control design is stability-guaranteed NMB control.

[1] In [100], flatness-based nonlinear control for position tracking of electro-hydraulic systems was proposed. In [101], high-gain disturbance observer-based backstepping control without a tracking error constraint was proposed for electro-hydraulic systems. In the experiments described in [100] and [101], a single-DOF boom was driven using a hydraulic actuator.

[2] The end-effector positioning accuracy is a function of the actuator's positioning accuracy (scaled by the link kinematics). Thus, the performance indicators in Table 4.1 might not give a realistic picture of the control performance of the entire manipulator if large deviations occur in the control performances of the joints.

As Tables 4.1 and 4.2 show, the state-of-the-art control accuracy, in terms of performance indicator ρ_{fs}, is obtained in publication **P.I**. Moreover, stability-guaranteed NMB control methods dominate the control of hydraulic manipulators.

Table 4.1: Performance indicator ρ_{fs} in actuator space

Study	ρ_{fs} [s]	DOFs (Driven actuators)	Stab. NMBC
Publication **P.I**	0.0030†	3	✓
Won 2015 [101]	0.0032*	1‡	✓
Koivumäki 2013 [121]	0.0039†	2	✓
Kim 2015 [100]	0.0048*	1‡	✓
Bech 2013 [107]	0.0044*	2	✓
Zhu 2005 [120]	0.0050	6	✓
Bu 2001 [96]	0.0050	1$^{\diamond}$	✓
Conrad 1996 (AMAC) [106]	0.0087$^{\bullet}$	2	-
Mattila 2000 [111]	0.0130	2	-
Conrad 1996 (LPAC) [106]	0.0160$^{\bullet}$	2	-

†With the fastest trajectory data; see Fig. 13 in publication **P.I** and Fig. 10 in [121].
*The measured velocity data were not reported; the maximum velocity is estimated from the sinusoidal desired position trajectory. See Figs. 2 and 10(e) in [101], Fig. 6 in [100], and Figs. 4 and 14 (MRACV) in [107].
‡A single-DOF electro-hydraulic system. In the experiments, a single-DOF boom was driven.
$^{\diamond}$The experiments were conducted with a three-joint hydraulic arm. However, in the experiments only one joint was driven, and the two others were fixed.
$^{\bullet}$See Fig. 8(f) in [106] for AMAC and LPAC. The measured velocity data were not reported; the text reports that the maximum velocity was limited to 2 rad/s. This value is used to compute ρ_{fs}.

Table 4.2: Performance indicator ρ_{fs} in Cartesian space

Study	ρ_{fs} [s]	DOFs (Driven actuators)	Stab. NMBC
Publication **P.I**	0.0050†	3	✓
Sirouspour 2001 [52]	0.0100*	6$^{\bullet}$	✓
Zhu 2005 [120]	0.0150	6	✓
Egeland 1987 [102]	0.0380	8	-
Chang 2002 [115]	0.0450*	3	-
Kalmari 2015 [124]	0.1200$^{\diamond}$	4	-
Tsukamoto 2002 [114]	0.1260‡	6	-
Nguyen 2000 [109]	0.3150*	3	-

†With the fastest trajectory data; see Fig. 4.3.
*The measured velocity data were not reported; the maximum velocity is estimated from the sinusoidal desired position trajectory. See Fig. 6 in [52], Figs. 10 and 16(a) in [115], and Fig. 6 in [109].
$^{\bullet}$Stewart-Gough parallel manipulator (not a serial manipulator).
$^{\diamond}$The value for the maximum tracking error was selected after the first round when the tracking error settled; see Fig. 5.4 in [124].
‡A circular reference trajectory with a radius of 0.17 m was driven with angular velocity $\omega = \pi/5$ rad/s. A maximum trajectory error of 13.51 mm was reported.

4.2 Hybrid Motion/Force Control (Publication P.II)

In experiments with hybrid motion/force control, the controller's ability to maintain a constant contact force in constrained motion was studied using three maximum contact force f_{max} trajectories. The end-effector target frame $\{\mathbf{G}\}$, where the contact occurs, is shown in Fig. 4.2. This frame is aligned with respect to the system base frame $\{\mathbf{B}\}$ (whose Y-axis is aligned with respect to gravity). The contact occurs on the surface of pallet 2 (after removing pallet 1 and metal sheet; see Fig. 4.2). In the driven test trajectory, the desired contact force along the Y-axis of frame $\{\mathbf{G}\}$ (shown in black in Fig. 4.4) is first changed from the initial contact force $f_{init} \approx 0$ to the desired maximum contact force f_{max} over 2 s. Then, the end-effector is instructed to travel a distance of 0.5 m within 5 s while the desired maximum contact force was maintained. Finally, the desired contact force changes back to zero in 2 s.

The main results in publication **P.II** are shown in Figs. 4.4 and 4.5. In Fig. 4.4, the contact force tracking performances (along the Y-axis of frame $\{\mathbf{G}\}$) are given under the maximum contact force trajectories $f_{max} = -2000$ N, $f_{max} = -4000$ N, and $f_{max} = -8000$ N. The measured end-effector contact forces are shown in green. As these plots show, the measured contact forces accurately track the desired force trajectories in all three cases with different maximum contact forces.

Fig. 4.5 shows the end-effector position tracking errors (along the X-axis of frame $\{\mathbf{G}\}$) under the maximum contact force trajectories $f_{max} = -2000$ N, $f_{max} = -4000$ N, and $f_{max} = -8000$ N. The maximum position tracking errors in these cases remain well below 10 mm. This can be considered a significant result in light of the manipulator scale, which has a reach of about 3.2 m. Fig. 4.5 shows that the most challenging phase for position tracking control under contact force/motion control seems to be the force transition from the maximum force back to zero (see time interval 7–9 s). In this phase, the maximum contact force has a notable effect on the position tracking accuracy, whereas in the first two phases (see 0–7 s in Fig. 4.5), the effect of the contact force on the position tracking accuracy appears minimal.

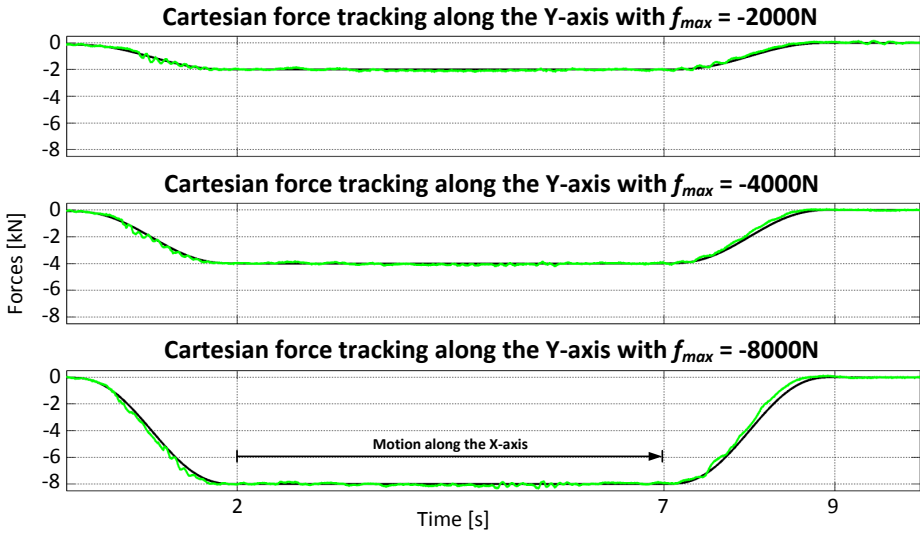

Figure 4.4: Contact force tracking along the Y-axis of frame $\{\mathbf{G}\}$. The measured contact forces are shown with green lines, and their reference trajectories are shown with black lines.

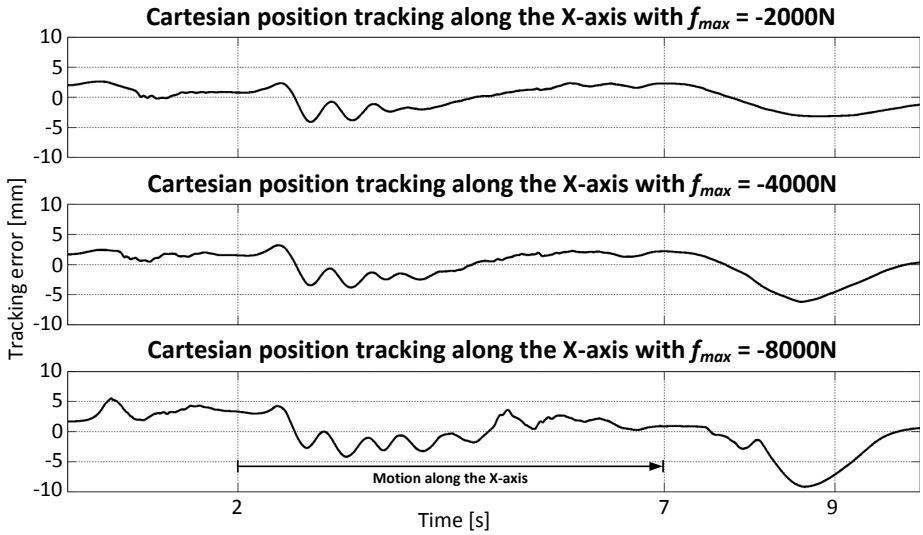

Figure 4.5: Cartesian position tracking errors along the X-axis of frame {**G**}.

Table 4.3 provides the maximum contact force tracking errors of Fig. 4.4 in the downward force transition phase (time interval 0 – 2 s), in the constrained motion phase (time interval 2 – 7 s), and in the upward force transition phase (7 – 9 s). As this table shows, with all force trajectories the highest contact force tracking error occurs in the force transition phases. In addition, the maximum contact force tracking error in the constrained motion phases is less than half of that in the respective force transitions. This has great practical relevance because the controllability of the maximum contact force is usually more important than the controllability of the force transition phases.

Table 4.3: Absolute values of the maximum force tracking errors [N]

$f_{max} = -2000$ N		
Force trans. ⇓	Constr. motion	Force trans. ⇑
400 N	178 N	237 N
$f_{max} = -4000$ N		
Force trans. ⇓	Constr. motion	Force trans. ⇑
454 N	214 N	352 N
$f_{max} = -8000$ N		
Force trans. ⇓	Constr. motion	Force trans. ⇑
585 N	331 N	697 N

The evaluation of the methods for constrained motion control of hydraulic manipulators is much more challenging compared to the evaluation of the free-space control performance. Robotic contact control methods can be roughly divided into methods originating from the hybrid position/force control and from impedance control, and these methods differ greatly (see [135]). Thus, it is hard to find a unifying indicator. To evaluate the dynamic performance of the force tracking control of the proposed hybrid motion/force controller, in line with (4.1), the following performance indicator is used:

$$\rho_{\mathrm{hmf}} = \frac{\max(|{}^{\mathbf{G}}f_{\mathrm{yd}} - {}^{\mathbf{G}}f_{\mathrm{y}}|)}{\max(|{}^{\mathbf{G}}\dot{f}_{\mathrm{yd}}|)} \tag{4.2}$$

where ${}^{\mathbf{G}}f_{yd}$ is the desired position vector, and ${}^{\mathbf{G}}f_{\mathrm{y}}$ is the measured position vector. Note that in (4.2), the desired trajectory ${}^{\mathbf{G}}\dot{f}_{yd}$ is used in the nominator instead of the measured value ${}^{\mathbf{G}}\dot{f}_{\mathrm{y}}$. This is due to the differentiation noises that occur in ${}^{\mathbf{G}}\dot{f}_{\mathrm{y}}$ (${}^{\mathbf{G}}\dot{f}_{\mathrm{y}}$ is estimated from the noisy cylinder chamber pressure data, which has already been filtered once). With the maximum contact force trajectory $f_{max} = -8000$ N, the value $\rho_{\mathrm{hmf}} = 0.095$ (s) is obtained. No comparative data from previous studies are available. The performance indicator ρ_{hmf} used in this study can be used as a benchmark for future studies.

4.3 Impedance Control (Publication P.III)

In the experiments with the proposed impedance control in publication **P.III**, the controller's ability to provide compliant constrained-motion behaviour for the manipulator was studied. The end-effector target frame $\{\mathbf{G}\}$, where the contact occurs, is shown in Fig. 4.2. This frame is aligned with respect to the system base frame $\{\mathbf{B}\}$ (whose Y-axis is aligned with respect to gravity). Fig. 4.6 shows one of the driven test cases in publication **P.III**, where the contact occurred at the surface of the first pallet (when the metal sheet was removed; see Fig. 4.2). In the first plot, the desired Cartesian path is shown in black, in which the end-effector was first instructed to travel a distance of -0.5 m along the Y-axis of frame $\{\mathbf{B}\}$ in 3 s. Then, a distance of 0.5 m was driven along the X-axis in 3 s. Finally, a distance of 0.5 m was driven along the Y-axis in 3 s. The collision velocity was approximately -0.26 m/s. The measured Cartesian path is shown in red. The contact point is shown with a blue circle. As this plot shows, the proposed controller delimits the end-effector position when contact with the environment occurs, thus preventing excessive contact forces from being applied to the environment.

The second plot in Fig. 4.6 shows the position tracking error along the X-axis of frame

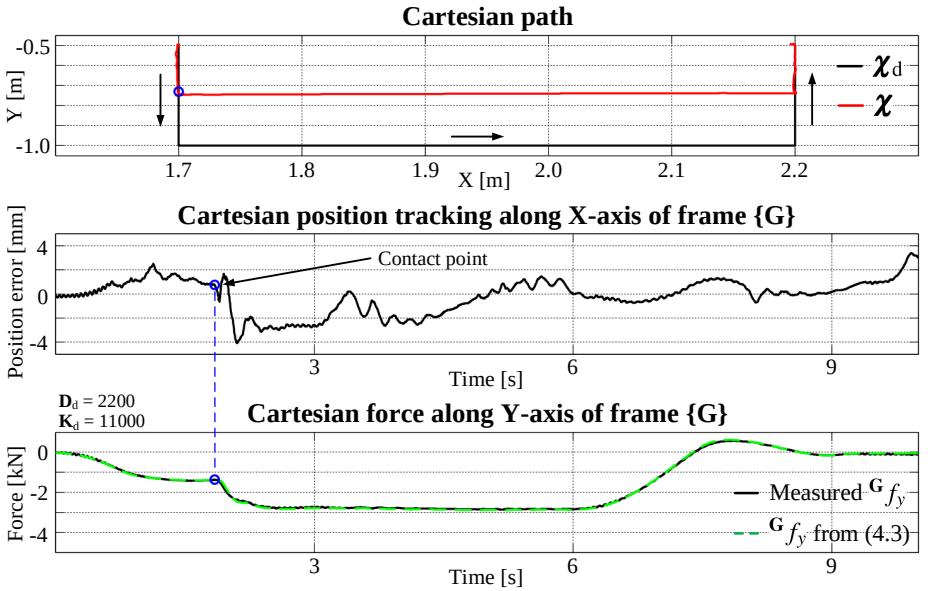

Figure 4.6: Test Case 2: Environmental contact on the surface of the second pallet (see Fig. 4.2). The first plot shows the desired Cartesian position path in black and the measured Cartesian path in red. The second plot shows the Cartesian position tracking along the X-axis of the frame $\{\mathbf{G}\}$. The last plot shows the measured Cartesian contact force (along the Y-axis of the frame $\{\mathbf{G}\}$) in black. The contact force suggested by the target impedance law (4.3) is shown in green.

$\{\mathbf{G}\}$, in which direction the manipulator was made stiff. The contact point is shown with a blue circle. As this plot shows, the maximum position tracking error is well below 4 mm for the test trajectory. This can be considered a significant result in light of the manipulator scale, which has a reach of about 3.2 m.

The last plot in Fig. 4.6 shows the measured contact force exerted by the manipulator on the environment (shown in black) along the Y-axis of frame $\{\mathbf{G}\}$, the direction in which the manipulator was made compliant. The contact point is shown with a blue circle. As this plot shows, the proposed controller efficiently limits the contact force (applied by the manipulator on the environment and expressed along the Y-axis of frame $\{\mathbf{G}\}$) to approximately -2800 N when contact with the environment is established. Because contact forces were estimated from the cylinder chamber pressures, inaccuracies exist in the estimates; therefore, the measured end-effector force before contact is not zero. It was also observed in publication **P.III** that the smaller velocity yields a better contact force estimation in free space. This occurs because system inertia and piston friction were not considered in the contact force estimation.

As addressed in Theorem 1 in publication **P.III**, the target impedance behaviour by Hogan [133] should be achieved for the manipulator when the diagonal positive-definite matrices $\mathbf{\Lambda}_f$ and $\mathbf{\Lambda}_\chi$ are defined according to Condition 1 in publication **P.III**. Consequently, the measured contact force should correspond to the contact force ${}^{\mathbf{G}}f_y$ suggested by Hogan's target impedance law [133] with the neglected inertia term, i.e.,[3]

$$ {}^{\mathbf{G}}f_y = \boldsymbol{y}_f[\mathbf{D}_\mathrm{d}(\dot{\boldsymbol{\chi}}_\mathrm{d} - \dot{\boldsymbol{\chi}}) + \mathbf{K}_\mathrm{d}(\boldsymbol{\chi}_\mathrm{d} - \boldsymbol{\chi}) + {}^{\mathbf{G}}\boldsymbol{f}_\mathrm{d}] \tag{4.3} $$

where $\boldsymbol{y}_f = [0\ 1]$, ${}^{\mathbf{G}}\boldsymbol{f}_\mathrm{d} = [0\ 0]^T$; $\mathbf{D}_\mathrm{d} \in \mathbb{R}^{2\times 2}$ and $\mathbf{K}_\mathrm{d} \in \mathbb{R}^{2\times 2}$ are diagonal positive-definite matrices and characterize the desired damping and stiffness (desired impedance parameters); and $(\dot{\boldsymbol{\chi}}_\mathrm{d} - \dot{\boldsymbol{\chi}})$ and $(\boldsymbol{\chi}_\mathrm{d} - \boldsymbol{\chi})$ are variables from the driven test cases. As the last plot in Fig. 4.6 shows, the measured contact force (shown in black) corresponds nearly perfectly to the contact force suggested by (4.3) (shown in green).

To evaluate the control performance of the impedance control methods, the following performance indicator can be used:

$$ \rho_\mathrm{imp} = \frac{\max(|{}^{\mathbf{G}}f_\mathrm{imp} - {}^{\mathbf{G}}f_\mathrm{mes}|)}{L_\mathrm{reach}} \tag{4.4} $$

where ${}^{\mathbf{G}}f_\mathrm{imp}$ is the contact force suggested by the actual impedance control law, ${}^{\mathbf{G}}f_\mathrm{mes}$ is the measured contact force, and L_reach denotes the maximum reach of the manipulator. In (4.4), the maximum absolute deviation $\max(|{}^{\mathbf{G}}f_\mathrm{imp} - {}^{\mathbf{G}}f_\mathrm{mes}|)$ is scaled with the system maximum reach in order to compare systems of different sizes. The smaller the ρ_imp, the better the performance. Using the data in the last plot in Fig. 4.6, the value of $\rho_\mathrm{imp} = 53.1$ (N/m) is obtained. No comparative data from previous studies are available. The performance indicator ρ_imp used in this study can be used as a benchmark for future studies.

4.4 Variable Impedance Control (Publication P.IV)

In the first experiment with the proposed variable impedance control in publication **P.IV**, the end-effector was collided with the metal sheet (see Fig. 4.2) during the driven test

[3]Note that the target impedance law by Hogan [133] is not directly involved in the control laws; rather it is used to define $\mathbf{\Lambda}_f$ and $\mathbf{\Lambda}_\chi$ in the proposed variable impedance-like control law (31) in publication **P.III**; see Condition 1 and Remark 3 in publication **P.III**.

trajectory to demonstrate the manipulator's compliant behaviour in the constrained motion. The end-effector target frame {**G**}, where the contact occurs, is shown in Fig. 4.2. This frame is aligned with respect to the system base frame {**B**} (whose Y-axis is aligned with respect to gravity). Fig. 4.7(a) shows the driven test trajectory (in black), in which the end-effector was first instructed to travel a distance of −0.5 m along the Y-axis of frame {**B**} in 6 s. Then, a distance of 0.5 m was driven along the X-axis in 3 s. Finally, a distance of 0.5 m was driven along the Y-axis in 6 s. The contact with the metal sheet occurred in approximately −0.73 m on the Y-axis, and the collision velocity was approximately −0.15 m/s. As the green line (the measured Cartesian path) in Fig. 4.7(a) shows, in contact the proposed controller delimits the motion of the end-effector along the Y-axis, preventing excessive contact forces (by becoming compliant).

Fig. 4.7(b) shows the Cartesian position tracking error along the X-axis of frame {**G**}, the direction in which the end-effector motion is not constrained. As this plot shows, the Cartesian position error remains very small (the manipulator has a reach of 3.2 m) through the driven test trajectory. A slight disturbance can be observed in the transition from free space to constrained motion (see time 2.9 s) and during the motion along the X-axis (see 6−9 s).

Fig. 4.7(c) shows the Cartesian position tracking error along the Y-axis of frame {**G**}, the direction in which the end-effector motion is constrained. In free-space motion, accurate position tracking is obtained. Evidently, in constrained motion the tracking error becomes significantly greater.

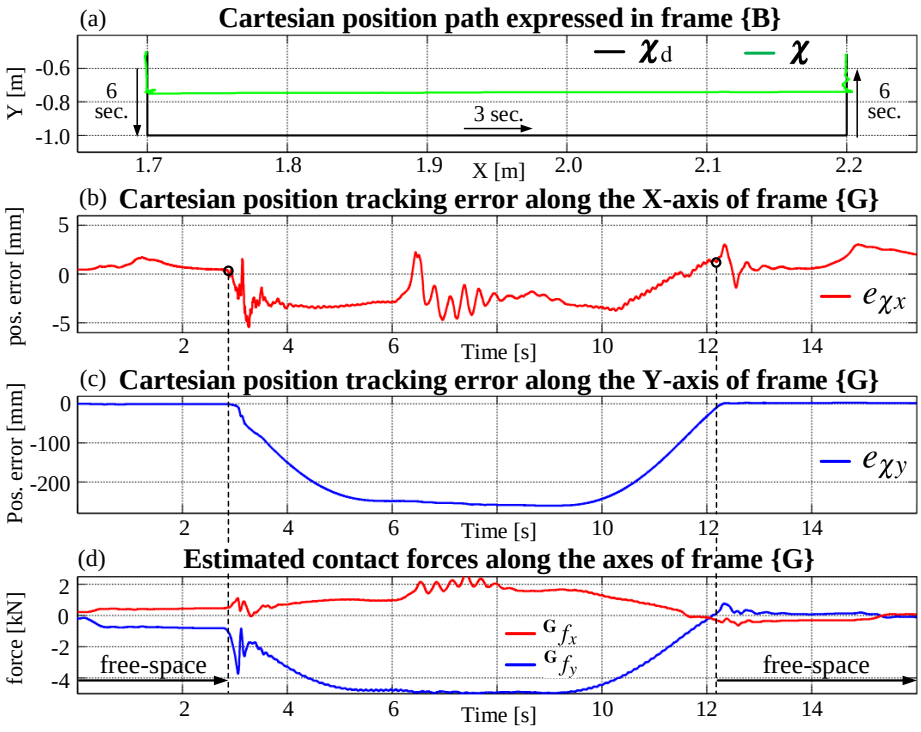

Figure 4.7: The first plot shows the desired Cartesian position path in black and the measured path in green. The second plot and the third plot show the Cartesian position tracking errors along the frame {**G**} X-axis and Y-axis, respectively. The last plot shows the estimated Cartesian contact forces along the axes of frame {**G**}.

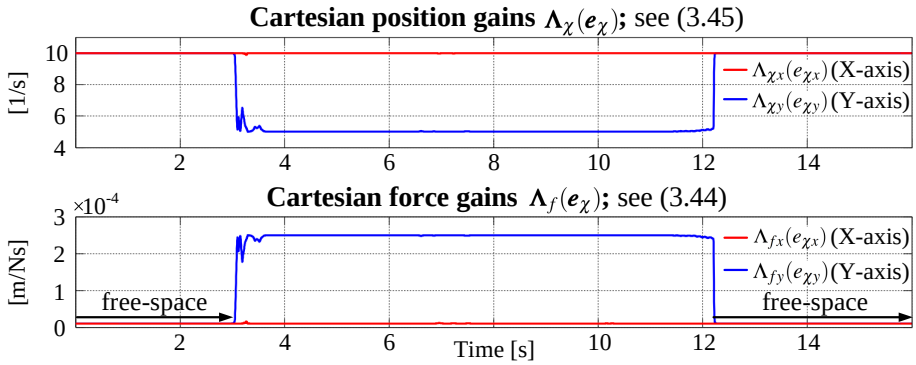

Figure 4.8: The behaviour of the Cartesian position feedback gains and force feedback gains.

Fig. 4.7(d) shows the contact forces along the X-axis (${}^{\mathbf{G}}f_x$) and the Y-axis (${}^{\mathbf{G}}f_y$) in frame $\{\mathbf{G}\}$. As this plot shows, the proposed controller prevents excessive contact forces (by becoming compliant), delimiting the contact force on the Y-axis to -5000 N (despite motion dynamics along the X-axis at the maximum velocity of 0.3 m/s). Note that in free-space motions, contact force estimation errors exist (i.e., ${}^{\mathbf{G}}f_x \neq 0$ and ${}^{\mathbf{G}}f_y \neq 0$).

Despite the contact force estimation errors in Fig. 4.7(d), very accurate position tracking in free space is obtained in Fig. 4.7(b) and Fig. 4.7(c). This is due to the proposed variable impedance control laws (3.42)–(3.45). Fig. 4.8 shows the behaviours of $\mathbf{\Lambda}_\chi(\boldsymbol{e}_\chi)$ and $\mathbf{\Lambda}_f(\boldsymbol{e}_\chi)$ in (3.42) during the driven test trajectory. In free space, the manipulator is stiff; high position gains and low force gains (see times 0–2.9 s and 12.2–16 s in Fig. 4.8). When contact with the metal sheet occurs, the manipulator becomes compliant on the constrained Y-axis (low $\Lambda_{\chi y}$, high Λ_{fy}, because $|e_{\chi y}| > a_{ey}$) but remains stiff in the non-constrained X-axis (high $\Lambda_{\chi x}$, low Λ_{fx}, because $|e_{\chi x}| < a_{ex}$). The manipulator's stiffness can be set with the upper bounds ($\overline{\mathrm{D}}_{dx}$, $\overline{\mathrm{D}}_{dy}$, $\overline{\mathrm{K}}_{dx}$, and $\overline{\mathrm{K}}_{dy}$), and compliance can be set with the lower bounds ($\underline{\mathrm{D}}_{dx}$, $\underline{\mathrm{D}}_{dy}$, $\underline{\mathrm{K}}_{dx}$, and $\underline{\mathrm{K}}_{dy}$).

If the force-sensorless contact force estimation method is used with the (constant) impedance control method (proposed in publication **P.III**), the greater the estimation error in free-space motions, the worse the free-space position tracking accuracy. To investigate the free-space position tracking improvement with the proposed variable impedance control compared to the proposed impedance control, in the second set of experiments the same test trajectory as shown in black in Fig. 4.7(a) was driven in free space (i.e., when pallets and metal sheet were removed) with both methods. The desired

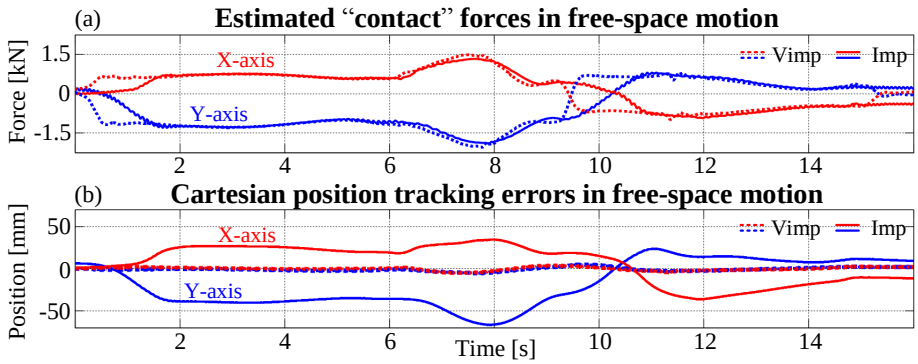

Figure 4.9: Comparison of the impedance control (in Section 3.3.3) and the variable impedance control (in Section 3.3.4) using the force-sensorless contact force estimation.

damping and stiffness for the (constant) impedance control were selected in relation to the variable impedance control lower bounds, so that the manipulator is compliant at all times.

Fig. 4.9 shows the results of the driven free-space motion trajectory. In this figure, the dashed lines show the results with the proposed variable impedance control, and the solid lines show the results with the (constant) impedance control. Although in Fig. 4.9(a) approximately the same contact force estimation errors occur in both cases, superior free-space position tracking accuracy is obtained with the variable impedance control ($|e_{\chi x}|, |e_{\chi y}| < 5$ mm) compared to impedance control ($|e_{\chi x}| < 36$ mm, $|e_{\chi y}| < 67$ mm); see Fig. 4.9(b).

4.5 Adaptive and Nonlinear Model-Based Control of VDAPPs (Unpublished Manuscript P.V)

The VDAPP studied in unpublished manuscript **P.V** is shown in Fig. 3.7. The variables (p_{s}, $\dot{p}_{\mathrm{s}}$, $\dot{\alpha}$, and p_{cp}) discussed in the following subsections are illustrated in this figure. As discussed earlier, the dynamic behaviour of the system is highly nonlinear and can be described with a fourth-order differential equation. Next, in Section 4.5.1, the experimental results in unpublished manuscript **P.V** are presented with the known-parameter control design (i.e., without parameter adaptation). Then, Section 4.5.2 shows the respective results with the adaptive control design.

4.5.1 Results for Known-Parameter Control

Fig. 4.10 shows the results for known-parameter control design. The first plot shows the tracking performance for the main feedback variable. The desired discharge pressure p_{sd} is shown in black, and the measured discharge pressure p_{s} is shown in grey. The absolute maximum discharge pressure tracking error for the test trajectory is approximately 10.13 bar (5.9 percent of the test trajectory's peak-to-peak amplitude).

Plots 2–4 in Fig. 4.10 show the tracking performance for the subsidiary feedback variables ($\dot{p}_{\mathrm{s}}$, $\dot{\alpha}$, and p_{cp}) with the known-parameter control design. The second plot shows the required first-order discharge pressure dynamics $\dot{p}_{sr}$ in black, and its controlled variable $\dot{p}_{\mathrm{s}}$ in grey. The third plot shows the desired swash plate angular velocity $\dot{\alpha}_d$ in black and its controlled variable $\dot{\alpha}$ in grey. The last plot shows the desired control piston chamber pressure $p_{\mathrm{cp}d}$ in black and its controlled variable p_{cp} in grey.

4.5.2 Results for Adaptive Control

Fig. 4.11 shows the main results in unpublished manuscript **P.V**, i.e., the control performance with the adaptive control design. The first plot shows the tracking performance for the main feedback variable. The desired discharge pressure p_{sd} is shown in black, and the measured discharge pressure p_{s} is shown in grey. The absolute maximum discharge pressure tracking error for the test trajectory is 1.36 bar (0.8 percent of the test trajectory's peak-to-peak amplitude). This is an improvement of approximately seven times compared to the results with the known-parameter control design.

Plots 2–4 in Fig. 4.11 show the tracking performance for the subsidiary feedback variables ($\dot{p}_{\mathrm{s}}$, $\dot{\alpha}$, and p_{cp}) with the adaptive control design. The second plot shows the required first-order discharge pressure dynamics $\dot{p}_{sr}$ in black and its controlled variable $\dot{p}_{\mathrm{s}}$ in grey.

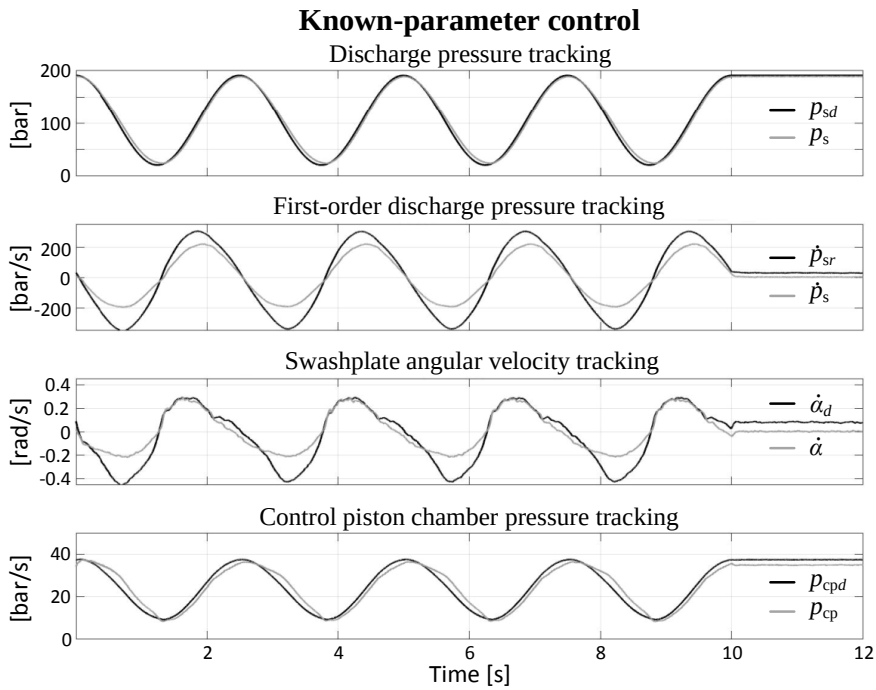

Figure 4.10: The known-parameter control design. The tracking performance of the system's feedback variables p_s, $\dot{p}_s$, $\dot{\alpha}$, and p_{cp}. The reference trajectories are given in black, and the measured variables are given in grey.

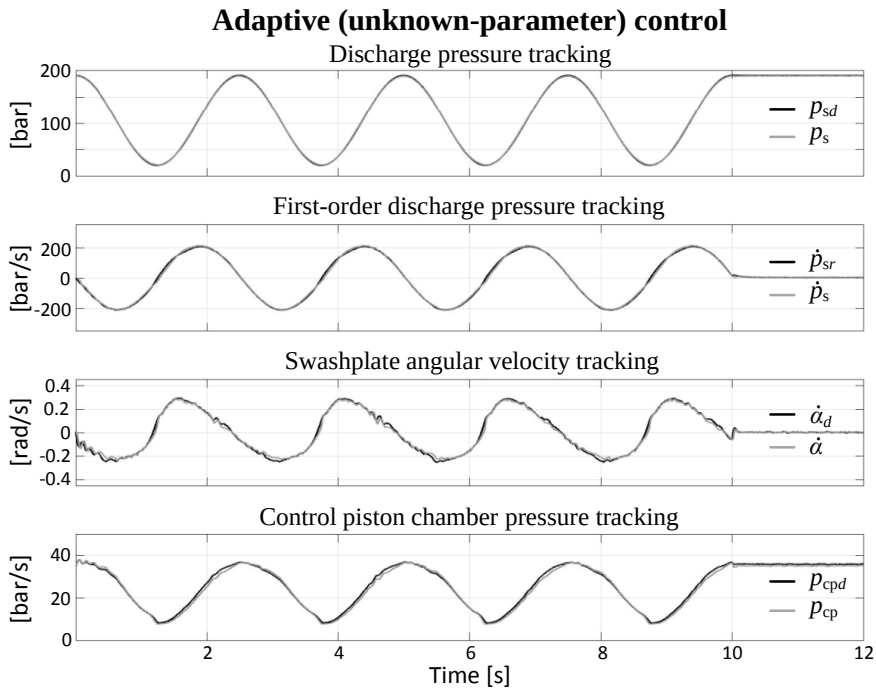

Figure 4.11: The adaptive control design. The tracking performance of the system's feedback variables p_s, $\dot{p}_s$, $\dot{\alpha}$, and p_{cp}. The reference trajectories are given in black, and the measured variables are given in grey.

The third plot shows the desired swash plate angular velocity $\dot{\alpha}_d$ in black and its controlled variable $\dot{\alpha}$ in grey. The last plot shows the desired control piston chamber pressure $p_{\mathrm{cp}d}$ in black and its controlled variable p_{cp} in grey. As these plots show, a very accurate trajectory tracking performance is achieved for all subsidiary feedback variables.

As Figs. 4.10 and 4.11 demonstrate, the adaptive control design, with the rapid parameter adaptation law [24, Definition 2.12], is superior to known-parameter control. In [120] and publication **P.II**, corresponding results were obtained for the control of the hydraulic manipulator, where the results using the rapid parameter adaptation law were superior compared to the known-parameter control design (in [120] and publication **P.II**, a first-order differentiable projection function in (3.3) was used instead of the second-order differentiable version in (3.4) used in unpublished manuscript **P.V**).

In [171], the desired discharge pressure was varied between 50 and 100 bars using a sinusoidal desired pressure trajectory. To compare the control performances between the proposed method and the results in [171], the following performance indicator ρ_{p} is proposed:

$$\rho_{\mathrm{p}} = \frac{\max\{|p_{\mathrm{s}d} - p_{\mathrm{s}}|\}}{\max\{|\dot{p}_{\mathrm{s}}|\}} \tag{4.5}$$

which evaluates the tracking error with respect to the rate of applied dynamics. The smaller the ρ_{p}, the better the control performance. Using the data in Fig. 4.11, for the proposed method, $\rho_{\mathrm{p}} = \frac{1.36 \text{ bar}}{213 \text{ bar/s}} \approx 0.00064$ (s) can be measured. Surprisingly, for the best results in [171] (see Fig. 11(a) in [171]), the same value $\rho_{\mathrm{p}} = \frac{1 \text{ bar}}{157 \text{ bar/s}} \approx 0.00064$ (s) is obtained ($\dot{p}_{\mathrm{s}}$ was not reported in [171]; thus, $\max\{|\dot{p}_{\mathrm{s}}|\}$ in ρ_{p} was estimated from the pressure profile $p_{\mathrm{s}d}(t) = [75 - 25\cos(2\pi t)]$ bar).

However, it is evident that the discharge pressure range of 170 bars with the minimum pressure of 20 bars (see the first plot in Fig. 4.11) is much more challenging than the discharge pressure range of 50 bars with the minimum pressure of 50 bars (the test trajectory in [171]). This is due to the highly nonlinear operation space of VDAPPs. The absolute maximum discharge pressure tracking error with the proposed method is only 0.8 percent of the test trajectory's peak-to-peak amplitude. In [171], this same value is 2 percent. This was expected due to the proposed controller's proper handling of swash plate dynamics. Thus, it can be concluded that the proposed controller has a comparative ratio to [171], in view of (4.5), but tested in a larger operation range.

The main emphasis in unpublished manuscript **P.V** was to design a high-performance discharge pressure tracking controller for VDAPPs, whose dynamic behaviours are highly nonlinear and can be described by a fourth-order differential equation. As the results in Fig. 4.11 indisputably verify, the proposed control method is capable of rigorously addressing the highly nonlinear dynamic behaviours of the truly complex VDAPP in a very large operational range. However, it is valid to mention that the results in Fig. 4.11 are restricted to use with passive system loads (constant orifice as the system load), whereas in [171] the pump performance was also verified with varying loads.

5 Discussion

This section presents a summary of how all the RPs, described in Section 1.6, are addressed.

5.1 High Performance (RP 1)

The developed controller(s) should be capable of 1) rigorously addressing the highly nonlinear dynamic behaviour of the entire system and 2) realizing the state-of-the-art control performance.

The main emphasis in this thesis was high-performance stability-guaranteed NMB control of hydraulic manipulators. First, in publication **P.I**, the state-of-the-art NMB Cartesian position tracking controller in free-space motions was designed for the hydraulic robotic manipulator (see the results in Section 4.1) and the controller's ability to rigorously address the highly nonlinear dynamic behaviour of the system was verified. As the results clearly demonstrate, the proposed controller is able to rigorously cope with the highly nonlinear dynamic behaviour of the hydraulic system: The shape of the Cartesian position tracking error curves remains almost unchanged in spite of the driven velocity. The results of this publication provide a rigorous basis for contact control experiments, where rigorously addressed system dynamics is the priority.

Due to the superior results in free-space motions (and verification of the rigorously addressed system dynamics), advanced results were anticipated in the contact control experiments. This anticipation was not groundless. The results in Sections 4.2–4.4 demonstrate superior control performances with the hybrid motion/force control (publication **P.II**), impedance control (publication **P.III**), and variable impedance control (publication **P.IV**).

An objective evaluation of results should be the cornerstone of all scientific research. Such evaluation also speeds up technology transfer between academia and industry and promotes the most advanced practices in a given field. However, in robotics and automation, objective evaluation and benchmarking of the state of the art can be very challenging. In this thesis, a unifying performance indicator ρ_{fs} (the ratio of the maximum position tracking error with respect to the maximum velocity) was used to evaluate the different free-space control methods, demonstrating the state-of-the-art control performance with the proposed method in publication **P.I**. Unfortunately, no comparative data were available in previous studies for the objective evaluation of the proposed hybrid motion/force control method and the impedance control method.[1] However, based on observations on the

[1] To evaluate the control performance of the hybrid motion/force control methods, the performance indicator ρ_{hmf} in equation (4.2) was proposed in Section 4.2. To evaluate the control performance of the impedance control methods, the performance indicator ρ_{imp} in equation (4.4) was proposed in Section 4.3.

superiority of the stability-guaranteed NMB control methods (see Tables 4.1 and 4.2 in Section 4.1) and the superior control accuracies demonstrated in Sections 4.2–4.4, this thesis also provided a new state of the art in constrained motion control with hydraulic manipulators. The results (the performance indicator values) in Sections 4.1–4.3 can be used as the new benchmark for evaluating the performance of future studies.

Unpublished manuscript **P.V** proposed NMB control for VDAPPs, for the first time without using linearization or order reduction. As the results in Section 4.5.2 show, the proposed control design method is capable of rigorously addressing the highly nonlinear dynamic behaviours of truly complex systems (in unpublished manuscript **P.V** with a VDAPP) in a very large operational range and with an accurate tracking performance. Comparing these results to a state-of-the-art study [171], with the proposed performance indicator ρ_{p} in equation (4.5), a similar performance was measured. However, a wider pressure range (i.e., nonlinear operating space) was covered with the proposed controller.

Thus, it can be concluded that with the proposed control methods for hydraulic robotic manipulators (in publications **P.I**–**P.IV**) and with the proposed control method for VDAPPs (in unpublished manuscript **P.V**), the proposed controllers are capable of rigorously addressing the highly nonlinear dynamic behaviour of the systems and realizing the state-of-the-art control performance.

5.2 Adaptive Control (RP 2)

The developed controller(s) should be capable of addressing a wide variety of system parameter uncertainties in hydraulic robotic systems.

All the controllers developed in publications **P.I**–**P.IV** and in unpublished manuscript **P.V** include the possibility of parameter adaptation for the uncertain parameters in the subsystems' dynamics. In publication **P.I**, the parameter adaptation was not incorporated in the controller, but it can be easily designed, as shown in publications **P.II**–**P.IV**. Thus, there might even be room to improve the free-space motion control performance demonstrated in publication **P.I** if parameter adaptation is enabled.

The adaptive control designs used in this thesis are the rapid parameter adaptation laws shown in (3.3) and (3.4) (proposed by Zhu in [24, 35]). As Figs. 4.10 and 4.11 in Section 4.5 clearly demonstrate, the adaptive control design, which uses the rapid parameter adaptation law (3.4), is superior to known-parameter control. In [120] and publication **P.II**, corresponding results were obtained for control of the hydraulic manipulator, where the results using the rapid parameter adaptation law were superior compared to the known-parameter control design. Thus, it can be concluded that the rapid parameter adaptation laws 1) provide an efficient method for compensating model parameter uncertainties and 2) can significantly improve the control performance of highly nonlinear hydraulic systems.

5.3 Stability-Guaranteed (RP 3)

A rigorous stability proof should be provided for the developed NMB controller(s).

A rigorous stability proof is provided for all the controllers proposed in publications **P.I**–**P.IV** and in unpublished manuscript **P.V**. This is due to the subsystem-dynamics-based VDC (and its unique VPF and *virtual stability* features; see Definitions 6 and 7), which allows the system control design and the stability analysis to be performed at the

subsystems level, without imposing additional approximations. This method enabled the author to tackle the longstanding problem of stability-guaranteed NMB control of hydraulic manipulators in constrained motion, characterized as one of the open problems in the category of NMB control of hydraulic manipulators. This is one of the main contributions of this thesis.

As another important contribution, in unpublished manuscript **P.V**, a novel rigorous control method for stability-guaranteed NMB control was proposed by extending the control design principles of VDC from robotic systems to a broader group of dynamic systems. Similar to VDC, the proposed method allows the independent control design of the individual subsystems as long as "stability connectors" (similar to VPFs in VDC) are properly handled. This allows flexibility in the stability-guaranteed NMB control design. In contrast, the well-known backstepping control design framework imposes unnecessary restrictions on the forms a system must take for the procedure to follow.

As the results in Sections 4.1–4.5 demonstrate, there is a clear interconnection between the stability-guaranteed NMB control design and state-of-the-art control performance. *The contributions of this thesis reveal that the stability-guaranteed designs of control systems should be considered not only as an academic advancement but also as necessity to create state-of-the-art control practices that will eventually benefit industry.*

5.4 Real-Time Applicable (RP 4)

The developed controller(s) should be computationally deterministic and applicable to real-time control. The computational burden of Lagrange-based control methods (see Section 1.1) should be avoided to provide the possibility (in future studies) of extending the proposed methods to complex robotic systems in which the number of DOF of motion can easily exceed thirty.

As discussed in Chapter 3, compared to the Lagrange method, the Newton-Euler method is more fundamental and computationally more efficient as it exploits the typical open structure of the manipulator kinematic chain. Indeed, with the Lagrange-based control methods, the complexity (computational burden) of robot dynamics is proportional to the fourth power of the number of DOF of motion.

The VDC approach is the first control method to take full advantage of the Newton-Euler method without imposing additional approximations on the control design. With subsystem-dynamics-based VDC, the control computations are proportional to the number of subsystems, not to the fourth power of the number of DOF of motion. Furthermore, these control computations can be performed locally at the subsystem level, even with embedded hardware/software with an ultrahigh sampling rate, as demonstrated in [39]. Thus, the VDC approach (which is used as the underlying control design framework in this thesis) overcomes the longstanding problem of computational burden in NMB control of robotic systems, originating from the use of Lagrange-based control methods.

In light of the above, although a relatively "simple" two-DOF hydraulic manipulator was used as the experimental platform to validate the proposed controllers, the proposed subsystem-dynamics-based methods in publications **P.I**–**P.IV** are extendable to more complex robotic systems (where the number of DOF of motion can easily exceed thirty) with real-time control applicability.

5.5 Modularity (RP 5)

The developed controller(s) should be composed of elementary modular "subsystems" similar to the "subsystems" of a real robotic system, such that changes to the original system affect only the respective local control equations associated with this subsystem, while the other control equations associated with the rest of the system remain unchanged. Once designed, the ensemble, e.g., a hydraulic manipulator with its control, should be able to be "plugged" into another system, without redesigning the control for the entire system. The controller architecture should allow the replacement of the actuators, e.g., from hydraulic to electric, without substantial controller redesign.

As addressed in the book *Virtual Decomposition Control - Towards Hyper Degrees of Freedom Robots* [24], one of the advantages of using the VDC approach is that a change in the dynamics of a subsystem (such as substituting a hydraulic actuator for an electrical motor) affects only the respective local control equations associated with this subsystem, while keeping the control equations associated with the rest of the system unchanged. In addition, as shown in publication **P.I**, extra subsystems can even be added to the system while keeping the control equations associated with the original system unchanged. Thus, VDC has brought a concept of modularity for the first time to control systems engineering with its subsystem-dynamics-based control design architecture.

VDC has enabled the use of a "plug-and-play" type of modular control system structures (subsystems), using the concepts of VPF (see Definition 6) and *virtual stability* (see Definition 7); if every subsystem qualifies as virtually stable, VPFs among subsystems cancel each other out at every VCP, eventually leading to the stability of the entire system. Consequently, this means that the designed system, e.g., the hydraulic manipulator used in this thesis, can be "plugged" into another system using the concepts of VPFs and *virtual stability*. In addition, the general control system structures for the rigid links and joints can be used as "building blocks" to design truly complex robotic systems with real-time control applicability (see the previous section).

5.6 Force Estimation (RP 6)

A practical solution for force-sensorless contact force control should be provided, because the typically six-DOF force/moment sensors (at the system end-effector) are sensitive to shocks and overloading, a situation that frequently occurs in hydraulic operations.

Publication **P.II** proposed a novel method for force-sensorless contact force estimation for hydraulic robotic manipulators. Taking full advantage of the accurate system modeling of VDC, the existing dynamic model of the system was used to address this task. As the results in Sections 4.2 – 4.4 demonstrate, force-sensorless constrained motion control can be realized for hydraulic robotic manipulators, despite their highly nonlinear dynamic behaviour. Because in the scope of this thesis major simplifications were made in the contact force estimation (the system inertia and piston frictions were neglected; see the discussion in Section 1.7), as demonstrated in publication **P.III**, the greater the driven velocity, the worse the contact force estimation in free-space motions.[2] Thus, in publication **P.IV**, the main emphasis was on improving the Cartesian free-space position control accuracy in force-sensorless contact force control with hydraulic manipulators. With the proposed method, the manipulator can be made stiff along the unconstrained

[2]Note that when the system comes into contact with the environment, the velocity along the direction of the constrained motion becomes relatively slow, enabling an accurate contact force estimation.

motion (enabling accurate position tracking performance) and compliant along the constrained motion (preventing excessive contact forces).

5.7 Experimentally Verified (RP 7)

The developed controller(s) should be practically implemented and experimentally verified.

All controllers proposed in publications **P.I**–**P.IV** and in unpublished manuscript **P.V** were experimentally verified with the machinery available at the heavy laboratory at the IHA. As usual for high-performance control systems implementation, high-end hardware components (e.g., control valves, pressure sensors, and real-time control system) were used to realize the control system. More detailed information about the hardware components can be found in publication **P.II** (the control setup for the hydraulic robotic manipulator) and in unpublished manuscript **P.V** (the control setup for the VDAPP).

5.8 Energy Efficiency (RP 8)

An advanced control for the VDAPP should be designed that provides the possibility of reducing energy consumption. The designed controller should meet the features defined in Sections 5.1 through 5.4 and 5.7.

In addition to the highly nonlinear dynamic behaviour of hydraulic robotic manipulators, the lack of energy efficiency is another fundamental challenge in hydraulic systems. Unpublished manuscript **P.V** proposed a NMB control for VDAPPs, for the first time without using linearization or order reduction. The parameter adaptation was enabled for all parameters in the subsystems' dynamics. The system stability was rigorously guaranteed with asymptotic convergence. As the experimental results in Section 4.5.2 show, very accurate discharge pressure tracking was obtained with the proposed method. This provides the possibility of reductions in energy consumption. The results of this method and a state-of-the-art study [171] were compared, and the measured performance indicator value was similar. However, a much wider pressure range (i.e., nonlinear operating space) was covered with the proposed controller.

One limitation of the proposed method is that it was verified with only a constant orifice as the system load (the state-of-the-art methods in [169] and [171] were verified with varying loads). Thus, more detailed experiments with varying loads are still needed for the proposed method in unpublished manuscript **P.V** to verify the feasibility of providing energy consumption reductions for hydraulic robotic systems.

6 Conclusion and Future Work

This compendium thesis proposed experimentally verified rigorous foundations for high-performance NMB control of hydraulic robotic manipulators, including free-space motion control and different constrained motion controls. In Chapter 1, three fundamental challenges in hydraulic robotic systems were identified: 1) The dynamic behaviour of hydraulic systems is highly nonlinear, making especially their force control in constrained motions a truly challenging task, 2) traditional hydraulic systems lack energy efficiency, and 3) when moving toward complex hydraulic robotic systems (even with hyper-DOF of motion), high-performance control in real time is a substantial challenge with the commonly used Lagrange-based control design methods. Publications **P.I**–**P.IV** concentrated on the first challenge and demonstrated the state-of-the-art control performance in their own subcategories (free-space motion control in publication **P.I**, hybrid motion/force control in publication **P.II**, impedance control in publication **P.III**, and variable impedance control in publication **P.IV**). Unpublished manuscript **P.V** concentrated on the second challenge and demonstrated a method for reducing the hydraulic systems' energy consumption with electro-hydraulically controlled VDAPPs. The third challenge was addressed by using the VDC approach as an underlying control design framework.

As shown in the previous section, all the RPs (summarized in Section 1.6) were addressed in this thesis. The restrictions of the proposed methods can be found in Section 1.7. The scientific contributions **C1**–**C9** of this thesis are given in Section 1.8 and can be found in the attached papers as follows: Contribution **C1** was originally presented in publication **P.I**, contributions **C2** and **C3** were originally presented in publication **P.II**, contributions **C4**–**C6** were originally presented in publication **P.III**, contribution **C7** was originally presented in publication **P.IV**, and contributions **C8** and **C9** can be found in unpublished manuscript **P.V**. Contributions **C2**, **C5**, **C6**, and **C8** are emphasized as the main contributions of this thesis, with the following features:

- Contribution **C2** solved the longstanding open problem of a stability-guaranteed NMB control design in constrained motion;
- Contribution **C5** discovered a special connection between the proposed impedance control parameters and the targeted impedance, making stability-guaranteed hydraulic robot impedance control possible;
- Contribution **C6** proposed a stability-guaranteed NMB controller for hydraulic robotic manipulators for the first time covering both free-space motion and constrained motion;
- Contribution **C8** proposed a rigorous new NMB control design method, extending the control design principles of VDC from robotic systems to a broader group of dynamic systems.

All full-dynamics-based control designs in this thesis (in publications **P.I**–**P.IV** and in

unpublished manuscript **P.V**) are rigorously stability guaranteed. As shown in Chapter 4, *the contributions of this thesis reveal that the stability-guaranteed designs of control systems should be considered not only an academic advancement but also a necessity to create state-of-the-art control practices that will eventually benefit industry.*

The methods presented in this thesis can be implemented in (robotic) systems ranging from conventional working machines (e.g., in construction, forestry, mining, and agricultural machines) to advanced robotic systems, without restrictions on the complexity of the system's mechanical structure. This is because the VDC approach (which was used as the underlying control design framework in this thesis) overcomes the longstanding problem of the computational burden in complete-dynamic-based control using the Lagrange method. It provides the possibility of realizing real-time control of complex robotic systems (where the number of the DOF of motion can easily exceed thirty), without imposing additional approximations.[1]

The VDC approach has also brought a modularity for the first time to control systems engineering, enabling modular control design locally at the subsystem level. These modular control components for the robotic system's rigid links and joints can be used as building blocks to design truly complex robotic systems. The VDC approach also allows "plug-and-play" control system structures, because the designed system, e.g., the hydraulic manipulator used in this thesis, can be "plugged" into other systems using the concept of VPF (see Definition 6) as long as the constraints of *virtual stability* (see Definition 7) are satisfied. Consequently, the results of this thesis represent a significant step toward the ultimate goal, which is to design an energy-efficient and high-performance real-time control for complex robotic systems with rigorously addressed system stability.

[1] In the subsystem-dynamics-based VDC, the control computations are proportional to the number of subsystems, not to the fourth power of the number of DOF of motion as in complete-dynamic-based control using the Lagrange method. Furthermore, the control computations in VDC can be performed locally at the subsystem level, even with embedded hardware/software with an ultrahigh sampling rate, as is shown in [39].

Bibliography

[1] L. Sciavicco and B. Siciliano, *Modeling and Control of Robot Manipulators*. London: Springer, 2000.

[2] R. Jazar, *Theory of applied robotics: kinematics, dynamics, and control*. Springer Science & Business Media, 2010.

[3] B. Siciliano and O. Khatib, *Springer handbook of robotics*. Springer Science & Business Media, 2008.

[4] EU Robotics, "Strategic research agenda for robotics in europe 2014 – 2020," 2014, [Cited: 15.3.2016]. [Online]. Available: https://eu-robotics.net/downloads/downloads/

[5] PAL Robotics, "REEM-C humanoid robots," [cited 29.6.2016]. [Online]. Available: Available:http://pal-robotics.com/en/products/reem-c/

[6] Boston Dynamics, "Robots," [cited 10.6.2016]. [Online]. Available: http://www.bostondynamics.com/

[7] X. Rong, Y. Li, J. Ruan, and B. Li, "Design and simulation for a hydraulic actuated quadruped robot," *J. mechanical science and technology*, vol. 26, no. 4, pp. 1171 – 1177, 2012.

[8] S.-H. Hyon, D. Suewaka, Y. Torii, N. Oku, and H. Ishida, "Development of a fast torque-controlled hydraulic humanoid robot that can balance compliantly," in *IEEE-RAS 15th Int. Conf. on Humanoid Robots (Humanoids)*, 2015, pp. 576 – 581.

[9] S. Kuindersma, R. Deits, M. Fallon, A. Valenzuela, H. Dai, F. Permenter, T. Koolen, P. Marion, and R. Tedrake, "Optimization-based locomotion planning, estimation, and control design for the atlas humanoid robot," *Autonomous Robots*, vol. 40, no. 3, pp. 429 – 455, 2016.

[10] C. Semini, N. G. Tsagarakis, E. Guglielmino, M. Focchi, F. Cannella, and D. G. Caldwell, "Design of HyQ – a hydraulically and electrically actuated quadruped robot," *Journal of Systems and Control Engineering*, vol. 225, pp. 831 – 849, 2011.

[11] daVinci Surgery, "Surgery robot," [cited 29.6.2016]. [Online]. Available: http://www.davincisurgery.com/da-vinci-surgery/da-vinci-surgical-system/

[12] Menzi Muck, "Walking excavators," [cited 29.6.2016]. [Online]. Available: http://www.menzimuck.com/en/product-groups/menzi-muck-walking-excavators/

[13] M. Hutter, P. Leemann, S. Stevsic, A. Michel, D. Jud, M. Hoepflinger, R. Siegwart, R. Figi, C. Caduff, M. Loher, and S. Tagmann, "Towards optimal force distribution for walking excavators," in *IEEE Int. Conf. on Advanced Robotics (ICAR)*, 2015, pp. 295–301.

[14] F. Lewis, C. Abdallah, and D. Dawson, *Control of robot manipulators*. Macmillan Pub. Co., 1993.

[15] I. Hunter, J. Hollerbach, and J. Ballantyne, "A comparative analysis of actuator technologies for robotics," *Robotics Review*, vol. 2, pp. 299–342, 1991.

[16] C. Mavroidis, C. Pfeiffer, and M. Mosley, "5.1 conventional actuators, shape memory alloys, and electrorheological fluids," *Automation, miniature robotics, and sensors for nondestructive testing and evaluation*, vol. 4, p. 189, 2000.

[17] K. Yunt, "A hybrid robust lyapunov controller for dynamic catch, grasp and carry maneuvers," *ASME J. Dyn. Syst., Meas., Control*, vol. 137, no. 8, pp. 1–11, 2015.

[18] Y. Bengio, A. Courville, and P. Vincent, "Representation learning: A review and new perspectives," *IEEE Trans. on Pattern Analysis and Machine Intelligence*, vol. 35, no. 8, pp. 1798–1828, 2013.

[19] Y. LeCun, Y. Bengio, and G. Hinton, "Deep learning," *Nature*, vol. 521, no. 7553, pp. 436–444, 2015.

[20] W. Ryan, "How Google's self-driving cars detect and avoid obstacles," Sep. 2014. [Online]. Available: http://www.extremetech.com/extreme/189486-how-googles-self-driving-cars-detect-and-avoid-obstacles

[21] J. Ramsey, "Self-driving cars to be tested on Virginia highways," *Richmond Times-Dispatch*, Jan. 2015. [Online]. Available: http://www.bbc.com/news/technology-28551069

[22] Google, "Google Self-Driving Car Project," [cited 28.7.2016]. [Online]. Available: https://www.google.com/selfdrivingcar/

[23] IEEE Spectrum, "Self-Driving Cars," [cited 2.9.2016]. [Online]. Available: http://spectrum.ieee.org/transportation/self-driving

[24] W.-H. Zhu, *Virtual Decomposition Control - Toward Hyper Degrees of Freedom Robots*. Springer-Verlag, 2010.

[25] H. Asada and J.-J. Slotine, *Robot analysis and control*. John Wiley & Sons, 1986.

[26] J. J. Craig, *Introduction to robotics: mechanics and control*. Pearson Prentice Hall Upper Saddle River, 2005, vol. 3.

[27] J. Y. S. Luh, M. W. Walker, and R. P. C. Paul, "On-line computational scheme for mechanical manipulators," *ASME J. Dyn. Syst., Meas., Control*, vol. 102, no. 2, pp. 69–76, 1980.

[28] M. Krstić, I. Kanellakopoulos, and P. Kokotović, *Nonlinear and Adaptive Control Design*. John Wiley & Sons, Inc., 1995.

[29] T.-S. Li, D. Wang, G. Feng, and S.-C. Tong, "A DSC approach to robust adaptive NN tracking control for strict-feedback nonlinear systems," *IEEE Trans. Syst. Man Cybern., Part B, Cybern.*, vol. 40, no. 3, pp. 915–927, 2010.

[30] Y. Li, S. Tong, and Y. Li, "Observer-based adaptive fuzzy backstepping dynamic surface control design and stability analysis for mimo stochastic nonlinear systems," *Nonlinear Dynamics*, vol. 69, no. 3, pp. 1333–1349, 2012.

[31] J. Liu, "Observer-based backstepping dynamic surface control for stochastic nonlinear strict-feedback systems," *Neural Computing and Applications*, vol. 24, no. 5, pp. 1067–1077, 2014.

[32] N. G. Shakev and A. V. Topalov, "Continuous sliding mode control of a quadrotor," in *Recent Advances in Sliding Modes: From Control to Intelligent Mechatronics*. Springer, 2015, pp. 441–458.

[33] W.-H. Zhu, Y.-G. Xi, Z.-J. Zhang, Z. Bien, and J. De Schutter, "Virtual decomposition based control for generalized high dimensional robotic systems with complicated structure," *IEEE Trans. Robot. Autom.*, vol. 13, no. 3, pp. 411–436, 1997.

[34] W.-H. Zhu, Z. Bien, and J. De Schutter, "Adaptive motion/force control of multiple manipulators with joint flexibility based on virtual decomposition," *IEEE Trans. Autom. Control*, vol. 43, no. 1, pp. 46–60, 1998.

[35] W.-H. Zhu and J. De Schutter, "Adaptive control of mixed rigid/flexible joint robot manipulators based on virtual decomposition," *IEEE Trans. Robot. Autom.*, vol. 15, no. 2, pp. 310–317, 1999.

[36] W.-H. Zhu and J. De Schutter, "Control of two industrial manipulators rigidly holding an egg," *IEEE Control Systems*, vol. 19, no. 2, pp. 24–30, 1999.

[37] W.-H. Zhu and J. De Schutter, "Experimental verifications of virtual-decomposition-based motion/force control," *IEEE Trans. Robot. Autom.*, vol. 18, no. 3, pp. 379–386, 2002.

[38] W.-H. Zhu and G. Vukovich, "Virtual decomposition control for modular robot manipulators," in *Proc. IFAC World Congress*, Sep. 2011, pp. 13 486–13 491.

[39] W.-H. Zhu, T. Lamarche, E. Dupuis, D. Jameux, P. Barnard, and G. Liu, "Precision control of modular robot manipulators: The VDC approach with embedded FPGA," *IEEE Trans. Robot.*, vol. 29, no. 5, pp. 1162–1179, 2013.

[40] A. Alleyne and R. Liu, "On the limitations of force tracking control for hydraulic servosystems," *ASME J. Dyn. Syst., Meas., Control*, vol. 121, no. 2, pp. 184–190, 1999.

[41] J. Watton, *Fluid Power Systems: modelling, simulation, analog and microcomputer control*. New York: Prentice Hall, 1989.

[42] K. Edge, "The control of fluid power systems–responding to the challenges," *Proc IMechE, Part I: J. Syst. Control Eng.*, vol. 211, no. 2, pp. 91–110, 1997.

[43] B. Yao, F. Bu, and G. Chiu, "Non-linear adaptive robust control of electro-hydraulic systems driven by double-rod actuators," *Int. J. of Control*, vol. 74, no. 8, pp. 761–775, 2001.

[44] M. Vukobratovic, *Dynamics and robust control of robot-environment interaction*. World Scientific, 2009, vol. 2.

[45] C. An and J. Hollerbach, "Dynamic stability issues in force control of manipulators," in *Proc. of American Control Conference*, 1987, pp. 821–827.

[46] C. An and J. Hollerbach, "Kinematic stability issues in force control of manipulators," in *Proc. of IEEE Int. Conf. on Robotics and Automation*, vol. 4, 1987, pp. 897–903.

[47] C. An and J. Hollerbach, "The role of dynamic models in cartesian force control of manipulators," *Int. J. Robot. Res.*, vol. 8, no. 4, pp. 51–72, 1989.

[48] H. Zhang, "Kinematic stability of robot manipulators under force control," in *Proc. of IEEE Int. Conf. on Robotics and Automation*, 1989, pp. 80–85.

[49] S. Eppinger and W. Seering, "Understanding bandwidth limitations in robot force control," in *Proc. of IEEE Int. Conf. on Robotics and Automation*, vol. 4, 1987, pp. 904–909.

[50] S. Eppinger and W. Seering, "Three dynamic problems in robot force control," in *Proc. of IEEE Int. Conf. on Robotics and Automation*, 1989, pp. 392–397.

[51] T. Yoshikawa, "Force control of robot manipulators," in *Proc. of Int. Conf. on Robotics and Automation*, vol. 1, Apr. 2000, pp. 220–226.

[52] M. Sirouspour and S. Salcudean, "Nonlinear control of hydraulic robots," *IEEE Trans. on Robotic and Automation*, vol. 17, no. 2, pp. 759–765, Apr. 2001.

[53] A. Stolt, M. Linderoth, A. Robertsson, and R. Johanson, "Force controlled robotic assembly without a force sensor," in *IEEE Int. Conf. on Robotics and Automation*, 2012, pp. 1538–1543.

[54] A. Stolt, M. Linderoth, A. Robertsson, and R. Johanson, "Detection of contact force transient in robotic assembly," in *IEEE Int. Conf. on Robotics and Automation*, 2015, pp. 962–968.

[55] European Commission, "Energy efficiency directive," 2012, [Cited: 9.3.2016]. [Online]. Available: https://ec.europa.eu/energy/en/topics/energy-efficiency/energy-efficiency-directive

[56] C2ES, "Energy and climate goals of China's 12th five-year plan," 2011, [Cited: 9.3.2016]. [Online]. Available: http://www.c2es.org/docUploads/energy-climate-goals-china-twelfth-five-year-plan.pdf

[57] J. Johnson, *Design of electrohydraulic systems for industrial motion control*. Parker Hannifin Corporation, 1995.

[58] J. Grabbel and M. Ivantysynova, "An investigation of swash plate control concepts for displacement controlled actuators," *Int. J. Fluid Power*, vol. 6, no. 2, pp. 19–36, 2005.

[59] R. Hippalgaonkar and M. Ivantysynova, "Optimal power management for DC hydraulic hybrid multi-actuator machines–Parts I-II," *ASME J. Dyn. Syst., Meas., Control*, vol. 138, no. 5, 2016.

[60] G. Zeiger and A. Akers, "Torque on the swashplate of an axial piston pump," *ASME J. Dyn. Syst., Meas., Control*, vol. 107, no. 3, pp. 220–226, 1985.

[61] G. Zeiger and A. Akers, "Dynamic analysis of an axial piston pump swashplate control," *Proc. IMechE, Part C: J. Mech. Eng. Sci.*, vol. 200, no. 1, pp. 49–58, 1986.

[62] S. Kim, H. Cho, and C. Lee, "A parameter sensitivity analysis for the dynamic model of a variable displacement axial piston pump," *Proc. IMechE, Part C: J. Mech. Eng. Sci.*, vol. 201, no. 4, pp. 235–243, 1987.

[63] G. Schoenau, R. Burton, and G. Kavanagh, "Dynamic analysis of a variable displacement pump," *ASME J. Dyn. Syst., Meas., Control*, vol. 112, no. 1, pp. 122–132, 1990.

[64] N. Manring and R. Johnson, "Swivel torque within a variable-displacement pump," in *Proc. 46th National Conf. on Fluid Power*, 1994, pp. 13–24.

[65] N. Manring and R. Johnson, "Modeling and designing a variable-displacement open-loop pump," *ASME J. Dyn. Syst., Meas., Control*, vol. 118, no. 2, pp. 267–271, 1996.

[66] N. Manring, "The torque on the input shaft of an axial-piston swash-plate type hydrostatic pump," *ASME J. Dyn. Syst., Meas., Control*, vol. 120, no. 1, pp. 57–62, 1998.

[67] N. Manring and F. Damtew, "The control torque on the swash plate of an axial-piston pump utilizing piston-bore springs," *ASME J. Dyn. Syst., Meas., Control*, vol. 123, no. 3, pp. 471–478, 2001.

[68] S. Kim, H. Cho, and C. Lee, "Stability analysis of a load-sensing hydraulic system," *Proc. IMechE, Part A: J. Power and Energy*, vol. 202, no. 2, pp. 79–88, 1988.

[69] P. Krus, "On load sensing fluid power systems," Ph.D. dissertation, Linköping University, Sweden, 1988.

[70] J. Chiriboga, M.-W. Thein, and E. Misawa, "Input-output feedback linearization control of a load-sensing hydraulic servo system," in *Proc. 4th IEEE Conf. on Control Applications*, 1995, pp. 910–915.

[71] Y. Sakurai, T. Nakada, and K. Tanaka, "Design method of an intelligent oil-hydraulic system (load sensing oil-hydraulic system)," in *Proc. IEEE Int. Symp. on Intelligent Control*, 2002, pp. 626–630.

[72] D. Wu, R. Burton, G. Schoenau, and D. Bitner, "Establishing operating points for a linearized model of a load sensing system," *Int. J. Fluid Power*, vol. 3, no. 2, pp. 47–54, 2002.

[73] H. Pedersen, T. Andersen, and M. Hansen, "Controlling a conventional LS-pump based on electrically measured LS-pressure," in *Proc. Bath/ASME Symp. on Fluid Power & Motion Control*, 2008.

[74] G. Jayaraman and S. Lunzman, "Parameter estimation of an electronic load sensing pump using the recursive least squares algorithm," in *Proc. 49th IEEE Conf. on Decision and Control*, 2010, pp. 3445–3450.

[75] G. Jayaraman and S. Lunzman, "Modeling and analysis of an electronic load sensing pump," in *Proc. IEEE Int. Conf. on Control Applications*, 2011, pp. 82–87.

[76] D. Lovrec and S. Ulaga, "Pressure control in hydraulic systems with variable or constant pumps?" *Experimental Techniques*, vol. 31, no. 2, pp. 33–41, 2007.

[77] M. Ehsan, W. Rampen, and S. Salter, "Modeling of digital-displacement pump-motors and their application as hydraulic drives for nonuniform loads," *ASME J. Dyn. Syst., Meas., Control*, vol. 122, no. 1, pp. 210–115, Jun. 1997.

[78] M. Heikkilä and M. Linjama, "Displacement control of a mobile crane using a digital hydraulic power management system," *Mechatronics - The Science of Intelligent Machines*, vol. 23, no. 4, pp. 452–461, 2013.

[79] M. Karvonen, M. Heikkilä, M. Huova, and M. Linjama, "Analysis by simulation of different control algorithms of a digital hydraulic two-actuator system," *Int. J. of Fluid Power*, vol. 15, pp. 33–44, Mar. 2014.

[80] J. Taylor, W. Rampen, D. Abrahams, and A. Latham, "Demonstration of a digital displacement hydraulic hybrid bus," in *2015 JSAE Annual Congress (Spring)*, Yokohama, 2015.

[81] M. Heikkilä, "Energy Efficient Boom Actuation Using a Digital Hydraulic Power Management System," Ph.D. dissertation, Tampere University of Technology, Finland, 2016.

[82] FMC Technlogies, "Schilling ORION manual," [cited 13.6.2016]. [Online]. Available: http://www.fmctechnologies.com/en/SchillingRobotics/Technical-Manuals.aspx

[83] Cybernetix, "MAESTRO Hydraulic arm," [cited 13.6.2016]. [Online]. Available: http://www.cybernetix.fr/en/produit/69/bras-manipulateurs

[84] Hydraulics&Pneumatics Magazine, "Leakage prevention," Jan. 2012. [Online]. Available: http://hydraulicspneumatics.com/fluid-power-basics/system-design

[85] Hydraulics&Pneumatics Magazine: A Staff Report, "Noise control in hydraulic systems," Jan. 2012. [Online]. Available: http://hydraulicspneumatics.com/fluid-power-basics/system-design

[86] BBC News, Technology, "US military shelves Google robot plan over 'noise concerns'," Dec. 2015, [cited 23.3.2016]. [Online]. Available: http://www.bbc.com/news/technology-35201183

[87] R. Wilkes, "Getting to the root of hydraulic noise problems," *Hydraulics & pneumatics*, vol. 51, no. 6, pp. 59–60, 1998.

[88] J. Vihonen, J. Honkakorpi, J. Tuominen, J. Mattila, and A. Visa, "Linear accelerometers and rate gyros for rotary joint angle estimation of heavy-duty mobile manipulators using forward kinematic modeling," *IEEE/ASME Trans. Mechatronics*, vol. 21, no. 3, pp. 1765–1774, 2016.

[89] K. Edge, "On the control of electrohydraulic systems–some recent research contributions," in *The 8th Scandinavian Int. Conf. on Fluid Power (SICFP)*. Tampere, Finland, May 2003.

[90] A. Alleyne and J. Hedrick, "Nonlinear adaptive control of active suspensions," *IEEE Trans. Control Syst. Technol.*, vol. 3, no. 1, pp. 94 – 101, 1995.

[91] A. Alleyne and R. Liu, "A simplified approach to force control for electro-hydraulic systems," *Control Engineering Practice*, vol. 8, no. 12, pp. 1347 – 1356, 2000.

[92] G. A. Sohl and J. E. Bobrow, "Experiments and simulations on the nonlinear control of a hydraulic servosystem," *IEEE Trans. Control Syst. Technol.*, vol. 7, no. 2, pp. 238 – 247, 1999.

[93] M. Sirouspour and S. Salcudean, "On the nonlinear control of hydraulic servo-systems," in *Proc. of IEEE Conf. on Robot. and Autom.*, vol. 2, 2000, pp. 1276 – 1282.

[94] N. Niksefat, Q. Wu, and N. Sepehri, "Stable control of an electro-hydraulic actuator during contact tasks: Theory and experiments," in *Proc. of American Control Conference*, vol. 6, 2000, pp. 4114 – 4118.

[95] N. Niksefat, Q. Wu, and N. Sepehri, "Design of a lyapunov controller for an electro-hydraulic actuator during contact tasks," *ASME J. Dyn. Syst., Meas., Control*, vol. 123, no. 2, pp. 299 – 307, 2001.

[96] F. Bu and B. Yao, "Desired compensation adaptive robust control of single-rod electro-hydraulic actuator," in *Proc. of American Control Conference*, vol. 5. IEEE, 2001, pp. 3926 – 3931.

[97] C. Guan and S. Pan, "Adaptive sliding mode control of electro-hydraulic system with nonlinear unknown parameters," *Control Engineering Practice*, vol. 16, no. 11, pp. 1275 – 1284, 2008.

[98] C. Guan and S. Pan, "Nonlinear adaptive robust control of single-rod electro-hydraulic actuator with unknown nonlinear parameters," *IEEE Trans. Control Syst. Technol.*, vol. 16, no. 3, pp. 434 – 445, 2008.

[99] P. Nakkarat and S. Kuntanapreeda, "Observer-based backstepping force control of an electrohydraulic actuator," *Control Engineering Practice*, vol. 17, no. 8, pp. 895 – 902, 2009.

[100] W. Kim, D. Won, and M. Tomizuka, "Flatness-based nonlinear control for position tracking of electrohydraulic systems," *IEEE/ASME Trans. Mechatronics*, vol. 20, no. 1, pp. 197 – 206, 2015.

[101] D. Won, W. Kim, D. Shin, and C. Chung, "High-gain disturbance observer-based backstepping control with output tracking error constraint for electro-hydraulic systems," *IEEE Trans. Control Syst. Technol.*, vol. 23, no. 2, pp. 787 – 795, 2015.

[102] O. Egeland, "Cartesian control of a hydraulic redundant manipulator," in *Proc. of IEEE Int. Conf. Robotics and Automation*, vol. 4, 1987, pp. 2081 – 2086.

[103] S. Habibi and R. Richards, "Computed-torque and variable-structure multi-variable control of a hydraulic industrial robot," *Proc. IMechE, Part I: J. Syst. Control Eng.*, vol. 205, no. 2, pp. 123 – 140, 1991.

[104] K. Edge and F. de Almeida, "Decentralized adaptive control of a directly driven hydraulic manipulator: Parts 1-2," *Proc. IMechE, Part I: J. Syst. Control Eng.*, vol. 209, no. 3, pp. 191 – 196, 1995.

[105] T. Corbet, N. Sepehri, and P. Lawrence, "Fuzzy control of a class of hydraulically actuated industrial robots," *IEEE Trans. Control Syst. Technol.*, vol. 4, no. 4, pp. 419 – 426, 1996.

[106] F. Conrad, "Transputer control of hydraulic actuators and robots," *IEEE Trans. Ind. Electron.*, vol. 43, no. 1, pp. 38 – 47, 1996.

[107] M. M. Bech, T. O. Andersen, H. Pedersen, and L. Schmidt, "Experimental evaluation of control strategies for hydraulic servo robot," in *Proc. of IEEE Int. Conf. on Mechatronics and Automation (ICMA)*, 2013, pp. 342 – 347.

[108] S. Habibi, "Sliding mode control of a hydraulic industrial robot," *ASME J. Dyn. Syst., Meas., Control*, vol. 121, no. 2, pp. 312 – 318, 1999.

[109] Q. Nguyen, Q. Ha, D. Rye, and H. Durrant-Whyte, "Force/position tracking for electrohydraulic systems of a robotic excavator," in *Proc. of the 39th IEEE Conf. on Decision and Control*, vol. 5, 2000, pp. 5224 – 5229.

[110] I. Yung, C. Vazquez, and L. Freidovich, "Automation of front end loaders: Self leveling task," in *20th IEEE Int. Conf. on Emerging Technologies and Factory Automation*, 2015, pp. 1 – 7.

[111] J. Mattila and T. Virvalo, "Energy-efficient motion control of a hydraulic manipulator," in *IEEE Int. Conf. on Robotics and Automation*, vol. 3, Apr. 2000, pp. 3000 – 3006.

[112] F. Bu and B. Yao, "Observer based coordinated adaptive robust control of robot manipulators driven by single-rod hydraulic actuators," in *Proc. of IEEE Int. Conf. on Robotics and Automation*, vol. 3, 2001, pp. 3034 – 3039.

[113] M. Honegger and P. Corke, "Model-based control of hydraulically actuated manipulators," in *IEEE Int. Conf. on Robotics and Automation*, vol. 3, 2001, pp. 2553 – 2559.

[114] N. Tsukamoto and S. Yokota, "Two-degree-of-freedom control with parallel feedforward compensators," in *Proc. of the JFPS Int. Symposium on Fluid Power*, vol. 2002, no. 5-2. The Japan Fluid Power System Society, 2002, pp. 597 – 602.

[115] P. Chang and S.-J. Lee, "A straight-line motion tracking control of hydraulic excavator system," *Mechatronics*, vol. 12, no. 1, pp. 119 – 138, 2002.

[116] A. Bonchis, P. Corke, and D. Rye, "Experimental evaluation of position control methods for hydraulic systems," *IEEE Trans. Control Syst. Technol.*, vol. 10, no. 6, pp. 876 – 882, 2002.

[117] O. Becker, I. Pietsch, and J. Hesselbach, "Robust task-space control of hydraulic robots," in *Proc. IEEE Int. Conf. on Robotics and Automation*, vol. 3, 2003, pp. 4360 – 4365.

[118] E. Papadopoulos, B. Mu, and R. Frenette, "On modeling, identification, and control of a heavy-duty electrohydraulic harvester manipulator," *IEEE/ASME Trans. Mechatronics*, vol. 8, no. 2, pp. 178 – 187, 2003.

[119] H. Zeng and N. Sepehri, "Adaptive backstepping control of hydraulic manipulators with friction compensation using lugre model," in *American Control Conference*, 2006, pp. 3164 – 3169.

[120] W.-H. Zhu and J. Piedboeuf, "Adaptive output force tracking control of hydraulic cylinders with applications to robot manipulators," *ASME J. Dyn. Syst., Meas., Control*, vol. 127, no. 2, pp. 206 – 217, Jun. 2005.

[121] J. Koivumäki and J. Mattila, "The automation of multi degree of freedom hydraulic crane by using virtual decomposition control," in *Proc. IEEE/ASME Int. Conf. Adv. Intell. Mechatronics*, Jul. 2013, pp. 912 – 919.

[122] J. Koivumäki and J. Mattila, "An energy-efficient high performance motion control of a hydraulic crane applying virtual decomposition control," in *Proc. IEEE/RJS Int. Conf. Intell. Robots Syst.*, Nov. 2013, pp. 4426 – 4433.

[123] D. Ortiz Morales, S. Westerberg, P. La Hera, U. Mettin, L. Freidovich, and A. Shiriaev, "Increasing the level of automation in the forestry logging process with crane trajectory planning and control," *Journal of Field Robotics*, vol. 31, no. 3, pp. 343 – 363, 2014.

[124] J. Kalmari, "Nonlinear model predictive control of a hydraulic forestry crane," Ph.D. dissertation, Aalto University, Finland, 2015.

[125] B. Eriksson and J.-O. Palmberg, "Individual metering fluid power systems: challenges and opportunities," *Proc. IMechE, Part I: J. Syst. Control Eng.*, vol. 225, no. 2, pp. 196 – 211, 2011.

[126] L. Ge, Z. Dong, W. Huang, L. Quan, J. Yang, and W. Li, "Research on the performance of hydraulic excavator with pump and valve combined separate meter in and meter out circuits," in *IEEE Int. Conf. on Fluid Power and Mechatronics*, 2015, pp. 37 – 41.

[127] D. H. Kim, J.-Y. Kang, and K.-I. Lee, "Robust tracking control design for a 6 DOF parallel manipulator," *J. of Robotic Systems*, vol. 17, no. 10, pp. 527 – 547, 2000.

[128] H. S. Kim, Y. M. Cho, and K.-I. Lee, "Robust nonlinear task space control for 6 DOF parallel manipulator," *Automatica*, vol. 41, no. 9, pp. 1591 – 1600, 2005.

[129] Y. Pi and X. Wang, "Trajectory tracking control of a 6-DOF hydraulic parallel robot manipulator with uncertain load disturbances," *Control Eng. Practice*, vol. 19, no. 2, pp. 185 – 193, 2011.

[130] Y. Pi and X. Wang, "Observer-based cascade control of a 6-DOF parallel hydraulic manipulator in joint space coordinate," *Mechatronics*, vol. 20, no. 6, pp. 648 – 655, 2010.

[131] S.-H. Chen and L.-C. Fu, "Observer-based backstepping control of a 6-dof parallel hydraulic manipulator," *Control Eng. Practice*, vol. 36, pp. 100 – 112, 2015.

[132] M. Raibert and J. Craig, "Hybrid position/force control of manipulators," *ASME J. Dyn. Syst., Meas., Control*, vol. 103, no. 2, pp. 126–133, 1981.

[133] N. Hogan, "Impedance control: An approach to manipulation: Parts I-III," *ASME J. Dyn. Syst., Meas., Control*, vol. 107, no. 1, pp. 1–24, 1985.

[134] D. Whitney, "Historical perspective and state of the art in robot force control," in *Proc. of IEEE Int. Conf. on Robotics and Automation*, vol. 2, 1985, pp. 262–268.

[135] M. Vukobratović and A. Tuneski, "Contact control concepts in manipulation robotics – an overview," *IEEE Trans. Ind. Electron.*, vol. 41, no. 1, pp. 12–24, Feb. 1994.

[136] O. Khatib, "A unified approach for motion and force control of robot manipulators: The operational space formulation," *IEEE Trans. Robot. Autom.*, vol. 3, no. 1, pp. 43–53, 1987.

[137] J. De Schutter and H. Van Brussel, "Compliant robot motion: Parts I-II," *Int. J. Robot. Res.*, vol. 7, no. 4, pp. 3–17, 1988.

[138] N. McClamroch and D. Wang, "Feedback stabilization and tracking of constrained robots," *IEEE Trans. Autom. Control*, vol. 33, no. 5, pp. 419–426, 1988.

[139] S. Chiaverini and L. Sciavicco, "The parallel approach to force/position control of robotic manipulators," *IEEE Trans. Robot. Autom.*, vol. 9, no. 4, pp. 361–373, 1993.

[140] J. Pratt, C.-M. Chew, A. Torres, P. Dilworth, and G. Pratt, "Virtual model control: An intuitive approach for bipedal locomotion," *Int. J. Robot. Res.*, vol. 20, no. 2, pp. 129–143, 2001.

[141] M. Ostoja-Starzewski and M. Skibniewski, "A master-slave manipulator for excavation and construction tasks," *Robotics and Autonomous Systems*, vol. 4, no. 4, pp. 333–337, 1989.

[142] M. Dunnigan, D. Lane, A. Clegg, and I. Edwards, "Hybrid position/force control of a hydraulic underwater manipulator," in *Proc. IEE Control Theory and Applications*, vol. 143, no. 2, 1996, pp. 145–151.

[143] D. Lane, M. Dunnigan, A. Clegg, P. Dauchez, and L. Cellier, "A comparison between robust and adaptive hybrid position/force control schemes for hydraulic underwater manipulators," *Trans. of the Institute of Measurement and Control*, vol. 19, no. 2, pp. 107–116, 1997.

[144] A. Clegg, "Self-tuning position and force control of a hydraulic manipulator," Ph.D. dissertation, Heriot-Watt University, 2000.

[145] B. Heinrichs, N. Sepehri, and A. Thornton-Trump, "Position-based impedance control of an industrial hydraulic manipulator," *IEEE Control Systems*, vol. 17, no. 1, pp. 46–52, 1997.

[146] Q. Ha, Q. Nguyen, D. Rye, and H. Durrant-Whyte, "Robust impedance control of excavator dynamics," in *Proc. of the Int. Conf. on Field and Service Robotics*, 1999, pp. 226–231.

[147] Q. Ha, Q. Nguyen, D. Rye, and H. Durrant-Whyte, "Impedance control of a hydraulically actuated robotic excavator," *Automation in Construction*, vol. 9, no. 5–6, pp. 421–435, 2000.

[148] S. Tafazoli, S. Salcudean, K. Hashtrudi-Zaad, and P. Lawrence, "Impedance control of a teleoperated excavator," *IEEE Trans. Control Syst. Technol.*, vol. 10, no. 3, pp. 355–367, 2002.

[149] S. Salcudean, S. Tafazoli, P. Lawrence, and I. Chau, "Impedance control of a teleoperated mini excavator," in *Proc. of the 8th Int. IEEE Conf. on Advanced Robotics*, 1997, pp. 19–25.

[150] S. Salcudean, S. Tafazoli, K. Hashtrudi-Zaad, P. Lawrence, and C. Reboulet, "Evaluation of impedance and teleoperation control of a hydraulic mini-excavator," in *Experimental Robotics V*. Springer, 1998, pp. 227–240.

[151] S. Salcudean, K. Hashtrudi-Zaad, S. Tafazoli, S. DiMaio, and C. Reboulet, "Bilateral matched-impedance teleoperation with application to excavator control," *IEEE Control Systems*, vol. 19, no. 6, pp. 29–37, 1999.

[152] T. Itoh, I. Suzuki, and T. Matsui, "Adaptive impedance control for a hydraulic robot without joint torque sensors based on improved minimal controller synthesis algorithm," in *Proc. of the JFPS Int. Symp. on Fluid Power*, vol. 2002, no. 5-2, 2002, pp. 609–614.

[153] H. Zeng and N. Sepehri, "On tracking control of cooperative hydraulic manipulators," *Int. J. of Control*, vol. 80, no. 3, pp. 454–469, 2007.

[154] H. Zeng, "Nonlinear control of co-operating hydraulic manipulators," Ph.D. dissertation, University of Manitoba, 2007.

[155] T. Boaventura, G. A. Medrano-Cerda, C. Semini, J. Buchli, and D. G. Caldwell, "Stability and performance of the compliance controller of the quadruped robot HyQ," in *Proc. of IEEE/RSJ Int. Conf. on Intel. Robots and Systems (IROS)*, 2013, pp. 1458–1464.

[156] C. Semini, V. Barasuol, T. Boaventura, M. Frigerio, M. Focchi, D. G. Caldwell, and J. Buchli, "Towards versatile legged robots through active impedance control," *Int. J. Robot. Res.*, vol. 34, no. 7, pp. 1003–1020, 2015.

[157] T. Boaventura, J. Buchli, C. Semini, and D. G. Caldwell, "Model-based hydraulic impedance control for dynamic robots," *IEEE Trans. Robot.*, vol. 31, no. 6, pp. 1324–1336, 2015.

[158] F. Ficuciello, L. Villani, and B. Siciliano, "Variable impedance control of redundant manipulators for intuitive human–robot physical interaction," *IEEE Trans. Robot.*, vol. 31, no. 4, pp. 850–863, 2015.

[159] M. Howard, D. Braun, and S. Vijayakumar, "Transferring human impedance behavior to heterogeneous variable impedance actuators," *IEEE Trans. Robot.*, vol. 29, no. 4, pp. 847–862, 2013.

[160] F. Ferraguti, C. Secchi, and C. Fantuzzi, "A tank-based approach to impedance control with variable stiffness." in *Proc. IEEE Int. Conf. Robot. Autom.*, 2013, pp. 4948–4953.

[161] F. Petit and A. Albu-Schaffer, "Cartesian impedance control for a variable stiffness robot arm," in *Proc. IEEE/RSJ Int. Con. Intell. Robots and Syst.*, 2011, pp. 4180 – 4186.

[162] J. Buchli, F. Stulp, E. Theodorou, and S. Schaal, "Learning variable impedance control," *Int. J. Robot. Res.*, vol. 30, no. 7, pp. 820 – 833, 2011.

[163] T. Tsumugiwa, R. Yokogawa, and K. Hara, "Variable impedance control with virtual stiffness for human-robot cooperative peg-in-hole task," in *Proc. IEEE/RSJ Int. Con. Intell. Robots and Syst.*, vol. 2, 2002, pp. 1075 – 1081.

[164] R. Dubey, T. Chan, and S. Everett, "Variable damping impedance control of a bilateral telerobotic system," *IEEE Control Systems*, vol. 17, no. 1, pp. 37 – 45, 1997.

[165] R. Ikeura and H. Inooka, "Variable impedance control of a robot for cooperation with a human," in *Proc. IEEE Int. Conf. Robot. Autom.*, vol. 3, 1995, pp. 3097 – 3102.

[166] S. Lin and A. Akers, "Optimal control theory applied to pressure-controlled axial piston pump design," *ASME J. Dyn. Syst., Meas., Control*, vol. 112, no. 3, pp. 475 – 481, 1990.

[167] H. Du and N. Manring, "A single-actuator control design for hydraulic variable displacement pumps," in *Proc. Am. Control Conf.*, vol. 6, 2001, pp. 4484 – 4489.

[168] P. Dean and R. Fales, "Modern control design for a variable displacement hydraulic pump," in *Proc. Am. Control Conf.*, 2007, pp. 3535 – 3540.

[169] W. Kemmetmüller, F. Fuchshumer, and A. Kugi, "Nonlinear pressure control of self-supplied variable displacement axial piston pumps," *Control Engineering Practice*, vol. 18, no. 1, pp. 84 – 93, 2010.

[170] K. Guo and J. Wei, "Adaptive robust control of variable displacement pumps," in *Proc. Am. Control Conf.*, 2013, pp. 1112 – 1117.

[171] J. Wei, K. Guo, J. Fang, and Q. Tian, "Nonlinear supply pressure control for a variable displacement axial piston pump," *Proc. IMechE, Part I: J. Syst. Control Eng.*, pp. 1 – 11, 2015.

[172] L.-W. Tsai, *Robot analysis: the mechanics of serial and parallel manipulators*. John Wiley & Sons, 1999.

[173] J. Y. S. Luh and Y.-F. Zheng, "Computation of input generalized forces for robots with closed kinematic chain mechanisms," *IEEE Journal on Robotics and Automation*, vol. 1, no. 2, pp. 95 – 103, 1985.

[174] M. W. Walker, "Adaptive control of manipulators containing closed kinematic loops," *IEEE Trans. Robot. Autom.*, vol. 6, no. 1, pp. 10 – 19, 1990.

[175] J. E. Slotine and W. Li, *Applied Nonlinear Control*. Prentice Hall, 1991.

[176] G. Tao, "A simple alternative to the barbalat lemma," *IEEE Trans. Autom. Control*, vol. 42, no. 5, 1997.

[177] J. E. Colgate and N. Hogan, "Robust control of dynamically interacting systems," *International journal of Control*, vol. 48, no. 1, pp. 65 – 88, 1988.

[178] N. Hogan, "On the stability of manipulators performing contact tasks," *IEEE Journal on Robotics and Automation*, vol. 4, no. 6, pp. 677–686, 1988.

[179] K. Kronander and A. Billard, "Stability considerations for variable impedance control," *IEEE Trans. Robot.*, vol. 32, no. 5, pp. 1298–1305, 2016.

[180] F. Bonsignorio and A. del Pobil, "Toward replicable and measurable robotics research [from the guest editors]," *IEEE Robotics & Automation Magazine*, vol. 22, no. 3, pp. 32–32, 2015.

Publication P.I

Janne Koivumäki and Jouni Mattila, "High Performance Non-Linear Motion/Force Controller Design for Redundant Hydraulic Construction Crane Automation", *Automation in Construction*, vol. 51, pp. 59–77, Jan. 2015.

The original print of this publication is available online (DOI: 10.1016/j.autcon.2014.12.014)

Automation in Construction 51 (2015) 59–77

Contents lists available at ScienceDirect

Automation in Construction

journal homepage: www.elsevier.com/locate/autcon

High performance nonlinear motion/force controller design for redundant hydraulic construction crane automation

Janne Koivumäki *, Jouni Mattila [1]

Tampere University of Technology, Department of Intelligent Hydraulics and Automation, P.O. Box 589 (Korkeakoulunkatu 6), FIN-33101 Tampere, Finland

ARTICLE INFO

Article history:
Received 25 January 2014
Received in revised form 16 September 2014
Accepted 15 December 2014
Available online 10 January 2015

Keywords:
Hydraulic construction cranes
Robust control
Nonlinear model-based control
Virtual decomposition control
Cartesian space control
Stability

ABSTRACT

In this paper, a stability-guaranteed Cartesian free-space motion control for the redundant articulated hydraulic construction crane is addressed in order to increase system safety and productivity. To cope with the nonlinearities of coupled mechanical linkage dynamics of articulated systems and the inherently strong nonlinearities of hydraulic actuator dynamics, the proposed controller is designed based on the recently introduced Virtual Decomposition Control (VDC) approach. The VDC approach, which was developed especially for the control of complex robotic systems, allows the conversion of the control problem of the entire system to a control problem of individual subsystems, while rigorously guaranteeing the stability of the entire hydraulic system. In the experiments it is demonstrated that, the proposed controller is able to extensively cope with the highly nonlinear nature of the articulated hydraulic system, and an improved control performance is achieved compared to the current state-of-the-art studies in the category of the hydraulic robot manipulators.

1. Introduction

Hydraulically actuated articulated cranes are widely utilized on construction sites. These machines are used, e.g., in heavy-duty material handling, and the transported materials are often hung high up above the ground, causing safety concerns when human life is at risk. Usually the control of these construction cranes is carried out through the direct open-loop control of each individual actuator. This type of crane control scheme requires a skilled and trained operator in order to achieve safe and fluent system motions. Still, crane operator errors do happen, which lies at the root of 73% of all crane accidents [1]. Moreover, in the hands of unskilled operators, severe crane structure damages and damages to the surrounding environments can also happen.

Hydraulic actuators are well-known for their high power-to-weight ratio, rapid responses, compactness and reliable performance [2]. However, contrary to electric actuators, one of the drawbacks of hydraulic actuators has been the complexity in their force control [3], as these actuators are inherently velocity sources, which translates to strong nonlinearities in actuator dynamics [2–4]. Thus, force controller design for hydraulic systems poses significant controller design challenges. Also, the nonlinearities of the coupled mechanical linkage dynamics in multiple Degrees Of Freedom (DOF) systems pose additional challenges for controller design [5]. Moreover, the control problem of hydraulic manipulators that use hydraulic cylinder actuators becomes more challenging as kinematics and the dynamics of mechanical linkages become more complex in these systems due to the existence of closed chain structures. As a result, the general control methods which are successfully applied to electric manipulators, e.g., control methods that neglect actuator dynamics but use manipulator rigid body dynamics alone, cannot be effectively applied to articulated hydraulic manipulators [4]. Thus, in order to achieve high performance motion/force control for these hydraulic machines, the utilization of nonlinear model-based control methods is inevitable (see discussion, e.g., in [6]).

Even though most of the attention regarding manipulators' free-space motion control has been on controlling electrically driven manipulators, different control strategies have been developed in recent decades for hydraulically driven manipulators (see e.g., papers [4,7–17]). As discussed in [4], one design challenge related to the nonlinear, model-based control of hydraulic manipulators has been the lack of stability proofs for proposed control laws. In [15], the L2 and L∞ stability of hydraulic cylinders' both the pressure force error and the output force error was quaranteed for a six-joint hydraulic manipulator. Also, few control approaches based on backstepping (see [4,12,16]) provided quaranteed stability for hydraulic manipulators.

In this paper, a stability-guaranteed, nonlinear, model-based controller design, which is based on the Virtual Decomposition Control (VDC) approach, is proposed for the Cartesian free-space control of hydraulic manipulators. In the proposed controller design, only the joints' position sensors and the actuators' chamber pressure sensors are needed (e.g., expensive load cells were utilized in the experiments in [15,16]). This has a great practical importance for construction machines because these sensors can easily be implemented and retrofitted into existing

* Corresponding author. Tel.: +358 40 8490 241.
E-mail addresses: janne.koivumaki@tut.fi (J. Koivumäki), jouni.mattila@tut.fi (J. Mattila).
[1] Tel.: +358 40 8490 241.

http://dx.doi.org/10.1016/j.autcon.2014.12.014
0926-5805/

systems. Even though one redundant DOF is added to the studied system, the control performance of the VDC-based controller is improved compared to the authors' previous study [17]. In addition, the addition of a local subsystem, i.e., one DOF actuator and its respective control, does not affect the system's overall stability or control performance. The experiments demonstrate that with the proposed controller design, improved motion control performance is achieved compared to the current state-of-the-art studies.

This paper is organized as follows: In Section 2, mathematical foundations for an applied control method are given. In Section 3, the essence of the VDC approach is described briefly. The system modeling and the system controller design are given in Section 4. In Section 5, the stability of the system is addressed with the detailed proves. The experimental set-up and the implementation issues are discussed in Section 6. Experimental results, comparison to the current state-of-the-art studies, and discussion about the control performance of the proposed controller are given in Section 7. Finally, a conclusion is given.

2. Mathematical foundation

Consider an orthogonal three-dimensional coordinate system {**A**}, called frame {**A**} for simplicity, attached in the rigid body. Let ${}^{A}v \in \mathbb{R}^3$ and ${}^{A}\omega \in \mathbb{R}^3$ be the linear and angular velocity vectors of frame {**A**}, expressed in frame {**A**}. To facilitate the transformations of velocities among different frames, the linear/angular velocity vector of frame {**A**} can be written, in view of [18], as

$$ {}^{\mathbf{A}}V \overset{\text{def}}{=} \begin{bmatrix} {}^{\mathbf{A}}\mathbf{v} \\ {}^{\mathbf{A}}\boldsymbol{\omega} \end{bmatrix} \in \mathbb{R}^6. \tag{1} $$

Let ${}^{A}f \in \mathbb{R}^3$ and ${}^{A}m \in \mathbb{R}^3$ be the force and moment vectors applied to the origin of frame {**A**}, expressed in frame {**A**}. Similar to Eq. (1), the force/moment vector in frame {**A**} can be written, in view of [18], as

$$ {}^{\mathbf{A}}F \overset{\text{def}}{=} \begin{bmatrix} {}^{\mathbf{A}}\mathbf{f} \\ {}^{\mathbf{A}}\mathbf{m} \end{bmatrix} \in \mathbb{R}^6. \tag{2} $$

Now, consider two given frames, denoted as {**A**} and {**B**}, being fixed to a common rigid body. As stated in [18], the following relations hold

$$ {}^{\mathbf{B}}V = {}^{\mathbf{A}}\mathbf{U}_{\mathbf{B}}^{T\,\mathbf{A}}V \tag{3} $$

$$ {}^{\mathbf{A}}F = {}^{\mathbf{A}}\mathbf{U}_{\mathbf{B}}\,{}^{\mathbf{B}}F \tag{4} $$

where ${}^{A}U_B \in \mathbb{R}^{6\times 6}$ denotes a force/moment transformation matrix that transforms the force/moment vector measured and expressed in frame {**B**} to the same force/moment vector measured and expressed in frame {**A**}.

Let frame {**A**} be fixed to a rigid body. The dynamic equation of the rigid body in free motion, expressed in frame {**A**}, can be written as

$$ \mathbf{M}_{\mathbf{A}}\frac{d}{dt}\left({}^{\mathbf{A}}V\right) + \mathbf{C}_{\mathbf{A}}\left({}^{\mathbf{A}}\boldsymbol{\omega}\right){}^{\mathbf{A}}V + \mathbf{G}_{\mathbf{A}} = {}^{\mathbf{A}}F^{*} \tag{5} $$

where ${}^{\mathbf{A}}F^{*} \in \mathbb{R}^6$ is the net force/moment vector of the rigid body, $M_A \in \mathbb{R}^{6\times 6}$ denotes the mass matrix, $C_A({}^{A}\omega) \in \mathbb{R}^{6\times 6}$ denotes the matrix of Coriolis and centrifugal terms and $G_A \in \mathbb{R}^6$ denotes the gravity terms.

Now, let ${}^{A}V_r \in \mathbb{R}^6$ be the required vector (a design vector to be specified later) of ${}^{A}V \in \mathbb{R}^6$. In view of [18], the linear parametrization expression for the required rigid body dynamics can be written as

$$ \mathbf{Y}_{\mathbf{A}}\theta_{\mathbf{A}} \overset{\text{def}}{=} \mathbf{M}_{\mathbf{A}}\frac{d}{dt}\left({}^{\mathbf{A}}V_{\mathrm{r}}\right) + \mathbf{C}_{\mathbf{A}}\left({}^{\mathbf{A}}\boldsymbol{\omega}\right){}^{\mathbf{A}}V_{\mathrm{r}} + \mathbf{G}_{\mathbf{A}}. \tag{6} $$

The detailed expressions of the regressor matrix $Y_A \in \mathbb{R}^{6\times 13}$ and the parameter vector $\theta_A \in \mathbb{R}^{13}$ are given in [18]. Expressing rigid body dynamics in the form of Eq. (6) allows one to incorporate parameter adaptation for uncertain parameters in $\theta_A \in \mathbb{R}^{13}$ into the control equations of VDC. However, parameter adaptation is not addressed in this paper but should be the subject of future studies.

3. Virtual decomposition control

The VDC approach (see [18] and [19]) can be applied to any mechanical complex systems, e.g., construction machines, without restrictions on target systems. In addition, the approach can be easily applied to hybrid machines, in which some actuators are actuated electrically and some hydraulically. Beyond mechanical systems, the VDC approach can also be applied for electrical circuits, as addressed in [18].

The essence of the VDC approach is that the controller uses the dynamics of subsystems rather than the dynamics of the entire system. Thus, in the VDC approach the control problem of a complex robotic system can be converted into the control problem of individual subsystems leading to the fact that no matter how complicated the initial system is, the dynamics of the subsystems remain relatively simple with fixed dynamics structures invariant to target systems [18]. One advantage of the VDC approach is that changing the dynamics of a subsystem (such as substituting a hydraulic actuator for an electrical motor) only affects the respective local control equations associated with this subsystem while keeping the control equations associated with the rest of the system unchanged. This might have practical importance in many construction devices, e.g., for system retrofitting or actuator replacement in case of failures.

The first step in the VDC approach is to virtually decompose an original system into subsystems, i.e., *objects* and *open chains*, by placing conceptual *virtual cutting points* (VCP). The entire system is then represented as a simple oriented graph. Each subsystem corresponds to a node and each VCP corresponds to a directed edge whose direction defines the force reference direction. Thus, a VCP is simultaneously interpreted as a *driving VCP* by one subsystem (from which the force/moment vector is exerted or the directed edge is pointing away) and as a *driven VCP* by another subsystem (to which the force/moment vector is exerted or the directed edge is pointing to). In a simple oriented graph, no loops are allowed to form from the VCPs directions [18].

In the VDC approach the control objective is to design a velocity controller that takes care of the complete dynamics of the system. In addition, a variety of control objectives, such as motion control and internal force control, can be implemented into the VDC control laws without restrictions on the target system. [18]

After the required control equations for the decomposed subsystems are defined, the focus is on the properties each subsystem should have in order to maintain the stability of the entire system. In the *virtual stability* analysis, the introduction of a scalar term namely *virtual power flow* (VPF) plays an important role. VPFs uniquely define dynamic interactions among the subsystems in every VCP at which virtual "disconnection" is placed, and is defined in [18] as

Definition 1. The virtual power flow with respect to a frame {**A**} can be defined as the inner product of the linear/angular velocity vector error and the force/moment vector error as

$$ p_{\mathbf{A}} = \left({}^{\mathbf{A}}V_{\mathrm{r}} - {}^{\mathbf{A}}V\right)^{T}\left({}^{\mathbf{A}}F_{\mathrm{r}} - {}^{\mathbf{A}}F\right) \tag{7} $$

where ${}^{\mathbf{A}}V_r \in \mathbb{R}^6$ and ${}^{\mathbf{A}}F_r \in \mathbb{R}^6$ represent the required vectors (to be specified later) of ${}^{\mathbf{A}}V \in \mathbb{R}^6$ and ${}^{\mathbf{A}}F \in \mathbb{R}^6$, respectively.

The following simplified[2] form of Definition 2.17. from [18] provides a *virtual stability* of subsystem.

[2] The parameter adaptation is not addressed in this study.

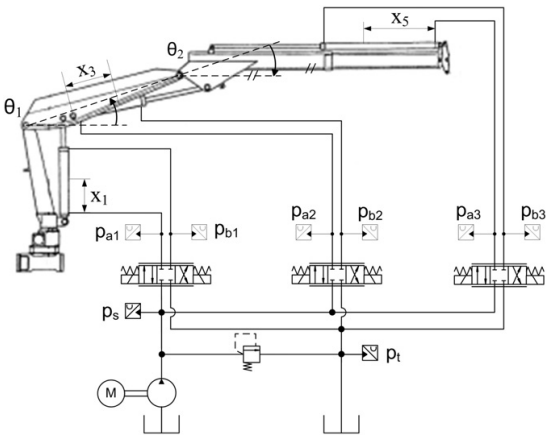

Fig. 1. Control set-up for the studied crane.

Definition 2. A subsystem is said to be virtually stable with its affiliated vector $\mathbf{x}(t)$ being a virtual function in L_∞ and its affiliated vector $\mathbf{y}(t)$ being a virtual function in L_2, if and only if there exists a non-negative accompanying function

$$v(t) \geq \frac{1}{2}\mathbf{x}(t)^T \mathbf{P}\mathbf{x}(t) \tag{8}$$

such that

$$\dot{v}(t) \leq -\mathbf{y}(t)^T \mathbf{Q}\mathbf{y}(t) + p_{\mathbf{A}} - p_{\mathbf{C}} \tag{9}$$

holds, and where **P** and **Q** are two block-diagonal positive-definite matrices and $p_{\mathbf{A}}$ and $p_{\mathbf{C}}$ denote the VPFs (by Definition 1) at frames {**A**} (in driven VCP) and {**C**} (in driving VCP), respectively.

Finally, Theorem 2.1 in [18] proves the L_2 and L_∞ stability of the entire system, when every subsystem is *virtually stable* in the sense of Definition 2.

4. Control of hydraulic crane

The hydraulic manipulator studied in this paper is a redundant crane operating in the vertical plane. The system contains three hydraulic cylinders, namely a lift cylinder, tilt cylinder and extension cylinder, and each cylinder is controlled with a four-way valve. Though a three-actuator system is studied, the approach presented in this paper is extendable to systems of any number of actuators. The control set-up of the studied manipulator is illustrated in Fig. 1.

4.1. Virtual decomposition and simple oriented graph presentation

Using the VDC approach, the studied system is first virtually decomposed into *object* and *open chain* structures by placing conceptual VCPs. Note that all existing *closed chain* structures are further decomposed into *open chain* structures, so that only *object* and *open chain* structures exist in the system. The virtual decomposition of the studied system is illustrated in Fig. 2.

After being virtually decomposed, the studied system is represented as a simple oriented graph (see Fig. 3), to represent dynamic interactions among subsystems.

4.2. Frame attachment

After the virtual decomposition and a simple oriented graph representation, fixed body frames are attached to the decomposed subsystems to describe motion and force specifications. The decomposed subsystems with their attached frames are illustrated in Figs. 4–10. For the attached frames, in Figs. 4–10, the *z*-axis is pointing out from the paper. The rigid links in the system *open chains* (see Figs. 8–10) are named according to their fixed body frames.

For the attached frames at VCPs (see Fig. 2), denoted in blue in Figs. 4–10, the following relations hold

$$\{\mathbf{T}_{o3}\} = \{\mathbf{T}_5\}, \tag{10}$$

$$\{\mathbf{T}_{oi}\} = \{\mathbf{T}_{cn}\} = \{\mathbf{T}_{j_p}\} = \{\mathbf{T}_{j_r}\}, \tag{11}$$

with $j_p = 2n - 1, j_r = 2n$ and $n = i, \forall\, i \in \{1, 2\}$,

$$\{\mathbf{B}_{o2}\} = \{\mathbf{B}_5\}, \tag{12}$$

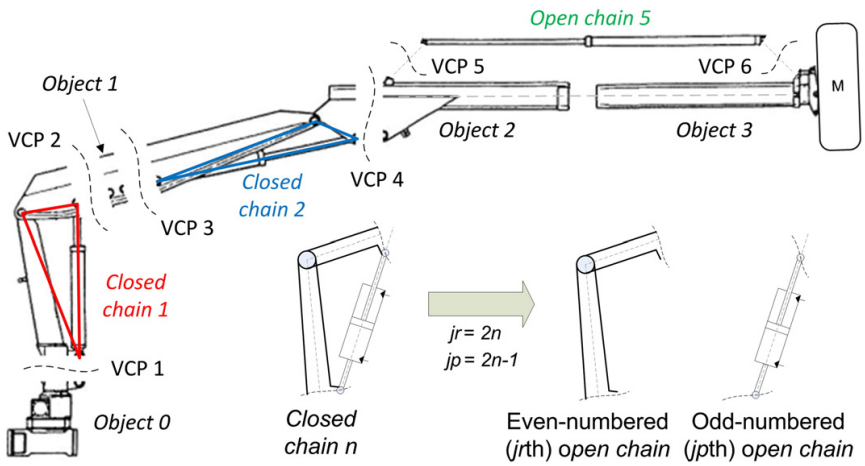

Fig. 2. Virtual decomposition of the studied system.

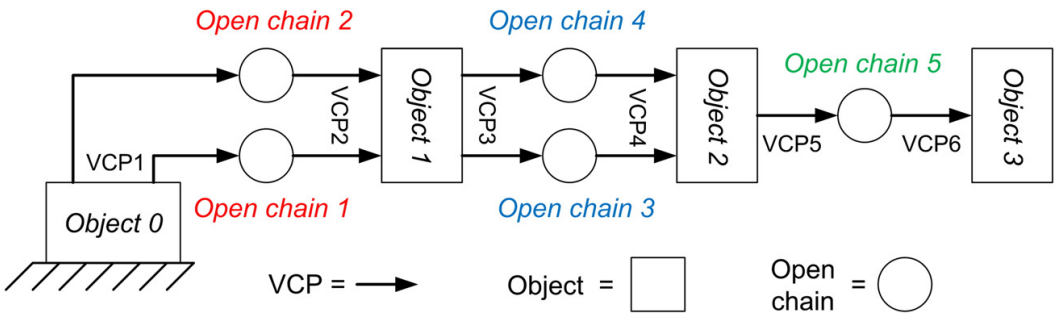

Fig. 3. A simple oriented graph.

and

$$\{\mathbf{B}_{oi}\} = \{\mathbf{B}_{cn}\} = \{\mathbf{B}_{j_p}\} = \{\mathbf{B}_{j_r}\} \tag{13}$$

with $j_p = 2n - 1, j_r = 2n$ and $n = i + 1, \forall\, i \in \{0, 1\}$.

In Eqs. (11) and (13) subscript i denotes the number of *objects*, subscript n denotes the number of *closed chains*, subscript j_r denotes the number of revolute *open chains* (even-numbered *open chains*), and subscript j_p denotes the number of the prismatic *open chains* (odd-numbered *open chains*). In addition, subscript k will be used to describe number of the system actuator, i.e., hydraulic cylinder, later in the subsection 4.5 and thereinafter.

In Eq. (10), $\{\mathbf{T}_{o3}\}$ denotes the frame attached at the *driving VCP* of the 3rd *object* and $\{\mathbf{T}_5\}$ denotes the frame attached at the *driving VCP* of the 5th *open chain*. In Eq. (11), $\{\mathbf{T}_{oi}\}$ denotes the frame attached at the *driven VCP* of the ith *object*, $\{\mathbf{T}_{cn}\}$ denotes the frame attached at the *driving VCP* of the nth *closed chain*, $\{\mathbf{T}_{j_p}\}$ denotes the frame attached at the *driving VCP* of the j_pth *open chain* and $\{\mathbf{T}_{j_r}\}$ denotes the frame attached at the *driving VCP* of the j_rth *open chain*.

Respectively, in Eq. (12), $\{\mathbf{B}_{o2}\}$ denotes the frame attached at the *driving VCP* of the 2nd *object* and $\{\mathbf{B}_5\}$ denotes the frame attached at the *driven VCP* of the 5th *open chain*. In Eq. (13), $\{\mathbf{B}_{oi}\}$ denotes the frame attached at the *driving VCP* of the ith *object*, $\{\mathbf{B}_{cn}\}$ denotes the frame attached at the *driven VCP* of the nth *closed chain*, $\{\mathbf{B}_{j_p}\}$ denotes frame attached at the *driven VCP* of the j_pth *open chain* and $\{\mathbf{B}_{j_r}\}$ denotes the frame attached at the *driven VCP* of the j_rth *open chain*.

In the ith *object*, $\forall\, i \in \{0, 3\}$, frame $\{\mathbf{O}_i\}$, denoted as green in Figs. 4–7, is attached at the center of mass of the ith *object* to describe the motion and force specifications. The frame $\{\mathbf{O}_i\}$ is aligned with respect to frame $\{\mathbf{T}_{oi}\}$.

In view of Eq. (13), the frames $\{\mathbf{B}_{j_p}\}$ and $\{\mathbf{B}_{j_r}\}$ in the *driven VCP* of the nth *closed chain* are fixed to frame $\{\mathbf{B}_{cn}\}$ and frames $\{\mathbf{T}_{j_p}\}$ and $\{\mathbf{T}_{j_r}\}$ in the *driving VCP* of the nth *closed chain* are fixed to frame $\{\mathbf{T}_{cn}\}$ (see Figs. 8–10). Moreover, frame $\{\mathbf{B}_{cn}\}$ is fixed such that its x-axis points toward joint j_r (see Fig. 9). Thus, in the j_pth *open chain*, one "extra" frame, compared to j_rth and 5th *open chain*, exists, as rotation from the frame $\{\mathbf{B}_{j_p}\}$ in toward the axis of the actuation of the kth cylinder, i.e., to frame $\{\mathbf{B}_{j_p1}\}$, is needed.

Finally, in all *open chains* the "joint frames", denoted as red in Figs. 8–10, are attached to the *subsidiary VCPs* of *open chains*. With these *open chain* second rigid link fixed frames the *open chain* joint rotations/translations can be considered.

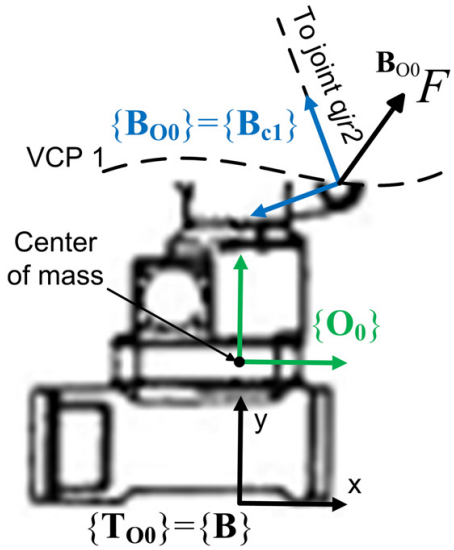

Fig. 4. Object 0.

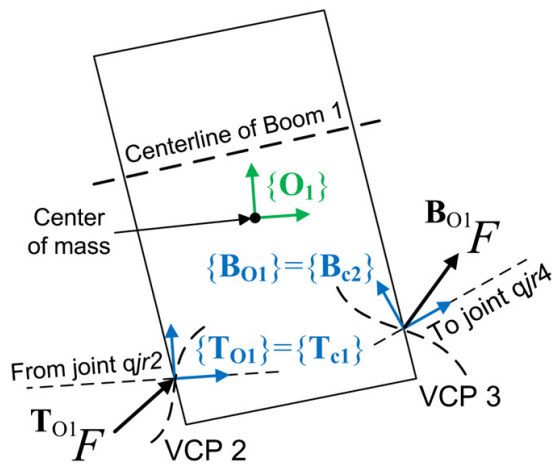

Fig. 5. Object 1.

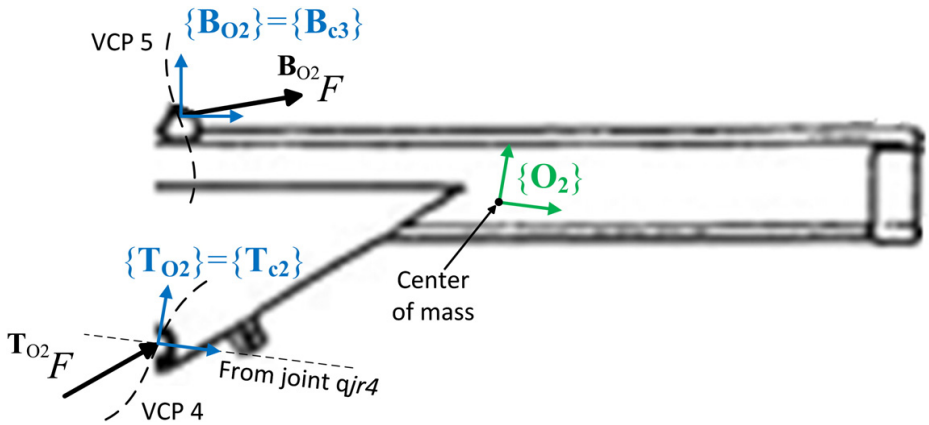

Fig. 6. Object 2.

4.3. Kinematics of the system

In this section the kinematic relations of the studied system will be given. First, in subsection 4.3.1, the kinematic relations between system joint variables in *n*th *closed chain* will be defined. Then, in subsections 4.3.2–4.3.5, all system linear/angular velocity vectors in the subsystems are given.

4.3.1. Kinematics of joints

The relations between joint variables $q_{j_r}, q_{j_p1}, q_{j_p2}$ and x_{j_p} (see Figs. 8 and 9) in the *n*th *closed chain* can be written as

$$x_{j_p} = \sqrt{L_{j_r}^2 + L_{j_r1}^2 + 2L_{j_r}L_{j_r1}\cos\left(q_{j_r}\right)} - x_{j_p0} \tag{14}$$

$$q_{j_p1} = \cos^{-1}\left(\frac{L_{j_r1}^2 - \left(x_{j_p} + x_{j_p0}\right)^2 - L_{j_r}^2}{-2\left(x_{j_p} + x_{j_p0}\right)L_{j_r}}\right) \tag{15}$$

$$q_{j_p2} = \cos^{-1}\left(\frac{L_{j_r}^2 - \left(x_{j_p} + x_{j_p0}\right)^2 - L_{j_r1}^2}{-2\left(x_{j_p} + x_{j_p0}\right)L_{j_r1}}\right) \tag{16}$$

with $j_p = 2n-1, j_r = 2n, \forall\, n \in \{1,2\}$, and where L_{j_r} and L_{j_r1} denote the link lengths in j_rth *open chain*.

In view of Eqs. (14), (15) and (16) the joint velocities $\dot{q}_{j_r}, \dot{q}_{j_p1}, \dot{q}_{j_p2}$ and $\dot{x}_{j_p}$ in the *n*th *closed chain* can be written as

$$\dot{x}_{j_p} = -\frac{L_{j_r}L_{j_r1}\sin\left(q_{j_r}\right)}{x_{j_p} + x_{j_p0}}\dot{q}_{j_r} \tag{17}$$

$$\dot{q}_{j_p1} = -\frac{\left(x_{j_p} + x_{j_p0}\right) - L_{j_r}\cos\left(q_{j_p1}\right)}{\left(x_{j_p} + x_{j_p0}\right)L_{j_r}\sin\left(q_{j_p1}\right)}\dot{x}_{j_p} \tag{18}$$

$$\dot{q}_{j_p2} = -\frac{\left(x_{j_p} + x_{j_p0}\right) - L_{j_r1}\cos\left(q_{j_p2}\right)}{\left(x_{j_p} + x_{j_p0}\right)L_{j_r1}\sin\left(q_{j_p2}\right)}\dot{x}_{j_p} \tag{19}$$

with $j_p = 2n-1, j_r = 2n, \forall\, n \in \{1,2\}$.

Next, the linear/angular velocity vectors of the studied system can be computed frame by frame along a simple oriented graph by propagating from *object 0* to *object 3*, while covering *closed chain 1*, *object 1*, *closed chain 2*, *object 2* and *open chain 5*.

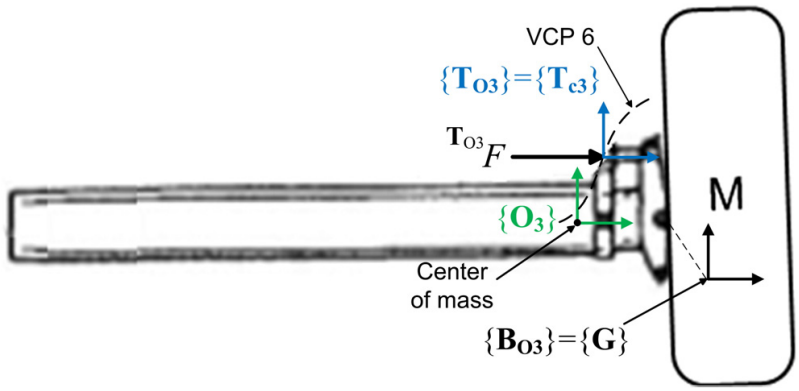

Fig. 7. Object 3.

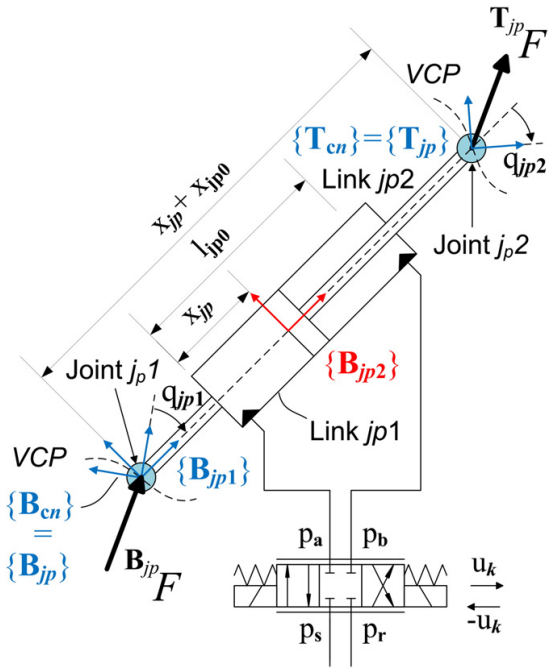

Fig. 8. The j_pth prismatic open chain, i.e. kth cylinder.

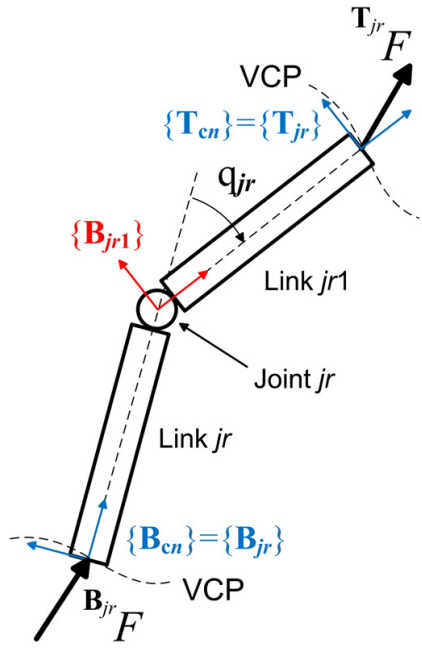

Fig. 9. The j_rth revolute open chain.

4.3.2. Velocity vectors in the virtual cutting points

In view of Eqs. (10)–(13) the following relations hold at the VCPs of the system

$$^{\mathbf{T}_{o3}}V = {}^{\mathbf{T}_5}V, \tag{20}$$

$$^{\mathbf{T}_{oi}}V = {}^{\mathbf{T}_{cn}}V = {}^{\mathbf{T}_{jp}}V = {}^{\mathbf{T}_{jr}}V \tag{21}$$

with $j_p = 2n-1, j_r = 2n$ and $n = i, \forall\, i \in \{1,2\}$,

$$^{\mathbf{B}_{o2}}V = {}^{\mathbf{B}_5}V, \tag{22}$$

and

$$^{\mathbf{B}_{oi}}V = {}^{\mathbf{B}_{cn}}V = {}^{\mathbf{B}_{jp}}V = {}^{\mathbf{B}_{jr}}V \tag{23}$$

with $j_p = 2n-1, j_r = 2n$ and $n = i+1, \forall\, i \in \{0,1\}$.

4.3.3. Velocity vectors in the objects

In view (Eq. (3)), the following relations hold for the velocity transformations of ith *object*, $\forall\, i \in \{0,3\}$

$$\begin{aligned} ^{\mathbf{O}_i}V &= {}^{\mathbf{T}_{oi}}\mathbf{U}^T_{\mathbf{O}_i}\,{}^{\mathbf{T}_{oi}}V \\ &= {}^{\mathbf{B}_{oi}}\mathbf{U}^T_{\mathbf{O}_i}\,{}^{\mathbf{B}_{oi}}V. \end{aligned} \tag{24}$$

4.3.4. Velocity vectors in the closed chains

In view of Fig. 9 and Eq. (3), the linear/angular velocity vectors in the j_rth revolute *open chain* can be written as

$$^{\mathbf{B}_{j_r1}}V = -\mathbf{z}_\tau \dot{q}_{j_r} + {}^{\mathbf{B}_{j_r}}\mathbf{U}^T_{\mathbf{B}_{j_r1}}\,{}^{\mathbf{B}_{j_r}}V \tag{25}$$

$$^{\mathbf{T}_{j_r}}V = {}^{\mathbf{B}_{j_r1}}\mathbf{U}^T_{\mathbf{T}_{j_r}}\,{}^{\mathbf{B}_{j_r1}}V \tag{26}$$

with $j_r = 2n, \forall\, n \in \{1,2\}$, and $z_\tau = [0\ 0\ 0\ 0\ 0\ 1]^T$.

Similarly, in view of Fig. 8 and Eq. (3), the linear/angular velocity vectors in the j_pth prismatic *open chain* can be written as

$$^{\mathbf{B}_{j_p1}}V = -\mathbf{z}_\tau \dot{q}_{j_p1} + {}^{\mathbf{B}_{j_p}}\mathbf{U}^T_{\mathbf{B}_{j_p1}}\,{}^{\mathbf{B}_{j_p}}V \tag{27}$$

$$^{\mathbf{B}_{j_p2}}V = \mathbf{x}_f \dot{x}_{j_p} + {}^{\mathbf{B}_{j_p1}}\mathbf{U}^T_{\mathbf{B}_{j_p2}}\,{}^{\mathbf{B}_{j_p1}}V \tag{28}$$

$$^{\mathbf{T}_{j_p}}V = -\mathbf{z}_\tau \dot{q}_{j_p2} + {}^{\mathbf{B}_{j_p2}}\mathbf{U}^T_{\mathbf{T}_{j_p}}\,{}^{\mathbf{B}_{j_p2}}V, \tag{29}$$

with $j_p = 2n-1, \forall\, n \in \{1,2\}$, and $x_f = [1\ 0\ 0\ 0\ 0\ 0]^T$.

4.3.5. Velocity vectors in 5th actuated open chain

In view of Fig. 10 and Eq. (3), the linear/angular velocity vectors in the 5th prismatic *open chain* can be written as

$$^{\mathbf{B}_{51}}V = \mathbf{x}_f \dot{x}_5 + {}^{\mathbf{B}_5}\mathbf{U}^T_{\mathbf{B}_{51}}\,{}^{\mathbf{B}_5}V \tag{30}$$

$$^{\mathbf{T}_5}V = {}^{\mathbf{B}_{51}}\mathbf{U}^T_{\mathbf{T}_5}\,{}^{\mathbf{B}_{51}}V. \tag{31}$$

4.4. Dynamics of the system

After all the linear/angular velocity vectors of the system have been specified, the dynamics of the studied system can be computed along the opposite directions of the simple oriented graph, starting from

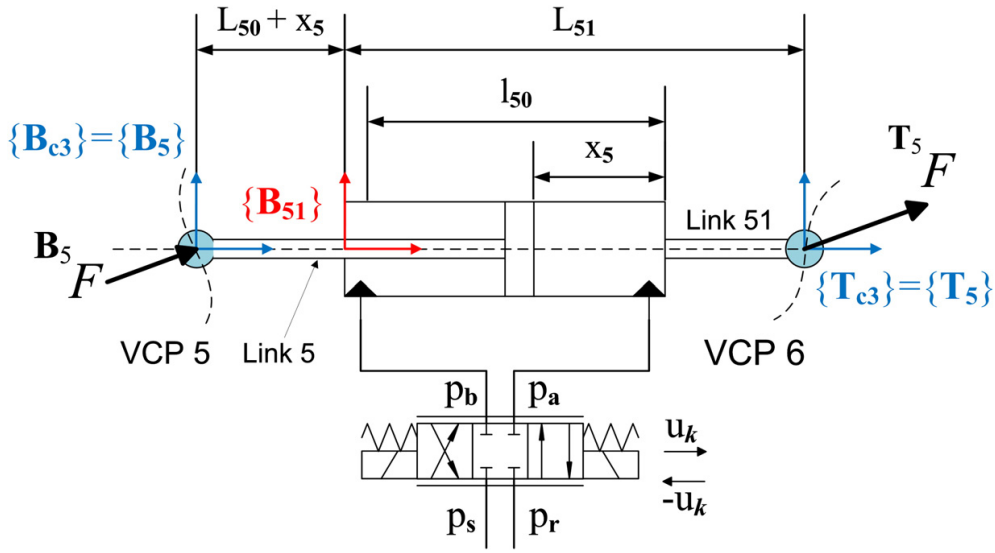

Fig. 10. The 5th prismatic open chain, i.e. 3rd cylinder.

object 3 toward *object 0*, while covering *open chain 5*, *object 2*, *closed chain 2*, *object 1*, and *closed chain 1*.

For the purpose of this study, the following assumption is made

Assumption 1. The friction torques of the three unactuated rotational joints in nth closed chain (see Figs. 9 and 8) are zero.

4.4.1. Dynamics of the objects

The net force/moment vector ${}^{O_i}F^* \in \mathbb{R}^6$ of the *i*th *object*, $\forall\, i \in \{0, 3\}$, can be expressed in view of Eq. (5) as

$$\mathbf{M}_{\mathbf{O}_i}\frac{d}{dt}\left({}^{\mathbf{O}_i}V\right) + \mathbf{C}_{\mathbf{O}_i}\left({}^{\mathbf{O}_i}\omega\right){}^{\mathbf{O}_i}V + \mathbf{G}_{\mathbf{O}_i} = {}^{\mathbf{O}_i}F^*. \tag{32}$$

On the other hand, the net force/moment vectors of *i*th *object*, $\forall\, i \in \{0, 3\}$, can be given as

$${}^{\mathbf{O}_i}F^* = {}^{\mathbf{O}_i}\mathbf{U}_{\mathbf{T}_{oi}}\,{}^{\mathbf{T}_{oi}}F - {}^{\mathbf{O}_i}\mathbf{U}_{\mathbf{B}_{oi}}\,{}^{\mathbf{B}_{oi}}F. \tag{33}$$

Note that in view of Eqs. (10)–(13) the following force/moment relations at the VCPs hold

$${}^{\mathbf{T}_{o3}}F = {}^{\mathbf{T}_5}F \tag{34}$$

$${}^{\mathbf{T}_{oi}}F = {}^{\mathbf{T}_{cn}}F \tag{35}$$

with $n = i$, $\forall\, i \in \{1, 2\}$, and

$${}^{\mathbf{B}_{o2}}F = {}^{\mathbf{B}_5}F \tag{36}$$

$${}^{\mathbf{B}_{oi}}F = {}^{\mathbf{B}_{cn}}F \tag{37}$$

with $n = i + 1$, $\forall\, i \in \{0, 1\}$.

4.4.2. Dynamics of the 5th open chain

The dynamics of the link 51 (cylinder case) and the link 5 (cylinder piston) in the 5th *open chain* can be expressed in view (Eq. (5)) as

$$\mathbf{M}_{\mathbf{B}_{51}}\frac{d}{dt}\left({}^{\mathbf{B}_{51}}V\right) + \mathbf{C}_{\mathbf{B}_{51}}\left({}^{\mathbf{B}_{51}}\omega\right){}^{\mathbf{B}_{51}}V + \mathbf{G}_{\mathbf{B}_{51}} = {}^{\mathbf{B}_{51}}F^* \tag{38}$$

$$\mathbf{M}_{\mathbf{B}_5}\frac{d}{dt}\left({}^{\mathbf{B}_5}V\right) + \mathbf{C}_{\mathbf{B}_5}\left({}^{\mathbf{B}_5}\omega\right){}^{\mathbf{B}_5}V + \mathbf{G}_{\mathbf{B}_5} = {}^{\mathbf{B}_5}F^*. \tag{39}$$

Note that the force/moment vector ${}^{\mathbf{T}_5}F \in \mathbb{R}^6$ at the *driving VCP* of 5th *open chain* can be solved with Eq. (33) (with $i = 3$) and with Eq. (34). Now, the force/moment vectors, i.e., the force resultants of rigid links, in 5th *open chain* can be covered by

$${}^{\mathbf{B}_{51}}F = {}^{\mathbf{B}_{51}}F^* + {}^{\mathbf{B}_{51}}\mathbf{U}_{\mathbf{T}_5}\,{}^{\mathbf{T}_5}F \tag{40}$$

$${}^{\mathbf{B}_5}F = {}^{\mathbf{B}_5}F^* + {}^{\mathbf{B}_5}\mathbf{U}_{\mathbf{B}_{51}}\,{}^{\mathbf{B}_{51}}F. \tag{41}$$

In Eq. (41), ${}^{\mathbf{B}_5}F \in \mathbb{R}^6$ denotes the force/moment vector at the *driven VCP* of 5th *open chain*. Furthermore, the piston force of the 3rd cylinder can be computed from Eq. (40) as

$$f_{c3} = \mathbf{x}_f^{T\,\mathbf{B}_{51}}F \tag{42}$$

4.4.3. Dynamics of the closed chains

In view of Assumption 1, the torque constraints at the three unactuated joints in *n*th *closed chain* can be expressed by

$$\mathbf{z}_\tau^{T\,\mathbf{T}_{jp}}F = 0 \tag{43}$$

$$\mathbf{z}_\tau^{T\,\mathbf{B}_{jr1}}F = 0 \tag{44}$$

$$\mathbf{z}_\tau^{T\,\mathbf{B}_{jp1}}F = \mathbf{z}_\tau^{T\,\mathbf{B}_{jp1}}\mathbf{U}_{\mathbf{B}_{jp}}\,{}^{\mathbf{B}_{jp}}F = 0. \tag{45}$$

The dynamics of the link j_r, link j_r1, link j_p1 and j_p2 (see Figs. 9 and 8) in the system *n*th *closed chain*, $\forall\, n \in \{1, 2\}$, can be expressed in view of Eq. (5) as

$$\mathbf{M}_{\mathbf{B}_{jr}}\frac{d}{dt}\left({}^{\mathbf{B}_{jr}}V\right) + \mathbf{C}_{\mathbf{B}_{jr}}\left({}^{\mathbf{B}_{jr}}\omega\right){}^{\mathbf{B}_{jr}}V + \mathbf{G}_{\mathbf{B}_{jr}} = {}^{\mathbf{B}_{jr}}F^* \tag{46}$$

$$\mathbf{M}_{\mathbf{B}_{jr1}}\frac{d}{dt}\left({}^{\mathbf{B}_{jr1}}V\right) + \mathbf{C}_{\mathbf{B}_{jr1}}\left({}^{\mathbf{B}_{jr1}}\omega\right){}^{\mathbf{B}_{jr1}}V + \mathbf{G}_{\mathbf{B}_{jr1}} = {}^{\mathbf{B}_{jr1}}F^* \tag{47}$$

$$\mathbf{M}_{\mathbf{B}_{jp1}}\frac{d}{dt}\left({}^{\mathbf{B}_{jp1}}V\right) + \mathbf{C}_{\mathbf{B}_{jp1}}\left({}^{\mathbf{B}_{jp1}}\omega\right){}^{\mathbf{B}_{jp1}}V + \mathbf{G}_{\mathbf{B}_{jp1}} = {}^{\mathbf{B}_{jp1}}F^* \tag{48}$$

$$\mathbf{M}_{\mathbf{B}_{j_{p2}}}\frac{d}{dt}\left({}^{\mathbf{B}_{j_{p2}}}V\right)+\mathbf{C}_{\mathbf{B}_{j_{p2}}}\left({}^{\mathbf{B}_{j_{p2}}}\omega\right)^{\mathbf{B}_{j_{p2}}}V+\mathbf{G}_{\mathbf{B}_{j_{p2}}}={}^{\mathbf{B}_{j_{p2}}}F^{*}. \tag{49}$$

Note that the force/moment vector ${}^{\mathbf{T}_{cn}}F\in\mathbb{R}^6$, with $n=i$, $\forall\, i\in\{1,2\}$, in *driving VCP* of *n*th *closed chain* can be solved with Eq. (33) and with Eq. (35). Now, the force/moment vectors, i.e., the force resultants of rigid links, in *n*th *closed chain* can be covered by the following equations:

$${}^{\mathbf{T}_{cn}}F={}^{\mathbf{T}_{j_r}}F+{}^{\mathbf{T}_{j_p}}F \tag{50}$$

$${}^{\mathbf{T}_{j_r}}F=\alpha_{j_r}{}^{\mathbf{T}_{cn}}F+{}^{\mathbf{T}_{cn}}\eta \tag{51}$$

$${}^{\mathbf{T}_{j_p}}F=\alpha_{j_p}{}^{\mathbf{T}_{cn}}F-{}^{\mathbf{T}_{cn}}\eta \tag{52}$$

$${}^{\mathbf{B}_{j_{r1}}}F={}^{\mathbf{B}_{j_{r1}}}F^{*}+{}^{\mathbf{B}_{j_{r1}}}\mathbf{U}_{\mathbf{T}_{j_r}}{}^{\mathbf{T}_{j_r}}F \tag{53}$$

$${}^{\mathbf{B}_{j_r}}F={}^{\mathbf{B}_{j_r}}F^{*}+{}^{\mathbf{B}_{j_r}}\mathbf{U}_{\mathbf{B}_{j_{r1}}}{}^{\mathbf{B}_{j_{r1}}}F \tag{54}$$

$${}^{\mathbf{B}_{j_{p2}}}F={}^{\mathbf{B}_{j_{p2}}}F^{*}+{}^{\mathbf{B}_{j_{p2}}}\mathbf{U}_{\mathbf{T}_{j_p}}{}^{\mathbf{T}_{j_p}}F \tag{55}$$

$${}^{\mathbf{B}_{j_p}}F={}^{\mathbf{B}_{j_p}}\mathbf{U}_{\mathbf{B}_{j_{p1}}}{}^{\mathbf{B}_{j_{p1}}}F^{*}+{}^{\mathbf{B}_{j_p}}\mathbf{U}_{\mathbf{B}_{j_{p2}}}{}^{\mathbf{B}_{j_{p2}}}F \tag{56}$$

$${}^{\mathbf{B}_{cn}}F={}^{\mathbf{B}_{j_r}}F+{}^{\mathbf{B}_{j_p}}F. \tag{57}$$

In Eq. (57), ${}^{\mathbf{B}_{cn}}F\in\mathbb{R}^6$, with $n=i+1$, $\forall\, i\in\{0,1\}$, denotes the force/moment vector in *driven VCP* of *n*th *closed chain*. Furthermore, in Eqs. (51) and (52), α_{j_r} and α_{j_p} denote the load distribution factors, so that $\alpha_{j_r}+\alpha_{j_p}=1$ hold, and ${}^{\mathbf{T}_{cn}}\eta\in\mathbb{R}^6$ denotes the internal force vector, where three meaningful elements (forces in x and y and moment in z) can be determined by satisfying the three constraints in Eqs. (43)–(45). Note that ${}^{\mathbf{T}_{cn}}\eta$ disappears in ${}^{\mathbf{B}_{cn}}F$ in Eq. (57).

The piston force of *k*th cylinder in *n*th *closed chain* can be computed from Eq. (55) as

$$f_{ck}=\mathbf{x}_f^{T\,\mathbf{B}_{j_{p2}}}F \tag{58}$$

with $k=n, j_p=2n-1$, and $\forall\, n\in\{1,2\}$.

4.5. Dynamics of the actuators

After addressing the dynamics and control issues of rigid bodies (rigid links and objects), the fluid dynamics and control of actuated j_pth prismatic joints, i.e., *k*th hydraulic cylinder, with $j_p=k-1$, $\forall\, k\in\{1,3\}$, need to be considered. As discussed, e.g., in [18], the dynamics of control valves can be ignored if a high-bandwidth servo valves are used and they are markedly faster than system dynamics.

Piston friction makes a large difference between the cylinder output force (given in Eqs. (42) and (58)) and chamber pressure-induced force [18]. Thus, in order to achieve appropriate piston force control, it is necessary to implement a friction model for *k*th cylinder piston. A piston force for the *k*th cylinder piston can be defined as

$$f_{pk}=f_{ck}+f_{fk} \tag{59}$$

where f_{ck}, $\forall\, k\in\{1,3\}$, denotes the output force of the *k*th cylinder defined in Eq. (42) or (58), and f_{fk} denotes the linear parametrized friction model defined in [15].

The flow rates Q_{ak} and Q_{bk} entering into or out from the chambers A and B, respectively, can be written as

$$Q_{ak}=c_{pk1}v(p_s-p_{ak})u_kS(u_k)+c_{nk1}v(p_{ak}-p_r)u_kS(-u_k) \tag{60}$$

$$Q_{bk}=-c_{pk2}v(p_s-p_{bk})u_kS(-u_k)-c_{nk2}v(p_{bk}-p_r)u_kS(u_k) \tag{61}$$

where $c_{pk1}>0$, $c_{nk1}>0$, $c_{pk2}>0$ and $c_{nk2}>0$, are four flow coefficients of control valve, p_{ak} and p_{bk} are chamber pressures of chamber A and chamber B, respectively, u_k is control voltage of valve, p_s is a system supply pressure, p_r is a pressure of system fluid return line and $S(u_k)$ a selective function defined as

$$S(u_k)\overset{\text{def}}{=}\begin{cases}1, & \text{if } u_k>0\\ 0, & \text{if } u_k\le 0\end{cases} \tag{62}$$

and $v(\Delta p)$ is a pressure-drop related function defined as

$$v(\Delta p)=\text{sign}(\Delta p)\sqrt{|\Delta p|} \tag{63}$$

The pressure dynamics of the chamber A and the chamber B can be written as

$$\dot{p}_{ak}=\frac{\beta}{A_{ak}x_{j_p}}\left(Q_{ak}-A_{ak}\dot{x}_{j_p}\right) \tag{64}$$

$$\dot{p}_{bk}=\frac{\beta}{A_{bk}\left(l_{j_p0}-x_{j_p}\right)}\left(Q_{bk}+A_{bk}\dot{x}_{j_p}\right), \tag{65}$$

respectively. In Eqs. (64) and (65), β denotes the bulk modulus of fluid, A_{ak} and A_{bk} are the piston areas in chamber A and chamber B of *k*th cylinder, respectively, x_{j_p} and $\dot{x}_{j_p}$ are the piston position and the piston velocity of the *k*th cylinder, respectively, and l_{j_p0} denotes maximum stroke of the *k*th cylinder.

The piston chamber pressure-induced force of *k*th cylinder can be expressed as

$$f_{pk}=A_{ak}p_{ak}-A_{bk}p_{bk} \tag{66}$$

Then, premultiplying A_{ak} and A_{bk} to Eqs. (64) and (65), respectively, differentiating Eq. (66) and using Eqs. (60) and (61) yields

$$\dot{f}_{pk}=\beta\left[u_{fk}-\left(\frac{A_{ak}}{x_{j_p}}+\frac{A_{bk}}{l_{j_p0}-x_{j_p}}\right)\dot{x}_{j_p}\right] \tag{67}$$

where the control valve voltage related term u_{fk} can be written as

$$\begin{aligned}u_{fk}&=\frac{Q_{ak}}{x_{j_p}}-\frac{Q_{bk}}{l_{j_p0}-x_{j_p}}\\&=\left(\frac{c_{pk1}v(p_s-p_{ak})}{x_{j_p}}+\frac{c_{nk2}v(p_{bk}-p_r)}{l_{j_p0}-x_{j_p}}\right)u_kS(u_k)\\&\quad+\left(\frac{c_{pk2}v(p_s-p_{bk})}{l_{j_p0}-x_{j_p}}+\frac{c_{nk1}v(p_{ak}-p_r)}{x_{j_p}}\right)u_kS(-u_k).\end{aligned} \tag{68}$$

The following assumption, that the piston of *k*th cylinder never reaches its two ends, is made.

Assumption 2. In the scope of this study the following relation holds

$$0<x_{j_p}<l_{j_p0}. \tag{69}$$

Now, the Assumption 2 provides that

$$\left(\frac{c_{pk1}v(p_s-p_{ak})}{x_{j_p}}+\frac{c_{nk2}v(p_{bk}-p_r)}{l_{j_p0}-x_{j_p}}\right)>0 \tag{70}$$

$$\left(\frac{c_{pk2}v(p_s-p_{bk})}{l_{j_p0}-x_{j_p}}+\frac{c_{nk1}v(p_{ak}-p_r)}{x_{j_p}}\right)>0 \tag{71}$$

hold, letting the control valve voltage of the kth cylinder to be solved from Eq. (68) as

$$u_k = \frac{1}{\left(\frac{c_{pk1}v(p_s-p_{ak})}{x_{j_p}}+\frac{c_{nk2}v(p_{bk}-p_r)}{l_{j_p0}-x_{j_p}}\right)}u_{fk}S(u_{fk}) + \frac{1}{\left(\frac{c_{pk2}v(p_s-p_{bk})}{l_{j_p0}-x_{j_p}}+\frac{c_{nk1}v(p_{ak}-p_r)}{x_{j_p}}\right)}u_{fk}S(-u_{fk}) \tag{72}$$

as a non-singular solution for Eq. (72) can be provided in view of Eqs. (70) and (71).

4.6. Control equations

This section specifies the control equations for the studied hydraulic crane. First, in subsection 4.6.1, the kinematic relations (inverse kinematics) from the desired Cartesian motions to the desired joint space motions are given. As the control objective in VDC is to make the controlled actual velocities track the required velocities [18], in subsection 4.6.2, this will lead to introduction of new design vectors, namely the required linear/angular velocity vectors ${}^{\mathbf{A}}V_r \in \mathbb{R}^6$. Based on the required linear/angular velocity vectors, other design vectors, namely the required net force/moment vectors ${}^{\mathbf{A}}F_r^* \in \mathbb{R}^6$, will be defined in subsection 4.6.3. The required system force/moment transformations are defined in subsection 4.6.4, and finally, in subsection 4.6.5, the control equations for the *k*th hydraulic cylinder will be given.

4.6.1. Inverse kinematics for redundant manipulators

The kinematic relationship between the Cartesian space and the joint space of the studied system (see Fig. 1) can be expressed as

$$\begin{bmatrix}\dot{X}_d\\ \dot{Y}_d\end{bmatrix} = \mathbf{J}\begin{bmatrix}\dot{\theta}_{1d}\\ \dot{\theta}_{2d}\\ \dot{x}_{5d}\end{bmatrix} \tag{73}$$

where $\mathbf{J} \in \mathbb{R}^{2\times 3}$ is a Jacobian matrix.

The problem of system inverse kinematics is in defining system joint variables in terms of end-effector motions. Assume the desired Cartesian motion trajectory ($\dot{X}_d$ and $\dot{Y}_d$) for manipulator end-effector to be known. For redundant manipulator an infinite number of joint velocity vectors exist for given Cartesian velocity vector [20]. However, as discussed e.g., in [20] and [21], the joint space velocities can be solved from Cartesian space velocities, i.e., from Eq. (73), as

$$\begin{bmatrix}\dot{\theta}_{1d}\\ \dot{\theta}_{2d}\\ \dot{x}_{5d}\end{bmatrix} = \mathbf{J}_W^*\begin{bmatrix}\dot{X}_d\\ \dot{Y}_d\end{bmatrix} \tag{74}$$

where *weighted Jacobian pseudoinverse* $\mathbf{J}_W^* \in \mathbb{R}^{3\times 2}$ can be defined as

$$\mathbf{J}_W^* = \mathbf{W}^{-1}\mathbf{J}^T\left(\mathbf{J}\mathbf{W}^{-1}\mathbf{J}^T\right)^{-1} \tag{75}$$

and where $\mathbf{W} \in \mathbb{R}^{3\times 3}$ is an appropriately chosen weighting matrix, providing methods to define one specific solution from an infinite number of joint velocity vectors. In this paper a weighted least-norm solution [20] is utilized for defining $\mathbf{W}$.

4.6.2. Required velocity vectors

Note the fact that desired joint space angles θ_{1d} and θ_{2d}, which can be solved from Eq. (74), can be converted to desired *closed chain* angles q_{j_rd}. Furthermore, the desired closed chain angles q_{j_rd} can be converted to corresponding desired piston positions x_{j_pd} by reusing Eq. (14). Similar, the desired joint space velocities $\dot{\theta}_{1d}$ and $\dot{\theta}_{2d}$ can be converted desired *closed chain* velocities $\dot{q}_{j_rd}$, and further to the desired piston velocities $\dot{x}_{j_pd}$, by reusing Eq. (17).

Now, the required piston velocities, with integrated piston position feedback, can be written in view of [18] as

$$\dot{x}_{j_pr} = \dot{x}_{j_pd} + \lambda_k\left(x_{j_pd}-x_{j_p}\right) \tag{76}$$

with $j_p = 2k-1, \forall\, k \in \{1,3\}$ and where $\lambda_k > 0$ denotes the position error feedback gain. The remaining required joint velocities in *n*th *closed chain* can be solved with Eq. (76) by reusing Eqs. (17)–(19).

Finally, the required linear/angular velocity vectors in the studied subsystems can be computed by reusing Eqs. (20)–(31) as

$${}^{\mathbf{T}_{o3}}V_r = {}^{\mathbf{T}_5}V_r \tag{77}$$

$${}^{\mathbf{T}_{oi}}V_r = {}^{\mathbf{T}_{ci}}V_r = {}^{\mathbf{T}_{jp}}V_r = {}^{\mathbf{T}_{jr}}V_r \tag{78}$$

with $j_p = 2n-1, j_r = 2n$ and $n = i, \forall\, i \in \{1,2\}$,

$${}^{\mathbf{B}_{o2}}V_r = {}^{\mathbf{B}_5}V_r \tag{79}$$

$${}^{\mathbf{B}_{oi}}V_r = {}^{\mathbf{B}_{ci}}V_r = {}^{\mathbf{B}_{jp}}V_r = {}^{\mathbf{B}_{jr}}V_r \tag{80}$$

with $j_p = 2n-1, j_r = 2n$ and $n = i+1, \forall\, i \in \{0,1\}$,

$${}^{\mathbf{O}_i}V_r = {}^{\mathbf{T}_{oi}}\mathbf{U}_{\mathbf{O}_i}^T\,{}^{\mathbf{T}_{oi}}V_r = {}^{\mathbf{B}_{oi}}\mathbf{U}_{\mathbf{O}_i}^T\,{}^{\mathbf{B}_{oi}}V_r,\ \forall i \in \{0,3\} \tag{81}$$

$${}^{\mathbf{B}_{jr1}}V_r = -\mathbf{z}_\tau\dot{q}_{j_r\mathrm{r}} + {}^{\mathbf{B}_{jr}}\mathbf{U}_{\mathbf{B}_{jr1}}^T\,{}^{\mathbf{B}_{jr}}V_r \tag{82}$$

$${}^{\mathbf{T}_{jr}}V_r = {}^{\mathbf{B}_{jr1}}\mathbf{U}_{\mathbf{T}_{jr}}^T\,{}^{\mathbf{B}_{jr1}}V_r \tag{83}$$

$${}^{\mathbf{B}_{jp1}}V_r = -\mathbf{z}_\tau\dot{q}_{j_p1r} + {}^{\mathbf{B}_{jp}}\mathbf{U}_{\mathbf{B}_{jp1}}^T\,{}^{\mathbf{B}_{jp}}V_r \tag{84}$$

$${}^{\mathbf{B}_{jp2}}V_r = \mathbf{x}_f\dot{x}_{j_pr} + {}^{\mathbf{B}_{jp1}}\mathbf{U}_{\mathbf{B}_{jp2}}^T\,{}^{\mathbf{B}_{jp1}}V_r \tag{85}$$

$${}^{\mathbf{T}_{jp}}V_r = -\mathbf{z}_\tau\dot{q}_{j_p2r} + {}^{\mathbf{B}_{jp2}}\mathbf{U}_{\mathbf{T}_{jp}}^T\,{}^{\mathbf{B}_{jp2}}V_r \tag{86}$$

$${}^{\mathbf{B}_{51}}V_r = \mathbf{x}_f\dot{x}_{5r} + {}^{\mathbf{B}_5}\mathbf{U}_{\mathbf{B}_{51}}^T\,{}^{\mathbf{B}_5}V_r \tag{87}$$

$${}^{\mathbf{T}_5}V_r = {}^{\mathbf{B}_{51}}\mathbf{U}_{\mathbf{T}_5}^T\,{}^{\mathbf{B}_{51}}V_r \tag{88}$$

with $j_p = 2n-1, j_r = 2n$ and $\forall\, n \in \{1,2\}$.

4.6.3. Required net force/moment vectors

After obtaining all the required linear/angular velocity vectors for the studied subsystems, new design vectors, namely the required net force/moment vectors ${}^{\mathbf{A}}F_r^* \in \mathbb{R}^6$ for the system objects and the rigid links in *open chains*, can be specified in view of [18] as

$${}^{\mathbf{A}}F_r^* = \mathbf{Y}_{\mathbf{A}}\theta_{\mathbf{A}} + \mathbf{K}_{\mathbf{A}}\left({}^{\mathbf{A}}V_r - {}^{\mathbf{A}}V\right) \tag{89}$$

by substituting frames $\{\mathbf{O}_i\}$, $\{\mathbf{B}_{j_r}\}$, $\{\mathbf{B}_{j_r1}\}$, $\{\mathbf{B}_{j_p1}\}$, $\{\mathbf{B}_{j_p2}\}$, $\{\mathbf{B}_5\}$ and $\{\mathbf{B}_{51}\}$ for frame $\{\mathbf{A}\}$ in Eq. (89), with $\forall\, i \in \{0,3\}, j_p = 2n-1$ and $j_r = 2n, \forall\, n \in \{1,2\}$. Moreover, in Eq. (89) $\mathbf{K}_{\mathbf{A}} \in \mathbb{R}^{6\times 6}$ denotes a positive-definite gain matrix characterizing the rigid links velocity feedback control. The term $\mathbf{Y}_{\mathbf{A}}\theta_{\mathbf{A}}$ denotes the model-based feedforward compensation term and is specified in Eq. (6).

4.6.4. Required force/moment transformations

In addition to Eq. (89), the required net force/moment vectors of *i*th *object*, $\forall\, i \in \{0, 3\}$, can be given, by reusing Eq. (33), as

$$ {}^{\mathbf{O}_i}F_r^* = {}^{\mathbf{O}_i}\mathbf{U}_{\mathbf{T}_{oi}}\,{}^{\mathbf{T}_{oi}}F_r - {}^{\mathbf{O}_i}\mathbf{U}_{\mathbf{B}_{oi}}\,{}^{\mathbf{B}_{oi}}F_r. \tag{90} $$

Note that for the scope of this study contacts with system environment are omitted and no external forces are exerted into the tip of the manipulator, leading to ${}^{\mathbf{G}}F_r = {}^{\mathbf{B}_{o3}}F_r = [0\ 0\ 0\ 0\ 0\ 0]^T$. Now, the required force/moment vector ${}^{\mathbf{T}_{o3}}F_r \in \mathbb{R}^6$, i.e., the required force resultants, in the *driving VCP* of *object 3* can be solved from Eq. (90), utilizing Eq. (89).

The required torque constraints at the three unactuated joints in *n*th *closed chain* can be expressed, by reusing Eqs. (43)–(45), as

$$ \mathbf{z}_\tau^{T\,\mathbf{T}_{j_p}} F_r = 0 \tag{91} $$

$$ \mathbf{z}_\tau^{T\,\mathbf{B}_{j_r 1}} F_r = 0 \tag{92} $$

$$ \mathbf{z}_\tau^{T\,\mathbf{B}_{j_p 1}} F_r = \mathbf{z}_\tau^{T\,\mathbf{B}_{j_p 1}} \mathbf{U}_{\mathbf{B}_{j_p}}\,{}^{\mathbf{B}_{j_p}}F_r = 0. \tag{93} $$

Now, the required force/moment vectors can be obtained by reusing Eqs. (34)–(37), (40), (41), (43) –(45), and Eqs. (50)–(57) as

$$ {}^{\mathbf{T}_{o3}}F_r = {}^{\mathbf{T}_5}F_r \tag{94} $$

$$ {}^{\mathbf{T}_{oi}}F_r = {}^{\mathbf{T}_{cn}}F_r \tag{95} $$

with $n = i$, $\forall\, i \in \{1, 2\}$,

$$ {}^{\mathbf{B}_{o2}}F_r = {}^{\mathbf{B}_5}F_r \tag{96} $$

$$ {}^{\mathbf{B}_{oi}}F_r = {}^{\mathbf{B}_{cn}}F_r \tag{97} $$

with $n = i + 1$, $\forall\, i \in \{0, 1\}$,

$$ {}^{\mathbf{B}_{51}}F_r = {}^{\mathbf{B}_{51}}F_r^* + {}^{\mathbf{B}_{51}}\mathbf{U}_{\mathbf{T}_5}\,{}^{\mathbf{T}_5}F_r \tag{98} $$

$$ {}^{\mathbf{B}_5}F_r = {}^{\mathbf{B}_5}F_r^* + {}^{\mathbf{B}_5}\mathbf{U}_{\mathbf{B}_{51}}\,{}^{\mathbf{B}_{51}}F_r \tag{99} $$

$$ {}^{\mathbf{T}_{cn}}F_r = {}^{\mathbf{T}_{jr}}F_r + {}^{\mathbf{T}_{jp}}F_r \tag{100} $$

$$ {}^{\mathbf{T}_{jr}}F_r = \alpha_{j_r}\,{}^{\mathbf{T}_{cn}}F_r + {}^{\mathbf{T}_{cn}}\eta_r \tag{101} $$

$$ {}^{\mathbf{T}_{jp}}F_r = \alpha_{j_p}\,{}^{\mathbf{T}_{cn}}F_r - {}^{\mathbf{T}_{cn}}\eta_r \tag{102} $$

$$ {}^{\mathbf{B}_{jr1}}F_r = {}^{\mathbf{B}_{jr1}}F_r^* + {}^{\mathbf{B}_{jr1}}\mathbf{U}_{\mathbf{T}_{j_r}}\,{}^{\mathbf{T}_{jr}}F_r \tag{103} $$

$$ {}^{\mathbf{B}_{jr}}F_r = {}^{\mathbf{B}_{jr}}F_r^* + {}^{\mathbf{B}_{jr}}\mathbf{U}_{\mathbf{B}_{jr1}}\,{}^{\mathbf{B}_{jr1}}F_r \tag{104} $$

$$ {}^{\mathbf{B}_{jp2}}F_r = {}^{\mathbf{B}_{jp2}}F_r^* + {}^{\mathbf{B}_{jp2}}\mathbf{U}_{\mathbf{T}_{jp}}\,{}^{\mathbf{T}_{jp}}F_r \tag{105} $$

$$ {}^{\mathbf{B}_{jp}}F_r = {}^{\mathbf{B}_{jp}}\mathbf{U}_{\mathbf{B}_{jp1}}\,{}^{\mathbf{B}_{jp1}}F_r^* + {}^{\mathbf{B}_{jp}}\mathbf{U}_{\mathbf{B}_{jp2}}\,{}^{\mathbf{B}_{jp2}}F_r \tag{106} $$

$$ {}^{\mathbf{B}_{cn}}F_r = {}^{\mathbf{B}_{jr}}F_r + {}^{\mathbf{B}_{jp}}F_r \tag{107} $$

with $j_p = 2n - 1$, $j_r = 2n$ and $\forall\, n \in \{1, 2\}$. In Eqs. (101) and (101), ${}^{\mathbf{T}_{cn}}\eta_r \in \mathbb{R}^6$ denotes the required internal force vector, where three meaningful elements (the required forces in *x* and *y* and the required moment in *z*) can be determined by satisfying the three constraints in Eqs. (91)–(93). Note that ${}^{\mathbf{T}_{cn}}\eta_r$ disappears in ${}^{\mathbf{B}_{cn}}F_r$ in Eq. (107).

Similar to Eq. (42), the required piston force of the 3rd cylinder can be written as

$$ f_{c3r} = \mathbf{x}_f^{T\,\mathbf{B}_{51}} F_r \tag{108} $$

and similar to Eq. (58), the required piston force of *k*th cylinder in *n*th *closed chain* can be written as

$$ f_{ckr} = \mathbf{x}_f^{T\,\mathbf{B}_{j_p 2}} F_r \tag{109} $$

with $j_p = 2k - 1$, and $\forall\, k \in \{1, 2\}$.

4.6.5. Control of the kth actuator

By reusing Eq. (59), the required piston force of *k*th cylinder piston can be written as

$$ f_{pkr} = f_{ckr} + f_{fk} \tag{110} $$

where f_{ckr}, $\forall\, k \in \{1, 3\}$, denotes the required piston force.

In view of Eq. (67), the desired control valve voltage related term u_{fkd}, enhanced with a piston force and piston velocity feedbacks, can be written as

$$ u_{fkd} = \left(\frac{1}{\beta_k}\right)\dot{f}_{pkr} + \left(\frac{A_{ak}}{x_{j_p}} + \frac{A_{bk}}{l_{j_p 0} - x_{j_p}}\right)\dot{x}_{j_p} + k_{fk}\left(f_{pkr} - f_{pk}\right) + k_{xk}\left(\dot{x}_{j_p r} - \dot{x}_{j_p}\right) \tag{111} $$

where $k_{fk} > 0$ and $k_{xk} > 0$ are two feedback gains, $\dot{x}_{j_p r}$ is obtained from Eq. (76), f_{pkr} is obtained from Eq. (108) or (109), and $\dot{x}_{j_p}$ and f_{pk} are the measured piston velocity and piston force of the *k*th cylinder, respectively.

Finally, in view of Eq. (72), the control voltage for the control valve of the *k*th cylinder, $\forall\, k \in \{1, 3\}$, can be written as

$$ \begin{aligned} u_k = {} & \frac{1}{\left(\dfrac{c_{pk1}\upsilon(p_s - p_{ak})}{x_{j_p}} + \dfrac{c_{nk2}\upsilon(p_{bk} - p_r)}{l_{j_p 0} - x_{j_p}}\right)} u_{fkd} S(u_{fkd}) \\ & + \frac{1}{\left(\dfrac{c_{pk2}\upsilon(p_s - p_{bk})}{l_{j_p 0} - x_{j_p}} + \dfrac{c_{nk1}\upsilon(p_{ak} - p_r)}{x_{j_p}}\right)} u_{fkd} S(-u_{fkd}). \end{aligned} \tag{112} $$

The main features of the controller design, described in the Sections 4.6.2–4.6.5, is illustrated in Fig. 11. The last block in the Fig. 11, represents an actual studied crane and outputs of this block $\left(p_{ak},\ p_{bk},\ x_{j_p} \text{and } \dot{x}_{j_p}\right)$ are measured system variables.

5. Stability analysis

In this section, the *virtual stability* (in the sense of Definition 2) of subsystems (see Figs. 4–10) is addressed. First, in subsections 5.1–5.4, the *virtual stability* of *i*th *object*, j_rth *open chain*, j_pth *open chain*, and 5th *open chain*, respectively, are given. Then, in subsection 5.5, it is shown how the *virtual stability* of subsystems converge to stability of the entire system.

5.1. Virtual stability of objects

The following theorem ensures that the *i*th *object* of studied system (see Figs. 4–7) qualifies to be *virtually stable* in the sense of Definition 2.

Theorem 1. The ith object described by Eqs. (24), (32) and (33), combined with its respective control Eqs. (81), (89) with frame $\{\mathbf{O}_i\}$ and Eq. (90), is virtually stable with its affiliated vector ${}^{\mathbf{O}_i}V_r - {}^{\mathbf{O}_i}V$ being a

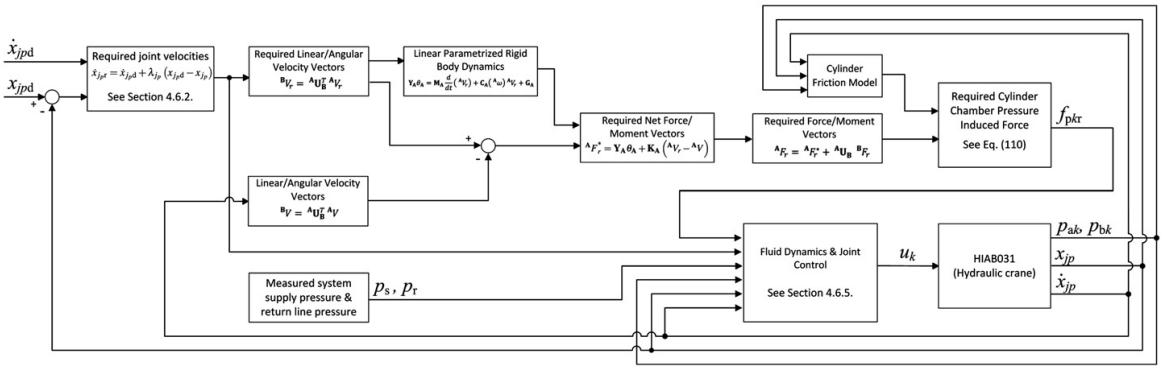

Fig. 11. The designed controller structure.

virtual function in both L_2 and L_∞ in the sense of Definition 2, as there can be found non-negative accompanying function

$$\nu_{oi} = \frac{1}{2}\left({}^{\mathbf{O}_i}V_r - {}^{\mathbf{O}_i}V\right)^T \mathbf{M}_{\mathbf{O}_i}\left({}^{\mathbf{O}_i}V_r - {}^{\mathbf{O}_i}V\right) \tag{113}$$

such that

$$\dot{\nu}_{oi} = -\left({}^{\mathbf{O}_i}V_r - {}^{\mathbf{O}_i}V\right)^T \mathbf{K}_{\mathbf{O}_i}\left({}^{\mathbf{O}_i}V_r - {}^{\mathbf{O}_i}V\right) + p_{\mathbf{T}_{oi}} - p_{\mathbf{B}_{oi}} \tag{114}$$

holds $\forall\, i \in \{0, 3\}$.

Proof. See Appendix A. ■

5.2. Virtual stability of unactuated j_rth revolute open chain

The following theorem ensures that the j_rth unactuated revolute *open chain* (see Fig. 9) qualifies to be *virtually stable* in the sense of Definition 2.

Theorem 2. The j_rth unactuated revolute open chain described by Eqs. (25), (26), (44), (46), (47), (53) and (54), combined with its respective control Eqs. (82), (83), (89) with frame $\{\mathbf{B}_{j_r}\}$, Eq. (89) with frame $\{\mathbf{B}_{j_r1}\}$, Eqs. (92), (103), and (104), is virtually stable with its affiliated vectors ${}^{\mathbf{B}_{j_r}}V_r - {}^{\mathbf{B}_{j_r}}V$ and ${}^{\mathbf{B}_{j_r1}}V_r - {}^{\mathbf{B}_{j_r1}}V$ being virtual functions in both L_2 and L_∞ in the sense of Definition 2, as there can be found non-negative accompanying function

$$\nu_{j_r} = \nu_{\mathbf{B}_{j_r}} + \nu_{\mathbf{B}_{j_r1}} \tag{115}$$

where

$$\nu_{\mathbf{B}_{j_r}} = \frac{1}{2}\left({}^{\mathbf{B}_{j_r}}V_r - {}^{\mathbf{B}_{j_r}}V\right)^T \mathbf{M}_{\mathbf{B}_{j_r}}\left({}^{\mathbf{B}_{j_r}}V_r - {}^{\mathbf{B}_{j_r}}V\right) \tag{116}$$

$$\nu_{\mathbf{B}_{j_r1}} = \frac{1}{2}\left({}^{\mathbf{B}_{j_r1}}V_r - {}^{\mathbf{B}_{j_r1}}V\right)^T \mathbf{M}_{\mathbf{B}_{j_r1}}\left({}^{\mathbf{B}_{j_r1}}V_r - {}^{\mathbf{B}_{j_r1}}V\right) \tag{117}$$

such that

$$\begin{aligned}\dot{\nu}_{j_r} = &-\left({}^{\mathbf{B}_{j_r}}V_r - {}^{\mathbf{B}_{j_r}}V\right)^T \mathbf{K}_{\mathbf{B}_{j_r}}\left({}^{\mathbf{B}_{j_r}}V_r - {}^{\mathbf{B}_{j_r}}V\right)\\ &-\left({}^{\mathbf{B}_{j_r1}}V_r - {}^{\mathbf{B}_{j_r1}}V\right)^T \mathbf{K}_{\mathbf{B}_{j_r1}}\left({}^{\mathbf{B}_{j_r1}}V_r - {}^{\mathbf{B}_{j_r1}}V\right)\\ &+ p_{\mathbf{B}_{j_r}} - p_{\mathbf{T}_{j_r}}\end{aligned} \tag{118}$$

holds with $j_r = 2n$, $\forall\, n \in \{1, 2\}$.

Proof. See Appendix B. ■

5.3. Virtual stability of actuated j_pth prismatic open chain

The following Theorem, based on the Lemma 1 and Lemma 2, ensures that the j_pth actuated prismatic *open chain*, i.e., kth cylinder (see Fig. 8), driven by the hydraulic fluid, qualifies to be *virtually stable* in the sense of Definition 2.

Lemma 1. Consider the j_pth prismatic open chain described by Eqs. (27)–(29), (43), (45), (48), (49), (55), (56), and (58), and combined with the control (Eqs. (84)–(86), (89)) with frame $\{\mathbf{B}_{j_p1}\}$, Eq. (89) with frame $\{\mathbf{B}_{j_p2}\}$, Eqs. (91), (93), (105), (106), and (109). Let the non-negative accompanying function for the j_pth open chain be

$$\nu_{\mathrm{oc}_{j_p}} = \nu_{\mathbf{B}_{j_p1}} + \nu_{\mathbf{B}_{j_p2}} \tag{119}$$

where

$$\nu_{\mathbf{B}_{j_p1}} = \frac{1}{2}\left({}^{\mathbf{B}_{j_p1}}V_r - {}^{\mathbf{B}_{j_p1}}V\right)^T \mathbf{M}_{\mathbf{B}_{j_p1}}\left({}^{\mathbf{B}_{j_p1}}V_r - {}^{\mathbf{B}_{j_p1}}V\right) \tag{120}$$

$$\nu_{\mathbf{B}_{j_p2}} = \frac{1}{2}\left({}^{\mathbf{B}_{j_p2}}V_r - {}^{\mathbf{B}_{j_p2}}V\right)^T \mathbf{M}_{\mathbf{B}_{j_p2}}\left({}^{\mathbf{B}_{j_p2}}V_r - {}^{\mathbf{B}_{j_p2}}V\right). \tag{121}$$

Then, the time derivative of Eq. (119) can be expressed by

$$\begin{aligned}\dot{\nu}_{\mathrm{oc}_{j_p}} = &-\left({}^{\mathbf{B}_{j_p1}}V_r - {}^{\mathbf{B}_{j_p1}}V\right)^T \mathbf{K}_{\mathbf{B}_{j_p1}}\left({}^{\mathbf{B}_{j_p1}}V_r - {}^{\mathbf{B}_{j_p1}}V\right)\\ &-\left({}^{\mathbf{B}_{j_p2}}V_r - {}^{\mathbf{B}_{j_p2}}V\right)^T \mathbf{K}_{\mathbf{B}_{j_p2}}\left({}^{\mathbf{B}_{j_p2}}V_r - {}^{\mathbf{B}_{j_p2}}V\right)\\ &+\left(\dot{x}_{j_pr} - \dot{x}_{j_p}\right)\left(f_{\mathrm{ckr}} - f_{\mathrm{ck}}\right) + p_{\mathbf{B}_{j_p}} - p_{\mathbf{T}_{j_p}}\end{aligned} \tag{122}$$

with $j_p = 2n - 1$, $\forall\, n \in \{1, 2\}$.

Proof. See Appendix C. ■

Note that the appearance of $\left(\dot{x}_{j_pr} - \dot{x}_{j_p}\right)\left(f_{\mathrm{ckr}} - f_{\mathrm{ck}}\right)$ in the right hand side of Eq. (122) prevents the *virtual stability* of the j_pth *open chain*, i.e., kth cylinders, $\forall\, k \in \{1, 2\}$, from being held at this point. This term will be addressed in Lemma 2.

Lemma 2. Consider the kth hydraulic cylinder, $\forall\, k \in \{1, 3\}$, dynamics described by Eqs. (59), (67) and (68) and combined with the control Eqs. (110) and (111). Let the non-negative accompanying function for the dynamics of kth hydraulic cylinder be

$$\nu_{\mathrm{dk}} = \frac{1}{2\beta}\left(f_{\mathrm{pkr}} - f_{\mathrm{pk}}\right)^2. \tag{123}$$

Then, the time derivative of Eq. (123) can be expressed by

$$\dot{\nu}_{dk} = -k_{fk}\left(f_{pkr}-f_{pk}\right)^2 - k_{fk}\left(\dot{x}_{j_p r}-\dot{x}_{j_p}\right)\left(f_{ckr}-f_{ck}\right) \tag{124}$$

with $j_p = 2k-1, \forall\, k \in \{1,3\}$.

Proof. See Appendix D. ■

Theorem 3. The j_pth actuated prismatic open chain, i.e., kth cylinder, driven by hydraulic fluid and described by Eqs. (27)–(29), (43), (45), (48), (49), (55), (56), (58), (59), (67) and (68), and combined with its control Eqs. (84)–(86), (89) with frame $\{\mathbf{B}_{j_p 1}\}$, Eq. (89) with frame $\{\mathbf{B}_{j_p 2}\}$, Eqs. (91), (93), (105), (106), (109), (110), (111), is virtually stable with its affiliated vectors ${}^{\mathbf{B}_{jp1}}V_r - {}^{\mathbf{B}_{jp1}}V$ and ${}^{\mathbf{B}_{jp2}}V_r - {}^{\mathbf{B}_{jp2}}V$ and variable $f_{pkr} - f_{pk}$ being virtual functions in both L_2 and L_∞ in the sense of Definition 2.

Proof. The proof for Theorem 3 follows directly from Lemma 1 and Lemma 2. Define the non-negative accompanying function of the j_pth actuated prismatic *open chain*, i.e. *k*th cylinder, driven by hydraulic fluid as

$$\nu_{j_p} = \nu_{\mathrm{oc}_{j_p}} + \frac{\nu_{dk}}{k_{xk}} \tag{125}$$

where $\nu_{\mathrm{oc}_{j_p}}$ and ν_{dk} are defined by Eqs. (119) and (123), respectively. Then, it follows from Eqs. (122) and (124) that

$$\begin{aligned}\dot{\nu}_{j_p} &= \dot{\nu}_{\mathrm{oc}_{j_p}} + \frac{\dot{\nu}_{dk}}{k_{xk}} \\ &= -\left({}^{\mathbf{B}_{jp1}}V_r - {}^{\mathbf{B}_{jp1}}V\right)^T \mathbf{K}_{\mathbf{B}_{jp1}} \left({}^{\mathbf{B}_{jp1}}V_r - {}^{\mathbf{B}_{jp1}}V\right) \\ &\quad -\left({}^{\mathbf{B}_{jp2}}V_r - {}^{\mathbf{B}_{jp2}}V\right)^T \mathbf{K}_{\mathbf{B}_{jp2}} \left({}^{\mathbf{B}_{jp2}}V_r - {}^{\mathbf{B}_{jp2}}V\right) \\ &\quad -k_{fk}\left(f_{pkr}-f_{pk}\right)^2 + p_{\mathbf{B}_{j_p}} - p_{\mathbf{T}_{j_p}}\end{aligned} \tag{126}$$

holds with $j_p = 2n-1, \forall\, n \in \{1,2\}$.

Consider the fact that the j_pth actuated prismatic *open chain* driven by hydraulic fluid, i.e. *k*th cylinder, has one *driving VCP* associated with frame $\{\mathbf{T}_{j_p}\}$ and one *driven VCP* associated with frame $\{\mathbf{B}_{j_p}\}$. Using Eqs. (119), (123), (125) and (126) completes the proof of *virtual stability* of the j_pth actuated prismatic *open chain* driven by hydraulic fluid, i.e. *k*th cylinder, with $j_p = 2k-1, \forall\, k \in \{1,2\}$, in the sense of Definition 2. ■

5.4. Virtual stability of actuated 5th prismatic open chain

The following Theorem, based on the Lemma 2 and Lemma 3, ensures that the 5th actuated prismatic *open chain*, i.e., 3rd cylinder (see Fig. 10), driven by the hydraulic fluid, qualifies to be *virtually stable* in the sense of Definition 2.

Lemma 3. Consider the 5th prismatic open chain described by Eqs. (30), (31) and Eqs. (38)–(42), and combined with the control Eqs. (87), (88), (89) with $\{\mathbf{B}_5\}$, Eq. (89) with $\{\mathbf{B}_{51}\}$, Eqs. (98) and (99). Let the non-negative accompanying function for the 5th open chain be

$$\nu_{\mathrm{oc}_5} = \nu_{\mathbf{B}_5} + \nu_{\mathbf{B}_{51}} \tag{127}$$

where

$$\nu_{\mathbf{B}_5} = \frac{1}{2}\left({}^{\mathbf{B}_5}V_r - {}^{\mathbf{B}_5}V\right)^T \mathbf{M}_{\mathbf{B}_5} \left({}^{\mathbf{B}_5}V_r - {}^{\mathbf{B}_5}V\right) \tag{128}$$

$$\nu_{\mathbf{B}_{51}} = \frac{1}{2}\left({}^{\mathbf{B}_{51}}V_r - {}^{\mathbf{B}_{51}}V\right)^T \mathbf{M}_{\mathbf{B}_{51}} \left({}^{\mathbf{B}_{51}}V_r - {}^{\mathbf{B}_{51}}V\right). \tag{129}$$

Then, the time derivative of Eq. (127) can be expressed by

$$\begin{aligned}\dot{\nu}_{\mathrm{oc}_5} &= -\left({}^{\mathbf{B}_5}V_r - {}^{\mathbf{B}_5}V\right)^T \mathbf{K}_{\mathbf{B}_5} \left({}^{\mathbf{B}_5}V_r - {}^{\mathbf{B}_5}V\right) \\ &\quad -\left({}^{\mathbf{B}_{51}}V_r - {}^{\mathbf{B}_{51}}V\right)^T \mathbf{K}_{\mathbf{B}_{51}} \left({}^{\mathbf{B}_{51}}V_r - {}^{\mathbf{B}_{51}}V\right) \\ &\quad + \left(\dot{x}_{5r} - \dot{x}_5\right)\left(f_{c3r} - f_{c3}\right) + p_{\mathbf{B}_5} - p_{\mathbf{T}_5}.\end{aligned} \tag{130}$$

Proof. The 5th prismatic *open chain* poses a similar structure compared to the j_pth prismatic *open chain* (see Fig. 8). The proof for Lemma 3 can be obtained in a similar manner as for Lemma 1 in Appendix C. ■

Theorem 4. The 5th actuated prismatic open chain, i.e., 3rd cylinder, driven by hydraulic fluid and described by Eqs. (30), (31), (38)–(42), (59), (67), and (68), and combined with its control Eqs. (87), (88), (89) with $\{\mathbf{B}_5\}$, Eq. (89) with $\{\mathbf{B}_{51}\}$, Eqs. (98), (99), (108), (110) and (111), is virtually stable with its affiliated vectors ${}^{\mathbf{B}_5}V_r - {}^{\mathbf{B}_5}V$ and ${}^{\mathbf{B}_{51}}V_r - {}^{\mathbf{B}_{51}}V$ and variable $f_{p3r} - f_{p3}$ being virtual functions in both L_2 and L_∞ in the sense of Definition 2.

The proof for Theorem 4 follows directly from Lemma 2 (with $k = 3$) and Lemma 3. Define the non-negative accompanying function of the 5th actuated prismatic *open chain*, i.e. 3rd cylinder, driven by hydraulic fluid as

$$\nu_5 = \nu_{\mathrm{oc}_5} + \frac{\nu_{d3}}{k_{x3}} \tag{131}$$

where ν_{d3} and ν_{oc_5} are defined by Eqs. (123) and (127), respectively. Then, it follows from Eq. (124) with $k = 3$ and Eq. (130) that

$$\begin{aligned}\dot{\nu}_5 &= \dot{\nu}_{\mathrm{oc}_5} + \frac{\dot{\nu}_{d3}}{k_{x3}} \\ &= -\left({}^{\mathbf{B}_5}V_r - {}^{\mathbf{B}_5}V\right)^T \mathbf{K}_{\mathbf{B}_5} \left({}^{\mathbf{B}_5}V_r - {}^{\mathbf{B}_5}V\right) \\ &\quad -\left({}^{\mathbf{B}_{51}}V_r - {}^{\mathbf{B}_{51}}V\right)^T \mathbf{K}_{\mathbf{B}_{51}} \left({}^{\mathbf{B}_{51}}V_r - {}^{\mathbf{B}_{51}}V\right) \\ &\quad -k_{f3}\left(f_{p3r}-f_{p3}\right)^2 + p_{\mathbf{B}_5} - p_{\mathbf{T}_5}\end{aligned} \tag{132}$$

holds.

Consider the fact that the 5th actuated prismatic *open chain* driven by hydraulic fluid, i.e. 3rd cylinder, has one *driving VCP* associated with frame $\{\mathbf{T}_5\}$ and one *driven VCP* associated with frame $\{\mathbf{B}_5\}$. Using Eq. (123) with $k = 3$, Eqs. (127), (131) and (132) completes the proof of *virtual stability* of the 5th actuated prismatic *open chain* driven by hydraulic fluid, i.e. 3rd cylinder, in the sense of Definition 2. ■

5.5. Stability of entire system

According to Theorem 2.1 in [18], the *virtual stabilities* of all subsystems will converge to the overall stability of the entire system. This is because all the VPFs will cancel each other as if each positive VPF (in *driven cutting point*) is connected to its corresponding negative VPF (in *driving cutting point*).

Proof. The non-negative accompanying function for the entire hydraulic system (see Fig. 1), decomposed into subsystems by placing conceptual VCPs (see Fig. 2), and presented in a simple oriented graph (see Fig. 3), can be written as

$$\nu = \nu_{oi} + \nu_{j_p} + \nu_{j_r} + \nu_5 \tag{133}$$

and using Eq. (113), (115), (125), and Eq. (131) for Eq. (133).

Then, the derivative of Eq. (133) can be written, in view of Eqs. (114), (118), (122) and (132), as

$$\begin{aligned}\dot{\nu} = &-\sum_{\{A\}\in\Phi} \left({}^{\mathbf{A}}V_r - {}^{\mathbf{A}}V\right)^T \mathbf{K}_{\mathbf{A}} \left({}^{\mathbf{A}}V_r - {}^{\mathbf{A}}V\right) - k_{fk}\left(f_{pkr}-f_{pk}\right)^2 + p_{\mathbf{T}_{Oi}} \\ &- p_{\mathbf{B}_{Oi}} + p_{\mathbf{B}_{j_r}} - p_{\mathbf{T}_{j_r}} + p_{\mathbf{B}_{j_p}} - p_{\mathbf{T}_{j_p}} + p_{\mathbf{B}_5} - p_{\mathbf{T}_5}\end{aligned} \tag{134}$$

with $\forall\, k \in \{1, 3\}$ and where set Φ contains frames $\{\mathbf{O}_i\}$, $\{\mathbf{B}_{j_r}\}$, $\{\mathbf{B}_{j_r1}\}$, $\{\mathbf{B}_{j_p1}\}$, $\{\mathbf{B}_{j_p2}\}$, $\{\mathbf{B}_5\}$ and $\{\mathbf{B}_{51}\}$ with $\forall\, i \in \{0, 3\}$, $j_p = 2n - 1$, $j_r = 2n$, $\forall\, n \in \{1, 2\}$. Then, in view of Eqs. (20)–(23), (34)–(37), (50), (77)–(80), (94)–(97) and (100), $p_{\mathbf{B}_{00}} = p_{\mathbf{B}_1} + p_{\mathbf{B}_2}$, $p_{\mathbf{B}_{01}} = p_{\mathbf{B}_3} + p_{\mathbf{B}_4}$, $p_{\mathbf{B}_{02}} = p_{\mathbf{B}_5}$, $p_{\mathbf{T}_{01}} = p_{\mathbf{T}_1} + p_{\mathbf{T}_2}$, $p_{\mathbf{T}_{02}} = p_{\mathbf{T}_3} + p_{\mathbf{T}_4}$, and $p_{\mathbf{T}_{03}} = p_{\mathbf{T}_5}$. Now, this leads that all VPFs, apart from $p_{\mathbf{T}_{00}}$ and $p_{\mathbf{B}_{03}}$ are canceled out from Eq. (134). However, for the known $p_{\mathbf{T}_{00}} = 0$ (zero base velocity) and $p_{\mathbf{B}_{03}} = 0$ (zero end-effector external force), it can be seen that all the VPFs are canceled out from Eq. (134).

Thus, it follows from Lemma 2.3 in [18] that

$$f_{pkr} - f_{pk} \in L_2 \cap L_\infty \tag{135}$$

$$^{\mathbf{A}}V_r - {}^{\mathbf{A}}V \in L_2 \cap L_\infty, \tag{136}$$

are guaranteed, $\forall\, k \in \{1, 3\}$ and by substituting frames $\{\mathbf{O}_i\}$, $\{\mathbf{B}_{j_r}\}$, $\{\mathbf{B}_{j_r1}\}$, $\{\mathbf{B}_{j_p1}\}$, $\{\mathbf{B}_{j_p2}\}$, $\{\mathbf{B}_5\}$ and $\{\mathbf{B}_{51}\}$ for frame $\{\mathbf{A}\}$ in Eq. (136).

Then, in view of Eqs. (28), (30), (85) and (87), expression (136) imply that

$$\dot{x}_{j_p r} - \dot{x}_{j_p} \in L_2 \cap L_\infty, \tag{137}$$

holds, with $j_p = 2k - 1$, $\forall\, k \in \{1, 3\}$, leading to

$$x_{j_p d} - x_{j_p} \in L_2 \cap L_\infty. \tag{138}$$

Given a bounded $\dot{x}_{j_p r}$, the boundedness of $\dot{x}_{j_p}$ is ensured from Eq. (137). Then, when $\ddot{x}_{j_p r} \in L_\infty$ holds for all actuated joints, it follows that f_{ckr} in Eq. (109) is bounded, which implies $f_{pkr} \in L_\infty$ from Eq. (110). Thus, $f_{pk} \in L_\infty$ is ensured from Eq. (135), such that $|f_{pk}| \le \gamma_p$ holds with γ_p being a positive constant. The asymptotic convergence of all L_2 signals with bounded derivatives can be ensured from Lemma 2.8. in [18]. ■

6. Experimental set-up and implementation issues

The experimental set-up consisted of the following hardware components and properties:

- dSpace DS1103 controller board
- dimensions for cylinders 1 and 2: 80/45 × 545, and for cylinder 3: 50/30 × 1012
- payload of 475 kg, denoted as M in Fig. 2
- for cylinders 1 and 2, zero-lapped linear servovalves (100 dm^3/min @ $\Delta p = 3.5$ MPa per notch), with a bandwidth of 100 Hz @ ±5% signals are used
- for cylinder 3, zero-lapped linear servovalve (4 dm^3/min @ $\Delta p = 3.5$ MPa per notch), with a bandwidth of 100 Hz @ ±5% signals is used
- Heidenhain ROD 456 incremental encoder (5000 inc/rev) with IVB interpolation units for joints 1 and 2, providing a theoretical piston position resolution $< 1.2 \cdot 10^{-3}$ mm
- Sick Stegmann DG60L incremental encoder (10,000 inc/rev) with cable transducer (200 mm/rev) for cylinder 3 providing a theoretical piston position resolution $5.0 \cdot 10^{-3}$ mm
- Druck PTX1400 pressure transmitters with an operating pressure range of 25 MPa
- controller sample time $T_s = 3$ ms.

Expensive load cells were not used in the experiments to measure the system's piston forces (f_{pk}, $\forall\, k \in \{1, 3\}$). As Eq. (66) shows, an alternative method of obtaining the cylinder's piston force is to use the cylinder chambers' pressure data. Note that the cylinder chambers' pressure measurements are necessary for the controller (see Eq. (112)). For the automation of hydraulic construction cranes, chamber pressure measurements provide a practical solution since retrofitting the pressure sensors is much easier than retrofitting the piston load cells.

It is well-known that, especially with small increments and high sampling rate, a simple and often used approximation for the derivative, namely backward difference, often leads to a noisy differentiated signals. As in our study [22] was discussed and experimentally verified, a finite difference method [23], defined as

$$\dot{y}(t) \approx \frac{1}{T_s} \sum_{k=0}^{n-1} C_k y(t - kT_s), \tag{139}$$

enhanced with a Geometric Moving Average (GMA) filter [24], defined as

$$y(k) = (1-\gamma) y(k-1) + \gamma u(k), \tag{140}$$

provide an effective method to produce noise suppressed differentiated signals. In this study, this method was used for $\frac{d}{dt}\left({}^{\mathbf{A}}V_r\right)$ in $\mathbf{Y_A}$ in Eq. (89) and for $\dot{f}_{pkr}$ and $\dot{x}_{j_p}$ in Eq. (111). Moreover, in Eq. (139), weights $C = [5\ 3\ 1\ -1\ -3\ -5]/35$ were used. In Eq. (140), the most recent input $u(k)$ is weighted by γ and past values are weighted by $(1 - \gamma)$. The value $\gamma = 0.04$ was used to compromise between disturbance attenuation and low phase lag.

Utilized VDC feedback gains are given in Table 1.

The parameters of rigid bodies in vector $\theta_A \in \mathbb{R}^{13}$ were identified by utilizing the CAD (computer-aided design) software. Accurate CAD models of all *objects* (see Figs. 4–7) and rigid links in *open chains* (see Figs. 8–10) were generated and the components in $\theta_A \in \mathbb{R}^{13}$ (mass $m_{\mathbf{A}}$, distances ${}^{\mathbf{A}}d_{mx}$ and ${}^{\mathbf{A}}d_{my}$ from the rigid body frame $\{\mathbf{A}\}$, along the x and y axes, to the center of mass, and mass moments of inertias $I_{\mathbf{A}zz}$) were solved from CAD models. Utilized non-zero rigid body parameters of rigid bodies are given in Table 2. Note that only parameters of moving rigid bodies having dynamics are given and thus object 0 and link 2 are omitted in Table 2.

In Fig. 12 the workspace of the studied manipulator without extension cylinder is shown with the black line and the additional workspace provided by the extension cylinder is delimited with the black dotted line. The workspace, in which the environment imposed constraints such as the ground, roof and the manipulator's own structure are taken in consideration, is shown with the blue line. The driven Cartesian parallelogram path is shown with the red line. In the driven path, the Cartesian point-to-point transition times (a desired execution time between two Cartesian parallelogram corner points [A, B, C, D]), defining the Cartesian velocity trajectory and utilized in this study, were selected to be $t_{f2} = 2$s, $t_{f4} = 4$s and $t_{f8} = 8$s. The motion trajectories between the Cartesian points were carried out by utilizing a fifth order Quintic rest-to-rest trajectory generator.

The same Cartesian parallelogram path was used in our previous studies [17] and [22], allowing fair comparison to result achieved in this paper. In order to get consistent Cartesian position paths for the different test cases, in this study a desired Cartesian motion trajectory generator, to produce a desired Cartesian path given in Fig. 12, was utilized instead of operator-defined desired Cartesian motions, e.g., with joystick. However, the results achieved with a desired Cartesian motion trajectory generator are self-evidently transferable for the operator-defined Cartesian space motion control.

Table 1
Controller feedback parameters.

Cylinder 1	Cylinder 2	Cylinder 3
$k_{x1} = 0.03$	$k_{x2} = 0.04$	$k_{x3} = 0.012$
$k_{f1} = 5 \cdot 10^{-8}$	$k_{f2} = 6 \cdot 10^{-8}$	$k_{f3} = 1.2 \cdot 10^{-8}$
$\lambda_1 = 25$	$\lambda_2 = 28$	$\lambda_3 = 35$
In Eq. (89), $\mathbf{K_A} = 500 \cdot \mathbf{I}_6$, for all rigid links		

Table 2
Utilized non-zero rigid body parameters.

Rigid body	Body frame	$m_{\mathbf{A}}$ [kg]	${}^{\mathbf{A}}d_{mx}$ [m]	${}^{\mathbf{A}}d_{my}$ [m]	$I_{\mathbf{A}zz}$ [$kg \cdot m^2$]
O_1	$\{\mathbf{O}_1\}$	6.2	0.023	0.149	0.065
O_2	$\{\mathbf{O}_2\}$	35.8	0.335	0.275	6.045
O_3	$\{\mathbf{O}_3\}$	570.2	0.255	−0.127	67.058
L_{11}	$\{\mathbf{B}_{11}\}$	17.4	0.358	0	3.131
L_{12}	$\{\mathbf{B}_{12}\}$	10.4	0.330	0	1.683
L_{21}	$\{\mathbf{B}_{21}\}$	18.8	0.179	0.124	1.239
L_{31}	$\{\mathbf{B}_{31}\}$	17.4	0.358	0	3.131
L_{32}	$\{\mathbf{B}_{32}\}$	10.4	0.330	0	1.683
L_4	$\{\mathbf{B}_4\}$	75.8	0.493	0.162	27.906
L_{41}	$\{\mathbf{B}_{41}\}$	9.6	0.139	0.077	0.383
L_5	$\{\mathbf{B}_5\}$	6.7	0.671	0	3.606
L_{51}	$\{\mathbf{B}_{51}\}$	9.3	0.581	0	4.676

7. Experimental results

In Figs. 13–15 are given the measured system data under the Cartesian transition times t_{f2}, t_{f4} and t_{f8}, respectively (see meanings for tf2, tf4 and tf8 from previous Section 6). In these figures the same color code for the system actuators are used as in Figs. 2 and 3, so that red color denotes the cylinder 1 data, blue color denotes the cylinder 2 data and green color denotes the cylinder 3 data. The required reference trajectories for a piston velocities and piston forces are given in black. Note that y-axes in second and third plots in Figs. 13–15 are not given in the same scale with respect to each other in order to achieve a better view on the measured data.

The upmost plots in Figs. 13–15 present piston position tracking errors. The maximum piston position tracking errors with t_{f2} were 0.61 mm, 0.61 mm, and 0.47 mm for cylinder 1, cylinder 2 and cylinder 3, respectively, with t_{f4} these numbers were 0.45 mm, 0.57 mm and 0.25 mm, and with t_{f8} these numbers were 0.39 mm, 0.55 mm and 0.20 mm. As these plots illustrate, the proposed controller is able to track desired piston position trajectories accurately despite the utilized Cartesian transition time. Note that some static piston position errors occur in all Cartesian transition times. These static piston position tracking errors can be addressed by utilizing parameter adaptation, which was omitted in this study.

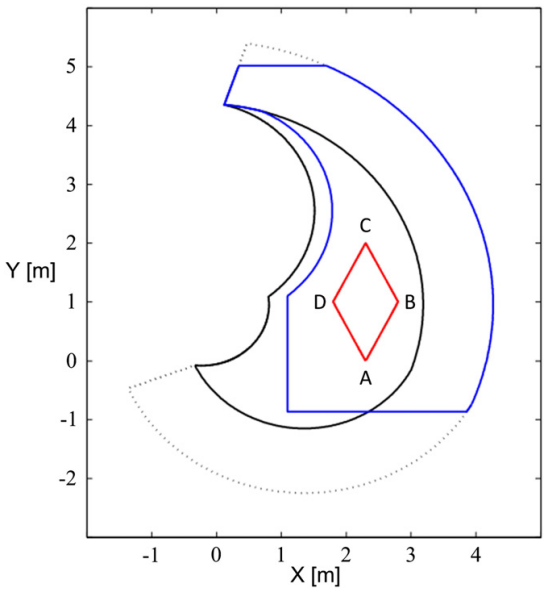

Fig. 12. Workspace with zero stroke of cylinder 3 (—), additional workspace provided by cylinder 3 (…), applicable structural workspace (—) and desired/driven Cartesian path (—).

The second plots in Figs. 13–15 show the measured piston velocities and their required reference trajectories. In the fast velocity trajectory, i.e., with t_{f2}, the maximum piston velocities were 0.206 m/s, 0.154 m/s and 0.050 m/s for cylinder 1, cylinder 2 and cylinder 3, respectively. In the medium velocity trajectory, i.e., with t_{f4}, the maximum piston velocities were 0.103 m/s, 0.078 m/s and 0.023 m/s for cylinder 1, cylinder 2 and cylinder 3, respectively, and in the slow velocity trajectory, i.e., with t_{f8}, these velocities were 0.052 m/s, 0.039 m/s and 0.011 m/s.

The control voltages are given in the third plots of Figs. 13–15. All the control valves operate within the control rate of ± 10 V. As Figs. 13 and 14 show, the smooth control valve voltages are achieved in the fast and medium velocity trajectories. In the slow velocity trajectory (see Fig. 13), slight jitter in the control voltage of control valve 3 can be noticed.

The last plots in Figs. 13–15 represent measured piston forces and their required reference trajectories. As these figures show, measured piston forces track well their reference trajectories with all driven Cartesian transition times. Because parameter adaptation was omitted in this study, it can be concluded that the system piston force trackings could be improved.

In the authors' previous study [17], the same hydraulic crane described in this paper was controlled with the VDC-based controller; however, only cylinders 1 and 2 were utilized (cylinder 3 was mechanically fixed). If the results obtained in the experiments (see Figs. 13–15) are compared to the corresponding results in [17], it can be seen that the quantization noises in the controlled signals are significantly reduced in this study compared to the results in [17]. This can be explained by the use of the noise-suppressing and low-phase-lag differentiating method (see Eqs. (139) and (140)), which was not used in [17].

In Zhu's studies, e.g., in [15] and [25], the ratio[3] of the maximum position tracking error ($\Delta x_{\max} = \max |x_{\text{des}} - x|$) to the maximum velocity ($v_{\max} = \max |\dot{x}|$) has been used as a performance indicator for the controller. Due to the lack of the existing research data for a hydraulic manipulators' Cartesian space motions, first, in Table 3 is given $\Delta x_{\max}/v_{\max}$ ratios in the actuator space for the current state-of-the-art multiple DOF manipulators. The $\Delta x_{\max}/v_{\max}$ ratio for this study is cylinder 1 data measured with t_{f2}, and it was the best recorded value for the manipulator. The smaller the ratio in Table 3 the better the control performance.

In Table 3, Authors' paper [17] provides the first published experimental results for the VDC based control of hydraulic manipulators. In [15], an adaptive output force control scheme for hydraulic cylinders was proposed by using direct output force measurement through load cells for 6-joint high-tech hydraulic robot, developed for Astronaut training purposes. In [13], 3-joint hydraulic robot arm was controlled based on the Desired Compensation Adaptive Robust Control (DCARC). In [11], an energy-efficient model-based computed torque controller for 2-joint hydraulic manipulator was proposed. As Table 3 shows, with the proposed controller an improved actuator control performance was achieved compared to the previous state-of-the-art studies.

Before the redundant DOF (i.e., the cylinder 3) was enabled in the system, the system was first driven only with cylinder 1 and cylinder 2, whereas *object* 2, *object* 3, and *open chain* 5 (see Figs. 6, 7 and 10) were treated as a one *object*. The same control gains as given in Table 1 were used for the cylinders 1 and 2. With this control set-up, the $\Delta x_{\max}/v_{\max}$ velocity trajectory was 0.0027 (s). This is a clear evident proof to the VDC concept that the addition of a local subsystem with its respective control will not affect the overall stability or control performances.

In the motion control of manipulators, it is obvious that, the most attention should be paid to the control accuracy of the manipulator end-effector. Fig. 16 shows the Cartesian position tracking errors for the proposed controller with all Cartesian transition times. As Fig. 16 shows, the

[3] The ratio of maximum position tracking error to the maximum velocity is given in SI Units.

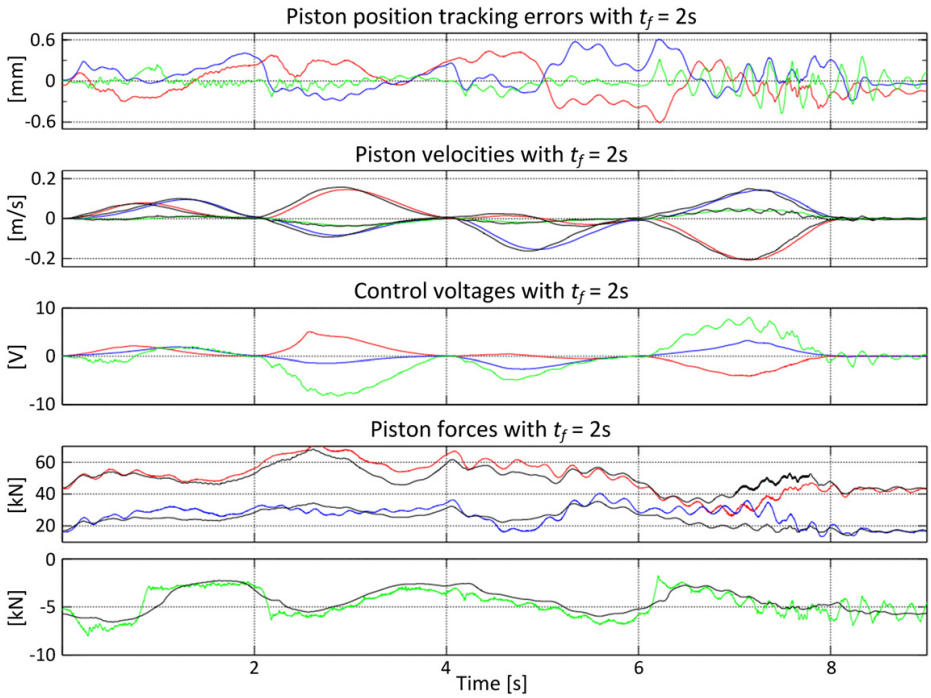

Fig. 13. Measured data under Cartesian transition time $t_f = 2$ s. Cylinder 1 data with (—), cylinder 2 data with (—), cylinder 3 data with (—) and reference trajectories with (—).

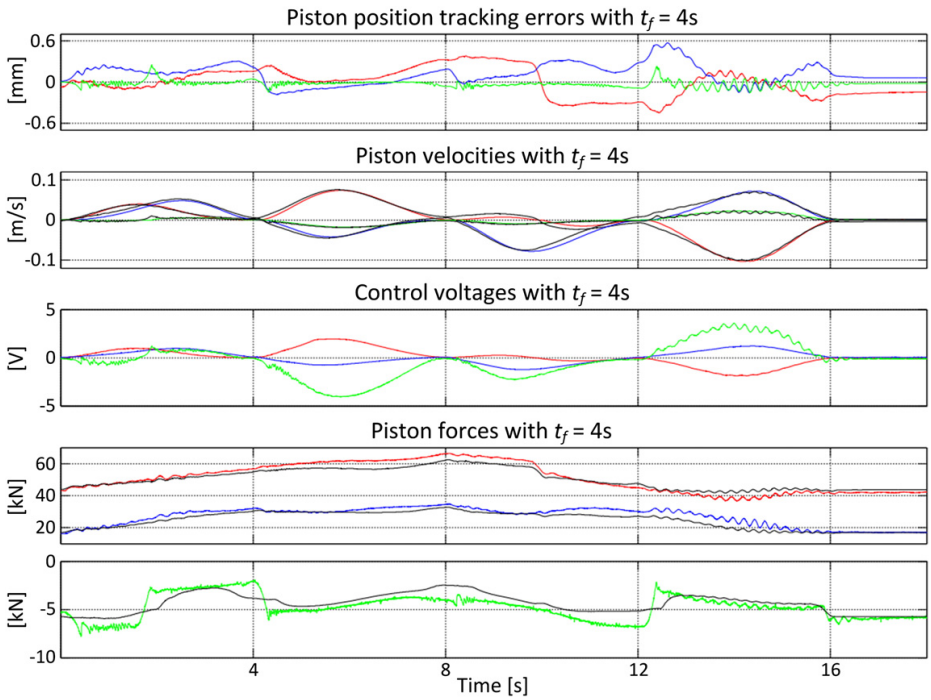

Fig. 14. Measured data under Cartesian transition time $t_f = 4$ s. Cylinder 1 data with (—), cylinder 2 data with (—), cylinder 3 data with (—) and reference trajectories with (—).

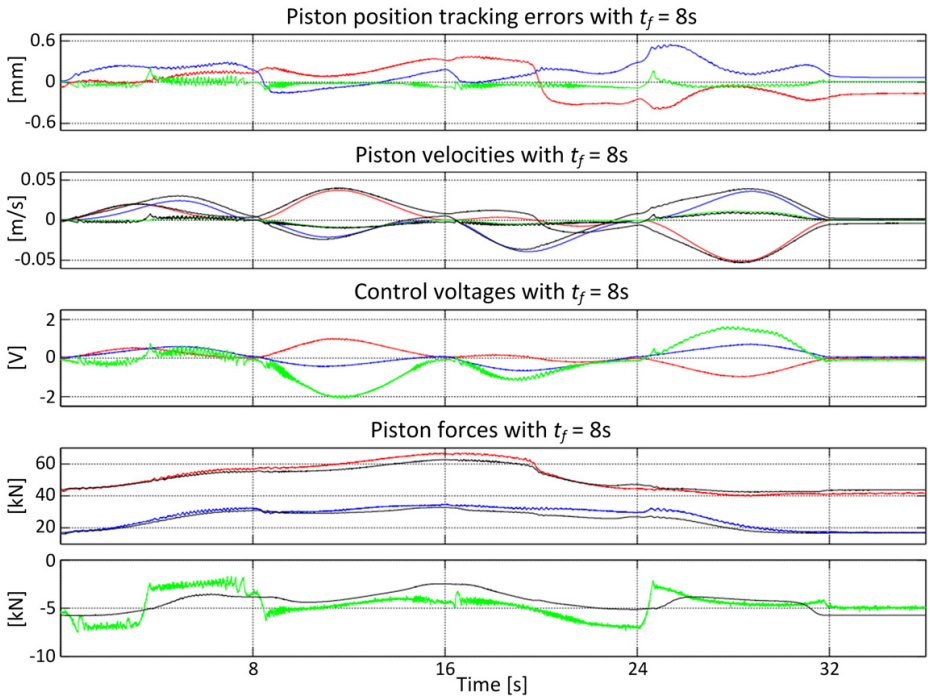

Fig. 15. Measured data under Cartesian transition time t_f = 8 s. Cylinder 1 data with (—), cylinder 2 data with (—), cylinder 3 data with (—) and reference trajectories with (—).

Table 3
Ratios of the maximum piston position tracking error to the maximum velocity.

Study	$\Delta x_{max}/v_{max}$	Reference
This study	0.0030 (s)	–
(Koivumäki 2013)	0.0039 (s)	[17]
(Zhu 2005)	0.0050 (s)	[15]
(Bu 2001)	0.0050 (s)	[13]
(Mattila 2000)	0.0130 (s)	[11]

Cartesian position tracking errors remain relatively small compared to the size of the system workspace (see Fig. 13) with all utilized Cartesian velocity trajectories. Also, the shape of the Cartesian position tracking error curves remain unchanged in spite of the utilized velocity trajectory. This clearly shows that the proposed controller is able to extensively cope with the highly nonlinear dynamical behavior of the hydraulic system and these tracking errors are mainly originating on the static error sources, e.g, from parameter uncertainties. The incorporation of the parameter adaptation, to reduce these static errors, will be the subject of our future studies.

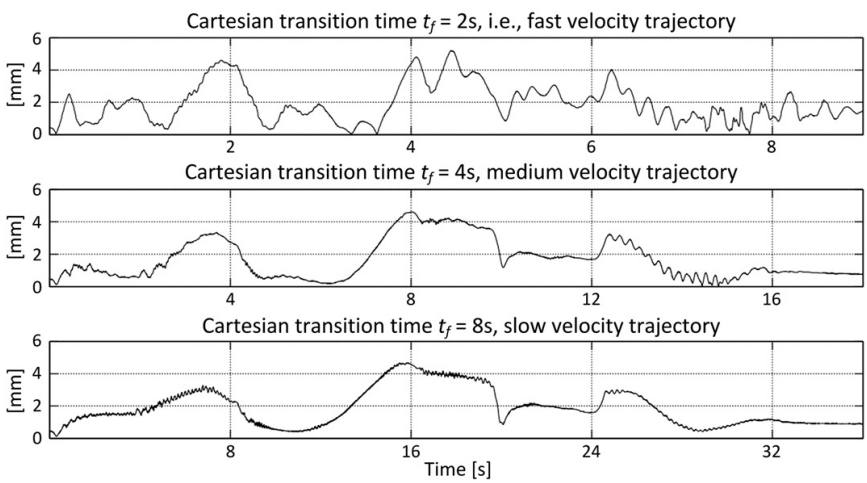

Fig. 16. Measured Cartesian position tracking errors under t_{f2}, t_{f4} and t_{f8}.

The computed maximum Cartesian position tracking errors in Fig. 16 were 5.20 mm, 4.60 mm and 4.67 mm, with t_{f2}, t_{f4} and t_{f8}, respectively, whereas the maximum Cartesian velocities were 1.05 m/s, 0.53 m/s and 0.26 m/s with t_{f2}, t_{f4} and t_{f8}, respectively. For the fast velocity trajectory t_{f2}, the $\Delta x_{\max}/v_{\max}$ ratio in the Cartesian space can measure to be 0.0050 (s).

Finally, in [15], the 6-joint high-tech hydraulic robot for astronaut training purposes was driven coordinately to track a circle in 3D with the maximum tangent velocity of 0.1 m/s and the maximum trajectory tracking error was measured to be about 1.5 mm. These give $\Delta x_{\max}/v_{\max}$ ratio for [15] to be 0.0150 (s). This value is three times larger as for the proposed controller in the fast velocity trajectory.

8. Conclusion

This paper addressed a stability-guaranteed Cartesian free-space motion control for redundant articulated hydraulic construction cranes to increase the system's safety and productivity. The motion controller, with the actuators' internal force control, was designed based on the VDC approach to cope with the highly nonlinear nature of the articulated hydraulic system. The proposed method provides a practical solution for controlling hydraulic construction devices because only the joints' angular encoders and the actuators' pressure sensors are needed. These sensors can easily be retrofitted into existing devices. As demonstrated in the experiments, the proposed controller could handle the nonlinear dynamic behavior of the hydraulic system. It was also demonstrated that, with the VDC concept, the addition of a local subsystem and its respective control equations would not affect the overall stability or control performances. Finally, compared to the previous state-of-the-art hydraulic robot manipulator studies, an improved Cartesian space (and also actuators') position control performance was achieved.

The parameter adaptation's effect on the system's control performance will be studied in the authors' future studies. The proposed controller will also be extended to address the contact forces between the manipulator and the environment.

Appendix A. Proof for Theorem 1

Consider the ith *object*, $\forall\, i \in \{0, 3\}$, (see Figs. 4–7) described by Eq. (32) and combined with its respective control Eq. (89) with frame $\{\mathbf{O}_i\}$. Subtracting Eq. (32) from Eq. (89) yields

$$\begin{aligned}{}^{\mathbf{O}_i}F_{\mathrm{r}}^{*} - {}^{\mathbf{O}_i}F^{*} = \mathbf{M}_{\mathbf{O}_i}\frac{d}{dt}\left({}^{\mathbf{O}_i}V_{\mathrm{r}} - {}^{\mathbf{O}_i}V\right) + \mathbf{C}_{\mathbf{O}_i}\left({}^{\mathbf{O}_i}\omega\right)\left({}^{\mathbf{O}_i}V_{\mathrm{r}} - {}^{\mathbf{O}_i}V\right) \\ + \mathbf{K}_{\mathbf{O}_i}\left({}^{\mathbf{O}_i}V_{\mathrm{r}} - {}^{\mathbf{O}_i}V\right).\end{aligned} \tag{A.1}$$

It follows from the skew-symmetric property of $\mathbf{C}_{\mathbf{O}_i}\left({}^{\mathbf{O}_i}\omega\right)$ that

$$\left({}^{\mathbf{O}_i}V_{\mathrm{r}} - {}^{\mathbf{O}_i}V\right)^{T}\mathbf{C}_{\mathbf{O}_i}\left({}^{\mathbf{O}_i}\omega\right)\left({}^{\mathbf{O}_i}V_{\mathrm{r}} - {}^{\mathbf{O}_i}V\right) = 0 \tag{A.2}$$

holds $\forall\, i \in \{0, 3\}$.

Now, if non-negative accompanying function ν_{oi} for ith *object* is chosen as proposed in Eq. (113), then it follows from (A.1) and (A.2) that time derivative of ν_{oi} can be derived to be as

$$\begin{aligned}\dot{\nu}_{oi} &= \left({}^{\mathbf{O}_i}V_{\mathrm{r}} - {}^{\mathbf{O}_i}V\right)^{T}\mathbf{M}_{\mathbf{O}_i}\frac{d}{dt}\left({}^{\mathbf{O}_i}V_{\mathrm{r}} - {}^{\mathbf{O}_i}V\right) \\ &= \left({}^{\mathbf{O}_i}V_{\mathrm{r}} - {}^{\mathbf{O}_i}V\right)^{T}\left[\left({}^{\mathbf{O}_i}F_{\mathrm{r}}^{*} - {}^{\mathbf{O}_i}F^{*}\right) - \mathbf{C}_{\mathbf{O}_i}\left({}^{\mathbf{O}_i}\omega\right)\left({}^{\mathbf{O}_i}V_{\mathrm{r}} - {}^{\mathbf{O}_i}V\right) - \mathbf{K}_{\mathbf{O}_i}\left({}^{\mathbf{O}_i}V_{\mathrm{r}} - {}^{\mathbf{O}_i}V\right)\right] \\ &= \left({}^{\mathbf{O}_i}V_{\mathrm{r}} - {}^{\mathbf{O}_i}V\right)^{T}\left({}^{\mathbf{O}_i}F_{\mathrm{r}}^{*} - {}^{\mathbf{O}_i}F^{*}\right) - \left({}^{\mathbf{O}_i}V_{\mathrm{r}} - {}^{\mathbf{O}_i}V\right)^{T}\mathbf{K}_{\mathbf{O}_i}\left({}^{\mathbf{O}_i}V_{\mathrm{r}} - {}^{\mathbf{O}_i}V\right).\end{aligned} \tag{A.3}$$

Furthermore, it follows from Definition 1, Eqs. (24), (33), (81) and (90) that

$$\begin{aligned}\left({}^{\mathbf{O}_i}V_{\mathrm{r}} - {}^{\mathbf{O}_i}V\right)^{T}\left({}^{\mathbf{O}_i}F_{\mathrm{r}}^{*} - {}^{\mathbf{O}_i}F^{*}\right) &= \left({}^{\mathbf{O}_i}V_{\mathrm{r}} - {}^{\mathbf{O}_i}V\right)^{T}{}^{\mathbf{O}_i}\mathbf{U}_{\mathbf{T}_{oi}}\left({}^{\mathbf{T}_{oi}}F_{\mathrm{r}} - {}^{\mathbf{T}_{oi}}F\right) \\ &\quad - \left({}^{\mathbf{O}_i}V_{\mathrm{r}} - {}^{\mathbf{O}_i}V\right)^{T}{}^{\mathbf{O}_i}\mathbf{U}_{\mathbf{B}_{oi}}\left({}^{\mathbf{B}_{oi}}F_{\mathrm{r}} - {}^{\mathbf{B}_{oi}}F\right) \\ &= \left[{}^{\mathbf{O}_i}\mathbf{U}_{\mathbf{T}_{oi}}^{T}\left({}^{\mathbf{O}_i}V_{\mathrm{r}} - {}^{\mathbf{O}_i}V\right)\right]^{T}\left({}^{\mathbf{T}_{oi}}F_{\mathrm{r}} - {}^{\mathbf{T}_{oi}}F\right) \\ &\quad - \left[{}^{\mathbf{O}_i}\mathbf{U}_{\mathbf{B}_{oi}}^{T}\left({}^{\mathbf{O}_i}V_{\mathrm{r}} - {}^{\mathbf{O}_i}V\right)\right]^{T}\left({}^{\mathbf{B}_{oi}}F_{\mathrm{r}} - {}^{\mathbf{B}_{oi}}F\right) \\ &= p_{\mathbf{T}_{oi}} - p_{\mathbf{B}_{oi}}.\end{aligned} \tag{A.4}$$

Substituting (A.4) into (A.3) yields

$$\dot{\nu}_{oi} = -\left({}^{\mathbf{O}_i}V_{\mathrm{r}} - {}^{\mathbf{O}_i}V\right)^{T}\mathbf{K}_{\mathbf{O}_i}\left({}^{\mathbf{O}_i}V_{\mathrm{r}} - {}^{\mathbf{O}_i}V\right) + p_{\mathbf{T}_{oi}} - p_{\mathbf{B}_{oi}}. \tag{A.5}$$

Consider the fact that the ith *object* has one *driving cutting point* associated with frame $\{\mathbf{B}_{oi}\}$ and one *driven cutting point* associated with frame $\{\mathbf{T}_{oi}\}$. Using Eqs. (113) and (A.5) completes the proof of *virtual stability* of ith *object*, $\forall\, i \in \{0, 3\}$, in the sense of Definition 2. ■

Appendix B. Proof for Theorem 1

Consider the j_rth unactuated revolute *open chain* (see Fig. 9) with $j_r = 2k, \forall\, k \in \{1, 2\}$. If non-negative accompanying function ν_{j_r} is chosen for j_rth *open chain* as proposed in Eqs. (115)–(117), then Eqs. (A.1)–(A.3) can be reused by substituting frames $\{\mathbf{B}_{j_r}\}$ and $\{\mathbf{B}_{j_r1}\}$ for frame $\{\mathbf{O}_i\}$, yielding

$$\dot{\nu}_{\mathbf{B}_{j_r}} = \left({}^{\mathbf{B}_{j_r}}V_{\mathrm{r}} - {}^{\mathbf{B}_{j_r}}V\right)^{T}\left({}^{\mathbf{B}_{j_r}}F_{\mathrm{r}}^{*} - {}^{\mathbf{B}_{j_r}}F^{*}\right) - \left({}^{\mathbf{B}_{j_r}}V_{\mathrm{r}} - {}^{\mathbf{B}_{j_r}}V\right)^{T}\mathbf{K}_{\mathbf{B}_{j_r}}\left({}^{\mathbf{B}_{j_r}}V_{\mathrm{r}} - {}^{\mathbf{B}_{j_r}}V\right) \tag{B.1}$$

$$\begin{aligned}\dot{\nu}_{\mathbf{B}_{j_r1}} &= \left({}^{\mathbf{B}_{j_r1}}V_{\mathrm{r}} - {}^{\mathbf{B}_{j_r1}}V\right)^{T}\left({}^{\mathbf{B}_{j_r1}}F_{\mathrm{r}}^{*} - {}^{\mathbf{B}_{j_r1}}F^{*}\right) \\ &\quad - \left({}^{\mathbf{B}_{j_r1}}V_{\mathrm{r}} - {}^{\mathbf{B}_{j_r1}}V\right)^{T}\mathbf{K}_{\mathbf{B}_{j_r1}}\left({}^{\mathbf{B}_{j_r1}}V_{\mathrm{r}} - {}^{\mathbf{B}_{j_r1}}V\right).\end{aligned} \tag{B.2}$$

Furthermore, it follows from Definition 1, Eqs. (25), (26), (44), (53), (54), (82), (83), (92), (103) and (104), that

$$\begin{aligned}&\left({}^{\mathbf{B}_{j_r}}V_{\mathrm{r}} - {}^{\mathbf{B}_{j_r}}V\right)^{T}\left({}^{\mathbf{B}_{j_r}}F_{\mathrm{r}}^{*} - {}^{\mathbf{B}_{j_r}}F^{*}\right) \\ &= \left({}^{\mathbf{B}_{j_r}}V_{\mathrm{r}} - {}^{\mathbf{B}_{j_r}}V\right)^{T}\left[\left({}^{\mathbf{B}_{j_r}}F_{\mathrm{r}} - {}^{\mathbf{B}_{j_r}}F\right) - {}^{\mathbf{B}_{j_r}}\mathbf{U}_{\mathbf{B}_{j_r1}}\left({}^{\mathbf{B}_{j_r1}}F_{\mathrm{r}} - {}^{\mathbf{B}_{j_r1}}F\right)\right] \\ &= p_{\mathbf{B}_{j_r}} - \left[{}^{\mathbf{B}_{j_r1}}\mathbf{U}_{\mathbf{B}_{j_r}}^{T}\left({}^{\mathbf{B}_{j_r}}V_{\mathrm{r}} - {}^{\mathbf{B}_{j_r}}V\right) + {}^{\mathbf{B}_{j_r1}}\mathbf{U}_{\mathbf{B}_{j_r}}^{T}\mathbf{z}_{\tau}\left(\dot{q}_{j_r\mathrm{r}} - \dot{q}_{j_r}\right)\right]^{T} \\ &\quad \times {}^{\mathbf{B}_{j_r}}\mathbf{U}_{\mathbf{B}_{j_r1}}\left({}^{\mathbf{B}_{j_r1}}F_{\mathrm{r}} - {}^{\mathbf{B}_{j_r1}}F\right) \\ &= p_{\mathbf{B}_{j_r}} - p_{\mathbf{B}_{j_r1}} - \left(\dot{q}_{j_r\mathrm{r}} - \dot{q}_{j_r}\right)\mathbf{z}_{\tau}^{T}\left({}^{\mathbf{B}_{j_r1}}F_{\mathrm{r}} - {}^{\mathbf{B}_{j_r1}}F\right) \\ &= p_{\mathbf{B}_{j_r}} - p_{\mathbf{B}_{j_r1}}\end{aligned} \tag{B.3}$$

$$\begin{aligned}&\left({}^{\mathbf{B}_{j_r1}}V_{\mathrm{r}} - {}^{\mathbf{B}_{j_r1}}V\right)^{T}\left({}^{\mathbf{B}_{j_r1}}F_{\mathrm{r}}^{*} - {}^{\mathbf{B}_{j_r1}}F^{*}\right) \\ &= \left({}^{\mathbf{B}_{j_r1}}V_{\mathrm{r}} - {}^{\mathbf{B}_{j_r1}}V\right)^{T}\left[\left({}^{\mathbf{B}_{j_r1}}F_{\mathrm{r}} - {}^{\mathbf{B}_{j_r1}}F\right) - {}^{\mathbf{B}_{j_r1}}\mathbf{U}_{\mathbf{T}_{j_r}}\left({}^{\mathbf{T}_{j_r}}F_{\mathrm{r}} - {}^{\mathbf{T}_{j_r}}F\right)\right] \\ &= p_{\mathbf{B}_{j_r1}} - \left[{}^{\mathbf{B}_{j_r1}}\mathbf{U}_{\mathbf{T}_{j_r}}^{T}\left({}^{\mathbf{B}_{j_r1}}V_{\mathrm{r}} - {}^{\mathbf{B}_{j_r1}}V\right)\right]^{T} \times \left({}^{\mathbf{T}_{j_r}}F_{\mathrm{r}} - {}^{\mathbf{T}_{j_r}}F\right) \\ &= p_{\mathbf{B}_{j_r1}} - p_{\mathbf{T}_{j_r}}.\end{aligned} \tag{B.4}$$

Substituting Eqs. (B.3) and (B.4) into Eqs. (B.1) and (B.2), respectively, yields

$$\begin{aligned}\dot{\nu}_{j_r} &= \dot{\nu}_{\mathbf{B}_{j_r}} + \dot{\nu}_{\mathbf{B}_{j_r1}} \\ &= -\left({}^{\mathbf{B}_{j_r}}V_{\mathrm{r}} - {}^{\mathbf{B}_{j_r}}V\right)^{T}\mathbf{K}_{\mathbf{B}_{j_r}}\left({}^{\mathbf{B}_{j_r}}V_{\mathrm{r}} - {}^{\mathbf{B}_{j_r}}V\right) \\ &\quad - \left({}^{\mathbf{B}_{j_r1}}V_{\mathrm{r}} - {}^{\mathbf{B}_{j_r1}}V\right)^{T}\mathbf{K}_{\mathbf{B}_{j_r1}}\left({}^{\mathbf{B}_{j_r1}}V_{\mathrm{r}} - {}^{\mathbf{B}_{j_r1}}V\right) + p_{\mathbf{B}_{j_r}} - p_{\mathbf{T}_{j_r}}.\end{aligned} \tag{B.5}$$

Consider the fact that the j_rth *open chain* has one *driving cutting point* associated with frame $\{\mathbf{T}_{j_r}\}$ and one *driven cutting point* associated with frame $\{\mathbf{B}_{j_r}\}$. Using Eqs. (115)–(117) and Eq. (B.5) completes the proof of *virtual stability* of the j_rth unactuated revolute *open chain*, with $j_r = 2k$, $\forall\, k \in \{1, 2\}$, in the sense of Definition 2. ■

Appendix C. Proof for Lemma 1

Consider the j_pth actuated prismatic *open chain* (see Fig. 8) with $j_p = 2k - 1$, $\forall\, k \in \{1, 2\}$. If non-negative accompanying function $\nu_{\mathrm{oc}_{j_p}}$ is chosen for j_pth *open chain* as proposed in Eqs. (119)–(121), then Eqs. (A.1)–(A.3) can be reused by substituting frames $\{\mathbf{B}_{j_p1}\}$ and $\{\mathbf{B}_{j_p2}\}$ for frame $\{\mathbf{O}_i\}$, yielding

$$\begin{aligned}\dot{\nu}_{\mathbf{B}_{j_p1}} = {} & \left({}^{\mathbf{B}_{j_p1}}V_{\mathrm{r}} - {}^{\mathbf{B}_{j_p1}}V\right)^T \left({}^{\mathbf{B}_{j_p1}}F^*_{\mathrm{r}} - {}^{\mathbf{B}_{j_p1}}F^*\right) \\ & - \left({}^{\mathbf{B}_{j_p1}}V_{\mathrm{r}} - {}^{\mathbf{B}_{j_p1}}V\right)^T \mathbf{K}_{\mathbf{B}_{j_p1}} \left({}^{\mathbf{B}_{j_p1}}V_{\mathrm{r}} - {}^{\mathbf{B}_{j_p1}}V\right)\end{aligned} \tag{C.1}$$

$$\begin{aligned}\dot{\nu}_{\mathbf{B}_{j_p2}} = {} & \left({}^{\mathbf{B}_{j_p2}}V_{\mathrm{r}} - {}^{\mathbf{B}_{j_p2}}V\right)^T \left({}^{\mathbf{B}_{j_p2}}F^*_{\mathrm{r}} - {}^{\mathbf{B}_{j_p2}}F^*\right) \\ & - \left({}^{\mathbf{B}_{j_p2}}V_{\mathrm{r}} - {}^{\mathbf{B}_{j_p2}}V\right)^T \mathbf{K}_{\mathbf{B}_{j_p2}} \left({}^{\mathbf{B}_{j_p2}}V_{\mathrm{r}} - {}^{\mathbf{B}_{j_p2}}V\right).\end{aligned} \tag{C.2}$$

Furthermore, it follows from Definition 1, Eqs. (27)–(29), (43), (45), (55), (56), (58), (84)–(86), (91), (93), (105), (106), and 109 that

$$\begin{aligned}& \left({}^{\mathbf{B}_{j_p1}}V_{\mathrm{r}} - {}^{\mathbf{B}_{j_p1}}V\right)^T \left({}^{\mathbf{B}_{j_p1}}F^*_{\mathrm{r}} - {}^{\mathbf{B}_{j_p1}}F^*\right) \\ & = \left({}^{\mathbf{B}_{j_p1}}V_{\mathrm{r}} - {}^{\mathbf{B}_{j_p1}}V\right)^T \left[\left({}^{\mathbf{B}_{j_p1}}F_{\mathrm{r}} - {}^{\mathbf{B}_{j_p}}F\right) \right. \\ & \quad \left. - {}^{\mathbf{B}_{j_p1}}\mathbf{U}_{\mathbf{B}_{j_p2}} \left({}^{\mathbf{B}_{j_p2}}F_{\mathrm{r}} - {}^{\mathbf{B}_{j_p2}}F\right)\right] \\ & = \left[{}^{\mathbf{B}_{j_p}}\mathbf{U}^T_{\mathbf{B}_{j_p1}} \left({}^{\mathbf{B}_{j_p}}V_{\mathrm{r}} - {}^{\mathbf{B}_{j_p}}V\right) - \mathbf{z}_\tau\left(\dot{q}_{j_p1\mathrm{r}} - \dot{q}_{j_p1}\right)\right]^T \\ & \quad \times {}^{\mathbf{B}_{j_p1}}\mathbf{U}_{\mathbf{B}_{j_p}} \left({}^{\mathbf{B}_{j_p}}F_{\mathrm{r}} - {}^{\mathbf{B}_{j_p}}F\right) \\ & \quad - \left[{}^{\mathbf{B}_{j_p2}}\mathbf{U}^T_{\mathbf{B}_{j_p1}} \left({}^{\mathbf{B}_{j_p2}}V_{\mathrm{r}} - {}^{\mathbf{B}_{j_p2}}V\right) \right. \\ & \quad \left. - {}^{\mathbf{B}_{j_p2}}\mathbf{U}^T_{\mathbf{B}_{j_p1}} \mathbf{x}_f\left(\dot{x}_{j_p\mathrm{r}} - \dot{x}_{j_p}\right)\right]^T \\ & \quad \times {}^{\mathbf{B}_{j_p1}}\mathbf{U}_{\mathbf{B}_{j_p2}} \left({}^{\mathbf{B}_{j_p2}}F_{\mathrm{r}} - {}^{\mathbf{B}_{j_p2}}F\right) \\ & = p_{\mathbf{B}_{j_p}} - \left(\dot{q}_{j_p1\mathrm{r}} - \dot{q}_{j_p1}\right)\mathbf{z}^T_\tau \left({}^{\mathbf{B}_{j_p1}}F_{\mathrm{r}} - {}^{\mathbf{B}_{j_p1}}F\right) \\ & \quad - p_{\mathbf{B}_{j_p2}} + \left(\dot{x}_{j_p\mathrm{r}} - \dot{x}_{j_p}\right)\mathbf{x}^T_f \left({}^{\mathbf{B}_{j_p2}}F_{\mathrm{r}} - {}^{\mathbf{B}_{j_p2}}F\right) \\ & = p_{\mathbf{B}_{j_p}} - p_{\mathbf{B}_{j_p2}} + \left(\dot{x}_{j_p\mathrm{r}} - \dot{x}_{j_p}\right)\left(f_{\mathrm{ckr}} - f_{\mathrm{ck}}\right)\end{aligned} \tag{C.3}$$

$$\begin{aligned}& \left({}^{\mathbf{B}_{j_p2}}V_{\mathrm{r}} - {}^{\mathbf{B}_{j_p2}}V\right)^T \left({}^{\mathbf{B}_{j_p2}}F^*_{\mathrm{r}} - {}^{\mathbf{B}_{j_p2}}F^*\right) \\ & = \left({}^{\mathbf{B}_{j_p2}}V_{\mathrm{r}} - {}^{\mathbf{B}_{j_p2}}V\right)^T \left[\left({}^{\mathbf{B}_{j_p2}}F_{\mathrm{r}} - {}^{\mathbf{B}_{j_p2}}F\right) \right. \\ & \quad \left. - {}^{\mathbf{B}_{j_p2}}\mathbf{U}_{\mathbf{I}_{j_p}} \left({}^{\mathbf{T}_{j_p}}F_{\mathrm{r}} - {}^{\mathbf{T}_{j_p}}F\right)\right] \\ & = p_{\mathbf{B}_{j_p2}} - \left[{}^{\mathbf{T}_{j_p}}\mathbf{U}^T_{\mathbf{B}_{j_p2}} \left({}^{\mathbf{T}_{j_p}}V_{\mathrm{r}} - {}^{\mathbf{T}_{j_p}}V\right) \right. \\ & \quad \left. + {}^{\mathbf{T}_{j_p}}\mathbf{U}^T_{\mathbf{B}_{j_p2}} \mathbf{z}_\tau\left(\dot{q}_{j_p2\mathrm{r}} - \dot{q}_{j_p2}\right)\right]^T \\ & \quad \times {}^{\mathbf{B}_{j_p2}}\mathbf{U}^T_{\mathbf{T}_{j_p}} \left({}^{\mathbf{T}_{j_p}}F_{\mathrm{r}} - {}^{\mathbf{T}_{j_p}}F\right) \\ & = p_{\mathbf{B}_{j_p2}} - p_{\mathbf{T}_{j_p}} - \left(\dot{q}_{j_p2\mathrm{r}} - \dot{q}_{j_p2}\right)\mathbf{z}^T_\tau \left({}^{\mathbf{T}_{j_p}}F_{\mathrm{r}} - {}^{\mathbf{T}_{j_p}}F\right) \\ & = p_{\mathbf{B}_{j_p2}} - p_{\mathbf{T}_{j_p}}.\end{aligned} \tag{C.4}$$

Substituting Eqs. (C.3) and (C.4) into Eqs. (C.1) and (C.2), respectively, yields that

$$\begin{aligned}\dot{\nu}_{\mathrm{oc}_{j_p}} = {} & \dot{\nu}_{\mathbf{B}_{j_p1}} + \dot{\nu}_{\mathbf{B}_{j_p2}} \\ = {} & -\left({}^{\mathbf{B}_{j_p1}}V_{\mathrm{r}} - {}^{\mathbf{B}_{j_p1}}V\right)^T \mathbf{K}_{\mathbf{B}_{j_p1}} \left({}^{\mathbf{B}_{j_p1}}V_{\mathrm{r}} - {}^{\mathbf{B}_{j_p1}}V\right) \\ & - \left({}^{\mathbf{B}_{j_p2}}V_{\mathrm{r}} - {}^{\mathbf{B}_{j_p2}}V\right)^T \mathbf{K}_{\mathbf{B}_{j_r1}} \left({}^{\mathbf{B}_{j_p2}}V_{\mathrm{r}} - {}^{\mathbf{B}_{j_p2}}V\right) \\ & + p_{\mathbf{B}_{j_p}} - p_{\mathbf{T}_{j_p}} + \left(\dot{x}_{j_p\mathrm{r}} - \dot{x}_{j_p}\right)\left(f_{\mathrm{ckr}} - f_{\mathrm{ck}}\right)\end{aligned} \tag{C.5}$$

holds with $j_p = 2k - 1$, $\forall\, k \in \{1, 2\}$. ■

Appendix D. Proof for Lemma 2

It follows from Eqs. (67) and (111) that

$$\frac{1}{\beta}\left(\dot{f}_{\mathrm{pkr}} - \dot{f}_{\mathrm{pk}}\right) = \left(u_{\mathrm{fkd}} - u_{\mathrm{fk}}\right) - k_{\mathrm{fk}}\left(f_{\mathrm{pkr}} - f_{\mathrm{pk}}\right) - k_{\mathrm{xk}}\left(\dot{x}_{j_p\mathrm{r}} - \dot{x}_{j_p}\right) \tag{D.1}$$

holds with $j_p = 2k - 1$, $\forall\, k \in \{1, 3\}$.

In addition, term u_{fkd} can be written, in view of Eq. (68) and Assumption 2, as

$$\begin{aligned}u_{\mathrm{fkd}} = {} & \left(\frac{c_{\mathrm{pk1}}\upsilon(p_{\mathrm{s}} - p_{\mathrm{ak}})}{x_{j_p}} + \frac{c_{\mathrm{nk2}}\upsilon(p_{\mathrm{bk}} - p_{\mathrm{r}})}{l_{j_p0} - x_{j_p}}\right) u_k S(u_k) \\ & + \left(\frac{c_{\mathrm{pk2}}\upsilon(p_{\mathrm{s}} - p_{\mathrm{bk}})}{l_{j_p0} - x_{j_p}} + \frac{c_{\mathrm{nk1}}\upsilon(p_{\mathrm{ak}} - p_{\mathrm{r}})}{x_{j_p}}\right) u_k S(-u_k).\end{aligned} \tag{D.2}$$

Now, in view of Eqs. (68) and (D.2), the following relation holds

$$u_{\mathrm{fkd}} - u_{\mathrm{fk}} = 0 \tag{D.3}$$

Then, taking time derivative of Eq. (123) and using Eqs. (59), (68), (110), (D.1), (D.2) and (D.3), yields that

$$\begin{aligned}\dot{\nu}_{\mathrm{dk}} = {} & \left(f_{\mathrm{pkr}} - f_{\mathrm{pk}}\right)\frac{1}{\beta}\left(\dot{f}_{\mathrm{pkr}} - \dot{f}_{\mathrm{pk}}\right) \\ = {} & \left(f_{\mathrm{pkr}} - f_{\mathrm{pk}}\right)\left(u_{\mathrm{fkd}} - u_{\mathrm{fk}}\right) - k_{\mathrm{fk}}\left(f_{\mathrm{pkr}} - f_{\mathrm{pk}}\right)^2 \\ & - k_{\mathrm{xk}}\left(\dot{x}_{j_p\mathrm{r}} - \dot{x}_{j_p}\right)\left(f_{\mathrm{pkr}} - f_{\mathrm{pk}}\right) \\ = {} & -k_{\mathrm{fk}}\left(f_{\mathrm{pkr}} - f_{\mathrm{pk}}\right)^2 - k_{\mathrm{xk}}\left(\dot{x}_{j_p\mathrm{r}} - \dot{x}_{j_p}\right)\left(f_{\mathrm{pkr}} - f_{\mathrm{pk}}\right) \\ = {} & -k_{\mathrm{fk}}\left(f_{\mathrm{pkr}} - f_{\mathrm{pk}}\right)^2 \\ & - k_{\mathrm{xk}}\left(\dot{x}_{j_p\mathrm{r}} - \dot{x}_{j_p}\right)\left(f_{\mathrm{pkr}} - f_{\mathrm{pk}} + f_{\mathrm{fk}} - f_{\mathrm{fk}}\right) \\ = {} & -k_{\mathrm{fk}}\left(f_{\mathrm{pkr}} - f_{\mathrm{pk}}\right)^2 \\ & - k_{\mathrm{xk}}\left(\dot{x}_{j_p\mathrm{r}} - \dot{x}_{j_p}\right)\left(f_{\mathrm{ckr}} - f_{\mathrm{ck}}\right)\end{aligned} \tag{D.4}$$

holds with $j_p = 2k - 1$, $\forall\, k \in \{1, 3\}$. ■

Appendix E. Supplementary data

Supplementary data to this article can be found online at http://dx.doi.org/10.1016/j.autcon.2014.12.014.

References

[1] R. Lovgren, Radical improvements in crane safety, ISO Focus. 1 (7) (2004) 21–93.
[2] J. Watton, Fluid Power Systems: Modelling, Simulation, Analog and Microcomputer Control, Prentice Hall, New York, 1989.
[3] A. Alleyne, R. Liu, On the limitations of force tracking control for hydraulic servosystems, J. Dyn. Syst. Meas. Control. 121 (2) (1999) 184–190.
[4] M. Sirouspour, S. Salcudean, Nonlinear control of hydraulic robots, IEEE Trans. Robot. Autom. 17 (2) (2001) 759–765.
[5] L. Sciavicco, B. Siciliano, Modeling and Control of Robot Manipulators, Springer, London, 2000.
[6] M.M. Bech, T.O. Andersen, H.C. Pedersen, L. Schmidt, Experimental evaluation of control strategies for hydraulic servo robot, Proc. of IEEE Int. Conf. on Mechatronics and Automation (ICMA), IEEE, 2013, pp. 342–347.
[7] O. Egeland, Cartesian control of a hydraulic redundant manipulator, Proc. of IEEE Int. Conf. on Robotics and Automation, IEEE, vol. 4, 1987, pp. 2081–2086.
[8] K. Edge, F.G. de Almeida, Decentralized adaptive control of a directly driven hydraulic manipulator: Parts 1-2, Proc. of the Institution of Mechanical Engineers, Part I, J. Syst. Control. Eng. 209 (3) (1995) 191–196.
[9] F. Conrad, Transputer control of hydraulic actuators and robots, IEEE Trans. Ind. Electron. 43 (1) (1996) 38–47.
[10] S. Habibi, Sliding mode control of a hydraulic industrial robot, J. Dyn. Syst. Meas. Control. 121 (2) (1999) 312–318.
[11] J. Mattila, T. Virvalo, Energy-efficient motion control of a hydraulic manipulator, IEEE Int. Conf. on Robotics and Automation, vol. 3, 2000, pp. 3000–3006.
[12] F. Bu, B. Yao, Observer based coordinated adaptive robust control of robot manipulators driven by single-rod hydraulic actuators, Proc. of IEEE Int. Conf. on Robotics and Automation, vol. 3, 2001, pp. 3034–3039.

[13] F. Bu, B. Yao, Desired compensation adaptive robust control of single-rod electro-hydraulic actuator, Proc. of American Control Conference, vol. 5, 2001, pp. 3926–3931.
[14] O. Becker, I. Pietsch, J. Hesselbach, Robust task-space control of hydraulic robots, Proc. IEEE Int. Conf. on Robotics and Automation, IEEE, vol. 3, 2003, pp. 4360–4365.
[15] W.-H. Zhu, J. Piedboeuf, Adaptive output force tracking control of hydraulic cylinders with applications to robot manipulators, Trans. ASME 127 (2005) 206–217.
[16] H. Zeng, N. Sepehri, Adaptive backstepping control of hydraulic manipulators with friction compensation using lugre model, American Control Conference, IEEE, 2006, pp. 3164–3169.
[17] J. Koivumäki, J. Mattila, The automation of multi degree of freedom hydraulic crane by using virtual decomposition control, IEEE/ASME Int. Conf. on Advanced Intelligent Mechatronics (AIM), 2013, pp. 912–919.
[18] W.-H. Zhu, Virtual Decomposition Control, Springer-Verlag, 2010.
[19] W.-H. Zhu, Y.-G. Xi, Z.-J. Zhang, Z. Bien, J. De Schutter, Virtual decomposition based control for generalized high dimensional robotic systems with complicated structure, IEEE Trans. Robot. Autom. 13 (3) (1997) 411–436.
[20] T. Chan, R. Dubey, A weighted least-norm solution based scheme for avoiding joint limits for redundant joint manipulators, IEEE Trans. Robot. Autom. 11 (2) (1995) 286–292.
[21] L. Beiner, J. Mattila, An improved pseudoinverse solution for redundant hydraulic manipulators, Robotica 17 (2) (1999) 173–179.
[22] J. Koivumäki, J. Honkakorpi, J. Vihonen, J. Mattila, Hydraulic manipulator virtual decomposition control with performance analysis using low-cost mems sensors, Submitted to IEEE/ASME Int. Conf. on Advanced Intelligent Mechatronics, 2014 (to be held in July. 8-11 at Besancon, France).
[23] A. Harrison, D. Stoten, Generalized finite difference method for optimal estimation of derivatives in real-time control problems, proceedings of the institution of mechanical engineers, Proc. of the Inst. of Mech. Eng., vol. 209, 1995, pp. 67–78.
[24] S. Roberts, Control charts based on geometric moving averages, Technometrics 1 (3) (1959) 239–250.
[25] W.-H. Zhu, G. Vukovich, Virtual decomposition control for modular robot manipulators, IFAC World Congress, 2011, pp. 13486–13491.

Publication P.II

Janne Koivumäki and Jouni Mattila, "Stability-Guaranteed Force-Sensorless Contact Force/Motion Control of Heavy-Duty Hydraulic Manipulators", *IEEE Transactions on Robotics*, vol. 31, no. 4, pp. 918 – 935, June 2015.

The original print of this publication is available online (DOI: 10.1109/TRO.2015.2441492)

Stability-Guaranteed Force-Sensorless Contact Force/Motion Control of Heavy-Duty Hydraulic Manipulators

Janne Koivumäki and Jouni Mattila

***Abstract*—In this paper, a force-sensorless, high-performance contact force/motion control approach is proposed for multiple-degree-of-freedom hydraulic manipulators. A rigorous stability proof for an entire hydraulic manipulator performing contact tasks is provided for the first time. The controller design for the manipulator is based on the recently introduced Virtual Decomposition Control (VDC) approach. As a significant novelty, the end-effector contact force is directly estimated from the manipulator's cylinder pressure data, which provides a practical solution for heavy-duty contact force control without engaging fragile force/torque sensors. In the experiments, the proposed controller achieved a force control accuracy of 4.1% at a desired contact force of 8000 N while in motion. This can be considered a significant result due to the hydraulic actuators' highly nonlinear behaviours, the coupled mechanical linkage dynamics and the complex interaction dynamics between the manipulator and the environment.**

***Index Terms*—hydraulic manipulators, contact force/motion control, contact force estimation, virtual decomposition control, nonlinear model-based control, stability analysis**

I. Introduction

HYDRAULIC robot manipulators with higher payload capabilities than their electrical counterparts have been widely used for heavy-duty operations for decades. In fact, the first industrial robot, introduced by George Devol in 1959, was driven by hydraulic actuators. For versatile hydraulic machines (e.g. construction, forestry, mining and agricultural machines), the operator-assisted automation functionalities that improve system operations and safety have not been adopted by the industry yet due to the complexity of their controls and the lack of sound theories. However, justification for having these functions does exist. For example, about 73% of all crane accidents are related to operator errors [1].

The force control of hydraulic systems is challenging [2]. In electric actuators, the relationship between the control input (electric current) and the actuator output (torque) is approximately linear. However, in hydraulic actuators, the relationship between control input (valve voltage/current) and actuator output (torque/force) is complex, dynamic and highly nonlinear since the actuator's (whose dynamical behaviour is nonlinear) output force is controlled indirectly with the control valve (whose dynamical behaviour is nonlinear). As result, the existing control methods, which have been applied successfully to electrically driven manipulators, cannot be applied directly to hydraulically actuated manipulators. In addition, the electrically driven manipulators usually have open-chain structures whereas the hydraulically actuated manipulators often use closed-chain structures to convert the linear motion of the hydraulic cylinders to a rotational motion. While they increase mechanical stiffness, closed-chain structures naturally complicate the kinematics and dynamics of the mechanical linkages in these systems. Treating a closed-chain structure as an open-chain structure (e.g. in [3] and [4]) may raise the question of inaccurate system modeling.

The design challenges mentioned above lead to the utilization of nonlinear model-based control methods to achieve better performance in hydraulic manipulator control. Surprisingly, very few research results exist for advance contact control in hydraulic manipulators compared to their electrical manipulator counterparts, as presented in [5]–[10] (see also historical overviews of the robot force control in [11]–[13]). The majority of available controls for hydraulic manipulators have mainly focused on free-space motion (see [3], [14]–[18]), despite that hydraulic manipulation usually involves mechanical contacts with the objects to be operated and the environment to be interacted.

In robotic contact control, system stability issues have drawn significant attention since the installation of the first industrial robots (Unimate in 1961 and Versatran in 1962). Two major types of instabilities can occur in the contact tasks: dynamic instability (caused by the interaction between the robot dynamics and the environment dynamics) and kinematic instability (caused by the kinematic coordinate transformations in the control implementations) [19]–[22]. In relation to hydraulic actuation, some single-Degree-of-Freedom (DOF) nonlinear stability-guaranteed solutions (see [23], [24]) exist in simplified cases; however, no research data are available on multiple-DOF solutions. Overall, few papers on the contact control of hydraulically actuated multiple-DOF manipulators are available. In [25], a nonlinear proportional-integral (NPI) controller was proposed for the impedance control of hydraulic manipulators, but the stability of the proposed controller designs were not discussed. In addition, Salcudean and Tafazoli studied impedance control of a teleoperated mini-excavator based on a simple proportional-derivative (PD) controller (see [4], [26]–[28]). A stability proof for a simple PD impedance

Manuscript received May 21, 2014; revised January 12, 2015; accepted April 24, 2015.

J. Koivumäki and J. Mattila are with the Department of Intelligent Hydraulics and Automation, Tampere University of Technology, FI-33101, Finland. (e-mails: janne.koivumaki@tut.fi, jouni.mattila@tut.fi)

This work was supported by the Academy of Finland under the project 'Cooperative heavy-duty hydraulic manipulators for sustainable subsea infrastructure installation and dismantling', grant no. 286553.

controller was provided in their work, but it was limited to the single-DOF hydraulic cylinder acting on the environment. In summary, the stability-guaranteed controller design for multiple-DOF hydraulic manipulators faces a formidable challenge even in free motion (see discussion e.g. in [14]) and, furthermore, remains an open problem for high-performance contact force/motion control.

An additional significant challenge in contact control in heavy-duty manipulation is the contact force measurement since force control requires force feedback. The conventional method of performing robot force control requires a six-DOF force/moment sensor, which is placed at the end-effector. Built using either strain-gauge technology or optics, this force sensor is usually sensitive to overloading, which is a situation that frequently occurs in heavy-duty operations. Moreover, in many heavy-duty contact tasks (e.g. excavation and logging) the use of these six-DOF force/moment sensors at the end-effector is not practically possible due to the nature of contact tasks. Thus, it motivates the development of new advanced solutions to eliminate the use of force sensors at the end-effector.

With the recently introduced Virtual Decomposition Control (VDC) approach [29], a number of significant control performance improvements have been reported in the free-space motion of both electrical and hydraulic manipulators (see [17], [18], [30]–[33]) and in the contact control of electrically driven manipulators (see [34], [35]). Based on VDC [29], [35], we intend in this paper to take a major step forward from existing control solutions for hydraulic manipulators by introducing for the first time a high-performance contact force/motion control for hydraulic manipulators by providing a rigorous stability proof for the entire manipulator (not only the actuator) performing contact tasks. In addition, a novel force-sensorless solution to estimate the end-effector contact force is proposed in this paper. The main contributions of this paper can be summarized as: 1) the stability of the entire hydraulic manipulator performing contact tasks is proved for the first time, 2) a force-sensorless contact force estimation method is proposed, and 3) superior contact force/motion control results are obtained for the highly nonlinear hydraulic manipulator interacting with the environment.

This paper is organized as follows. In Section II, the essential mathematical foundations are introduced. A solution for the force-sensorless contact force estimate for hydraulic manipulators is discussed in Section III. The VDC approach is introduced in Section IV and the proposed controller design is given, leading to the *virtual stability* for the studied subsystems. In Section V, the stability of the entire system is provided. In Section VI, experimental results for the contact force/motion-controlled hydraulic manipulator are given. Finally, conclusions are outlined in Section VII.

II. Mathematical Foundation

A. Dynamics of Rigid Body

Consider an orthogonal, three-dimensional coordinate system $\{\mathbf{A}\}$ (called frame $\{\mathbf{A}\}$ for simplicity) attached to the rigid body. Let ${}^{\mathbf{A}}\mathbf{v} \in \mathbb{R}^3$ and ${}^{\mathbf{A}}\boldsymbol{\omega} \in \mathbb{R}^3$ be the linear and angular velocity vectors of frame $\{\mathbf{A}\}$, expressed in frame $\{\mathbf{A}\}$. To facilitate the transformations of velocities among different frames, the linear/angular velocity vector of frame $\{\mathbf{A}\}$ can be written, in view of [29], as

$$ {}^{\mathbf{A}}V \stackrel{\text{def}}{=} \begin{bmatrix} {}^{\mathbf{A}}\mathbf{v} \\ {}^{\mathbf{A}}\boldsymbol{\omega} \end{bmatrix} \in \mathbb{R}^6. \tag{1} $$

Let ${}^{\mathbf{A}}\mathbf{f} \in \mathbb{R}^3$ and ${}^{\mathbf{A}}\mathbf{m} \in \mathbb{R}^3$ be the force and moment vectors applied to the origin of frame $\{\mathbf{A}\}$, expressed in frame $\{\mathbf{A}\}$. Similar to (1), the force/moment vector in frame $\{\mathbf{A}\}$ can be written, in view of [29], as

$$ {}^{\mathbf{A}}F \stackrel{\text{def}}{=} \begin{bmatrix} {}^{\mathbf{A}}\mathbf{f} \\ {}^{\mathbf{A}}\mathbf{m} \end{bmatrix} \in \mathbb{R}^6. \tag{2} $$

Now, consider two given frames, denoted as $\{\mathbf{A}\}$ and $\{\mathbf{B}\}$, fixed to a common rigid body. As stated in [29], the following relations hold:

$$ {}^{\mathbf{B}}V = {}^{\mathbf{A}}\mathbf{U}_{\mathbf{B}}^{T}\,{}^{\mathbf{A}}V \tag{3} $$

$$ {}^{\mathbf{A}}F = {}^{\mathbf{A}}\mathbf{U}_{\mathbf{B}}\,{}^{\mathbf{B}}F \tag{4} $$

where ${}^{\mathbf{A}}\mathbf{U}_{\mathbf{B}} \in \mathbb{R}^{6\times 6}$ denotes a force/moment transformation matrix that transforms the force/moment vector measured and expressed in frame $\{\mathbf{B}\}$ to the same force/moment vector measured and expressed in frame $\{\mathbf{A}\}$.

Let frame $\{\mathbf{A}\}$ be fixed to a rigid body. The dynamic equation of the rigid body, expressed in frame $\{\mathbf{A}\}$, can be written as

$$ \mathbf{M}_{\mathbf{A}}\frac{d}{dt}({}^{\mathbf{A}}V) + \mathbf{C}_{\mathbf{A}}({}^{\mathbf{A}}\boldsymbol{\omega})\,{}^{\mathbf{A}}V + \mathbf{G}_{\mathbf{A}} = {}^{\mathbf{A}}F^{*} \tag{5} $$

where ${}^{\mathbf{A}}F^{*} \in \mathbb{R}^6$ is the net force/moment vector of the rigid body expressed in frame $\{\mathbf{A}\}$, $\mathbf{M}_{\mathbf{A}} \in \mathbb{R}^{6\times 6}$ denotes the mass matrix, $\mathbf{C}_{\mathbf{A}}({}^{\mathbf{A}}\boldsymbol{\omega}) \in \mathbb{R}^{6\times 6}$ denotes the matrix of Coriolis and centrifugal terms and $\mathbf{G}_{\mathbf{A}} \in \mathbb{R}^6$ denotes the gravity terms. The detailed expressions can be found in [29].

Now, let ${}^{\mathbf{A}}V_{\mathrm{r}} \in \mathbb{R}^6$ be the required vector (a design vector to be specified later) of ${}^{\mathbf{A}}V \in \mathbb{R}^6$. In view of [29], the linear parameterization expression for the required rigid body dynamics can be written as

$$ \mathbf{Y}_{\mathbf{A}}\boldsymbol{\theta}_{\mathbf{A}} \stackrel{\text{def}}{=} \mathbf{M}_{\mathbf{A}}\frac{d}{dt}({}^{\mathbf{A}}V_{\mathrm{r}}) + \mathbf{C}_{\mathbf{A}}({}^{\mathbf{A}}\boldsymbol{\omega})\,{}^{\mathbf{A}}V_{\mathrm{r}} + \mathbf{G}_{\mathbf{A}}. \tag{6} $$

The detailed expressions of the regressor matrix $\mathbf{Y}_{\mathbf{A}} \in \mathbb{R}^{6\times 13}$ and the parameter vector $\boldsymbol{\theta}_{\mathbf{A}} \in \mathbb{R}^{13}$ are given in [29].

Finally, based on (6), the required net force/moment vector ${}^{\mathbf{A}}F^{*}_{\mathrm{r}} \in \mathbb{R}^6$ for the same rigid body can be specified as

$$ {}^{\mathbf{A}}F^{*}_{\mathrm{r}} = \mathbf{Y}_{\mathbf{A}}\hat{\boldsymbol{\theta}}_{\mathbf{A}} + \mathbf{K}_{\mathbf{A}}({}^{\mathbf{A}}V_{\mathrm{r}} - {}^{\mathbf{A}}V) \tag{7} $$

where $\mathbf{K}_{\mathbf{A}} \in \mathbb{R}^{6\times 6}$ denotes a positive-definite gain matrix characterizing the velocity feedback control for the rigid link and $\mathbf{Y}_{\mathbf{A}}\hat{\boldsymbol{\theta}}_{\mathbf{A}}$ denotes the model-based feedforward compensation term by using the required velocities, their time derivatives and the estimated parameters. As (7) implies, one innovation of the VDC approach is that it enables the parameter adaptation for the individual rigid body parameters. This has not been possible with the conventional control approaches, which have based on the complete dynamic models of robots.

B. Parameter Adaptation

The following projection function from [29] is used for parameter adaptation:

Definition 1: A projection function $\mathscr{P}(s(t),k,a(t),b(t),t) \in \mathbb{R}$ is a differentiable scalar function defined for $t \geqslant 0$ such that its time derivative is governed by

$$\dot{\mathscr{P}} = ks(t)\kappa \tag{8}$$

with

$$\kappa = \begin{cases} 0, & \text{if } \mathscr{P} \leqslant a(t) \text{ and } s(t) \leqslant 0 \\ 0, & \text{if } \mathscr{P} \geqslant b(t) \text{ and } s(t) \geqslant 0 \\ 1, & \text{otherwise} \end{cases}$$

where $s(t) \in \mathbb{R}$ is a scalar variable, $k > 0$ is a constant and $a(t) \leqslant b(t)$ holds.

The projection function defined in (8) has the following property: For any constant $\mathscr{P}_c$ subject to $a(t) \leqslant \mathscr{P}_c \leqslant b(t)$, it follows that

$$(\mathscr{P}_c - \mathscr{P})\left(s(t) - \frac{1}{k}\dot{\mathscr{P}}\right) \leqslant 0. \tag{9}$$

C. Virtual Cutting Points and a Simple Oriented Graph

In the VDC approach, the original system is virtually decomposed into the subsystems by placing conceptual *virtual cutting points* (VCP). A *cutting point* forms a virtual cutting surface on which three-dimensional force vectors and three-dimensional moment vectors can be exerted from one part to another. In [29], the virtual cutting point is defined as shown in Definition 2.

Definition 2: A cutting point is a directed separation interface that conceptually cuts through a rigid body. At the cutting point, two parts resulting from the virtual cut maintain equal positions and orientations. The cutting point is interpreted as a *driving cutting point* by one part and is simultaneously interpreted as a *driven cutting point* by another part. A force vector $\mathbf{f} \in \mathbb{R}^3$ and a moment vector $\mathbf{m} \in \mathbb{R}^3$ are exerted from one part to which the cutting point is interpreted as a *driving cutting point* to the other part to which the cutting point is interpreted as a *driven cutting point*.

After the original system is virtually decomposed into subsystems by placing VCPs, the system can be represented by a simple oriented graph. A simple oriented graph is defined in [29], as shown in Definition 3.

Definition 3: A graph consists of nodes and edges. A directed graph is a graph in which all edges have directions. An oriented graph is a directed graph in which each edge has a unique direction. A simple oriented graph is an oriented graph in which no loop is formed.

D. Virtual Stability

The unique feature of the VDC approach is the introduction of a scalar term, namely the *virtual power flow* [29]; see Definition 4. The *virtual power flows* uniquely define the dynamic interactions among the subsystems and play an important role in the definition of *virtual stability* [29], which is defined in a simplified form in Definition 5.

Definition 4: The *virtual power flow* with respect to frame $\{\mathbf{A}\}$ can be defined as the inner product of the linear/angular velocity vector error and the force/moment vector error as

$$p_{\mathbf{A}} = ({}^{\mathbf{A}}V_{\mathrm{r}} - {}^{\mathbf{A}}V)^T({}^{\mathbf{A}}F_{\mathrm{r}} - {}^{\mathbf{A}}F) \tag{10}$$

where ${}^{\mathbf{A}}V_{\mathrm{r}} \in \mathbb{R}^6$ and ${}^{\mathbf{A}}F_{\mathrm{r}} \in \mathbb{R}^6$ represent the required vectors of ${}^{\mathbf{A}}V \in \mathbb{R}^6$ and ${}^{\mathbf{A}}F \in \mathbb{R}^6$, respectively.

Definition 5: A subsystem with a *driven* VCP to which frame $\{\mathbf{A}\}$ is attached and a *driving* VCP to which frame $\{\mathbf{C}\}$ is attached is said to be *virtually stable* with its affiliated vector $\mathbf{x}(t)$ being a virtual function in L_∞ and its affiliated vector $\mathbf{y}(t)$ being a virtual function in L_2, if and only if there exists a non-negative accompanying function

$$v(t) \geqslant \frac{1}{2}\mathbf{x}(t)^T\mathbf{P}\mathbf{x}(t) \tag{11}$$

such that

$$\dot{v}(t) \leqslant -\mathbf{y}(t)^T\mathbf{Q}\mathbf{y}(t) - s(t) + p_{\mathbf{A}} - p_{\mathbf{C}} \tag{12}$$

holds, subject to

$$\int_0^\infty s(t)d\tau \geqslant -\gamma_s \tag{13}$$

with $0 \leqslant \gamma_s < \infty$, where $\mathbf{P}$ and $\mathbf{Q}$ are two block-diagonal positive-definite matrices and $p_{\mathbf{A}}$ and $p_{\mathbf{C}}$ denote the *virtual power flows* (by Definition 4) at frames $\{\mathbf{A}\}$ and $\{\mathbf{C}\}$, respectively.

III. Force-sensorless Contact Force Estimation

Force control requires force feedback. When a force sensor at the end-effector is eliminated, an alternative method of measuring the contact force must be provided using either hydraulic cylinder pressure sensors or cylinder rod loadcells. Unlike conventional force sensors that measure the exact six-dimensional contact forces and moments at the end-effector, the sum of the true contact forces (and moments) and the manipulator motion forces (and moments) governed by the manipulator inverse dynamics are measured by the cylinder pressure sensors. Now, consider a manipulator actuated with k hydraulic cylinders. The typical dynamics of this k-DOF manipulator can be expressed in the actuator space as

$$\mathbf{M}(\boldsymbol{x}_{\mathrm{c}})\ddot{\boldsymbol{x}}_{\mathrm{c}} + \mathbf{C}(\boldsymbol{x}_{\mathrm{c}},\dot{\boldsymbol{x}}_{\mathrm{c}})\dot{\boldsymbol{x}}_{\mathrm{c}} + \mathbf{G}(\boldsymbol{x}_{\mathrm{c}}) = \boldsymbol{f}_{\mathrm{c}} - \mathbf{J}_{\mathrm{x}}^{\mathrm{TC}}\boldsymbol{f}_{\mathrm{ee}} \tag{14}$$

where $\boldsymbol{x}_{\mathrm{c}} \in \mathbb{R}^k$ is the actuator's displacement vector, $\boldsymbol{f}_{\mathrm{c}} \in \mathbb{R}^k$ is the actuator's force vector, $\mathbf{J}_{\mathrm{x}} \in \mathbb{R}^{k\times k}$ is a Jacobian matrix mapping $\dot{\boldsymbol{x}}_{\mathrm{c}} \in \mathbb{R}^k$ to the velocity in Cartesian space where the contact happens and ${}^{\mathbf{C}}\boldsymbol{f}_{\mathrm{ee}} \in \mathbb{R}^k$ is the end-effector force vector expressed in the manipulator's Cartesian space coordinates. Note that in the conventional robot force control approaches, ${}^{\mathbf{C}}\boldsymbol{f}_{\mathrm{ee}}$ is measured using a force sensor placed at the end-effector.

Using digitalized position measurements to estimate acceleration is difficult and sometimes impractical. Thus, if only the angular encoders are available, the contact force can be estimated from (14) using the cylinder pressures[1] and removing the gravitational forces as

$${}^{\mathbf{C}}\hat{\boldsymbol{f}}_{\mathrm{ee}} = \mathbf{J}_{\mathrm{x}}^{-\mathrm{T}}[\boldsymbol{f}_{\mathrm{c}} - \mathbf{G}(\boldsymbol{x}_{\mathrm{c}})]. \tag{15}$$

[1]The actuator's pressure-induced force components in $\boldsymbol{f}_{\mathrm{c}}$ can be obtained later using (71) and (78).

An accurate estimation of $\mathbf{G}(\boldsymbol{x}_c)$ requires an accurate model of the system. The VDC approach, which is discussed in more detail in the next section, provides an efficient framework for this meaning. Each rigid link uses only the gravitation term in (5), i.e. ${}^{\mathbf{A}}F^* = \mathbf{G}_{\mathbf{A}}$. Then, similar to Sections IV-B2 and IV-C2 (more specifically (20), (21) with $\delta_f = 0$, (58)–(60) and (62)–(70)), the system gravity terms in the actuator space can be obtained, link by link, by propagating along the opposite direction of the simple oriented graph (see Fig. 3), beginning with the end-effector (from frame $\{\mathbf{G}\}$ in Fig. 2) and moving towards the system base (to frame $\{\mathbf{B}\}$ in Fig. 2).

Note that the scheme proposed in (15) works only in slow motions with negligible accelerations and velocities. In addition, if cylinder pressure sensors are used instead of cylinder rod loadcell sensors, the piston friction, which amounts to about 1∼2 kN, then comes into play. Fortunately, due to the heavy-duty hydraulic manipulator's special geometry, the piston's friction forces reflected in the end-effector are scaled down by an order of magnitude (10 times, for example) that depends on the manipulator's configurations. Therefore, if force control accuracy within 200 N is considered acceptable, there is no need to implement loadcell sensors. These sensors are necessary only when higher force control precision is required.

IV. Virtual Decomposition Control of the Manipulator

The VDC approach (see [29], [36]) has been developed especially for controlling complex robotic systems. The essence of this method is that the controller uses the dynamics of the subsystems (rigid links and joints) rather than the dynamics of the entire system. Thus, in the VDC approach, the control problem of a complex robotic system can be converted into a control problem of individual subsystems, which means that no matter how complicated the initial system is, the dynamics of the subsystems remain relatively simple with fixed dynamic structures invariant to target systems [29].

Due to the VDC's novel subsystem-dynamics-based control design, the control computations are proportional to the number of subsystems and can be performed even by locally embedded hardware/software [29], [33]. In contrast, with the conventional robotic control methods, where the controller design is based on the complete dynamic models of the robot, the complexity (computational burden) of robot dynamics is proportional to the fourth power of the number of DOFs of motion. Thus, with the conventional control methods, it is very difficult, if not impossible, to implement the control for a very complex systems (such as a humanoid robot) on a single computer [29].

One of the additional advantages of the VDC approach is that the change of the dynamics of a subsystem (e.g. substituting a hydraulic actuator for an electric motor) only affects the respective local control equations associated with this subsystem while keeping the control equations associated with the rest of the system unchanged [29]. In addition, as demonstrated in [18], more subsystems (actuators) can also be added into the original system without control performance deterioration while keeping the control equations of the original subsystems unchanged.

The first step in the VDC approach is to virtually decompose an original system into subsystems (i.e. *objects* and *open chains*) by placing conceptual VCPs (see Definition 2). Then, the decomposed subsystems are represented by a simple oriented graph imposing dynamic interactions among subsystems. The system's virtual decomposition and the simple oriented graph presentation are addressed in Section IV-A.

Then, the subsystems dynamic-based control is designed to make each subsystem qualified to be *virtually stable*. The virtue of the VDC is that, when all subsystems are virtually stable, the stability of the entire system is guaranteed. This is addressed in Section V.

A. Virtual Decomposition and Simple Oriented Graph

The two-DOF heavy-duty hydraulic manipulator studied here is shown in Fig. 1. As this figure illustrates, the manipulator is actuated by two hydraulic cylinders. Thus, two *closed-chain* structures exist in the system. The *closed chains* are emphasized with red triangles in Fig. 1. Though a two-DOF system is studied, the approach developed in this paper is extendable for systems with any number of actuators.

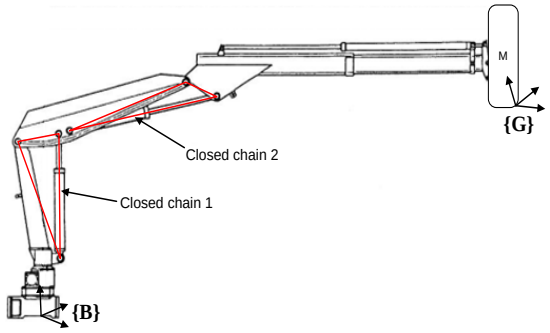

Fig. 1. The studied system, i.e. a two-DOF hydraulic manipulator.

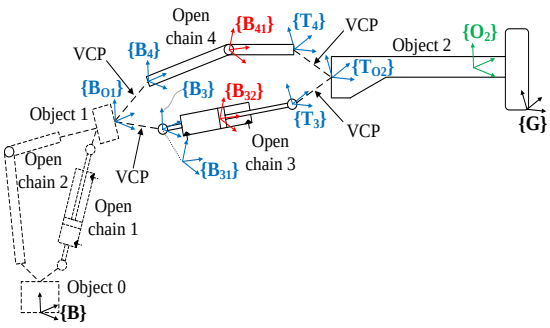

Fig. 2. Virtual decomposition of the studied system.

The virtually decomposed manipulator is given in Fig. 2. In this paper, the *object* 2 (interacting with the environment) and its adjoining *closed chain* 2, including actuated prismatic *open chain* 3 and unactuated revolute *open chain* 4, are studied in detail. The remaining subsystems (given at the dashed line in Fig. 2), which are treated here as a single subsystem, can be further decomposed with the similar approach presented.

In this paper, blue frames denote frames attached at the system VCPs, red frames denote frames attached at the *subsidiary* VCPs of the *open chains*, the green frame denotes the body-fixed frame attached at the center of mass of *object* 2 and black frames $\{\mathbf{B}\}$ and $\{\mathbf{G}\}$ denote the fixed system base and end-effector frames, respectively (see Fig. 2).

At the *driven* VCP of *closed chain* 2, frame $\{\mathbf{B}_{\mathrm{O1}}\}$ is fixed to the controlling point of the rest subsystem and is simultaneously fixed to link 4 of *open chain* 4 (see Fig. 6). In addition, the following relations hold:

$$\{\mathbf{B}_{\mathrm{O1}}\} = \{\mathbf{B}_3\} = \{\mathbf{B}_4\} \tag{16}$$

where $\{\mathbf{B}_3\}$ and $\{\mathbf{B}_4\}$ denote the frames at the *driven* VCPs of *open chain* 3 and *open chain* 4, respectively. Note that to express the dynamics of rigid links (see (5)) in *open chains*, the rigid link fixed frames must be attached. Thus, in *open chain* 3, frame $\{\mathbf{B}_{31}\}$ is attached and fixed to link 31 (see Fig. 5) for this purpose.

At the *subsidiary* VCPs of *open chain* 3 and *open chain* 4, frames $\{\mathbf{B}_{32}\}$ and $\{\mathbf{B}_{41}\}$ are fixed to link 32 and link 41, respectively (see Figs. 5 and 6).

At the *driving* VCP of *closed chain* 2, the frame $\{\mathbf{T}_{\mathrm{O2}}\}$ is fixed to the controlled point of *object* 2 (see Fig. 4) and is simultaneously fixed to link 41 of *open chain* 4 (see Fig. 6). In addition, the following relations hold:

$$\{\mathbf{T}_{\mathrm{O2}}\} = \{\mathbf{T}_3\} = \{\mathbf{T}_4\} \tag{17}$$

where $\{\mathbf{T}_3\}$ and $\{\mathbf{T}_4\}$ denote the frames at the *driving* VCPs of *open chain* 3 and *open chain* 4, respectively.

The simple oriented graph for the manipulator is given in Fig. 3. In this paper, the subsystems inside the dashed line in Fig. 3 are considered one subsystem (see the corresponding lines in Fig. 2). Each subsystem corresponds to a node, and each VCP corresponds to a directed edge whose direction defines the force reference direction. Thus, a VCP is simultaneously interpreted as a *driving* VCP by one subsystem (from which the force/moment vector is exerted or the directed edge is pointing away) and as a *driven* VCP by another subsystem (to which the force/moment vector is exerted or the directed edge points) [29].

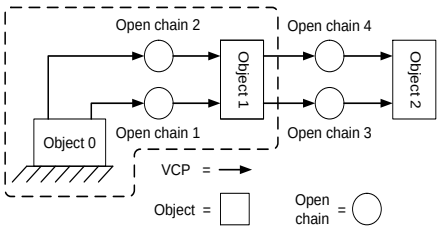

Fig. 3. A simple oriented graph of the studied system.

B. Object 2 – Kinematics, Dynamics, Control and Virtual Stability

In Sections IV-B1 and IV-B2, the kinematics and dynamics of *object* 2 are given. Then, the control of *object* 2 and contact force/motion control are specified in Sections IV-B3 and IV-B4, respectively. Finally, the *virtual stability* of *object* 2 is proven in Section IV-B5.

1) Kinematics of Object 2: *Object* 2, a decomposed subsystem of the manipulator, is shown in Fig. 4. Four frames are

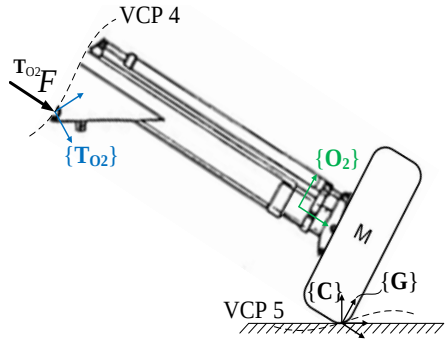

Fig. 4. *Object* 2 in the constrained motion.

attached in *object* 2. Frame $\{\mathbf{T}_{\mathrm{O2}}\}$ exists at the *driven* VCP of *object* 2, frame $\{\mathbf{O}_2\}$ is fixed to the center of mass, and two frames, namely $\{\mathbf{G}\}$ and $\{\mathbf{C}\}$, are attached at the contact point. As Fig. 4 shows, a unilateral constraint applies at the contact point with the environment. Frame $\{\mathbf{G}\}$ represents a manipulator's end-effector frame. Frame $\{\mathbf{C}\}$ is a target frame for the hybrid motion/force control. This frame has the same origin as frame $\{\mathbf{G}\}$, but it is aligned in relation to the system base frame $\{\mathbf{B}\}$ (see Fig. 2). In hybrid motion/force control, the desired end-effector velocity is described in relation to the X-axis of $\{\mathbf{C}\}$, whereas the desired contact force is described in relation to the Y-axis.

The linear/angular velocity vector ${}^{\mathbf{G}}V \in \mathbb{R}^6$ in frame $\{\mathbf{G}\}$ can be written as

$${}^{\mathbf{G}}V = \mathrm{diag}({}^{\mathbf{G}}\mathbf{R}_{\mathbf{C}}, {}^{\mathbf{G}}\mathbf{R}_{\mathbf{C}})\mathbf{N}_{\mathrm{s}}\dot{\chi} \tag{18}$$

where ${}^{\mathbf{G}}\mathbf{R}_{\mathbf{C}} \in \mathbb{R}^{3\times 3}$ denotes a rotation (directed cosine) matrix connecting frame $\{\mathbf{C}\}$ with frame $\{\mathbf{G}\}$, $\mathbf{N}_{\mathrm{s}} = [1\ 0\ 0\ 0\ 0\ 0]^T$, and $\dot{\chi} \in \mathbb{R}$ denotes the independent velocity coordinate, which is expressed along the X-axis of frame $\{\mathbf{C}\}$.

The following relations hold for *object* 2:

$$\begin{aligned} {}^{\mathbf{O}_2}V &= {}^{\mathbf{G}}\mathbf{U}_{\mathbf{O}_2}^T\, {}^{\mathbf{G}}V \\ &= {}^{\mathbf{T}_{\mathrm{O2}}}\mathbf{U}_{\mathbf{O}_2}^T\, {}^{\mathbf{T}_{\mathrm{O2}}}V. \end{aligned} \tag{19}$$

2) Dynamics of Object 2: The net force/moment vector ${}^{\mathbf{O}_2}F^* \in \mathbb{R}^6$ of *object* 2 can be expressed in view of (5) as

$$\mathbf{M}_{\mathbf{O}_2}\frac{d}{dt}({}^{\mathbf{O}_2}V) + \mathbf{C}_{\mathbf{O}_2}({}^{\mathbf{O}_2}\omega)\,{}^{\mathbf{O}_2}V + \mathbf{G}_{\mathbf{O}_2} = {}^{\mathbf{O}_2}F^*. \tag{20}$$

On the other hand, the net force/moment vector (i.e. force resultant equation) for *object* 2 can be written as

$${}^{\mathbf{O}_2}F^* = {}^{\mathbf{O}_2}\mathbf{U}_{\mathbf{T}_{\mathrm{o2}}}\, {}^{\mathbf{T}_{\mathrm{o2}}}F - \delta_{\mathrm{f}}\, {}^{\mathbf{O}_2}\mathbf{U}_{\mathbf{G}}\, {}^{\mathbf{G}}F \tag{21}$$

where

$$\delta_{\mathrm{f}} = \begin{cases} 0 & \text{approach motion} \\ 1 & \text{constrained motion.} \end{cases} \tag{22}$$

Referring back to Fig. 4, the end-effector contact force/moment vector ${}^{\mathbf{C}}F \in \mathbb{R}^6$, expressed in the contact motion/force constraint frame $\{\mathbf{C}\}$, can be written as

$${}^{\mathbf{C}}F = \mathbf{N}_{\mathrm{c}}\, {}^{\mathbf{C}}f_{\mathrm{ee}} \tag{23}$$

with

$$\mathbf{N}_{\mathrm{c}} = \begin{bmatrix} 1 & 0 & 0 & 0 & 0 & 0 \\ 0 & 1 & 0 & 0 & 0 & 0 \end{bmatrix}^T,$$

and ${}^{\mathbf{C}}f_{\mathrm{ee}} \in \mathbb{R}^2$ is a contact force vector at the end-effector. A methodology to estimate ${}^{\mathbf{C}}f_{\mathrm{ee}}$ without using conventional six-DOF force/moment sensors is discussed in Section III.

The contact force/moment vector ${}^{\mathbf{C}}F$ can be mapped into the motion space as $\psi \in \mathbb{R}$ and also into the constraint force space as $\varphi \in \mathbb{R}$. It follows that

$$\psi = \mathbf{N}_{\mathrm{s}}^T {}^{\mathbf{C}}F \tag{24}$$

$$\varphi = \mathbf{N}_{\mathrm{f}}^T {}^{\mathbf{C}}F \tag{25}$$

where $\mathbf{N}_{\mathrm{f}} = [0\ 1\ 0\ 0\ 0\ 0]^T$, subject to $\mathbf{N}_{\mathrm{s}}^T \mathbf{N}_{\mathrm{f}} = 0$.

Now, the contact force/moment vector ${}^{\mathbf{C}}F$ can be expressed in frame $\{\mathbf{G}\}$ as

$${}^{\mathbf{G}}F = \mathrm{diag}({}^{\mathbf{G}}\mathbf{R}_{\mathbf{C}}, {}^{\mathbf{G}}\mathbf{R}_{\mathbf{C}})(\mathbf{N}_{\mathrm{s}}\psi + \mathbf{N}_{\mathrm{f}}\varphi). \tag{26}$$

Then, let ψ be expressed in a linear parametrization form as

$$\psi = \mathrm{Y}_{\mathrm{s}}\theta_{\mathrm{s}} \tag{27}$$

where, according to (24), $\mathrm{Y}_{\mathrm{s}} = \psi$ and $\theta_{\mathrm{s}} = 1$.

3) Control of Object 2: This section addresses the VDC-based rigid body control of *object* 2.

In view of (19), the required velocity transformations in *object* 2 can be written as

$$\begin{aligned} {}^{\mathbf{O}_2}V_{\mathrm{r}} &= {}^{\mathbf{G}}\mathbf{U}_{\mathbf{O}_2}^T {}^{\mathbf{G}}V_{\mathrm{r}} \\ &= {}^{\mathbf{T}_{\mathrm{O2}}}\mathbf{U}_{\mathbf{O}_2}^T {}^{\mathbf{T}_{\mathrm{O2}}}V_{\mathrm{r}}. \end{aligned} \tag{28}$$

Then, in view of (7), the required net force/moment vector for *object* 2 can be written as

$${}^{\mathbf{O}_2}F_{\mathrm{r}}^* = \mathbf{Y}_{\mathbf{O}_2}\hat{\boldsymbol{\theta}}_{\mathbf{O}_2} + \mathbf{K}_{\mathbf{O}_2}({}^{\mathbf{O}_2}V_{\mathrm{r}} - {}^{\mathbf{O}_2}V). \tag{29}$$

With respect to (29), define

$$\mathbf{s}_{\mathbf{O}_2} = \mathbf{Y}_{\mathbf{O}_2}^T({}^{\mathbf{O}_2}V_{\mathrm{r}} - {}^{\mathbf{O}_2}V). \tag{30}$$

Then, (8) can be used to update the ith element of $\hat{\boldsymbol{\theta}}_{\mathbf{O}_2}$ as

$$\hat{\theta}_{\mathbf{O}_2 i} = \mathscr{P}(\mathrm{s}_{\mathbf{O}_2 i}, \rho_{\mathbf{O}_2 i}, \underline{\theta}_{\mathbf{O}_2 i}, \overline{\theta}_{\mathbf{O}_2 i}, t), \forall i \in \{1, 2, ..., 13\} \tag{31}$$

where $\hat{\theta}_{\mathbf{O}_2 i}$ denotes the ith element of $\hat{\boldsymbol{\theta}}_{\mathbf{O}_2}$, $\mathrm{s}_{\mathbf{O}_2 i}$ denotes the ith element of $\mathbf{s}_{\mathbf{O}_2}$, $\rho_{\mathbf{O}_2 i} > 0$ is the update gain, $\underline{\theta}_{\mathbf{O}_2 i}$ denotes the lower bound of $\theta_{\mathbf{O}_2 i}$ and $\overline{\theta}_{\mathbf{O}_2 i}$ denotes the upper bound of $\theta_{\mathbf{O}_2 i}$.

In relation to (21), the required force resultant equation can be written as

$${}^{\mathbf{O}_2}F_{\mathrm{r}}^* = {}^{\mathbf{O}_2}\mathbf{U}_{\mathbf{T}_{\mathrm{O2}}} {}^{\mathbf{T}_{\mathrm{O2}}}F_{\mathrm{r}} - \delta_{\mathrm{f}} {}^{\mathbf{O}_2}\mathbf{U}_{\mathbf{G}} {}^{\mathbf{G}}F_{\mathrm{r}}. \tag{32}$$

4) Contact Force/Motion Control: This section addresses the end-effector force control without using additional flexible mechanisms at the end-effector. The proposed hybrid motion/force control allows the manipulator to achieve the asymptotic stability of both motion control and force control for known contact geometry while retaining the properties of the impedance control for unknown contact geometry [35].

In the VDC approach, a control objective is to make the controlled actual velocities track the required velocities. Note that a required velocity differs from a desired velocity by including one or more terms related to control errors. In this study, the system motion control is described along the X-axis of the motion/force control frame $\{\mathbf{C}\}$. Thus, the required constraint velocity $\dot{\chi}_{\mathrm{r}} \in \mathbb{R}$ with embedded position feedback can be written as

$$\dot{\chi}_{\mathrm{r}} = \dot{\chi}_{\mathrm{d}} + \lambda_{\chi}(\chi_{\mathrm{d}} - \chi) \tag{33}$$

where $\dot{\chi}_{\mathrm{d}} \in \mathbb{R}$ denotes the desired independent velocity coordinate of the constrained robot manipulator, and $\lambda_{\chi} > 0$ is the position feedback gain. It can be seen from (33) that direct motion control along the Y-axis of $\{\mathbf{C}\}$ is not specified in the contact. This is addressed in the following equation.

Let $\varphi_{\mathrm{d}} \in \mathbb{R}$ be the desired vector of φ. In view of [35], the required linear/angular velocity vector of frame $\{\mathbf{G}\}$ can be written as

$${}^{\mathbf{G}}V_{\mathrm{r}} = \mathrm{diag}({}^{\mathbf{G}}\mathbf{R}_{\mathbf{C}}, {}^{\mathbf{G}}\mathbf{R}_{\mathbf{C}})\left[\mathbf{N}_{\mathrm{s}}\dot{\chi}_{\mathrm{r}} + \mathbf{N}_{\mathrm{f}} a_{\mathrm{f}}(\tilde{\varphi}_{\mathrm{d}} - \tilde{\varphi})\right] \tag{34}$$

where $a_{\mathrm{f}} > 0$ is a force feedback gain, $\mathbf{N}_{\mathrm{f}} a_{\mathrm{f}}(\tilde{\varphi}_{\mathrm{d}} - \tilde{\varphi})$ specifies the contact force error along the Y-axis of $\{\mathbf{C}\}$ and $\tilde{\varphi}_{\mathrm{d}} \in \mathbb{R}$ and $\tilde{\varphi} \in \mathbb{R}$ are subject to

$$\dot{\tilde{\varphi}}_{\mathrm{d}} = -c_{\mathrm{f}}\tilde{\varphi}_{\mathrm{d}} + c_{\mathrm{f}}\varphi_{\mathrm{d}} \tag{35}$$

$$\dot{\tilde{\varphi}} = -c_{\mathrm{f}}\tilde{\varphi} + c_{\mathrm{f}}\varphi \tag{36}$$

with $c_{\mathrm{f}} > 0$ being a gain.

In view of (26), the required force/moment vector in frame $\{\mathbf{G}\}$ can be written as

$${}^{\mathbf{G}}F_{\mathrm{r}} = \mathrm{diag}({}^{\mathbf{G}}\mathbf{R}_{\mathbf{C}}, {}^{\mathbf{G}}\mathbf{R}_{\mathbf{C}})(\mathbf{N}_{\mathrm{s}}\hat{\psi} + \mathbf{N}_{\mathrm{f}}\varphi_{\mathrm{d}}) \tag{37}$$

with

$$\hat{\psi} = \mathrm{Y}_{\mathrm{s}}\hat{\theta}_{\mathrm{s}}. \tag{38}$$

By defining

$$\mathrm{s}_{\mathrm{s}} = \mathrm{Y}_{\mathrm{s}}(\dot{\chi}_{\mathrm{r}} - \dot{\chi}) \tag{39}$$

$\hat{\theta}_{\mathrm{s}}$ in (38) can be updated by using (8) as

$$\hat{\theta}_{\mathrm{s}} = \mathscr{P}(\mathrm{s}_{\mathrm{s}}, \rho_{\mathrm{s}}, \underline{\theta}_{\mathrm{s}}, \overline{\theta}_{\mathrm{s}}, t) \tag{40}$$

where $\rho_{\mathrm{s}} > 0$ is the update gain, $\underline{\theta}_{\mathrm{s}}$ is the lower bound of θ_{s} and $\overline{\theta}_{\mathrm{s}}$ is the upper bound of θ_{s}.

5) Virtual Stability of Object 2: The following Lemma 1 and Theorem 1 ensure that *object* 2 qualifies to be *virtually stable* in the sense of Definition 5.

Lemma 1: It follows from (18), (19), (26), (27) and (34)–(40) that

$$\int_0^{\infty} p_{\mathbf{G}}(t)dt \geqslant -\gamma_s \tag{41}$$

holds with $0 \leqslant \gamma_s < \infty$.

Proof: See Appendix A. ∎

Theorem 1: Object 2, having contact to the environment and described by (18)–(21), (26) and (27), combined with its control equations (28), (29) and (32)–(38) and with the parameter adaptation (30), (31), (39) and (40), is virtually stable with its affiliated vector ${}^{\mathbf{O}_2}V_{\mathrm{r}} - {}^{\mathbf{O}_2}V$ being a virtual

function in both L_2 and L_∞ in the sense of Definition 5; This is because a non-negative accompanying function

$$v_{\mathbf{O}_2} = \frac{1}{2}({}^{\mathbf{O}_2}V_{\mathrm{r}} - {}^{\mathbf{O}_2}V)^T \mathbf{M}_{\mathbf{O}_2}({}^{\mathbf{O}_2}V_{\mathrm{r}} - {}^{\mathbf{O}_2}V) + \frac{1}{2}\sum_{i=1}^{13}\frac{(\theta_{\mathbf{O}_2 i} - \hat{\theta}_{\mathbf{O}_2 i})^2}{\rho_{\mathbf{O}_2 i}} \tag{42}$$

can be found such that

$$\dot{v}_{\mathbf{O}_2} \leqslant -({}^{\mathbf{O}_2}V_{\mathrm{r}} - {}^{\mathbf{O}_2}V)^T \mathbf{K}_{\mathbf{O}_2}({}^{\mathbf{O}_2}V_{\mathrm{r}} - {}^{\mathbf{O}_2}V) + p_{\mathbf{T}_{\mathrm{O2}}} - p_{\mathbf{G}} \tag{43}$$

holds, and according to Lemma 1,

$$\int_0^\infty p_{\mathbf{G}}(t)dt \geqslant -\gamma_s \tag{44}$$

holds with $0 \leqslant \gamma_s < \infty$. Moreover, in (43), $p_{\mathbf{T}_{\mathrm{O2}}}$ denotes the *virtual power flow* by Definition 4 in the *driven* VCP of object 2, and $p_{\mathbf{G}}$ characterizes the *virtual power flow* between the end-effector and the environment.

Proof: See Appendix B. ∎

C. Closed Chain 2 – Kinematics, Dynamics, Control and Virtual Stability

Closed chain 2 comprises *open chain* 3 and *open chain* 4 (see Figs. 5 and 6). Even though the VDC approach allows us to consider these *open chains* individually, their kinematic and dynamic behaviours still remain coupled. In Sections IV-C1 and IV-C2, the kinematics and dynamics of *closed chain* 2 are given. Then, the dynamics of the hydraulic cylinder are introduced in Section IV-C3. The control equations are given in Section IV-C4 and, finally, the *virtual stability* of *open chain* 3 and *open chain* 4 are proven in Sections IV-C5 and IV-C6, respectively.

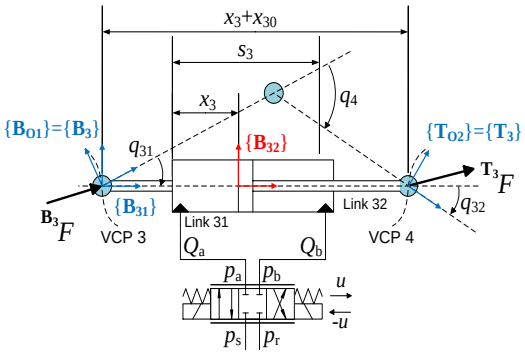

Fig. 5. The actuated prismatic *open chain* 3 with a hydraulic cylinder.

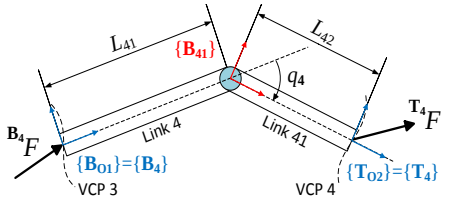

Fig. 6. The unactuated revolute *open chain* 4.

1) Kinematics of the Closed Chain: The actuated prismatic *open chain* 3 and the unactuated revolute *open chain* 4 are shown in Figs. 5 and 6, respectively. Note that the attachment of frames in these *open chains* is specified in section IV-A.

The relations among joint variables x_3, q_4, q_{31} and q_{32} (see Figs. 5 and 6) in the studied *closed chain* can be written as

$$x_3 = \sqrt{L_{41}^2 + L_{42}^2 + 2L_{41}L_{42}\cos(q_4)} - x_{30} \tag{45}$$

$$q_{31} = \cos^{-1}\left(\frac{L_{42}^2 - (x_3 + x_{30})^2 - L_{41}^2}{-2(x_3 + x_{30})L_{41}}\right) \tag{46}$$

$$q_{32} = \cos^{-1}\left(\frac{L_{41}^2 - (x_3 + x_{30})^2 - L_{42}^2}{-2(x_3 + x_{30})L_{42}}\right) \tag{47}$$

where L_{41} and L_{42} denote the link lengths in *open chain* 4 and x_{30} denotes the effective length of the hydraulic cylinder with zero piston stroke.

In view of (45), (46) and (47), the joint velocities $\dot{x}_3$, $\dot{q}_4$, $\dot{q}_{31}$ and $\dot{q}_{32}$ can be written as

$$\dot{x}_3 = -\frac{L_{41}L_{42}\sin(q_4)}{x_3 + x_{30}}\dot{q}_4 \tag{48}$$

$$\dot{q}_{31} = -\frac{(x_3 + x_{30}) - L_{41}\cos(q_{31})}{(x_3 + x_{30})L_{41}\sin(q_{31})}\dot{x}_3 \tag{49}$$

$$\dot{q}_{32} = -\frac{(x_3 + x_{30}) - L_{42}\cos(q_{32})}{(x_3 + x_{30})L_{42}\sin(q_{32})}\dot{x}_3. \tag{50}$$

Given ${}^{\mathbf{B}_{\mathrm{O1}}}V \in \mathbb{R}^6$ and in view of (16), (17), (45)–(50), and Figs. 5 and 6, the relationships among the linear/angular velocity vectors in *closed chain* 2 can be written as

$${}^{\mathbf{B}_{\mathrm{O1}}}V = {}^{\mathbf{B}_3}V = {}^{\mathbf{B}_4}V \tag{51}$$

$${}^{\mathbf{B}_{31}}V = -\mathbf{z}_\tau \dot{q}_{31} + {}^{\mathbf{B}_3}\mathbf{U}_{\mathbf{B}_{31}}^T {}^{\mathbf{B}_3}V \tag{52}$$

$${}^{\mathbf{B}_{32}}V = \mathbf{x}_f \dot{x}_3 + {}^{\mathbf{B}_{31}}\mathbf{U}_{\mathbf{B}_{32}}^T {}^{\mathbf{B}_{31}}V \tag{53}$$

$${}^{\mathbf{T}_3}V = -\mathbf{z}_\tau \dot{q}_{32} + {}^{\mathbf{B}_{32}}\mathbf{U}_{\mathbf{T}_3}^T {}^{\mathbf{B}_{32}}V \tag{54}$$

$${}^{\mathbf{B}_{41}}V = -\mathbf{z}_\tau \dot{q}_4 + {}^{\mathbf{B}_4}\mathbf{U}_{\mathbf{B}_{41}}^T {}^{\mathbf{B}_4}V \tag{55}$$

$${}^{\mathbf{T}_4}V = {}^{\mathbf{B}_{41}}\mathbf{U}_{\mathbf{T}_4}^T {}^{\mathbf{B}_{41}}V \tag{56}$$

$${}^{\mathbf{T}_{\mathrm{O2}}}V = {}^{\mathbf{T}_3}V = {}^{\mathbf{T}_4}V \tag{57}$$

where $\mathbf{z}_\tau = [0\ 0\ 0\ 0\ 0\ 1]^T$ and $\mathbf{x}_f = [1\ 0\ 0\ 0\ 0\ 0]^T$.

2) Dynamics of the Closed Chain: Referring back to Figs. 5 and 6, the following assumption for the three unactuated rotational joints in the system *closed chains* is made:

Assumption 1: The friction torques of the three unactuated rotational joints in the system *closed chains* are zero.

In view of Assumption 1, the torque constraints at the three unactuated joints of *closed chain* 2 can be expressed by

$$\mathbf{z}_\tau^T {}^{\mathbf{T}_3}F = 0 \tag{58}$$

$$\mathbf{z}_\tau^T {}^{\mathbf{B}_{41}}F = 0 \tag{59}$$

$$\mathbf{z}_\tau^T {}^{\mathbf{B}_{31}}F = \mathbf{z}_\tau^T {}^{\mathbf{B}_{31}}\mathbf{U}_{\mathbf{B}_3} {}^{\mathbf{B}_3}F = 0. \tag{60}$$

The dynamic equations of the rigid bodies (i.e. link 31, link 32, link 4 and link 41) in *closed chain* 2, can be written in view of (5) as

$$\mathbf{M}_{\mathbf{A}}\frac{d}{dt}({}^{\mathbf{A}}V) + \mathbf{C}_{\mathbf{A}}({}^{\mathbf{A}}\omega){}^{\mathbf{A}}V + \mathbf{G}_{\mathbf{A}} = {}^{\mathbf{A}}F^* \tag{61}$$

by substituting frames $\{\mathbf{B}_{31}\}$, $\{\mathbf{B}_{32}\}$, $\{\mathbf{B}_4\}$ and $\{\mathbf{B}_{41}\}$ for frame $\{\mathbf{A}\}$.

Note that the force/moment vector ${}^{\mathbf{T}_{O2}}F \in \mathbb{R}^6$ at the *driving* VCP of *closed chain* 2 can be solved from (21). Then, the force/moment vectors in this *closed chain* can be written as

$$
\begin{aligned}
{}^{\mathbf{T}_{O2}}F &= {}^{\mathbf{T}_3}F + {}^{\mathbf{T}_4}F && (62)\\
{}^{\mathbf{T}_3}F &= \alpha_3 {}^{\mathbf{T}_{O2}}F - {}^{\mathbf{T}_{O2}}\boldsymbol{\eta} && (63)\\
{}^{\mathbf{T}_4}F &= \alpha_4 {}^{\mathbf{T}_{O2}}F + {}^{\mathbf{T}_{O2}}\boldsymbol{\eta} && (64)\\
{}^{\mathbf{B}_{32}}F &= {}^{\mathbf{B}_{32}}F^* + {}^{\mathbf{B}_{32}}\mathbf{U}_{\mathbf{T}_3}\,{}^{\mathbf{T}_3}F && (65)\\
{}^{\mathbf{B}_3}F &= {}^{\mathbf{B}_3}\mathbf{U}_{\mathbf{B}_{31}}\,{}^{\mathbf{B}_{31}}F^* + {}^{\mathbf{B}_3}\mathbf{U}_{\mathbf{B}_{32}}\,{}^{\mathbf{B}_{32}}F && (66)\\
{}^{\mathbf{B}_{41}}F &= {}^{\mathbf{B}_{41}}F^* + {}^{\mathbf{B}_{41}}\mathbf{U}_{\mathbf{T}_4}\,{}^{\mathbf{T}_4}F && (67)\\
{}^{\mathbf{B}_4}F &= {}^{\mathbf{B}_4}F^* + {}^{\mathbf{B}_4}\mathbf{U}_{\mathbf{B}_{41}}\,{}^{\mathbf{B}_{41}}F && (68)\\
{}^{\mathbf{B}_{O1}}F &= {}^{\mathbf{B}_3}F + {}^{\mathbf{B}_4}F. && (69)
\end{aligned}
$$

In (69), ${}^{\mathbf{B}_{O1}}F \in \mathbb{R}^6$ denotes the force/moment vector at the *driven* VCP of the *closed chain* 2. Furthermore, in (63) and (64), α_3 and α_4 denote the load distribution factors, so that $\alpha_3 + \alpha_4 = 1$ holds and ${}^{\mathbf{T}_{O2}}\boldsymbol{\eta} \in \mathbb{R}^6$ denotes the internal force vector, where three meaningful elements (forces in x and y and moment in z) can be determined by satisfying the three constraints in (58)–(60). Note that ${}^{\mathbf{T}_{O2}}\boldsymbol{\eta}$ disappears in ${}^{\mathbf{B}_{O1}}F$ in (69).

The piston force f_c of the cylinder in *closed chain* 2 can be computed from (65) as

$$f_c = \mathbf{x}_f^T {}^{\mathbf{B}_{32}}F. \tag{70}$$

3) Dynamics of the Hydraulic Cylinder: Piston friction makes a large difference between the cylinder output force (given in (70)) and the chamber pressure-induced force [29]. Thus, to achieve appropriate piston force control, it is necessary to implement a friction model for the cylinder piston. A chamber pressure-induced force for the cylinder piston can be defined as

$$f_p = f_c + \mathbf{Y}_f \boldsymbol{\theta}_f \tag{71}$$

where f_c denotes the output force of the cylinder piston defined in (70) and $\mathbf{Y}_f\boldsymbol{\theta}_f$ denotes the linear parameterized friction model defined in [16].

Referring back to Fig. 5, the flow rates Q_a and Q_b entering into the cylinder chambers can be written as

$$Q_a = c_{p1}\upsilon(p_s - p_a)uS(u) + c_{n1}\upsilon(p_a - p_r)uS(-u) \tag{72}$$

$$Q_b = -c_{n2}\upsilon(p_b - p_r)uS(u) - c_{p2}\upsilon(p_s - p_b)uS(-u) \tag{73}$$

where $c_{p1}, c_{n1}, c_{p2}, c_{n2} > 0$ are four flow coefficients of the control valve, p_a and p_b are chamber pressures of the cylinder, u is the valve control voltage, p_s is the system supply pressure, p_r is the pressure of the system fluid return line, $S(u)$ is a selective function defined as

$$S(u) \overset{\text{def}}{=} \begin{cases} 1, & \text{if } u > 0 \\ 0, & \text{if } u \le 0 \end{cases} \tag{74}$$

and $\upsilon(\Delta p)$ is the pressure-drop-related function defined as

$$\upsilon(\Delta p) = \text{sign}(\Delta p)\sqrt{|\Delta p|}. \tag{75}$$

The pressure dynamics of the cylinder chambers can be written as

$$\dot{p}_a = \frac{\beta}{A_a x_3}(Q_a - A_a \dot{x}_3) \tag{76}$$

$$\dot{p}_b = \frac{\beta}{A_b(s_3 - x_3)}(Q_b + A_b \dot{x}_3). \tag{77}$$

In (76) and (77), β denotes the bulk modulus of fluid; A_a and A_b denote the piston areas at both chambers; and s_3 denotes the maximum stroke of the cylinder piston.

The piston chamber pressure-induced force f_p can be expressed as

$$f_p = A_a p_a - A_b p_b. \tag{78}$$

Then, premultiplying A_a and A_b to (76) and (77), respectively, differentiating (78) and using (72) and (72) yields

$$\dot{f}_p = \beta\left[u_f - \left(\frac{A_a}{x_3} + \frac{A_b}{s_3 - x_3}\right)\dot{x}_3\right] \tag{79}$$

where the control valve voltage-related term u_f can be written as

$$
\begin{aligned}
u_f &= \frac{Q_a}{x_3} - \frac{Q_b}{s_3 - x_3}\\
&= \left(\frac{c_{p1}\upsilon(p_s - p_a)}{x_3} + \frac{c_{n2}\upsilon(p_b - p_r)}{s_3 - x_3}\right)uS(u)\\
&\quad + \left(\frac{c_{p2}\upsilon(p_s - p_b)}{s_3 - x_3} + \frac{c_{n1}\upsilon(p_a - p_r)}{x_3}\right)uS(-u)\\
&= -\mathbf{Y}_v(u)\boldsymbol{\theta}_v
\end{aligned} \tag{80}
$$

with

$$\mathbf{Y}_v(u) = \begin{bmatrix} -\frac{\upsilon(p_s - p_a)}{x_3}uS(u) \\ -\frac{\upsilon(p_a - p_r)}{x_3}uS(-u) \\ -\frac{\upsilon(p_s - p_b)}{s_3 - x_3}uS(-u) \\ -\frac{\upsilon(p_b - p_r)}{s_3 - x_3}uS(u) \end{bmatrix}^T \in \mathbb{R}^{1\times 4} \tag{81}$$

$$\boldsymbol{\theta}_v = \begin{bmatrix} c_{p1} & c_{n1} & c_{p2} & c_{n2} \end{bmatrix}^T \in \mathbb{R}^4. \tag{82}$$

The assumption that the piston never reaches its two ends is then made.

Assumption 2: The following relationship holds

$$0 < x_3 < s_3. \tag{83}$$

Under Assumption 2, the univalence between u and u_f in (80) exists, provided that

$$\left(\frac{c_{p1}\upsilon(p_s - p_a)}{x_3} + \frac{c_{n2}\upsilon(p_b - p_r)}{s_3 - x_3}\right) > 0 \tag{84}$$

$$\left(\frac{c_{p2}\upsilon(p_s - p_b)}{s_3 - x_3} + \frac{c_{n1}\upsilon(p_a - p_r)}{x_3}\right) > 0 \tag{85}$$

hold. Now, for the given u_f, a unique valve control voltage u can be found:

$$
\begin{aligned}
u &= \frac{1}{\left(\frac{c_{p1}\upsilon(p_s - p_a)}{x_3} + \frac{c_{n2}\upsilon(p_b - p_r)}{s_3 - x_3}\right)}u_f S(u_f)\\
&\quad + \frac{1}{\left(\frac{c_{p2}\upsilon(p_s - p_b)}{s_3 - x_3} + \frac{c_{n1}\upsilon(p_a - p_r)}{x_3}\right)}u_f S(-u_f).
\end{aligned} \tag{86}
$$

4) Control of the Closed Chain: The required piston velocities can be solved as

$$\begin{bmatrix}\dot{x}_{1\mathrm{r}}\\ \dot{x}_{3\mathrm{r}}\end{bmatrix}=\mathbf{J}_{\mathrm{x}}^{-1}\mathbf{N}_{\mathrm{c}}^{T}\,\mathrm{diag}({}^{\mathbf{C}}\mathbf{R}_{\mathbf{G}},{}^{\mathbf{C}}\mathbf{R}_{\mathbf{G}})\,{}^{\mathbf{G}}V_{\mathrm{r}} \tag{87}$$

where ${}^{\mathbf{G}}V_{\mathrm{r}}$ is obtained from (34).

The remaining required joint velocity variables ($\dot{q}_{4\mathrm{r}}$, $\dot{q}_{31\mathrm{r}}$ and $\dot{q}_{32\mathrm{r}}$) in *closed chain* 2 can be solved by reusing (45)–(50) as

$$\dot{q}_{4\mathrm{r}}=-\frac{x_3+x_{30}}{L_{41}L_{42}\sin(q_4)}\dot{x}_{3\mathrm{r}} \tag{88}$$

$$\dot{q}_{31\mathrm{r}}=-\frac{(x_3+x_{30})-L_{41}\cos(q_{31})}{(x_3+x_{30})L_{41}\sin(q_{31})}\dot{x}_{3\mathrm{r}} \tag{89}$$

$$\dot{q}_{32\mathrm{r}}=-\frac{(x_3+x_{30})-L_{42}\cos(q_{32})}{(x_3+x_{30})L_{42}\sin(q_{32})}\dot{x}_{3\mathrm{r}}. \tag{90}$$

According to (51)–(57), the required linear/angular velocity vectors in *closed chain* 2 can be written as

$${}^{\mathbf{B}_{01}}V_{\mathrm{r}}={}^{\mathbf{B}_3}V_{\mathrm{r}}={}^{\mathbf{B}_4}V_{\mathrm{r}} \tag{91}$$

$${}^{\mathbf{B}_{31}}V_{\mathrm{r}}=-\mathbf{z}_{\tau}\dot{q}_{31\mathrm{r}}+{}^{\mathbf{B}_3}\mathbf{U}_{\mathbf{B}_{31}}^{T}\,{}^{\mathbf{B}_3}V_{\mathrm{r}} \tag{92}$$

$${}^{\mathbf{B}_{32}}V_{\mathrm{r}}=\mathbf{x}_f\dot{x}_{3\mathrm{r}}+{}^{\mathbf{B}_{31}}\mathbf{U}_{\mathbf{B}_{32}}^{T}\,{}^{\mathbf{B}_{31}}V_{\mathrm{r}} \tag{93}$$

$${}^{\mathbf{T}_3}V_{\mathrm{r}}=-\mathbf{z}_{\tau}\dot{q}_{32\mathrm{r}}+{}^{\mathbf{B}_{32}}\mathbf{U}_{\mathbf{T}_3}^{T}\,{}^{\mathbf{B}_{32}}V_{\mathrm{r}} \tag{94}$$

$${}^{\mathbf{B}_{41}}V_{\mathrm{r}}=-\mathbf{z}_{\tau}\dot{q}_{4\mathrm{r}}+{}^{\mathbf{B}_4}\mathbf{U}_{\mathbf{B}_{41}}^{T}\,{}^{\mathbf{B}_4}V_{\mathrm{r}} \tag{95}$$

$${}^{\mathbf{T}_4}V_{\mathrm{r}}={}^{\mathbf{B}_{41}}\mathbf{U}_{\mathbf{T}_4}^{T}\,{}^{\mathbf{B}_{41}}V_{\mathrm{r}} \tag{96}$$

$${}^{\mathbf{T}_{02}}V_{\mathrm{r}}={}^{\mathbf{T}_3}V_{\mathrm{r}}={}^{\mathbf{T}_4}V_{\mathrm{r}}. \tag{97}$$

According to Assumption 1, the required torque constraints at the three unactuated joints in *closed chain* 2 can be expressed by reusing (58)–(60) as

$$\mathbf{z}_{\tau}^{T}\,{}^{\mathbf{T}_3}F_{\mathrm{r}}=0 \tag{98}$$

$$\mathbf{z}_{\tau}^{T}\,{}^{\mathbf{B}_{41}}F_{\mathrm{r}}=0 \tag{99}$$

$$\mathbf{z}_{\tau}^{T}\,{}^{\mathbf{B}_{31}}F_{\mathrm{r}}=\mathbf{z}_{\tau}^{T}\,{}^{\mathbf{B}_{31}}\mathbf{U}_{\mathbf{B}_3}\,{}^{\mathbf{B}_3}F_{\mathrm{r}}=0. \tag{100}$$

In view of (7), the required net force/moment vectors for the four rigid links in *closed chain* 2 can be specified as

$${}^{\mathbf{A}}F_{\mathrm{r}}^{*}=\mathbf{Y}_{\mathbf{A}}\hat{\boldsymbol{\theta}}_{\mathbf{A}}+\mathbf{K}_{\mathbf{A}}({}^{\mathbf{A}}V_{\mathrm{r}}-{}^{\mathbf{A}}V) \tag{101}$$

by substituting frames $\{\mathbf{B}_{31}\}$, $\{\mathbf{B}_{32}\}$, $\{\mathbf{B}_4\}$ and $\{\mathbf{B}_{41}\}$ for frame $\{\mathbf{A}\}$.

With respect to (101), define

$$\mathbf{s}_{\mathbf{A}}=\mathbf{Y}_{\mathbf{A}}^{T}({}^{\mathbf{A}}V_{\mathrm{r}}-{}^{\mathbf{A}}V). \tag{102}$$

Then, (8) can be used to update the ith element of $\hat{\boldsymbol{\theta}}_{\mathbf{A}}$ as

$$\hat{\theta}_{\mathbf{A}i}=\mathscr{P}(\mathrm{s}_{\mathbf{A}i},\rho_{\mathbf{A}i},\underline{\theta}_{\mathbf{A}i},\overline{\theta}_{\mathbf{A}i},t),\forall i\in\{1,2,...,13\} \tag{103}$$

where $\hat{\theta}_{\mathbf{A}i}$ denotes the ith element of $\hat{\boldsymbol{\theta}}_{\mathbf{A}}$, $\mathrm{s}_{\mathbf{A}i}$ denotes the ith element of $\mathbf{s}_{\mathbf{A}}$, $\rho_{\mathbf{A}i}>0$ is the update gain, $\underline{\theta}_{\mathbf{A}i}$ denotes the lower bound of $\theta_{\mathbf{A}i}$ and $\overline{\theta}_{\mathbf{A}i}$ denotes the upper bound of $\theta_{\mathbf{A}i}$.

Note that the required force/moment vector ${}^{\mathbf{T}_{02}}F_{\mathrm{r}}\in\mathbb{R}^6$ at the *driving* VCP of the *closed chain* 2 can be solved from (32). Then, according to (62)–(69), the required force/moment transformations in *closed chain* 2 can be written as

$${}^{\mathbf{T}_{02}}F_{\mathrm{r}}={}^{\mathbf{T}_3}F_{\mathrm{r}}+{}^{\mathbf{T}_4}F_{\mathrm{r}} \tag{104}$$

$${}^{\mathbf{T}_3}F_{\mathrm{r}}=\alpha_3\,{}^{\mathbf{T}_{02}}F_{\mathrm{r}}-{}^{\mathbf{T}_{02}}\boldsymbol{\eta}_{\mathrm{r}} \tag{105}$$

$${}^{\mathbf{T}_4}F_{\mathrm{r}}=\alpha_4\,{}^{\mathbf{T}_{02}}F_{\mathrm{r}}+{}^{\mathbf{T}_{02}}\boldsymbol{\eta}_{\mathrm{r}} \tag{106}$$

$${}^{\mathbf{B}_{32}}F_{\mathrm{r}}={}^{\mathbf{B}_{32}}F_{\mathrm{r}}^{*}+{}^{\mathbf{B}_{32}}\mathbf{U}_{\mathbf{T}_3}\,{}^{\mathbf{T}_3}F_{\mathrm{r}} \tag{107}$$

$${}^{\mathbf{B}_3}F_{\mathrm{r}}={}^{\mathbf{B}_3}\mathbf{U}_{\mathbf{B}_{31}}\,{}^{\mathbf{B}_{31}}F_{\mathrm{r}}^{*}+{}^{\mathbf{B}_3}\mathbf{U}_{\mathbf{B}_{32}}\,{}^{\mathbf{B}_{32}}F_{\mathrm{r}} \tag{108}$$

$${}^{\mathbf{B}_{41}}F_{\mathrm{r}}={}^{\mathbf{B}_{41}}F_{\mathrm{r}}^{*}+{}^{\mathbf{B}_{41}}\mathbf{U}_{\mathbf{T}_4}\,{}^{\mathbf{T}_4}F_{\mathrm{r}} \tag{109}$$

$${}^{\mathbf{B}_4}F_{\mathrm{r}}={}^{\mathbf{B}_4}F_{\mathrm{r}}^{*}+{}^{\mathbf{B}_4}\mathbf{U}_{\mathbf{B}_{41}}\,{}^{\mathbf{B}_{41}}F_{\mathrm{r}} \tag{110}$$

$${}^{\mathbf{B}_{01}}F_{\mathrm{r}}={}^{\mathbf{B}_3}F_{\mathrm{r}}+{}^{\mathbf{B}_4}F_{\mathrm{r}}. \tag{111}$$

In (105) and (106), ${}^{\mathbf{T}_{02}}\boldsymbol{\eta}_{\mathrm{r}}\in\mathbb{R}^6$ denotes the required internal force vector, where three meaningful elements (the required forces in x and y and the required moment in z) can be determined by satisfying the three constraints in (98)–(100). Note that ${}^{\mathbf{T}_{02}}\boldsymbol{\eta}_{\mathrm{r}}$ disappears in ${}^{\mathbf{B}_{01}}F_{\mathrm{r}}$ in (111).

The required piston force f_{cr} of the cylinder piston can be computed from (107) as

$$f_{\mathrm{cr}}=\mathbf{x}_f^{T}\,{}^{\mathbf{B}_{32}}F_{\mathrm{r}}. \tag{112}$$

The control laws for the hydraulic cylinder can be written as

$$f_{\mathrm{pr}}=f_{\mathrm{cr}}+\mathbf{Y}_{\mathrm{f}}\hat{\boldsymbol{\theta}}_{\mathrm{f}} \tag{113}$$

$$\begin{aligned}u_{\mathrm{fd}}&=\left(\frac{1}{\hat{\beta}}\right)\dot{f}_{\mathrm{pr}}+\left(\frac{\hat{A}_{\mathrm{a}}}{x_3}+\frac{\hat{A}_{\mathrm{b}}}{s_3-x_3}\right)\dot{x}_3\\&\quad+k_{\mathrm{f}}\left(f_{\mathrm{pr}}-f_{\mathrm{p}}\right)+k_{\mathrm{x}}\left(\dot{x}_{3\mathrm{r}}-\dot{x}_3\right)\\&=\mathbf{Y}_{\mathrm{d}}\hat{\boldsymbol{\theta}}_{\mathrm{d}}+k_{\mathrm{f}}\left(f_{\mathrm{pr}}-f_{\mathrm{p}}\right)+k_{\mathrm{x}}\left(\dot{x}_{3\mathrm{r}}-\dot{x}_3\right)\end{aligned} \tag{114}$$

with

$$\mathbf{Y}_{\mathrm{d}}=\begin{bmatrix}\dot{f}_{\mathrm{pr}} & \dfrac{\dot{x}_3}{x_3} & \dfrac{\dot{x}_3}{s_3-x_3}\end{bmatrix}\in\mathbb{R}^{1\times 3} \tag{115}$$

$$\boldsymbol{\theta}_{\mathrm{d}}=\begin{bmatrix}\dfrac{1}{\beta} & A_{\mathrm{a}} & A_{\mathrm{b}}\end{bmatrix}^{T}\in\mathbb{R}^3 \tag{116}$$

where $k_{\mathrm{f}}>0$ and $k_{\mathrm{x}}>0$ are two feedback gains.

Then, in view of (86), the control law for the control valve of the hydraulic cylinder can be written as

$$\begin{aligned}u=&\frac{1}{\left(\frac{\hat{c}_{\mathrm{p1}}\upsilon(p_{\mathrm{s}}-p_{\mathrm{a}})}{x_3}+\frac{\hat{c}_{\mathrm{n2}}\upsilon(p_{\mathrm{b}}-p_{\mathrm{r}})}{s_3-x_3}\right)}u_{\mathrm{fd}}S(u_{\mathrm{fd}})\\&+\frac{1}{\left(\frac{\hat{c}_{\mathrm{p2}}\upsilon(p_{\mathrm{s}}-p_{\mathrm{b}})}{s_3-x_3}+\frac{\hat{c}_{\mathrm{n1}}\upsilon(p_{\mathrm{a}}-p_{\mathrm{r}})}{x_3}\right)}u_{\mathrm{fd}}S(-u_{\mathrm{fd}}).\end{aligned} \tag{117}$$

where $\hat{c}_{\mathrm{p1}}$, $\hat{c}_{\mathrm{n1}}$, $\hat{c}_{\mathrm{p2}}$ and $\hat{c}_{\mathrm{n2}}$ are updated parameters for c_{p1}, c_{n1}, c_{p2} and c_{n2}, respectively.

In relation to (84) and (85), the conditions

$$\left(\frac{\hat{c}_{\mathrm{p1}}\upsilon(p_{\mathrm{s}}-p_{\mathrm{a}})}{x_3}+\frac{\hat{c}_{\mathrm{n2}}\upsilon(p_{\mathrm{b}}-p_{\mathrm{r}})}{s_3-x_3}\right)>0 \tag{118}$$

$$\left(\frac{\hat{c}_{\mathrm{p2}}\upsilon(p_{\mathrm{s}}-p_{\mathrm{b}})}{s_3-x_3}+\frac{\hat{c}_{\mathrm{n1}}\upsilon(p_{\mathrm{a}}-p_{\mathrm{r}})}{x_3}\right)>0 \tag{119}$$

must be satisfied to make (117) executable. Finally, control equation (117) can be inversely written in view of (80) as

$$u_{\mathrm{fd}}=-\mathbf{Y}_{\mathrm{v}}(u)\hat{\boldsymbol{\theta}}_{\mathrm{v}}. \tag{120}$$

The estimated parameter vectors $\hat{\boldsymbol{\theta}}_{\mathrm{f}}$, $\hat{\boldsymbol{\theta}}_{\mathrm{d}}$ and $\hat{\boldsymbol{\theta}}_{\mathrm{v}}$ in (113), (114) and (120), respectively, must be updated. Define

$$\mathbf{s}_{\mathrm{f}} = (\dot{x}_{3\mathrm{r}} - \dot{x}_3)\mathbf{Y}_{\mathrm{f}}^T \tag{121}$$

$$\mathbf{s}_{\mathrm{d}} = (f_{\mathrm{pr}} - f_{\mathrm{p}})\mathbf{Y}_{\mathrm{d}}^T \tag{122}$$

$$\mathbf{s}_{\mathrm{v}} = (f_{\mathrm{pr}} - f_{\mathrm{p}})\mathbf{Y}_{\mathrm{v}}^T. \tag{123}$$

The ith elements of $\hat{\boldsymbol{\theta}}_{\mathrm{f}}$, $\hat{\boldsymbol{\theta}}_{\mathrm{d}}$ and $\hat{\boldsymbol{\theta}}_{\mathrm{v}}$ are updated using the $\mathscr{P}$ function defined by (8) as

$$\hat{\theta}_{\mathrm{f}i} = \mathscr{P}(\mathrm{s}_{\mathrm{f}i}, \rho_{\mathrm{f}i}, \underline{\theta}_{\mathrm{f}i}, \overline{\theta}_{\mathrm{f}i}, t), \quad \forall i \in \{1,2,...,7\} \tag{124}$$

$$\hat{\theta}_{\mathrm{d}i} = \mathscr{P}(\mathrm{s}_{\mathrm{d}i}, \rho_{\mathrm{d}i}, \underline{\theta}_{\mathrm{d}i}, \overline{\theta}_{\mathrm{d}i}, t), \ \forall i \in \{1,2,3\} \tag{125}$$

$$\hat{\theta}_{\mathrm{v}i} = \mathscr{P}(\mathrm{s}_{\mathrm{v}i}, \rho_{\mathrm{v}i}, \underline{\theta}_{\mathrm{v}i}, \overline{\theta}_{\mathrm{v}i}, t), \ \forall i \in \{1,2,3,4\} \tag{126}$$

where $\hat{\theta}_{\mathrm{f}i}$, $\hat{\theta}_{\mathrm{d}i}$ and $\hat{\theta}_{\mathrm{v}i}$ denote the ith element of $\hat{\boldsymbol{\theta}}_{\mathrm{f}}$, $\hat{\boldsymbol{\theta}}_{\mathrm{d}}$ and $\hat{\boldsymbol{\theta}}_{\mathrm{v}}$, respectively; $\mathrm{s}_{\mathrm{f}i}$, $\mathrm{s}_{\mathrm{d}i}$ and $\mathrm{s}_{\mathrm{v}i}$ denote the ith element of $\mathbf{s}_{\mathrm{f}}$, $\mathbf{s}_{\mathrm{d}}$ and $\mathbf{s}_{\mathrm{v}}$, respectively; $\rho_{\mathrm{f}i} > 0$, $\rho_{\mathrm{d}i} > 0$ and $\rho_{\mathrm{v}i} > 0$ are the update gains; $\underline{\theta}_{\mathrm{f}i}$, $\underline{\theta}_{\mathrm{d}i}$ and $\underline{\theta}_{\mathrm{v}i}$ denote the lower bounds of $\theta_{\mathrm{f}i}$, $\theta_{\mathrm{d}i}$ and $\theta_{\mathrm{v}i}$, respectively; and $\overline{\theta}_{\mathrm{f}i}$, $\overline{\theta}_{\mathrm{d}i}$ and $\overline{\theta}_{\mathrm{v}i}$ denote the upper bounds of $\theta_{\mathrm{f}i}$, $\theta_{\mathrm{d}i}$ and $\theta_{\mathrm{v}i}$, respectively.

5) Virtual Stability of the Actuated Open Chain 3: Lemmas 2 and 3 and Theorem 2 ensure that the prismatic *open chain* 3 with the hydraulic cylinder (see Fig. 5) qualifies to be *virtually stable* in the sense of Definition 5.

Lemma 2: Consider the *open chain* 3 described by (52)–(54), (58), (60), (61) (with frames $\{\mathbf{B}_{31}\}$ and $\{\mathbf{B}_{32}\}$), (65), (66) and (70), combined with its respective control equations (92)–(94), (98), (100), (101) (with frames $\{\mathbf{B}_{31}\}$ and $\{\mathbf{B}_{32}\}$), (107), (108) and (112), and with the parameter adaptation (102) and (103) (with frames $\{\mathbf{B}_{31}\}$ and $\{\mathbf{B}_{32}\}$). Let the non-negative accompanying function for the actuated prismatic *open chain* 3 be

$$v_{\mathrm{oc}_3} = v_{\mathbf{B}_{31}} + v_{\mathbf{B}_{32}} \tag{127}$$

where

$$v_{\mathbf{B}_{31}} = \frac{1}{2}({}^{\mathbf{B}_{31}}V_{\mathrm{r}} - {}^{\mathbf{B}_{31}}V)^T \mathbf{M}_{\mathbf{B}_{31}}({}^{\mathbf{B}_{31}}V_{\mathrm{r}} - {}^{\mathbf{B}_{31}}V) + \frac{1}{2}\sum_{i=1}^{13}\frac{(\theta_{\mathbf{B}_{31}i} - \hat{\theta}_{\mathbf{B}_{31}i})^2}{\rho_{\mathbf{B}_{31}i}} \tag{128}$$

$$v_{\mathbf{B}_{32}} = \frac{1}{2}({}^{\mathbf{B}_{32}}V_{\mathrm{r}} - {}^{\mathbf{B}_{32}}V)^T \mathbf{M}_{\mathbf{B}_{32}}({}^{\mathbf{B}_{32}}V_{\mathrm{r}} - {}^{\mathbf{B}_{32}}V) + \frac{1}{2}\sum_{i=1}^{13}\frac{(\theta_{\mathbf{B}_{32}i} - \hat{\theta}_{\mathbf{B}_{32}i})^2}{\rho_{\mathbf{B}_{32}i}}. \tag{129}$$

Then, the time derivative of (127) can be expressed by

$$\dot{v}_{\mathrm{oc}_3} \leqslant -({}^{\mathbf{B}_{31}}V_{\mathrm{r}} - {}^{\mathbf{B}_{31}}V)^T \mathbf{K}_{\mathbf{B}_{31}}({}^{\mathbf{B}_{31}}V_{\mathrm{r}} - {}^{\mathbf{B}_{31}}V) - ({}^{\mathbf{B}_{32}}V_{\mathrm{r}} - {}^{\mathbf{B}_{32}}V)^T \mathbf{K}_{\mathbf{B}_{32}}({}^{\mathbf{B}_{32}}V_{\mathrm{r}} - {}^{\mathbf{B}_{32}}V) + (\dot{x}_{3\mathrm{r}} - \dot{x}_3)(f_{\mathrm{cr}} - f_{\mathrm{c}}) + p_{\mathbf{B}_3} - p_{\mathbf{T}_3}. \tag{130}$$

where $p_{\mathbf{B}_3}$ and $p_{\mathbf{T}_3}$ denote two *virtual power flows* by Definition 4 at the two VCPs of the *open chain* 3.

Proof: See Appendix C. ∎

Note that the appearance of $(\dot{x}_{3\mathrm{r}} - \dot{x}_3)(f_{\mathrm{cr}} - f_{\mathrm{c}})$ in the right-hand side of (130) prevents the *virtual stability* of the actuated prismatic *open chain* 3 from being held at this point. This term is addressed next in Lemma 3.

Lemma 3: Consider the hydraulic cylinder dynamics described by (71), (79) and (80), combined with the control equations (113)–(116) and (118)–(120), and with the parameter adaptation (121)–(126). Let the non-negative accompanying function for the dynamics of the hydraulic cylinder be

$$v_{\mathrm{d}} = \frac{1}{2\beta}(f_{\mathrm{pr}} - f_{\mathrm{p}})^2 + \frac{k_{\mathrm{x}}}{2}\sum_{i=1}^{7}\frac{(\theta_{\mathrm{f}i} - \hat{\theta}_{\mathrm{f}i})^2}{\rho_{\mathrm{f}i}} + \frac{1}{2}\sum_{i=1}^{3}\frac{(\theta_{\mathrm{c}i} - \hat{\theta}_{\mathrm{c}i})^2}{\rho_{\mathrm{c}i}} + \frac{1}{2}\sum_{i=1}^{4}\frac{(\theta_{\mathrm{v}i} - \hat{\theta}_{\mathrm{v}i})^2}{\rho_{\mathrm{v}i}}. \tag{131}$$

Then, the time derivative of (131) can be expressed by

$$\dot{v}_{\mathrm{d}} \leqslant -k_{\mathrm{f}}(f_{\mathrm{pr}} - f_{\mathrm{p}})^2 - k_{\mathrm{x}}(\dot{x}_{3\mathrm{r}} - \dot{x}_3)(f_{\mathrm{cr}} - f_{\mathrm{c}}). \tag{132}$$

Proof: See Appendix D. ∎

Theorem 2: The prismatic *open chain* 3 driven by hydraulic fluid and described by (52)–(54), (58), (60), (61) (with frames $\{\mathbf{B}_{31}\}$ and $\{\mathbf{B}_{32}\}$), (65), (66), (70), (71), (79) and (80), combined with its respective control equations (92)–(94), (98), (100), (101) (with frames $\{\mathbf{B}_{31}\}$ and $\{\mathbf{B}_{32}\}$), (107), (108), (112)–(116) and (118)–(120), and with the parameter adaptation (102) (with frames $\{\mathbf{B}_{31}\}$ and $\{\mathbf{B}_{32}\}$), (103) (with frames $\{\mathbf{B}_{31}\}$ and $\{\mathbf{B}_{32}\}$) and (121)–(126) is virtually stable with its affiliated vectors ${}^{\mathbf{B}_{31}}V_{\mathrm{r}} - {}^{\mathbf{B}_{31}}V$ and ${}^{\mathbf{B}_{32}}V_{\mathrm{r}} - {}^{\mathbf{B}_{32}}V$ and variable $f_{\mathrm{pr}} - f_{\mathrm{p}}$ being virtual functions in both L_2 and L_∞ in the sense of Definition 5.

Proof of Theorem 2: The proof for Theorem 2 follows directly from Lemmas 2 and 3. Define the non-negative accompanying function of the actuated prismatic *open chain* 3 driven by hydraulic fluid as

$$v_3 = v_{\mathrm{oc}_3} + \frac{v_{\mathrm{d}}}{k_{\mathrm{x}}} \tag{133}$$

where v_{oc_3} and v_{d} are defined by (127) and (131), respectively. Then, it follows from (130) and (132) that

$$\dot{v}_3 = \dot{v}_{\mathrm{oc}_3} + \frac{\dot{v}_{\mathrm{d}}}{k_{\mathrm{x}}} \leqslant -({}^{\mathbf{B}_{31}}V_{\mathrm{r}} - {}^{\mathbf{B}_{31}}V)^T \mathbf{K}_{\mathbf{B}_{31}}({}^{\mathbf{B}_{31}}V_{\mathrm{r}} - {}^{\mathbf{B}_{31}}V) - ({}^{\mathbf{B}_{32}}V_{\mathrm{r}} - {}^{\mathbf{B}_{32}}V)^T \mathbf{K}_{\mathbf{B}_{32}}({}^{\mathbf{B}_{32}}V_{\mathrm{r}} - {}^{\mathbf{B}_{32}}V) - \frac{k_{\mathrm{f}}}{k_{\mathrm{x}}}(f_{\mathrm{pr}} - f_{\mathrm{p}})^2 + p_{\mathbf{B}_3} - p_{\mathbf{T}_3} \tag{134}$$

holds.

Consider that the actuated prismatic *open chain* 3 driven by hydraulic fluid has one *driving* VCP associated with frame $\{\mathbf{T}_3\}$ and one *driven* VCP associated with frame $\{\mathbf{B}_3\}$. Using (127), (131), (133) and (134) completes the proof of *virtual stability* of the actuated prismatic *open chain* driven by hydraulic fluid in the sense of Definition 5. ∎

6) Virtual Stability of the Unactuated Open Chain 4: Theorem 3 ensures that the unactuated revolute *open chain* 4 (see Fig. 6) combined with its respective control equations qualifies to be *virtually stable* in the sense of Definition 5.

Theorem 3: The unactuated revolute *open chain* 4 described by (55), (56), (59), (61) (with frames $\{\mathbf{B}_4\}$ and $\{\mathbf{B}_{41}\}$), (67) and (68), combined with the control equations (95), (96), (99), (101) (with frames $\{\mathbf{B}_4\}$ and $\{\mathbf{B}_{41}\}$), (109) and (110) and with the parameter adaptation (102) and (103) (with frames

$\{\mathbf{B}_4\}$ and $\{\mathbf{B}_{41}\}$) is virtually stable with its affiliated vectors ${}^{\mathbf{B}_4}V_{\mathrm{r}} - {}^{\mathbf{B}_4}V$ and ${}^{\mathbf{B}_{41}}V_{\mathrm{r}} - {}^{\mathbf{B}_{41}}V$ being virtual functions in both L_2 and L_∞ in the sense of Definition 5; This is because a non-negative accompanying function

$$v_4 = v_{\mathbf{B}_4} + v_{\mathbf{B}_{41}} \tag{135}$$

can be found, where

$$\begin{aligned} v_{\mathbf{B}_4} = {} & \frac{1}{2}({}^{\mathbf{B}_4}V_{\mathrm{r}} - {}^{\mathbf{B}_4}V)^T \mathbf{M}_{\mathbf{B}_4}({}^{\mathbf{B}_4}V_{\mathrm{r}} - {}^{\mathbf{B}_4}V) \\ & + \frac{1}{2}\sum_{i=1}^{13} \frac{(\theta_{\mathbf{B}_4 i} - \hat{\theta}_{\mathbf{B}_4 i})^2}{\rho_{\mathbf{B}_4 i}} \end{aligned} \tag{136}$$

$$\begin{aligned} v_{\mathbf{B}_{41}} = {} & \frac{1}{2}({}^{\mathbf{B}_{41}}V_{\mathrm{r}} - {}^{\mathbf{B}_{41}}V)^T \mathbf{M}_{\mathbf{B}_{41}}({}^{\mathbf{B}_{41}}V_{\mathrm{r}} - {}^{\mathbf{B}_{41}}V) \\ & + \frac{1}{2}\sum_{i=1}^{13} \frac{(\theta_{\mathbf{B}_{41} i} - \hat{\theta}_{\mathbf{B}_{41} i})^2}{\rho_{\mathbf{B}_{41} i}} \end{aligned} \tag{137}$$

such that

$$\begin{aligned} \dot{v}_4 \leqslant {} & -({}^{\mathbf{B}_4}V_{\mathrm{r}} - {}^{\mathbf{B}_4}V)^T \mathbf{K}_{\mathbf{B}_4}({}^{\mathbf{B}_4}V_{\mathrm{r}} - {}^{\mathbf{B}_4}V) \\ & - ({}^{\mathbf{B}_{41}}V_{\mathrm{r}} - {}^{\mathbf{B}_{41}}V)^T \mathbf{K}_{\mathbf{B}_{41}}({}^{\mathbf{B}_{41}}V_{\mathrm{r}} - {}^{\mathbf{B}_{41}}V) \\ & + p_{\mathbf{B}_4} - p_{\mathbf{T}_4} \end{aligned} \tag{138}$$

holds and where $p_{\mathbf{B}_4}$ and $p_{\mathbf{T}_4}$ denote two *virtual power flows* by Definition 4 at the two VCPs of the *open chain* 4.

Proof: See Appendix E. ∎

V. Stability of the Entire System

In line with Theorems 1–3, the non-negative accompanying function for the remaining subsystem[2] (given in dashed lines in Figs. 2 and 3) can be written as

$$v_{\mathbf{R}} \geqslant 0 \tag{139}$$

subject to

$$\dot{v}_{\mathbf{R}} \leqslant -p_{\mathbf{B}_{\mathrm{O}1}} \tag{140}$$

where $p_{\mathbf{B}_{\mathrm{O}1}}$ denotes the VPF at the *driving* VCP of this subsystem.

In the sense of Theorem 2.1 in [29], the *virtual stability* of every subsystem ensures the stability of the entire system because at every VCP, a positive VPF (at a *driven* VCP) is connected to its corresponding negative VPF (at a *driving* VCP) in the adjacent subsystem. Thus, VPFs act as 'stability connectors' between subsystems; eventually, all the VPFs cancel each other out, leading to the stability of the entire system [29].

In view of (42), (133), (135) and (139), the non-negative accompanying function for the entire manipulator is chosen as

$$\begin{aligned} v = {} & v_{\mathbf{R}} + v_3 + v_4 + v_{\mathbf{O}_2} \\ \geqslant {} & \frac{1}{2}\sum_{\{\mathbf{A}\}\in\Phi} ({}^{\mathbf{A}}V_{\mathrm{r}} - {}^{\mathbf{A}}V)^T \mathbf{M}_{\mathbf{A}}({}^{\mathbf{A}}V_{\mathrm{r}} - {}^{\mathbf{A}}V) \\ & + \frac{1}{2\beta k_{\mathrm{x}}}(f_{\mathrm{pr}} - f_{\mathrm{p}})^2 \end{aligned} \tag{141}$$

[2]The *virtual stabilities* of *open chain* 1 and *open chain* 2 (see in Fig. 2), can be proven by following a procedure similar to that presented in Sections IV-C5 and IV-C6. The *virtual stabilities* of *object* 0 and *object* 1 can be proven directly with a simplified version of Theorem 1.

where set Φ contains frames $\{\mathbf{O}_2\}$, $\{\mathbf{B}_{31}\}$, $\{\mathbf{B}_{32}\}$, $\{\mathbf{B}_4\}$ and $\{\mathbf{B}_{41}\}$.

Then, in view of (43), (134), (138) and (140), the time derivative of (141) can be obtained as

$$\begin{aligned} \dot{v} \leqslant {} & -\sum_{\{\mathbf{A}\}\in\Phi} ({}^{\mathbf{A}}V_{\mathrm{r}} - {}^{\mathbf{A}}V)^T \mathbf{K}_{\mathbf{A}}({}^{\mathbf{A}}V_{\mathrm{r}} - {}^{\mathbf{A}}V) - \frac{k_{\mathrm{f}}}{k_{\mathrm{x}}}(f_{\mathrm{pr}} - f_{\mathrm{p}})^2 \\ & - p_{\mathbf{B}_{\mathrm{O}1}} + p_{\mathbf{B}_3} - p_{\mathbf{T}_3} + p_{\mathbf{B}_4} - p_{\mathbf{T}_4} + p_{\mathbf{T}_{\mathrm{O}2}} - p_{\mathbf{G}}. \end{aligned} \tag{142}$$

According to (51), (57), (62), (69), (91), (97), (104) and (111), it follows that

$$p_{\mathbf{B}_3} + p_{\mathbf{B}_4} = p_{\mathbf{B}_{\mathrm{O}1}} \tag{143}$$

$$p_{\mathbf{T}_3} + p_{\mathbf{T}_4} = p_{\mathbf{T}_{\mathrm{O}2}}. \tag{144}$$

Substituting (143) and (144) for (142), all the VPFs are cancelled out and $p_{\mathbf{G}}$ is subject to (41). Thus, it follows from Lemma 2.3 in [29] that

$${}^{\mathbf{A}}V_{\mathrm{r}} - {}^{\mathbf{A}}V \in L_2 \bigcap L_\infty, \ \forall \{\mathbf{A}\} \in \Phi \tag{145}$$

$$f_{\mathrm{pr}} - f_{\mathrm{p}} \in L_2 \bigcap L_\infty \tag{146}$$

hold, leading to

$$\dot{\chi}_{\mathrm{r}} - \dot{\chi} \in L_2 \bigcap L_\infty \tag{147}$$

$$\tilde{\varphi}_{\mathrm{d}} - \tilde{\varphi} \in L_2 \bigcap L_\infty \tag{148}$$

$$\dot{x}_{3\mathrm{r}} - \dot{x}_3 \in L_2 \bigcap L_\infty \tag{149}$$

from (18), (19), (28), (34), (53) and (93).

VI. Experiments

This section demonstrates the contact force/motion control performance of the proposed controller. The system set-up and implementation issues are outlined in Section VI-A. The experimental results are presented in Section VI-B, where contact force transition performance in stationary motion is studied, and in Section VI-C, where the controller's ability to maintain a desired constant contact force in constrained motion is studied.

A. Experiment Set-Up and Implementation Issues

The contact set-up for the experiments is shown in Fig. 7. For the environmental contact, a set of wooden pallets were placed on the rubber mat.

The experimental set-up consisted of the following hardware components:

- dSpace DS1103 system
- Dimensions for cylinders: 80/45x545
- 475 kg payload, denoted as M in Fig. 1
- Bosch 4WRPEH10 proportional valve (100 dm^3/min @ Δp = 3.5 MPa per notch) for cylinders with a bandwidth of 100 Hz @ $\pm$5% signals
- Heidenhain ROD 456 incremental encoder (5000 inc/rev) with IVB interpolation units for joints 1 and 2, providing a theoretical piston position resolution $< 1.2 \cdot 10^{-3}$ mm
- Druck PTX1400 pressure transmitters with an operating pressure range of 25 MPa

The controller sample time in the experiments was set to 3 ms since the control system turnaround time was measured at approximately 2.8 ms. The following controller feedback gains, given in Table I, were used in the experiments.

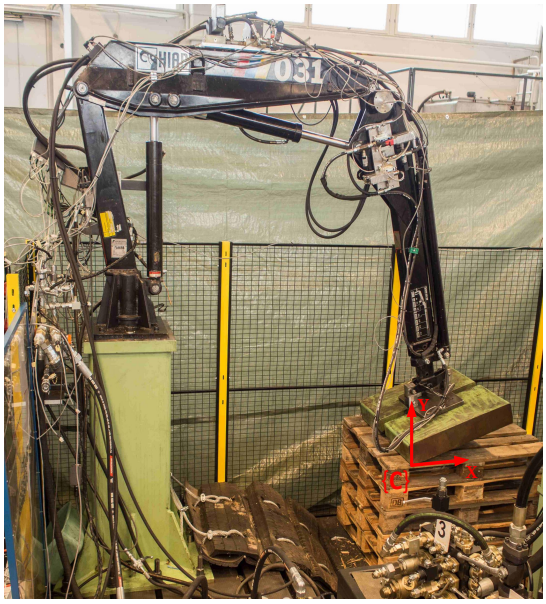

Fig. 7. The contact force/motion control set-up for the experiments. The manipulator's position in this figure shows when the contact force/motion control was enabled. The motion/force control frame $\{\mathbf{C}\}$, with directions X and Y, is marked in red.

TABLE I
CONTROLLER FEEDBACK GAINS

ACTUATOR SPACE FEEDBACK GAINS (see (114))	
Cylinder 1	Cylinder 2
$k_{x1} = 0.03\ [m]$	$k_{x2} = 0.03\ [m]$
$k_{f1} = 6.0 \cdot 10^{-8}\ [m^2/sN]$	$k_{f2} = 6.0 \cdot 10^{-8}\ [m^2/sN]$
RIGID BODY VELOCITY FEEDBACK GAINS (see (7))	
$\mathbf{K_A} = 500 \cdot \mathbf{I}_6\ [sN/m]$, for all rigid links	
CONTACT CONTROL FEEDBACK GAINS (see (33) and (34))	
$\lambda_\chi = 5\ [1/s]$	$a_f = 2.4 \cdot 10^{-4}\ [m/sN]$

B. Contact Force Transition Performance and Environment Stiffness

In the experiment, the end-effector was first driven in the free-space control mode ($\delta_f = 0$) to the initial position χ_{init} just above the wooden palettes, without contacting them (see Fig. 7). Then, the contact force control was enabled ($\delta_f = 1$) at time $t = 0$ (δ_f triggered also a desired contact force trajectory $\varphi_d(t)$ and desired motion trajectories $\chi_d(t)$ and $\dot{\chi}_d(t)$). Fig. 8 shows the measured contact force transition performances along the Y-axis of frame $\{\mathbf{C}\}$, while the end-effector was intended to remain stationary in the Cartesian X-coordinate. As this figure shows, the contact force φ was changed from its initial state[3], which was $\varphi_0 \approx 0$ N, to -8000 N in one, two and four seconds. The black lines in Fig. 8 show the desired contact force trajectories $\varphi_d(t)$, and the red, blue and green lines show the measured end-effector contact forces. As

[3]As outlined in Section III, the contact force is estimated from the hydraulic cylinder pressures. Thus, the contact force before the interaction might not be exactly zero.

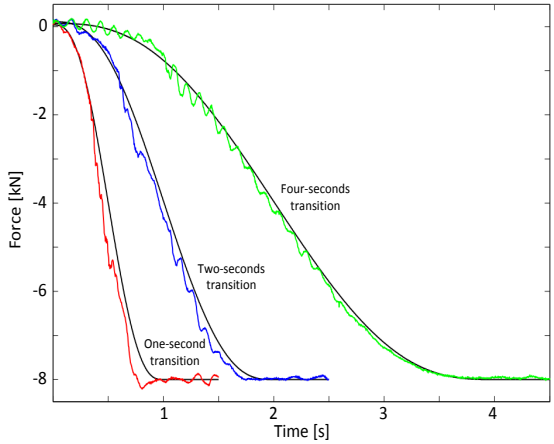

Fig. 8. Measured force transition performances at one-second force transition (—), two-seconds force transition (—) and four-seconds force transition (—). Desired force trajectories are shown with black (—).

seen in Fig. 8, the proposed controller achieves an accurate contact force transition tracking performance in all transition cases despite the manipulator's highly nonlinear dynamical behaviour and the complex interaction dynamics between the manipulator and the environment.

Fig. 9 shows the correspondence between an applied end-effector force and the measured displacement, with respect to the Y-axis of motion/force control frame $\{\mathbf{C}\}$ using a two-second desired force transition trajectory (blue line in Fig. 8). As seen in this figure, the interaction dynamics between the end-effector and the environment are not linear. The best estimated environment stiffness is approximately $2.25 \cdot 10^5 [\mathrm{N/m}]$.

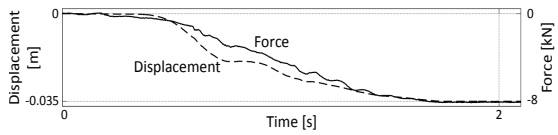

Fig. 9. Correspondence between applied end-effector force and measured displacement.

C. Contact Motion/Force Control

In the second set of experiments, the controller's ability to maintain a constant contact force in constrained motion was studied using three different maximum contact force f_{max} trajectories. During the experiments, the desired contact force $\varphi_d(t)$ was first changed from the initial measured force f_{init} to the desired maximum contact force f_{max} during two seconds (see first plot in Fig. 10). Then, the end-effector was instructed to travel a distance of 0.5 m in five seconds (see the desired motion trajectories in the second and third plots of Fig. 10), while the desired maximum contact force was maintained. Finally, the desired contact force was changed back to zero.

The main experimental results of this paper are given in Figs. 11–12. In Fig. 11, the contact force tracking performances (along the Y-axis of the frame $\{\mathbf{C}\}$) are given under the maximum contact force trajectories f_{max} = -2000 N, f_{max} = -4000 N and f_{max} = -8000 N. The measured end-effector contact forces are shown in green and their desired trajectories

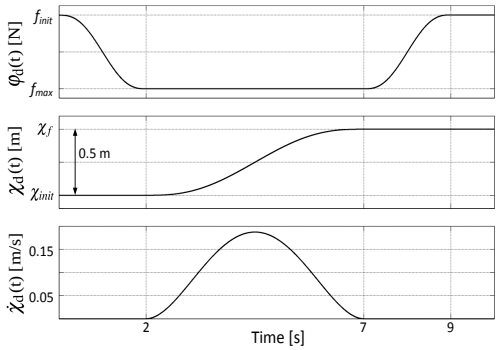

Fig. 10. Desired motion/force trajectories applied in the experiments.

TABLE II
ABSOLUTE VALUES OF THE MAXIMUM FORCE TRACKING ERRORS [N]

f_{max} = -2000 N		
Force trans. ⇓	Constr. motion	Force trans. ⇑
400 N	178 N	237 N
f_{max} = -4000 N		
Force trans. ⇓	Constr. motion	Force trans. ⇑
454 N	214 N	352 N
f_{max} = -8000 N		
Force trans. ⇓	Constr. motion	Force trans. ⇑
585 N	331 N	697 N

are shown in black. As these plots show, the measured contact forces accurately track their desired force trajectories in all three cases with different maximum contact forces.

Table II provides the maximum contact force tracking errors of Fig. 11 in the downwards force transition phase (time interval 0s–2s), in the constrained motion phase (time interval 2s–7s) and in the upwards force transition phase (7s–9s). As this table shows, with all force trajectories the highest contact force tracking error occurs in the force transition phases. In addition, the maximum contact force tracking error in the constraint motion phases is less than half of that in the respective force transitions. This has great practical relevance because the controllability of the maximum contact force is usually more important than the controllability of the force transition phases.

Fig. 12 shows the end-effector position tracking errors (along the X-axis of frame $\{\mathbf{C}\}$) under the maximum contact force trajectories f_{max} = -2000 N, f_{max} = -4000 N and f_{max} = -8000 N. The maximum position tracking errors in these cases remained well below 10 mm. This can be considered a significant result in light of the manipulator scale, which has a reach about 3.2 meters. Fig. 12 shows that the most challenging phase for position tracking control under contact force/motion control seems to be the force transition from the maximum force back to zero (see time interval 7s–9s). In this phase, the maximum contact force has a notable effect on the position tracking accuracy, whereas in the first two phases (see 0s–7s in Fig. 12), the effect of the contact force on the position tracking accuracy appears minimal.

As a supplementary result, the system's actuator space feedback variables (piston velocities and piston forces) and the cylinders' control valve voltages are shown in Figs. 13–15 under the contact force trajectories f_{max} = -2000 N, f_{max} = -4000 N and f_{max} = -8000 N, respectively. In these figures, red lines correspond to actuator 1; blue lines correspond to actuator 2; and black lines represent the required reference trajectories. As shown in the two upper plots in Figs. 13–15, the actuators' piston velocities and piston forces accurately track their required reference trajectories. No undesired high-frequency control jitter exists in the cylinder's control valve signals (see the third plots in Figs. 13–15).

VII. CONCLUSIONS

A high-performance contact force/motion controller for hydraulic manipulators has been proposed in this paper. To solve the long-standing problem of the lack of a stability-guaranteed, high-performance contact controller for multiple-

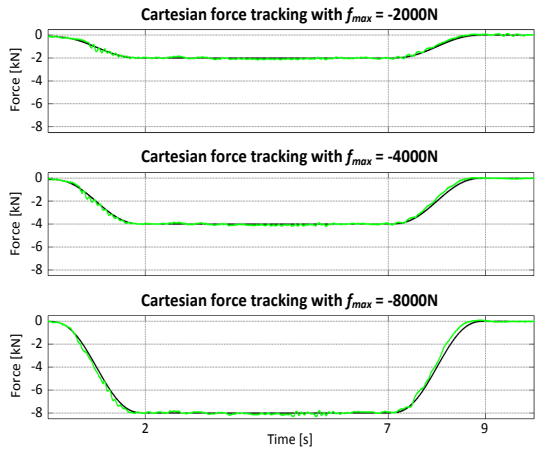

Fig. 11. Contact force tracking along the Y-axis of frame $\{\mathbf{C}\}$. Measured contact forces are shown with green lines (—) and their reference trajectories are shown with black lines (—).

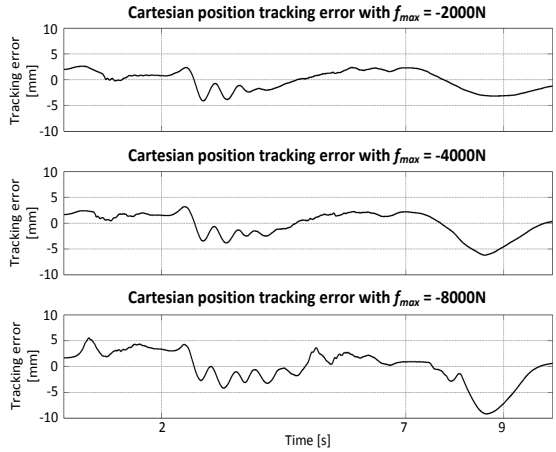

Fig. 12. Cartesian position tracking errors along the X-axis of frame $\{\mathbf{C}\}$.

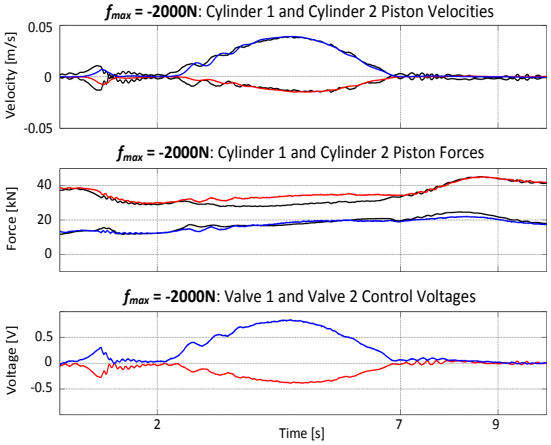

Fig. 13. Actuator space variables (piston velocities, piston forces and control voltages) under contact force trajectory f_{max} = -2000 N. Piston 1 variables are shown in red (—), piston 2 variables are shown in blue (—) and required trajectories are shown in black (—).

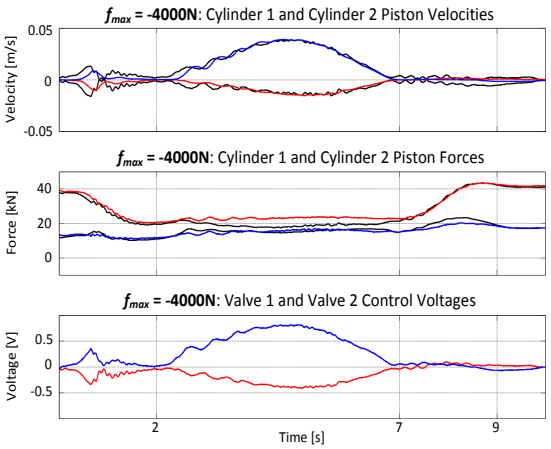

Fig. 14. Actuator space variables (piston velocities, piston forces and control voltages) under contact force trajectory f_{max} = -4000 N. Piston 1 variables are shown in red (—), piston 2 variables are shown in blue (—) and required trajectories are shown in black (—).

DOF hydraulic manipulators, this paper provides a rigorous stability proof for an entire hydraulic manipulator that performs contact tasks. The proposed controller design is based on the recently introduced Virtual Decomposition Control (VDC) approach to address the highly nonlinear nature of the hydraulic actuators, the coupled mechanical linkage dynamics and the complex interaction dynamics between the manipulator and the environment.

This paper also proposed a new method of performing contact force feedback control using hydraulic cylinder pressure measurements directly; this method aims to eliminate the use of end-effector force/torque sensors to cope with heavy-duty hydraulic manipulation. As demonstrated by the experiments, despite the highly nonlinear behaviour of the articulated hydraulic manipulator and the complex interaction dynamics between the manipulator and the environment, superior force tracking was achieved, which is invariant to the applied contact

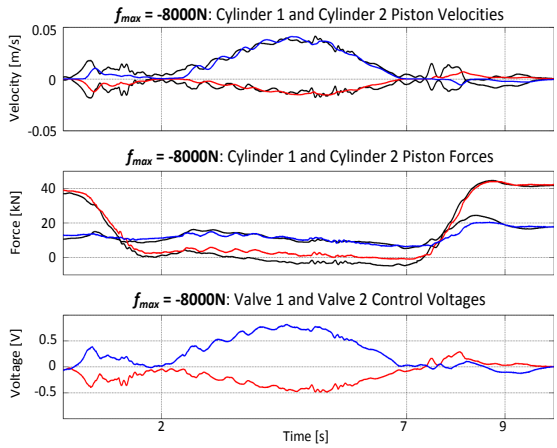

Fig. 15. Actuator space variables (piston velocities, piston forces and control voltages) under contact force trajectory f_{max} = -8000 N. Piston 1 variables are shown in red (—), piston 2 variables are shown in blue (—) and required trajectories are shown in black (—).

forces. With the maximum applied constant contact force of 8000 N, a maximum force tracking error as small as 331 N occurred under the constrained motion.

APPENDIX A
PROOF FOR LEMMA 1

It follows from (9), (10), (18), (19), (26), (27), (34)–(40) and properties $\mathbf{N}_s^T\mathbf{N}_s = 1$, $\mathbf{N}_f^T\mathbf{N}_f = 1$ and $\mathbf{N}_s^T\mathbf{N}_f = 0$ that

$$
\begin{aligned}
p_{\mathbf{G}} &= ({}^{\mathbf{G}}V_r - {}^{\mathbf{G}}V)^T({}^{\mathbf{G}}F_r - {}^{\mathbf{G}}F) \\
&= [\mathbf{N}_s(\dot{\chi}_r - \dot{\chi}) + \mathbf{N}_f a_f(\tilde{\varphi}_d - \tilde{\varphi})]^T \\
&\quad \times [\mathbf{N}_s(\hat{\psi} - \psi) + \mathbf{N}_f(\varphi_d - \varphi)] \\
&= (\dot{\chi}_r - \dot{\chi})(\hat{\psi} - \psi) + (\tilde{\varphi}_d - \tilde{\varphi})a_f(\varphi_d - \varphi) \\
&= -(\dot{\chi}_r - \dot{\chi})\mathbf{Y}_s(\theta_s - \hat{\theta}_s) + (\tilde{\varphi}_d - \tilde{\varphi})a_f(\varphi_d - \varphi) \\
&= -(\theta_s - \hat{\theta}_s)\left[s_s - \frac{\dot{\hat{\theta}}_s}{\rho_s}\right] - (\theta_s - \hat{\theta}_s)\frac{\dot{\hat{\theta}}_s}{\rho_s} \\
&\quad + (\tilde{\varphi}_d - \tilde{\varphi})a_f\left[\frac{1}{c_f}(\dot{\tilde{\varphi}}_d - \dot{\tilde{\varphi}}) + (\tilde{\varphi}_d - \tilde{\varphi})\right] \\
&\geqslant -(\theta_s - \hat{\theta}_s)\frac{\dot{\hat{\theta}}_s}{\rho_s} + (\tilde{\varphi}_d - \tilde{\varphi})\frac{a_f}{c_f}(\dot{\tilde{\varphi}}_d - \dot{\tilde{\varphi}})
\end{aligned} \tag{150}
$$

holds. Then, integrating (150) over time yields

$$
\begin{aligned}
\int_0^t p_{\mathbf{G}}(\tau)d\tau &\geqslant \frac{1}{2}\frac{(\theta_s - \hat{\theta}_s(t))^2}{\rho_s} - \frac{1}{2}\frac{(\theta_s - \hat{\theta}_s(0))^2}{\rho_s} \\
&\quad + \frac{a_f}{2c_f}(\tilde{\varphi}_d(t) - \tilde{\varphi}(t))^2 - \frac{a_f}{2c_f}(\tilde{\varphi}_d(0) - \tilde{\varphi}(0))^2 \\
&\geqslant -\frac{1}{2}\frac{(\theta_s - \hat{\theta}_s(0))^2}{\rho_s} - \frac{a_f}{2c_f}(\tilde{\varphi}_d(0) - \tilde{\varphi}(0))^2
\end{aligned} \tag{151}
$$

which validates (41). ■

APPENDIX B
PROOF FOR THEOREM 1

Consider *object* 2, i.e. rigid body, described by (20) and combined with its respective control equation (29). Subtracting (20) from (29) and rearranging terms yields

$$\begin{aligned}{}^{\mathbf{O}_2}F_{\mathrm{r}}^{*}-{}^{\mathbf{O}_2}F^{*}=\;&\mathbf{M}_{\mathbf{O}_2}\frac{d}{dt}({}^{\mathbf{O}_2}V_{\mathrm{r}}-{}^{\mathbf{O}_2}V)\\&+\mathbf{C}_{\mathbf{O}_2}({}^{\mathbf{O}_2}\omega)({}^{\mathbf{O}_2}V_{\mathrm{r}}-{}^{\mathbf{O}_2}V)-\mathbf{Y}_{\mathbf{O}_2}(\boldsymbol{\theta}_{\mathbf{O}_2}-\hat{\boldsymbol{\theta}}_{\mathbf{O}_2})\\&+\mathbf{K}_{\mathbf{O}_2}({}^{\mathbf{O}_2}V_{\mathrm{r}}-{}^{\mathbf{O}_2}V).\end{aligned}\tag{152}$$

It follows from the skew-symmetric property of $\mathbf{C}_{\mathbf{O}_2}({}^{\mathbf{O}_2}\omega)$ that

$$({}^{\mathbf{O}_2}V_{\mathrm{r}}-{}^{\mathbf{O}_2}V)^{T}\mathbf{C}_{\mathbf{O}_2}({}^{\mathbf{O}_2}\omega)({}^{\mathbf{O}_2}V_{\mathrm{r}}-{}^{\mathbf{O}_2}V)=0.\tag{153}$$

If a non-negative accompanying function for *object 2* is defined as proposed in (42), it follows from (9), (30), (31), (152) and (153) that the time derivative of (42) can be expressed by

$$\begin{aligned}\dot{v}_{\mathbf{O}_2}&=({}^{\mathbf{O}_2}V_{\mathrm{r}}-{}^{\mathbf{O}_2}V)^{T}\mathbf{M}_{\mathbf{O}_2}\frac{d}{dt}({}^{\mathbf{O}_2}V_{\mathrm{r}}-{}^{\mathbf{O}_2}V)\\&\quad-\sum_{i=1}^{13}(\theta_{\mathbf{O}_2 i}-\hat{\theta}_{\mathbf{O}_2 i})\frac{\dot{\hat{\theta}}_{\mathbf{O}_2}}{\rho_{\mathbf{O}_2 i}}\\&=-({}^{\mathbf{O}_2}V_{\mathrm{r}}-{}^{\mathbf{O}_2}V)^{T}\mathbf{C}_{\mathbf{O}_2}({}^{\mathbf{O}_2}\omega)({}^{\mathbf{O}_2}V_{\mathrm{r}}-{}^{\mathbf{O}_2}V)\\&\quad+({}^{\mathbf{O}_2}V_{\mathrm{r}}-{}^{\mathbf{O}_2}V)^{T}\mathbf{Y}_{\mathbf{O}_2}(\boldsymbol{\theta}_{\mathbf{O}_2}-\hat{\boldsymbol{\theta}}_{\mathbf{O}_2})\\&\quad-({}^{\mathbf{O}_2}V_{\mathrm{r}}-{}^{\mathbf{O}_2}V)^{T}\mathbf{K}_{\mathbf{O}_2}({}^{\mathbf{O}_2}V_{\mathrm{r}}-{}^{\mathbf{O}_2}V)\\&\quad+({}^{\mathbf{O}_2}V_{\mathrm{r}}-{}^{\mathbf{O}_2}V)^{T}({}^{\mathbf{O}_2}F_{\mathrm{r}}^{*}-{}^{\mathbf{O}_2}F^{*})\\&\quad-\sum_{i=1}^{13}(\theta_{\mathbf{O}_2 i}-\hat{\theta}_{\mathbf{O}_2 i})\frac{\dot{\hat{\theta}}_{\mathbf{O}_2}}{\rho_{\mathbf{O}_2 i}}\\&=-({}^{\mathbf{O}_2}V_{\mathrm{r}}-{}^{\mathbf{O}_2}V)^{T}\mathbf{K}_{\mathbf{O}_2}({}^{\mathbf{O}_2}V_{\mathrm{r}}-{}^{\mathbf{O}_2}V)\\&\quad+({}^{\mathbf{O}_2}V_{\mathrm{r}}-{}^{\mathbf{O}_2}V)^{T}({}^{\mathbf{O}_2}F_{\mathrm{r}}^{*}-{}^{\mathbf{O}_2}F^{*})\\&\quad+\sum_{i=1}^{13}\left\{(\theta_{\mathbf{O}_2 i}-\hat{\theta}_{\mathbf{O}_2 i})\left[\mathrm{s}_{\mathbf{O}_2 i}-\frac{\dot{\hat{\theta}}_{\mathbf{O}_2}}{\rho_{\mathbf{O}_2 i}}\right]\right\}\\&\leqslant-({}^{\mathbf{O}_2}V_{\mathrm{r}}-{}^{\mathbf{O}_2}V)^{T}\mathbf{K}_{\mathbf{O}_2}({}^{\mathbf{O}_2}V_{\mathrm{r}}-{}^{\mathbf{O}_2}V)\\&\quad+({}^{\mathbf{O}_2}V_{\mathrm{r}}-{}^{\mathbf{O}_2}V)^{T}({}^{\mathbf{O}_2}F_{\mathrm{r}}^{*}-{}^{\mathbf{O}_2}F^{*}).\end{aligned}\tag{154}$$

Furthermore, it follows from (10), (19), (21), (28) and (32) that in constrained motion, i.e. $\delta_f=1$, it can be written

$$\begin{aligned}&({}^{\mathbf{O}_2}V_{\mathrm{r}}-{}^{\mathbf{O}_2}V)^{T}({}^{\mathbf{O}_2}F_{\mathrm{r}}^{*}-{}^{\mathbf{O}_2}F^{*})\\&\quad=({}^{\mathbf{O}_2}V_{\mathrm{r}}-{}^{\mathbf{O}_2}V)^{T}{}^{\mathbf{O}_2}\mathbf{U}_{\mathbf{T}_{\mathrm{O}2}}({}^{\mathbf{T}_{\mathrm{O}2}}F_{\mathrm{r}}-{}^{\mathbf{T}_{\mathrm{O}2}}F)\\&\qquad-({}^{\mathbf{O}_2}V_{\mathrm{r}}-{}^{\mathbf{O}_2}V)^{T}{}^{\mathbf{O}_2}\mathbf{U}_{\mathbf{G}}({}^{\mathbf{G}}F_{\mathrm{r}}-{}^{\mathbf{G}}F)\\&\quad=\left[{}^{\mathbf{O}_2}\mathbf{U}_{\mathbf{T}_{\mathrm{O}2}}^{T}({}^{\mathbf{O}_2}V_{\mathrm{r}}-{}^{\mathbf{O}_2}V)\right]^{T}({}^{\mathbf{T}_{\mathrm{O}2}}F_{\mathrm{r}}-{}^{\mathbf{T}_{\mathrm{O}2}}F)\\&\qquad-\left[{}^{\mathbf{O}_2}\mathbf{U}_{\mathbf{G}}^{T}({}^{\mathbf{O}_2}V_{\mathrm{r}}-{}^{\mathbf{O}_2}V)\right]^{T}({}^{\mathbf{G}}F_{\mathrm{r}}-{}^{\mathbf{G}}F)\\&\quad=p_{\mathbf{T}_{\mathrm{O}2}}-p_{\mathbf{G}}.\end{aligned}\tag{155}$$

Substituting (155) into (154) yields

$$\begin{aligned}\dot{v}_{\mathbf{O}_2}\leqslant\;&-({}^{\mathbf{O}_2}V_{\mathrm{r}}-{}^{\mathbf{O}_2}V)^{T}\mathbf{K}_{\mathbf{O}_2}({}^{\mathbf{O}_2}V_{\mathrm{r}}-{}^{\mathbf{O}_2}V)\\&+p_{\mathbf{T}_{\mathrm{O}2}}-p_{\mathbf{G}}.\end{aligned}\tag{156}$$

Consider the fact that *object 2* has one *driven* VCP associated with frame $\{\mathbf{T}_{\mathrm{o}2}\}$. Using (42), (156) and Lemma 1 completes the proof of *virtual stability* of *object 2*, in the sense of Definition 5. ■

APPENDIX C
PROOF FOR LEMMA 2

Consider the actuated prismatic *open chain* 3, which contains two rigid links, namely link 31 and link 32, and is defined in Fig. 5. If the non-negative accompanying function is defined as proposed in (127)–(129), then it follows from (61) and (101)–(103) that (152)–(154) can be reused for the rigid links in *open chain* 3 (by substituting frames $\{\mathbf{B}_{31}\}$ and $\{\mathbf{B}_{32}\}$ for frame $\{\mathbf{O}_2\}$) and the time derivatives of (128) and (129) can be written as

$$\begin{aligned}\dot{v}_{\mathbf{B}_{31}}\leqslant\;&-({}^{\mathbf{B}_{31}}V_{\mathrm{r}}-{}^{\mathbf{B}_{31}}V)^{T}\mathbf{K}_{\mathbf{B}_{31}}({}^{\mathbf{B}_{31}}V_{\mathrm{r}}-{}^{\mathbf{B}_{31}}V)\\&+({}^{\mathbf{B}_{31}}V_{\mathrm{r}}-{}^{\mathbf{B}_{31}}V)^{T}({}^{\mathbf{B}_{31}}F_{\mathrm{r}}^{*}-{}^{\mathbf{B}_{31}}F^{*})\end{aligned}\tag{157}$$

$$\begin{aligned}\dot{v}_{\mathbf{B}_{32}}\leqslant\;&-({}^{\mathbf{B}_{32}}V_{\mathrm{r}}-{}^{\mathbf{B}_{32}}V)^{T}\mathbf{K}_{\mathbf{B}_{32}}({}^{\mathbf{B}_{32}}V_{\mathrm{r}}-{}^{\mathbf{B}_{32}}V)\\&+({}^{\mathbf{B}_{32}}V_{\mathrm{r}}-{}^{\mathbf{B}_{32}}V)^{T}({}^{\mathbf{B}_{32}}F_{\mathrm{r}}^{*}-{}^{\mathbf{B}_{32}}F^{*})\end{aligned}\tag{158}$$

respectively. Then, in view of (10), (52)–(54), (58), (60), (65), (66), (70), (92)–(94), (98), (100), (107), (108) and (112), it results in

$$\begin{aligned}&({}^{\mathbf{B}_{31}}V_{\mathrm{r}}-{}^{\mathbf{B}_{31}}V)^{T}({}^{\mathbf{B}_{31}}F_{\mathrm{r}}^{*}-{}^{\mathbf{B}_{31}}F^{*})\\&\quad=({}^{\mathbf{B}_{31}}V_{\mathrm{r}}-{}^{\mathbf{B}_{31}}V)^{T}\left[{}^{\mathbf{B}_{31}}\mathbf{U}_{\mathbf{B}_3}({}^{\mathbf{B}_3}F_{\mathrm{r}}-{}^{\mathbf{B}_3}F)\right.\\&\qquad\left.-{}^{\mathbf{B}_{31}}\mathbf{U}_{\mathbf{B}_{32}}({}^{\mathbf{B}_{32}}F_{\mathrm{r}}-{}^{\mathbf{B}_{32}}F)\right]\\&\quad=\left[{}^{\mathbf{B}_3}\mathbf{U}_{\mathbf{B}_{31}}^{T}({}^{\mathbf{B}_3}V_{\mathrm{r}}-{}^{\mathbf{B}_3}V)-\mathbf{z}_{\tau}(\dot{q}_{31\mathrm{r}}-\dot{q}_{31})\right]^{T}\\&\qquad\times{}^{\mathbf{B}_{31}}\mathbf{U}_{\mathbf{B}_3}({}^{\mathbf{B}_3}F_{\mathrm{r}}-{}^{\mathbf{B}_3}F)\\&\qquad-\left[{}^{\mathbf{B}_{32}}\mathbf{U}_{\mathbf{B}_{31}}^{T}({}^{\mathbf{B}_{32}}V_{\mathrm{r}}-{}^{\mathbf{B}_{32}}V)-{}^{\mathbf{B}_{32}}\mathbf{U}_{\mathbf{B}_{31}}^{T}\mathbf{x}_f(\dot{x}_{3\mathrm{r}}-\dot{x}_3)\right]^{T}\\&\qquad\times{}^{\mathbf{B}_{31}}\mathbf{U}_{\mathbf{B}_{32}}({}^{\mathbf{B}_{32}}F_{\mathrm{r}}-{}^{\mathbf{B}_{32}}F)\\&\quad=p_{\mathbf{B}_3}-(\dot{q}_{31\mathrm{r}}-\dot{q}_{31})\mathbf{z}_{\tau}^{T}({}^{\mathbf{B}_{31}}F_{\mathrm{r}}-{}^{\mathbf{B}_{31}}F)\\&\qquad-p_{\mathbf{B}_{32}}+(\dot{x}_{3\mathrm{r}}-\dot{x}_3)\mathbf{x}_f^{T}({}^{\mathbf{B}_{32}}F_{\mathrm{r}}-{}^{\mathbf{B}_{32}}F)\\&\quad=p_{\mathbf{B}_3}-p_{\mathbf{B}_{32}}+(\dot{x}_{3\mathrm{r}}-\dot{x}_3)(f_{\mathrm{cr}}-f_{\mathrm{c}})\end{aligned}\tag{159}$$

$$\begin{aligned}&({}^{\mathbf{B}_{32}}V_{\mathrm{r}}-{}^{\mathbf{B}_{32}}V)^{T}({}^{\mathbf{B}_{32}}F_{\mathrm{r}}^{*}-{}^{\mathbf{B}_{32}}F^{*})\\&\quad=({}^{\mathbf{B}_{32}}V_{\mathrm{r}}-{}^{\mathbf{B}_{32}}V)^{T}\left[({}^{\mathbf{B}_{32}}F_{\mathrm{r}}-{}^{\mathbf{B}_{32}}F)\right.\\&\qquad\left.-{}^{\mathbf{B}_{32}}\mathbf{U}_{\mathbf{T}_3}({}^{\mathbf{T}_3}F_{\mathrm{r}}-{}^{\mathbf{T}_3}F)\right]\\&\quad=p_{\mathbf{B}_{32}}-\left[{}^{\mathbf{T}_3}\mathbf{U}_{\mathbf{B}_{32}}^{T}({}^{\mathbf{T}_3}V_{\mathrm{r}}-{}^{\mathbf{T}_3}V)\right.\\&\qquad\left.+{}^{\mathbf{T}_3}\mathbf{U}_{\mathbf{B}_{32}}^{T}\mathbf{z}_{\tau}(\dot{q}_{32\mathrm{r}}-\dot{q}_{32})\right]^{T}\\&\qquad\times{}^{\mathbf{B}_{32}}\mathbf{U}_{\mathbf{T}_3}({}^{\mathbf{T}_3}F_{\mathrm{r}}-{}^{\mathbf{T}_3}F)\\&\quad=p_{\mathbf{B}_{32}}-p_{\mathbf{T}_3}-(\dot{q}_{32\mathrm{r}}-\dot{q}_{32})\mathbf{z}_{\tau}^{T}({}^{\mathbf{T}_3}F_{\mathrm{r}}-{}^{\mathbf{T}_3}F)\\&\quad=p_{\mathbf{B}_{32}}-p_{\mathbf{T}_3}.\end{aligned}\tag{160}$$

Substituting (159) and (160) into (157) and (158), respectively, results that

$$\begin{aligned}\dot{v}_{\mathrm{oc}_3}&=\dot{v}_{\mathbf{B}_{31}}+\dot{v}_{\mathbf{B}_{32}}\\&\leqslant-({}^{\mathbf{B}_{31}}V_{\mathrm{r}}-{}^{\mathbf{B}_{31}}V)^{T}\mathbf{K}_{\mathbf{B}_{31}}({}^{\mathbf{B}_{31}}V_{\mathrm{r}}-{}^{\mathbf{B}_{31}}V)\\&\quad-({}^{\mathbf{B}_{32}}V_{\mathrm{r}}-{}^{\mathbf{B}_{32}}V)^{T}\mathbf{K}_{\mathbf{B}_{32}}({}^{\mathbf{B}_{32}}V_{\mathrm{r}}-{}^{\mathbf{B}_{32}}V)\\&\quad+(\dot{x}_{3\mathrm{r}}-\dot{x}_3)(f_{\mathrm{cr}}-f_{\mathrm{c}})+p_{\mathbf{B}_3}-p_{\mathbf{T}_3}\end{aligned}\tag{161}$$

holds. ■

APPENDIX D
PROOF FOR LEMMA 3

It follows from (79), (80), (114)–(116) and (120) that

$$\frac{1}{\beta}(\dot{f}_{\rm pr}-\dot{f}_{\rm p})=\mathbf{Y}_{\rm v}(\boldsymbol{\theta}_{\rm v}-\hat{\boldsymbol{\theta}}_{\rm v})+\mathbf{Y}_{\rm d}(\boldsymbol{\theta}_{\rm d}-\hat{\boldsymbol{\theta}}_{\rm d}) -k_{\rm f}(f_{\rm pr}-f_{\rm p})-k_{\rm x}(\dot{x}_{3\rm r}-\dot{x}_3) \tag{162}$$

holds. Differentiating (131) with respect to time and using (9), (71), (113), (118) and (119), and the parameter adaptation (121)–(126) and (162) result that

$$\begin{aligned}\dot{v}_{\rm d}&=(f_{\rm pr}-f_{\rm p})\frac{1}{\beta}(\dot{f}_{\rm pr}-\dot{f}_{\rm p})-\sum_{i=1}^{7}k_{\rm x}(\theta_{{\rm f}i}-\hat{\theta}_{{\rm f}i})\frac{\dot{\hat{\theta}}_{{\rm f}i}}{\rho_{{\rm f}i}}\\&\quad-\sum_{i=1}^{3}(\theta_{{\rm d}i}-\hat{\theta}_{{\rm d}i})\frac{\dot{\hat{\theta}}_{{\rm d}i}}{\rho_{{\rm d}i}}-\sum_{i=1}^{4}(\theta_{{\rm v}i}-\hat{\theta}_{{\rm v}i})\frac{\dot{\hat{\theta}}_{{\rm v}i}}{\rho_{{\rm v}i}}\\&=(f_{\rm pr}-f_{\rm p})\mathbf{Y}_{\rm v}(\boldsymbol{\theta}_{\rm v}-\hat{\boldsymbol{\theta}}_{\rm v})+(f_{\rm pr}-f_{\rm p})\mathbf{Y}_{\rm d}(\boldsymbol{\theta}_{\rm d}-\hat{\boldsymbol{\theta}}_{\rm d})\\&\quad-k_{\rm f}(f_{\rm pr}-f_{\rm p})^2-k_{\rm x}(\dot{x}_{3\rm r}-\dot{x}_3)(f_{\rm pr}-f_{\rm p})\\&\quad-\sum_{i=1}^{7}k_{{\rm x}k}(\theta_{{\rm f}i}-\hat{\theta}_{{\rm f}i})\frac{\dot{\hat{\theta}}_{{\rm f}i}}{\rho_{{\rm f}i}}-\sum_{i=1}^{3}(\theta_{{\rm d}i}-\hat{\theta}_{{\rm d}i})\frac{\dot{\hat{\theta}}_{{\rm d}i}}{\rho_{{\rm d}i}}\\&\quad-\sum_{i=1}^{4}(\theta_{{\rm v}i}-\hat{\theta}_{{\rm v}i})\frac{\dot{\hat{\theta}}_{{\rm v}i}}{\rho_{{\rm v}i}}\\&=-k_{\rm f}(f_{\rm pr}-f_{\rm p})^2-k_{\rm x}(\dot{x}_{3\rm r}-\dot{x}_3)(f_{\rm cr}-f_{\rm c})\\&\quad+k_{\rm x}(\dot{x}_{3\rm r}-\dot{x}_3)\mathbf{Y}_{\rm f}(\boldsymbol{\theta}_{\rm f}-\hat{\boldsymbol{\theta}}_{\rm f})-\sum_{i=1}^{7}k_{\rm x}(\theta_{{\rm f}i}-\hat{\theta}_{{\rm f}i})\frac{\dot{\hat{\theta}}_{{\rm f}i}}{\rho_{{\rm f}i}}\\&\quad+(f_{\rm pr}-f_{\rm p})\mathbf{Y}_{\rm d}(\boldsymbol{\theta}_{\rm d}-\hat{\boldsymbol{\theta}}_{\rm d})-\sum_{i=1}^{3}(\theta_{{\rm d}i}-\hat{\theta}_{{\rm d}i})\frac{\dot{\hat{\theta}}_{{\rm d}i}}{\rho_{{\rm d}i}}\\&\quad+(f_{\rm pr}-f_{\rm p})\mathbf{Y}_{\rm v}(\boldsymbol{\theta}_{\rm v}-\hat{\boldsymbol{\theta}}_{\rm v})-\sum_{i=1}^{4}(\theta_{{\rm v}i}-\hat{\theta}_{{\rm v}i})\frac{\dot{\hat{\theta}}_{{\rm v}i}}{\rho_{{\rm v}i}}\\&\leqslant-k_{\rm f}(f_{\rm pr}-f_{\rm p})^2-k_{\rm x}(\dot{x}_{3\rm r}-\dot{x}_3)(f_{\rm cr}-f_{\rm c})\end{aligned} \tag{163}$$

holds. ■

APPENDIX E
PROOF FOR THEOREM 3

Consider the unactuated revolute *open chain* 4, which contains two rigid links, namely link 4 and link 41, and is defined in Fig. 6. If the non-negative accompanying function is defined as proposed in (135)–(137), then it follows from (61) and (101)–(103) that (152)–(154) can be reused for the rigid links in *open chain* 4 (by substituting frames $\{\mathbf{B}_4\}$ and $\{\mathbf{B}_{41}\}$ for frame $\{\mathbf{O}_2\}$) and the time derivatives of (136) and (137) can be written as

$$\begin{aligned}\dot{v}_{\mathbf{B}_4}&\leqslant-({}^{\mathbf{B}_4}V_{\rm r}-{}^{\mathbf{B}_4}V)^T\mathbf{K}_{\mathbf{B}_4}({}^{\mathbf{B}_4}V_{\rm r}-{}^{\mathbf{B}_4}V)\\&\quad+({}^{\mathbf{B}_4}V_{\rm r}-{}^{\mathbf{B}_4}V)^T({}^{\mathbf{B}_4}F_{\rm r}^*-{}^{\mathbf{B}_4}F^*)\end{aligned} \tag{164}$$

$$\begin{aligned}\dot{v}_{\mathbf{B}_{41}}&\leqslant-({}^{\mathbf{B}_{41}}V_{\rm r}-{}^{\mathbf{B}_{41}}V)^T\mathbf{K}_{\mathbf{B}_{41}}({}^{\mathbf{B}_{41}}V_{\rm r}-{}^{\mathbf{B}_{41}}V)\\&\quad+({}^{\mathbf{B}_{41}}V_{\rm r}-{}^{\mathbf{B}_{41}}V)^T({}^{\mathbf{B}_{41}}F_{\rm r}^*-{}^{\mathbf{B}_{41}}F^*)\end{aligned} \tag{165}$$

respectively. Then, in view of (10), (55), (56), (59), (67), (68), (95), (96), (99), (109) and (110), it results in

$$\begin{aligned}&({}^{\mathbf{B}_4}V_{\rm r}-{}^{\mathbf{B}_4}V)^T({}^{\mathbf{B}_4}F_{\rm r}^*-{}^{\mathbf{B}_4}F^*)\\&\quad=({}^{\mathbf{B}_4}V_{\rm r}-{}^{\mathbf{B}_4}V)^T\Big[({}^{\mathbf{B}_4}F_{\rm r}-{}^{\mathbf{B}_4}F)\\&\qquad-{}^{\mathbf{B}_4}\mathbf{U}_{\mathbf{B}_{41}}({}^{\mathbf{B}_{41}}F_{\rm r}-{}^{\mathbf{B}_{41}}F)\Big]\\&\quad=p_{\mathbf{B}_4}-\Big[{}^{\mathbf{B}_{41}}\mathbf{U}_{\mathbf{B}_4}^T({}^{\mathbf{B}_{41}}V_{\rm r}-{}^{\mathbf{B}_{41}}V)+{}^{\mathbf{B}_{41}}\mathbf{U}_{\mathbf{B}_4}^T\mathbf{z}_\tau(\dot{q}_{4\rm r}-\dot{q}_4)\Big]^T\\&\qquad\times{}^{\mathbf{B}_4}\mathbf{U}_{\mathbf{B}_{41}}({}^{\mathbf{B}_{41}}F_{\rm r}-{}^{\mathbf{B}_{41}}F)\\&\quad=p_{\mathbf{B}_4}-p_{\mathbf{B}_{41}}-(\dot{q}_{4\rm r}-\dot{q}_4)\mathbf{z}_\tau^T({}^{\mathbf{B}_{41}}F_{\rm r}-{}^{\mathbf{B}_{41}}F)\\&\quad=p_{\mathbf{B}_4}-p_{\mathbf{B}_{41}}\end{aligned} \tag{166}$$

$$\begin{aligned}&({}^{\mathbf{B}_{41}}V_{\rm r}-{}^{\mathbf{B}_{41}}V)^T({}^{\mathbf{B}_{41}}F_{\rm r}^*-{}^{\mathbf{B}_{41}}F^*)\\&\quad=({}^{\mathbf{B}_{41}}V_{\rm r}-{}^{\mathbf{B}_{41}}V)^T\Big[({}^{\mathbf{B}_{41}}F_{\rm r}-{}^{\mathbf{B}_{41}}F)\\&\qquad-{}^{\mathbf{B}_{41}}\mathbf{U}_{\mathbf{T}_4}({}^{\mathbf{T}_4}F_{\rm r}-{}^{\mathbf{T}_4}F)\Big]\\&\quad=p_{\mathbf{B}_{41}}-\Big[{}^{\mathbf{B}_{41}}\mathbf{U}_{\mathbf{T}_4}^T({}^{\mathbf{B}_{41}}V_{\rm r}-{}^{\mathbf{B}_{41}}V)\Big]^T({}^{\mathbf{T}_4}F_{\rm r}-{}^{\mathbf{T}_4}F)\\&\quad=p_{\mathbf{B}_{41}}-p_{\mathbf{T}_4}.\end{aligned} \tag{167}$$

Substituting (166) and (167) into (164) and (165), respectively, yields

$$\begin{aligned}\dot{v}_4&=\dot{v}_{\mathbf{B}_4}+\dot{v}_{\mathbf{B}_{41}}\\&=-({}^{\mathbf{B}_4}V_{\rm r}-{}^{\mathbf{B}_4}V)^T\mathbf{K}_{\mathbf{B}_4}({}^{\mathbf{B}_4}V_{\rm r}-{}^{\mathbf{B}_4}V)\\&\quad-({}^{\mathbf{B}_{41}}V_{\rm r}-{}^{\mathbf{B}_{41}}V)^T\mathbf{K}_{\mathbf{B}_{41}}({}^{\mathbf{B}_{41}}V_{\rm r}-{}^{\mathbf{B}_{41}}V)\\&\quad+p_{\mathbf{B}_4}-p_{\mathbf{T}_4}.\end{aligned} \tag{168}$$

Consider the fact that the unactuated revolute *open chain* 4 has one *driving* VCP associated with frame $\{\mathbf{T}_4\}$ and one *driven* VCP associated with frame $\{\mathbf{B}_4\}$. Using (135)–(137) and (168) completes the proof of *virtual stability* of the unactuated revolute *open chain* 4 in the sense of Definition 5. ■

REFERENCES

[1] R. Lovgren, "Radical improvements in crane safety," *ISO focus*, vol. 1, no. 7, pp. 21–93, 2004.

[2] A. Alleyne and R. Liu, "On the limitations of force tracking control for hydraulic servosystems," *Journal of Dynamic Systems, Measurement, and Control*, vol. 121, no. 2, pp. 184–190, 1999.

[3] J. Mattila and T. Virvalo, "Energy-efficient motion control of a hydraulic manipulator," in *IEEE Int. Conf. on Robotics and Automation*, Apr. 2000, vol. 3, pp. 3000–3006.

[4] S. Tafazoli et al., "Impedance control of a teleoperated excavator," *IEEE Trans. on Control Systems Technology*, vol. 10, no. 3, pp. 355–367, 2002.

[5] M.H. Raibert and J.J. Craig, "Hybrid position/force control of manipulators," *Journal of Dynamic Systems, Measurement, and Control*, vol. 103, no. 2, pp. 126–133, 1981.

[6] N. Hogan, "Impedance control: An approach to manipulation: Parts I-III," *Journal of Dynamic Systems, Measurement, and Control*, vol. 107, no. 1, pp. 1–24, 1985.

[7] O. Khatib, "A unified approach for motion and force control of robot manipulators: The operational space formulation," *IEEE Journal of Robotics and Automation*, vol. 3, no. 1, pp. 43–53, 1987.

[8] J. De Schutter and H. Van Brussel, "Compliant robot motion: Parts I-II," *The International Journal of Robotics Research*, vol. 7, no. 4, pp. 3–17, 1988.

[9] N.H. McClamroch and D. Wang, "Feedback stabilization and tracking of constrained robots," *IEEE Trans. on Automatic Control*, vol. 33, no. 5, pp. 419–426, 1988.

[10] S. Chiaverini and L. Sciavicco, "The parallel approach to force/position control of robotic manipulators," *IEEE Trans. on Robotics and Automation*, vol. 9, no. 4, pp. 361–373, 1993.

[11] D.E. Whitney, "Historical perspective and state of the art in robot force control," in *Proc. of IEEE Int. Conf. on Robotics and Automation*, 1985, vol. 2, pp. 262–268.

[12] M. Vukobratović and A. Tuneski, "Contact control concepts in manipulation robotics – an overview," *IEEE Trans. on Industrial Electronics*, vol. 41, no. 1, pp. 12–24, Feb. 1994.

[13] T. Yoshikawa, "Force control of robot manipulators," in *Proc. of Int. Conf. on Robotics and Automation*, Apr. 2000, vol. 1, pp. 220–226.

[14] M.R. Sirouspour and S.E. Salcudean, "Nonlinear control of hydraulic robots," *IEEE Trans. on Robotic and Automation*, vol. 17, no. 2, pp. 759–765, Apr. 2001.

[15] F. Bu and B. Yao, "Desired compensation adaptive robust control of single-rod electro-hydraulic actuator," in *Proc. of American Control Conference*, June 2001, vol. 5, pp. 3926–3931.

[16] W.-H. Zhu and J.C. Piedboeuf, "Adaptive output force tracking control of hydraulic cylinders with applications to robot manipulators," *Journal of Dynamic Systems, Measurement, and Control*, vol. 127, no. 2, pp. 206–217, June 2005.

[17] J. Koivumäki and J. Mattila, "The automation of multi degree of freedom hydraulic crane by using virtual decomposition control," in *IEEE/ASME Int. Conf. on Advanced Intelligent Mechatronics*, July 2013, pp. 912–919.

[18] J. Koivumäki and J. Mattila, "High performance non-linear motion/force controller design for redundant hydraulic construction crane automation," *Automation in Construction*, vol. 51, pp. 59–77, 2015.

[19] C.H. An and J.M. Hollerbach, "Dynamic stability issues in force control of manipulators," in *Proc. of American Control Conference*, 1987, pp. 821–827.

[20] C.H. An and J.M. Hollerbach, "Kinematic stability issues in force control of manipulators," in *Proc. of IEEE Int. Conf. on Robotics and Automation*, 1987, vol. 4, pp. 897–903.

[21] S.D. Eppinger and W.P. Seering, "Understanding bandwidth limitations in robot force control," in *Proc. of IEEE Int. Conf. on Robotics and Automation*, 1987, vol. 4, pp. 904–909.

[22] S.D. Eppinger and W.P. Seering, "Three dynamic problems in robot force control," in *Proc. of IEEE Int. Conf. on Robotics and Automation*, 1989, pp. 392–397.

[23] N. Niksefat, Q. Wu, and N. Sepehri, "Stable control of an electro-hydraulic actuator during contact tasks: Theory and experiments," in *Proc. of American Control Conference*, 2000, vol. 6, pp. 4114–4118.

[24] N. Niksefat, C.Q. Wu, and N. Sepehri, "Design of a lyapunov controller for an electro-hydraulic actuator during contact tasks," *Journal of Dynamic Systems, Measurement, and Control*, vol. 123, no. 2, pp. 299–307, 2001.

[25] B. Heinrichs, N. Sepehri, and A.B. Thornton-Trump, "Position-based impedance control of an industrial hydraulic manipulator," *IEEE Control Systems*, vol. 17, no. 1, pp. 46–52, 1997.

[26] S.E. Salcudean, S. Tafazoli, P.D. Lawrence, and I. Chau, "Impedance control of a teleoperated mini excavator," in *Proc. of the 8th Int. IEEE Conf. on Advanced Robotics, ICAR'97.*, 1997, pp. 19–25.

[27] S.E. Salcudean et al., "Evaluation of impedance and teleoperation control of a hydraulic mini-excavator," in *Experimental Robotics V*, pp. 227–240. Springer, 1998.

[28] S.E. Salcudean et al., "Bilateral matched-impedance teleoperation with application to excavator control," *IEEE Control Systems*, vol. 19, no. 6, pp. 29–37, 1999.

[29] W.-H. Zhu, *Virtual Decomposition Control - Toward Hyper Degrees of Freedom Robots*, Springer-Verlag, 2010.

[30] J. Koivumäki and J. Mattila, "An energy-efficient high performance motion control of a hydraulic crane applying virtual decomposition control," in *IEEE/RJS Int. Conf. on Intelligent Robots and Systems (IROS)*, Nov. 2013, pp. 4426–4433.

[31] J. Koivumäki, J. Honkakorpi, J. Vihonen, and J. Mattila, "Hydraulic manipulator virtual decomposition control with performance analysis using low-cost MEMS sensors," in *IEEE/ASME Int. Conf. on Advanced Intelligent Mechatronics (AIM)*, July 2014, pp. 910–917.

[32] W.-H. Zhu and G. Vukovich, "Virtual decomposition control for modular robot manipulators," in *IFAC World Congress*, Sept. 2011, pp. 13486–13491.

[33] W.-H. Zhu et al., "Precision control of modular robot manipulators: The VDC approach with embedded FPGA," *IEEE Trans. on Robotics*, vol. 29, no. 5, pp. 1162–1179, 2013.

[34] W.-H. Zhu and J. De Schutter, "Control of two industrial manipulators rigidly holding an egg," *IEEE Control Systems*, vol. 19, no. 2, pp. 24–30, 1999.

[35] W.-H. Zhu and J. De Schutter, "Experimental verifications of virtual-decomposition-based motion/force control," *IEEE Trans. on Robotics and Automation*, vol. 18, no. 3, pp. 379–386, 2002.

[36] W.-H. Zhu, Y.-G. Xi, Z.-J. Zhang, Z. Bien, and J. De Schutter, "Virtual decomposition based control for generalized high dimensional robotic systems with complicated structure," *IEEE Trans. on Robotics and Automation*, vol. 13, no. 3, pp. 411–436, 1997.

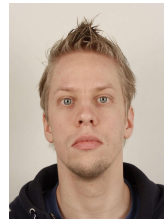

Janne Koivumäki received B.Sc. and M.Sc. (with honor) degrees in Automation Engineering from the Tampere University of Technology (TUT), Finland, in 2011 and 2012, respectively. He has worked at the Department of Intelligent Hydraulics and Automation (IHA), TUT, since 2011 and is currently pursuing a doctoral degree in Machine Automation. His research interests include a nonlinear model-based control of electro-hydraulic systems and hydraulic robotic manipulators, a contact force/motion control, an energy-efficiency of fluid power systems and a mobile manipulation.

Jouni Mattila Dr. Tech. Jouni Mattila received M.Sc. (Eng.) in 1995 and Dr. Tech. in 2000, both from the Tampere University of Technology (TUT), Finland. He was a visiting researcher at the University of British Columbia, Vancouver, BC, Canada from 1998 to 2000. As a senior systems engineering consultant, he has been involved in numerous industrial research projects, including the Sandvik AutoMine® with Hermia Group Ltd since 1996. He is currently a Professor in Machine Automation in the Department of Intelligent Hydraulics and Automation (IHA), TUT. For the past ten years, he has been a program manager on ITER fusion reactor maintenance projects involving research on heavy-duty hydraulic robotic manipulators. He currently coordinates the European Marie Curie project with 15 PhD students across the EU to develop mobile service robotics for scientific infrastructures, such as CERN. He has authored or coauthored more than 100 papers published in international journals and conference proceedings. His research interests include machine automation, preventive maintenance and developing fault-tolerant control systems for robotic manipulators and off-highway machinery.

Publication P.III

Janne Koivumäki and Jouni Mattila, "Stability-Guaranteed Impedance Control of Hydraulic Robotic Manipulators", *IEEE/ASME Transactions on Mechatronics*, 2016. [Accepted]

The original print of this publication is available online (DOI: 10.1109/TMECH.2016.2618912)

Stability-Guaranteed Impedance Control of Hydraulic Robotic Manipulators

Janne Koivumäki and Jouni Mattila, *Member, IEEE*

***Abstract*—In challenging robotic tasks, high-bandwidth closed-loop control performance of the system is required for successful task completion. One of the most critical factors inhibiting the wide-spread use of closed-loop contact control applications has been the control system stability problems. To prevent unstable system behavior, the need for rigorously addressed manipulator dynamics is substantial. This is because the contact dynamics between a manipulator and its environment can be drastic.**

In this paper, a novel Cartesian space impedance control method is proposed for hydraulic robotic manipulators. To address the highly nonlinear dynamic behaviour of the hydraulic manipulator, the system control is designed according to the subsystem-dynamics-based virtual decomposition control (VDC) approach. The unique features of VDC (*virtual power flow* and *virtual stability*) are used to analyze the interaction dynamics between the manipulator and the environment. Based on the desired impedance parameters and stability analysis, an explicit method to design the control gains for the proposed impedance control law is developed. The L_2 and L_∞ stability is guaranteed in both free-space motions and constrained motions.

Experimental results demonstrate that the hydraulic robotic manipulator is capable of adjusting its dynamic behaviour accurately in relation to the imposed target impedance behaviour. This provides compliant system behaviour, which is needed in many dynamically challenging robotic tasks.

***Index Terms*—hydraulic manipulators, impedance control, nonlinear model-based control, stability analysis, virtual decomposition control, virtual power flow.**

I. Introduction

ADVANCED robotic systems, such as humanoid robots, legged robots and exoskeletons, are currently receiving substantial attention in industry and academia. From a mechanical design perspective, hydraulic actuators provide an attractive solution for robotic systems because they can produce significant forces/torques for their size, are robust and can provide accurate motions. Indeed, hydraulic robotic systems, such as Boston Dynamics' BigDog, Cheetah and Atlas, and SARCOS' humanoids and exoskeletons, have already advanced the state-of-the-art in robotics. Academic in-depth research is also ongoing (e.g., IIT's HyQ and Shandong University's SCalf). For robotic systems, articulated limbs are crucially important subsystems because they can provide many versatile abilities, such as legged locomotion or manipulation of the environment. However, successful completion of these interactive tasks requires that the robotic system is capable of accurately controlling its interaction with the surrounding environment, with humans or with other devices.

However, force control of a single hydraulic actuator is challenging due to its highly nonlinear dynamic behaviour [1]. Moreover, control design for articulated robotic systems is greatly complicated by the nonlinear nature of the associated multibody dynamics. Impeded by these nonlinearities, an accurate contact control for articulated hydraulic robots becomes an extremely challenging task. In robotic contact control, system stability issues have drawn considerable attention since the installation of the first industrial robots, and numerous reasons for the unstable responses have been identified [2]–[6]. One reason is that contact dynamics between the robotic system and the environment can be drastic while robot nonlinear dynamics are not considered rigorously [4], [7].

The design challenges mentioned above have led to the utilization of nonlinear model-based control (NMBC) methods to achieve better dynamic performance for hydraulic robots, which is needed in dynamically challenging contact tasks. In contrast to linear control methods, NMBC methods (where the specific feedforward control term can be used for system nonlinearities) can theoretically provide "infinite" control bandwidth, as long as proper feedforward control is designed [8]. As introduced in many books on the control of robots, such as [9]–[11], typical NMBC designs are based on the complete dynamic models of robots using the Lagrangian formulation. However, for complex robots (such as humanoids), the implementation of complete-dynamics-based control becomes substantially challenging, because with these methods, the complexity (computational burden) of robot dynamics is proportional to the fourth power of the number of degrees of freedom (DOF) in motion [8].

Virtual decomposition control (VDC) [8], [12] is a unique subsystem-dynamics-based control method using the Newton-Euler formulation. A number of significant state-of-the-art control performance improvements have been reported with VDC with electrically-driven robots (see [13]–[18]) and with hydraulically-driven robots (see [19]–[23]). The subsystem-dynamics-based control of the VDC enables NMBC design with many attractive special features for (complex) robotic systems, including the following: 1) control computations are proportional to the number of subsystems and can be performed even by locally embedded hardware/software, 2) subsystem dynamics remain relatively simple with fixed dynamic structures invariant to the target system, 3) changing the control (or dynamics) of one subsystem does not affect the control equations within the rest of the system, 4) parameter uncertainties in the subsystem dynamics can be addressed with a parameter adaptation and 5) system stability analysis can be

Manuscript Submitted October 14, 2015; Accepted October 10, 2016.

J. Koivumäki and J. Mattila are with the Department of Intelligent Hydraulics and Automation, Tampere University of Technology, FI-33101 Finland (janne.koivumaki@tut.fi, jouni.mattila@tut.fi; tel: +358401981221).

This work was supported by the Academy of Finland under the project "Cooperative heavy-duty hydraulic manipulators for sustainable subsea infrastructure installation and dismantling", grant no. 286553.

addressed at a subsystem level using the unique features of VDC, *virtual power flow* (VPF) and *virtual stability*.

In this paper, a novel non-switching impedance control method is proposed. To address the highly nonlinear dynamic behavior of the hydraulic manipulator and to obtain the rigorous dynamic performance needed in contact control tasks, the manipulator's internal control is designed based on VDC. Interaction dynamics between the manipulator and the environment are analyzed using a VPF located at the contact point. Based on the analysis, an interconnection between the desired impedance parameters (characterizing system target impedance behaviour) and the parameters of the proposed novel impedance control method can be found such that impedance behavior can be designed for the system.

This paper provides the following contributions. 1) A novel non-switching impedance control method, including the VDC design and the proposed Cartesian space impedance control laws, is developed for hydraulic manipulators. 2) The impedance control is designed using the framework of VDC. 3) A rigorous stability proof for a hydraulic manipulator is provided for the first time to cover both free-space motions and constrained motions. 4) The experiments demonstrate the efficiency of the proposed method and rigorously support the mathematical theorems on the stability-guaranteed system behaviour and the target impedance behaviour.

This paper is organized as follows. Section II describes contact control strategies proposed for hydraulic robotic systems. Section III introduces the essential mathematical foundations needed in system control design. Section IV describes the proposed impedance control design and its VDC-based implementation. Section V concentrates on system stability issues. Section VI demonstrates contact control performance of the proposed controller. Conclusions are outlined in Section VII.

II. Related Works

The basic approaches for robotic force control are based on hybrid position/force control by Raibert [24] and impedance control by Hogan [25]. Historical overviews of robot force control can be found in [7], [26], [27]. With electrically-driven manipulators, the force control, as presented, e.g., in [24], [25], [28]–[32], has been extensively studied. Typically, hydraulic manipulators are built to operate heavy objects (e.g., logs) or to exert large forces on the physical environment (e.g., in excavation). Thus, it is rather surprising that only a few studies exist regarding force control in hydraulic robotic manipulators.

Heinrich et al. [33] implemented the impedance control technique for hydraulically-actuated manipulators for the first time. A nonlinear proportional-integral (NPI) controller was developed for joint control. The stability proof of the proposed controller design was not given.

Tafazoli et al. [34] (see also related studies in [35], [36]) studied the impedance control of a teleoperated mini-excavator, based on a simple proportional-derivative (PD) controller. Stability proof for a simple PD impedance controller was provided, but it was limited to a single-DOF hydraulic cylinder acting on the environment.

Zeng and Sepehri [37] proposed a nonlinear tracking control for multiple hydraulic manipulators handling a rigid object, where internal forces of coupled manipulators were controlled. The control design for the system was based on a backstepping methodology and the stability of the system was proven. However, the stability analysis was limited to situations where connection to the held object was already established. The experiments were carried out with two single-axis electro-hydraulic actuators, which were connected rigidly to the common object with spring mechanisms [38], preventing unilateral constraint.

Semini et al. [39] reported their recent results on the active impedance control of hydraulic quadruped robot HyQ. They used input-output feedback linearization to construct their model-based control design for the hydraulic leg. Rigorous stability proof for their control design was not provided.

A major step forward from the existing solutions was taken by Koivumäki and Mattila [23], who proposed a stability-guaranteed contact force/motion control for heavy-duty hydraulic manipulators. In this study, the highly nonlinear behaviour of the hydraulic manipulator was addressed with the VDC approach, and hybrid motion/force control was used to control end-effector motions and forces in their own subspaces. In the experiments, superior motion and force tracking performance were reported. In the control design, switching from free-space motion to constrained motion was utilized.

In summary, NMBC for hydraulic manipulators with non-switching contact control law and with rigorous stability proof in free-space and constrained motions is still an open problem. This problem is addressed in the present paper.

III. Mathematical Foundation

This section provides essential mathematical foundations needed in control system design.

A. Linear/Angular Velocity Vectors and Force/Moment Vectors

Consider an orthogonal, three-dimensional coordinate system $\{\mathbf{A}\}$ (called frame $\{\mathbf{A}\}$ for simplicity) attached to the rigid body. Let the linear/angular velocity vector of frame $\{\mathbf{A}\}$ be written as ${}^{\mathbf{A}}V = [{}^{\mathbf{A}}\mathbf{v}\ {}^{\mathbf{A}}\boldsymbol{\omega}]^T$, where ${}^{\mathbf{A}}\mathbf{v} \in \mathbb{R}^3$ and ${}^{\mathbf{A}}\boldsymbol{\omega} \in \mathbb{R}^3$ are the linear and angular velocity vectors of frame $\{\mathbf{A}\}$. Similarly, let the force/moment vector in frame $\{\mathbf{A}\}$ be written as ${}^{\mathbf{A}}F = [{}^{\mathbf{A}}\mathbf{f}\ {}^{\mathbf{A}}\mathbf{m}]^T$, where ${}^{\mathbf{A}}\mathbf{f} \in \mathbb{R}^3$ and ${}^{\mathbf{A}}\mathbf{m} \in \mathbb{R}^3$ are the force and moment vectors applied to the origin of frame $\{\mathbf{A}\}$, expressed in frame $\{\mathbf{A}\}$. Then, consider two given frames, denoted as $\{\mathbf{A}\}$ and $\{\mathbf{B}\}$, fixed to a common rigid body. The following relations hold

$$ {}^{\mathbf{B}}V = {}^{\mathbf{A}}\mathbf{U}_{\mathbf{B}}^{T}\,{}^{\mathbf{A}}V \tag{1} $$

$$ {}^{\mathbf{A}}F = {}^{\mathbf{A}}\mathbf{U}_{\mathbf{B}}\,{}^{\mathbf{B}}F \tag{2} $$

where ${}^{\mathbf{A}}\mathbf{U}_{\mathbf{B}} \in \mathbb{R}^{6\times 6}$ denotes a force/moment transformation matrix that transforms the force/moment vector measured and expressed in frame $\{\mathbf{B}\}$ to the same force/moment vector measured and expressed in frame $\{\mathbf{A}\}$.

B. Parameter Adaptation

The following projection function from [8] is used for parameter adaptation:

Definition 1: A projection function $\mathscr{P}(s(t),k,a(t),b(t),t) \in \mathbb{R}$ is a differentiable scalar function defined for $t \geqslant 0$ such that its time derivative is governed by

$$\dot{\mathscr{P}} = ks(t)\kappa \tag{3}$$

with

$$\kappa = \begin{cases} 0, & \text{if } \mathscr{P} \leqslant a(t) \text{ and } s(t) \leqslant 0 \\ 0, & \text{if } \mathscr{P} \geqslant b(t) \text{ and } s(t) \geqslant 0 \\ 1, & \text{otherwise} \end{cases}$$

where $s(t) \in \mathbb{R}$ is a scalar variable, $k > 0$ is a constant and $a(t) \leqslant b(t)$ holds.

The projection function defined in (3) has the following property: For any constant $\mathscr{P}_c$ subject to $a(t) \leqslant \mathscr{P}_c \leqslant b(t)$, it follows that

$$(\mathscr{P}_c - \mathscr{P})\left(s(t) - \frac{1}{k}\dot{\mathscr{P}}\right) \leqslant 0. \tag{4}$$

C. Virtual Cutting Points and a Simple Oriented Graph

In the VDC approach, the original system is virtually decomposed into the subsystems by placing conceptual *virtual cutting points* (VCPs). A *cutting point* forms a virtual cutting surface on which three-dimensional force vectors and three-dimensional moment vectors can be exerted from one part to another. The VCP is defined as shown in Definition 2.

Definition 2 [8]: A cutting point is a directed separation interface that conceptually cuts through a rigid body. At the cutting point, two parts resulting from the virtual cut maintain equal positions and orientations. The cutting point is interpreted as a *driving cutting point* by one part and is simultaneously interpreted as a *driven cutting point* by another part. A force vector $\mathbf{f} \in \mathbb{R}^3$ and a moment vector $\mathbf{m} \in \mathbb{R}^3$ are exerted from one part to which the cutting point is interpreted as a *driving cutting point* to the other part to which the cutting point is interpreted as a *driven cutting point*.

After the original system is virtually decomposed into subsystems by placing VCPs, the system can be represented by a simple oriented graph. A simple oriented graph is defined, as shown in Definition 3.

Definition 3 [8]: A graph consists of nodes and edges. A directed graph is a graph in which all edges have directions. An oriented graph is a directed graph in which each edge has a unique direction. A simple oriented graph is an oriented graph in which no loop is formed.

D. L_2 and L_∞ Stability

Definition 4 [8]: Lebesgue space, denoted as L_p with p being a positive integer, contains all Lebesgue measurable and integrable functions $f(t)$ subject to

$$\|f\|_p = \lim_{T\to\infty}\left[\int_0^T |f(t)|^p d\tau\right]^{\frac{1}{p}} < +\infty. \tag{5}$$

Two particular cases are considered:

(a) A Lebesgue measurable function $f(t)$ belongs to L_2 if and only if $\lim_{T\to\infty}\int_0^T |f(t)|^2 d\tau < +\infty$.

(b) A Lebesgue measurable function $f(t)$ belongs to L_∞ if and only if $\max_{t\in[0,\infty)}|f(t)| < +\infty$.

The following Lemma 1 (Lemma 2.3 in [8]) provides that a system is stable with its affiliated vector $\mathbf{x}(t)$ being a function in L_∞ and its affiliated vector $\mathbf{y}(t)$ being a function in L_2.

Lemma 1 [8]: Consider a non-negative differentiable function $\xi(t)$ defined as

$$\xi(t) \geqslant \frac{1}{2}\mathbf{x}(t)^T\mathbf{P}\mathbf{x}(t) \tag{6}$$

with $\mathbf{x}(t) \in \mathbb{R}^n$, $n \geqslant 1$ and $\mathbf{P} \in \mathbb{R}^{n\times n}$ being a symmetric positive-definite matrix. If the time derivative of $\xi(t)$ is Lebesgue integrable and governed by

$$\dot{\xi}(t) \leqslant -\mathbf{y}(t)^T\mathbf{Q}\mathbf{y}(t) - s(t) \tag{7}$$

where $\mathbf{y}(t) \in \mathbb{R}^m$, $m \geqslant 1$ and $\mathbf{Q} \in \mathbb{R}^{m\times m}$ being a symmetric positive-definite matrix and $s(t)$ is subject to

$$\int_0^\infty s(t)dt \geqslant -\gamma_0 \tag{8}$$

with $0 \leqslant \gamma_0 < \infty$, then it follows that $\xi(t) \in L_\infty$, $\mathbf{x}(t) \in L_\infty$ and $\mathbf{y}(t) \in L_2$ hold.

The following Lemma 2 provides that L_2 and L_∞ signal retains its properties after passing through a first-order multiple-input-multiple-output (MIMO) filter.

Lemma 2 [8]: Consider a first-order MIMO system described by

$$\dot{\mathbf{x}}(t) + \mathbf{K}\mathbf{x}(t) = \mathbf{u}(t) \tag{9}$$

with $\mathbf{x}(t) \in \mathbb{R}^n$, $\mathbf{u}(t) \in \mathbb{R}^n$, and $\mathbf{K} \in \mathbb{R}^{n\times n}$ being symmetrical and positive-definite. If $\mathbf{u}(t) \in L_2 \bigcap L_\infty$ holds, then $\mathbf{x}(t) \in L_2 \bigcap L_\infty$ and $\dot{\mathbf{x}}(t) \in L_2 \bigcap L_\infty$ hold.

The following Lemma 3 provides an asymptotic convergence for an error signal $e(t)$.

Lemma 3 [40]: If $e(t) \in L_2$ and $\dot{e}(t) \in L_\infty$, then $\lim_{t\to\infty} e(t) = 0$.

E. Virtual Stability

The unique feature of the VDC approach is the introduction of a scalar term, namely the *virtual power flow* (VPF); see Definition 5. VPFs uniquely define the dynamic interactions among the subsystems and play an important role in the definition of *virtual stability*, which is defined in Definition 6.

Definition 5 [8]: The VPF with respect to frame $\{\mathbf{A}\}$ can be defined as the inner product of the linear/angular velocity vector error and the force/moment vector error as

$$p_{\mathbf{A}} = ({}^{\mathbf{A}}V_{\mathrm{r}} - {}^{\mathbf{A}}V)^T({}^{\mathbf{A}}F_{\mathrm{r}} - {}^{\mathbf{A}}F) \tag{10}$$

where ${}^{\mathbf{A}}V_{\mathrm{r}} \in \mathbb{R}^6$ and ${}^{\mathbf{A}}F_{\mathrm{r}} \in \mathbb{R}^6$ represent the required vectors of ${}^{\mathbf{A}}V \in \mathbb{R}^6$ and ${}^{\mathbf{A}}F \in \mathbb{R}^6$, respectively.

Definition 6 [8]: A subsystem with a driven VCP to which frame $\{\mathbf{A}\}$ is attached and a driving VCP to which frame $\{\mathbf{C}\}$ is attached is said to be *virtually stable* with its affiliated vector $\mathbf{x}(t)$ being a virtual function in L_∞ and its affiliated vector $\mathbf{y}(t)$ being a virtual function in L_2, if and only if there exists a non-negative accompanying function

$$v(t) \geqslant \frac{1}{2}\mathbf{x}(t)^T\mathbf{P}\mathbf{x}(t) \tag{11}$$

such that

$$\dot{v}(t) \leqslant -\mathbf{y}(t)^T\mathbf{Q}\mathbf{y}(t) + p_{\mathbf{A}} - p_{\mathbf{C}} - s(t) \tag{12}$$

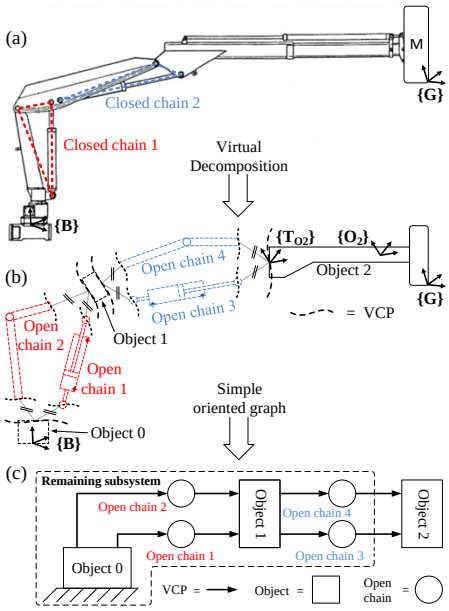

Fig. 1. The studied system. Subfigure (a) shows the original two-DOF hydraulic manipulator. Subfigure (b) shows a virtual decomposition of the system. Note the parallelism (//) in the VCPs. Subfigure (c) shows a simple oriented graph of the virtually decomposed system.

holds, subject to

$$\int_0^\infty s(t)dt \geqslant -\gamma_s \tag{13}$$

with $0 \leqslant \gamma_s < \infty$, where $\mathbf{P}$ and $\mathbf{Q}$ are two block-diagonal positive-definite matrices and $p_{\mathbf{A}}$ and $p_{\mathbf{C}}$ denote the VPFs (by Definition 5) at frames $\{\mathbf{A}\}$ and $\{\mathbf{C}\}$, respectively.

IV. Control of the Manipulator

This section addresses a design of novel impedance control method for a two-DOF hydraulic manipulator, which is shown in Fig. 1(a). Even though a two-DOF system is studied in this paper, the developed approach is extendable to systems with any number of actuators. First, to address the highly nonlinear behaviour of the hydraulic manipulator, Section IV-A shows the manipulator's internal control design based on the VDC approach. Then, Section IV-B introduces the novel impedance control method, designed using the framework of VDC.

A. Virtual Decomposition Control

The first step in the VDC approach is to virtually decompose an original system into subsystems (i.e., *objects* and *open chains*) by placing conceptual VCPs (see Definition 2). Then, the decomposed subsystems are represented by a simple oriented graph imposing dynamic interactions among subsystems. The system's virtual decomposition and the simple oriented graph presentation are addressed in Section IV-A1.

Then, the subsystem-dynamic-based control is designed to make each subsystem qualified to be *virtually stable*. The virtue of the VDC is that when all subsystems are virtually stable, the stability of the entire system can be guaranteed. This is addressed in Section V.

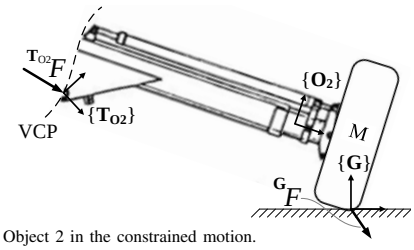

Fig. 2. Object 2 in the constrained motion.

1) Virtual Decomposition and Simple Oriented Graph: The virtually decomposed manipulator is shown in Fig. 1(b). As discussed, changing the control (or dynamics) of one subsystem does not affect the control equations within the rest of the system. In this study, only the control equations subject to Object 2 have been changed in relation to [23]. For this reason, only the control design for Object 2 (subsystem interacting with the environment) has been studied in detail in this paper. Control designs for the remaining subsystems, shown at the dashed line in Fig. 1(b), can be found in [23].

The simple oriented graph for the manipulator is shown in Fig. 1(c). In this paper, the subsystems inside the dashed line in Fig. 1(c) are considered as one subsystem; see the corresponding lines in Fig. 1(b). Each subsystem corresponds to a node, and each VCP corresponds to a directed edge whose direction defines the force reference direction. Thus, a VCP is simultaneously interpreted as a driving VCP by one subsystem (from which the force/moment vector is exerted or the directed edge is pointing away) and as a driven VCP by another subsystem (toward which the force/moment vector is exerted or the directed edge points) [8].

Next, in Sections IV-A2 through IV-A4, the kinematics, dynamics and control of Object 2 are given.

2) Object 2 – Kinematics: Fig. 2 shows the Object 2, to which frame $\{\mathbf{O}_2\}$ is fixed to describe the force and motion specifications. Frame $\{\mathbf{T}_{O2}\}$ exists at the driven VCP of Object 2, and frame $\{\mathbf{G}\}$ is the end-effector target frame where the contact occurs and in which the Cartesian motion and force control is specified.

The linear/angular velocity vector ${}^{\mathbf{G}}V \in \mathbb{R}^6$ in frame $\{\mathbf{G}\}$ can be written as

$${}^{\mathbf{G}}V = \mathbf{N}_c\dot{\boldsymbol{\chi}} \tag{14}$$

where $\dot{\boldsymbol{\chi}} \in \mathbb{R}^2$ is the Cartesian velocity vector and the mapping matrix $\mathbf{N}_c$ can be written as

$$\mathbf{N}_c = \begin{bmatrix} 1 & 0 & 0 & 0 & 0 & 0 \\ 0 & 1 & 0 & 0 & 0 & 0 \end{bmatrix}^T.$$

The following relations hold for Object 2:

$$\begin{aligned} {}^{\mathbf{O}_2}V &= {}^{\mathbf{G}}\mathbf{U}_{\mathbf{O}_2}^T\,{}^{\mathbf{G}}V \\ &= {}^{\mathbf{T}_{O2}}\mathbf{U}_{\mathbf{O}_2}^T\,{}^{\mathbf{T}_{O2}}V. \end{aligned} \tag{15}$$

3) Object 2 – Dynamics: The end-effector force/moment vector in frame $\{\mathbf{G}\}$ can be written as

$${}^{\mathbf{G}}F = \mathbf{N}_c{}^{\mathbf{G}}\boldsymbol{f} \tag{16}$$

where ${}^{\mathbf{G}}\boldsymbol{f} \in \mathbb{R}^2$ is a Cartesian contact force vector (exerted by the manipulator on the environment).

The net force/moment vector ${}^{\mathbf{O}_2}F^* \in \mathbb{R}^6$ of Object 2, expressed in frame $\{\mathbf{O}_2\}$, can be written in view of [8] as

$$\mathbf{M}_{\mathbf{O}_2}\frac{d}{dt}({}^{\mathbf{O}_2}V) + \mathbf{C}_{\mathbf{O}_2}({}^{\mathbf{O}_2}\omega)^{\mathbf{O}_2}V + \mathbf{G}_{\mathbf{O}_2} = {}^{\mathbf{O}_2}F^* \quad (17)$$

where $\mathbf{M}_{\mathbf{O}_2} \in \mathbb{R}^{6\times6}$ denotes the mass matrix, $\mathbf{C}_{\mathbf{O}_2}({}^{\mathbf{O}_2}\omega) \in \mathbb{R}^{6\times6}$ denotes the matrix of Coriolis and centrifugal terms and $\mathbf{G}_{\mathbf{O}_2} \in \mathbb{R}^6$ denotes the gravity terms.

On the other hand, the net force/moment vector (i.e., force resultant equation) for Object 2 can be written as

$${}^{\mathbf{O}_2}F^* = {}^{\mathbf{O}_2}\mathbf{U}_{\mathbf{T}_{\mathrm{o}2}}{}^{\mathbf{T}_{\mathrm{o}2}}F - {}^{\mathbf{O}_2}\mathbf{U}_{\mathbf{G}}{}^{\mathbf{G}}F. \quad (18)$$

4) Object 2 – Control: This section addresses the VDC-based rigid body control of Object 2.

Similar to (14), the required linear/angular velocity vector in the end-effector target frame $\{\mathbf{G}\}$ can be written as

$${}^{\mathbf{G}}V_{\mathrm{r}} = \mathbf{N}_{\mathrm{c}}\dot{\boldsymbol{\chi}}_{\mathrm{r}} \quad (19)$$

where $\dot{\boldsymbol{\chi}}_{\mathrm{r}} \in \mathbb{R}^2$ is the required Cartesian space velocity (design) vector specified later in (31).

In view of (15), the required velocity transformations in Object 2 can be written as

$$\begin{aligned}{}^{\mathbf{O}_2}V_{\mathrm{r}} &= {}^{\mathbf{G}}\mathbf{U}_{\mathbf{O}_2}^T{}^{\mathbf{G}}V_{\mathrm{r}}\\ &= {}^{\mathrm{To2}}\mathbf{U}_{\mathbf{O}_2}^T{}^{\mathrm{To2}}V_{\mathrm{r}}.\end{aligned} \quad (20)$$

Similar to (16), the required force/moment vector in the end-effector target frame $\{\mathbf{G}\}$ can be obtained as

$${}^{\mathbf{G}}F_{\mathrm{r}} = \mathbf{N}_{\mathrm{c}}{}^{\mathbf{G}}\boldsymbol{f}_{\mathrm{d}} \quad (21)$$

where ${}^{\mathbf{G}}\boldsymbol{f}_{\mathrm{d}} \in \mathbb{R}^2$ is a desired Cartesian contact force vector.

Then, in view of [8], the required net force/moment vector for Object 2 can be written as

$${}^{\mathbf{O}_2}F_{\mathrm{r}}^* = \mathbf{Y}_{\mathbf{O}_2}\widehat{\boldsymbol{\theta}}_{\mathbf{O}_2} + \mathbf{K}_{\mathbf{O}_2}({}^{\mathbf{O}_2}V_{\mathrm{r}} - {}^{\mathbf{O}_2}V) \quad (22)$$

with

$$\mathbf{Y}_{\mathbf{O}_2}\boldsymbol{\theta}_{\mathbf{O}_2} = \mathbf{M}_{\mathbf{O}_2}\frac{d}{dt}({}^{\mathbf{O}_2}V_{\mathrm{r}}) + \mathbf{C}_{\mathbf{O}_2}({}^{\mathbf{O}_2}\omega)^{\mathbf{O}_2}V_{\mathrm{r}} + \mathbf{G}_{\mathbf{O}_2} \quad (23)$$

where regressor matrix $\mathbf{Y}_{\mathbf{O}_2} \in \mathbb{R}^{6\times13}$ and parameter vector $\boldsymbol{\theta}_{\mathbf{O}_2} \in \mathbb{R}^{13}$ can be solved as shown in [8, in Appendix A]. Moreover, in (22), $\widehat{\boldsymbol{\theta}}_{\mathbf{O}_2}$ denotes the estimate of $\boldsymbol{\theta}_{\mathbf{O}_2}$ and $\mathbf{K}_{\mathbf{O}_2}$ is a symmetric positive-definite matrix characterizing the velocity feedback control.

The estimated parameter vector $\widehat{\boldsymbol{\theta}}_{\mathbf{O}_2}$ in (22) needs to be updated. Define

$$\mathbf{s}_{\mathbf{O}_2} = \mathbf{Y}_{\mathbf{O}_2}^T({}^{\mathbf{O}_2}V_{\mathrm{r}} - {}^{\mathbf{O}_2}V). \quad (24)$$

Then, (3) can be used to update the ith element of $\widehat{\boldsymbol{\theta}}_{\mathbf{O}_2}$ as

$$\widehat{\theta}_{\mathbf{O}_2 i} = \mathscr{P}(\mathrm{s}_{\mathbf{O}_2 i}, \rho_{\mathbf{O}_2 i}, \underline{\theta}_{\mathbf{O}_2 i}, \overline{\theta}_{\mathbf{O}_2 i}, t), \forall i \in \{1,2,...,13\} \quad (25)$$

where $\widehat{\theta}_{\mathbf{O}_2 i}$ denotes the ith element of $\widehat{\boldsymbol{\theta}}_{\mathbf{O}_2}$, $\mathrm{s}_{\mathbf{O}_2 i}$ denotes the ith element of $\mathbf{s}_{\mathbf{O}_2}$, $\rho_{\mathbf{O}_2 i} > 0$ is the update gain, and $\underline{\theta}_{\mathbf{O}_2 i}$ and $\overline{\theta}_{\mathbf{O}_2 i}$ denote the lower bound and the upper bound of $\theta_{\mathbf{O}_2 i}$.

In relation to (18), the required force resultant equation can be written as

$${}^{\mathbf{O}_2}F_{\mathrm{r}}^* = {}^{\mathbf{O}_2}\mathbf{U}_{\mathbf{T}_{\mathrm{O}2}}{}^{\mathrm{To2}}F_{\mathrm{r}} - {}^{\mathbf{O}_2}\mathbf{U}_{\mathbf{G}}{}^{\mathbf{G}}F_{\mathrm{r}}. \quad (26)$$

Finally, the following Lemma 4 is used to prove the *virtual stability* of Object 2.

Lemma 4: Consider Object 2, described by (15), (17) and (18), combined with its control equations (20), (22) and (26) and with the parameter adaptation (24) and (25). Let the non-negative accompanying function $v_{\mathbf{O}_2}$ be

$$\begin{aligned}v_{\mathbf{O}_2} = &\frac{1}{2}({}^{\mathbf{O}_2}V_{\mathrm{r}} - {}^{\mathbf{O}_2}V)^T\mathbf{M}_{\mathbf{O}_2}({}^{\mathbf{O}_2}V_{\mathrm{r}} - {}^{\mathbf{O}_2}V)\\ &+ \frac{1}{2}\sum_{i=1}^{13}\frac{(\theta_{\mathbf{O}_2 i} - \widehat{\theta}_{\mathbf{O}_2 i})^2}{\rho_{\mathbf{O}_2 i}}\end{aligned} \quad (27)$$

Then, the time derivative of (27) can be expressed by

$$\dot{v}_{\mathbf{O}_2} \leqslant -({}^{\mathbf{O}_2}V_{\mathrm{r}} - {}^{\mathbf{O}_2}V)^T\mathbf{K}_{\mathbf{O}_2}({}^{\mathbf{O}_2}V_{\mathrm{r}} - {}^{\mathbf{O}_2}V) + p_{\mathbf{T}_{\mathrm{O}2}} - p_{\mathbf{G}} \quad (28)$$

where $p_{\mathbf{T}_{\mathrm{O}2}}$ is the VPF by Definition 5 at the driven VCP of Object 2, and $p_{\mathbf{G}}$ characterizes the VPF between the end-effector and the environment.

Proof: The proof is similar to Appendix B in [23]. ■

Remark 1: Note that Object 2 has only one VCP (see Fig. 2) but two VPFs exists in (28). The VPF $p_{\mathbf{T}_{\mathrm{O}2}}$ locates at the VCP in Object 2. Thus, for the *virtual stability* of Object 2, a solution (which satisfies Definition 6) must be found for the VPF $p_{\mathbf{G}}$ in (28). This will be addressed later in Section V-A.

B. The Design of the Proposed Impedance Control

In this section, the impedance control law by Hogan [25] is introduced first in Section IV-B1. Then, the proposed Cartesian space impedance control laws are designed in Section IV-B2.

1) Impedance Control Law: In view of Hogan [25], the target impedance for the manipulator can be described as

$${}^{\mathbf{G}}\boldsymbol{f}_{\mathrm{d}} - {}^{\mathbf{G}}\boldsymbol{f} = -\mathbf{M}_{\mathrm{d}}(\ddot{\boldsymbol{\chi}}_{\mathrm{d}} - \ddot{\boldsymbol{\chi}}) - \mathbf{D}_{\mathrm{d}}(\dot{\boldsymbol{\chi}}_{\mathrm{d}} - \dot{\boldsymbol{\chi}}) - \mathbf{K}_{\mathrm{d}}(\boldsymbol{\chi}_{\mathrm{d}} - \boldsymbol{\chi}) \quad (29)$$

where $\mathbf{M}_{\mathrm{d}} \in \mathbb{R}^{2\times2}$, $\mathbf{D}_{\mathrm{d}} \in \mathbb{R}^{2\times2}$ and $\mathbf{K}_{\mathrm{d}} \in \mathbb{R}^{2\times2}$ are diagonal positive-definite matrices and characterize the desired inertia, damping and stiffness, respectively. Neglecting the inertia term in (29), the target impedance can be written as

$${}^{\mathbf{G}}\boldsymbol{f}_{\mathrm{d}} - {}^{\mathbf{G}}\boldsymbol{f} = -\mathbf{D}_{\mathrm{d}}(\dot{\boldsymbol{\chi}}_{\mathrm{d}} - \dot{\boldsymbol{\chi}}) - \mathbf{K}_{\mathrm{d}}(\boldsymbol{\chi}_{\mathrm{d}} - \boldsymbol{\chi}). \quad (30)$$

Then, the following Assumption 1 is made for the desired impedance parameters $\mathbf{D}_{\mathrm{d}}$ and $\mathbf{K}_{\mathrm{d}}$.

Assumption 1: The desired damping $\mathbf{D}_{\mathrm{d}}$ and stiffness $\mathbf{K}_{\mathrm{d}}$ are selected such that: 1) their ratio and magnitudes are not subject to unstable behavior in the overall system; and 2) the target impedance in (30) is attainable for the manipulator.

Assumption 1 imposes the condition that the impedance parameters $\mathbf{D}_{\mathrm{d}}$ and $\mathbf{K}_{\mathrm{d}}$ must be selected within the dynamic range of achievable impedance, so-called Z-width [41], which defines the combination of stiffness and damping that can be passively achieved by a certain mechanism. One method to define Z-width for hydraulic articulated systems is given in [42].

2) Proposed Impedance Control Laws: In the framework of VDC, the required velocity[1] serves as a reference trajectory for a system and the control objective is to make the controlled actual velocities track the required velocities. In this section, the

[1]The general format of a required velocity includes a desired velocity (which usually serves as a reference trajectory for a system) and one or more terms that are related to control errors [8].

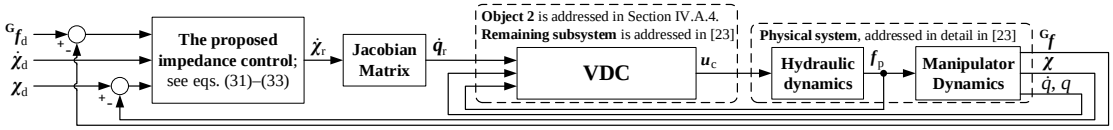

Fig. 3. Diagram of the designed novel impedance control for the hydraulic manipulator. The required Cartesian velocity $\dot{\boldsymbol{\chi}}_r$ is computed from (31). Then, the required joint velocity vector $\dot{\boldsymbol{q}}_r$ is solved using the Jacobian matrix. The detailed structure for the remaining subsystem (see Fig. 1) inside the VDC block can be found in [23]. The output $\boldsymbol{u}_c$ of the VDC block is the control signal for the hydraulic valves, which control the hydraulic cylinders. Finally, the motion dynamics of the manipulator is produced by the output force $\boldsymbol{f}_p$ of the hydraulic cylinders. Please see [23] for more details.

objective is to design such a control for the required Cartesian velocity vector $\dot{\boldsymbol{\chi}}_r \in \mathbb{R}^2$ in (19), which 1) realizes the Cartesian impedance behaviour for the manipulator and 2) qualifies Object 2 as *virtually stable* in the sense of Definition 6.

Let $\dot{\boldsymbol{\chi}}_r$ for the manipulator be designed as

$$\dot{\boldsymbol{\chi}}_r = \dot{\boldsymbol{\chi}}_d + \boldsymbol{\Lambda}_\chi(\boldsymbol{\chi}_d - \boldsymbol{\chi}) + \boldsymbol{\Lambda}_f({}^G\boldsymbol{f}_d - {}^G\boldsymbol{f}) \tag{31}$$

where $\boldsymbol{\Lambda}_\chi \in \mathbb{R}^{2\times 2}$ and $\boldsymbol{\Lambda}_f \in \mathbb{R}^{2\times 2}$ are two diagonal positive-definite matrices characterizing Cartesian position and force control, and let them be defined according to Condition 1.

Condition 1: The diagonal positive-definite matrices $\boldsymbol{\Lambda}_f$ and $\boldsymbol{\Lambda}_\chi$ are defined as

$$\boldsymbol{\Lambda}_f = \mathbf{D}_d^{-1} \tag{32}$$

$$\boldsymbol{\Lambda}_\chi = \mathbf{K}_d\mathbf{D}_d^{-1}. \tag{33}$$

Then, the following Theorem 1 provides that the target impedance behaviour (30) can be achieved for the system.

Theorem 1: Consider the proposed control law (31), which defines the required velocity behaviour for the system. If and only if the diagonal positive-definite matrices $\boldsymbol{\Lambda}_f$ and $\boldsymbol{\Lambda}_\chi$ in (31) are defined according to (32) and (33) in Condition 1, then the control law (31) equals the target impedance law (30).

Proof: See Appendix A. ∎

A diagram for the proposed control design is shown in Fig. 3.

Remark 2: Compared to the typical Cartesian free-space control law, term $\boldsymbol{\Lambda}_f({}^G\boldsymbol{f}_d - {}^G\boldsymbol{f})$ is included in (31). In this study, ${}^G\boldsymbol{f}_d = [0\ 0]^T$ is used. This enables a high control bandwidth in free space (see free-space results in [22]), provided that zero contact force is measured in free-space motions, i.e., $({}^G\boldsymbol{f}_d - {}^G\boldsymbol{f}) = \mathbf{0}$ holds. Alternatively, time-variant solutions for ${}^G\boldsymbol{f}_d$ are not excluded.

Remark 3: Note that the actual target impedance behavior in (30) is not directly involved in the system control; rather, the proposed impedance control law (31) with Condition 1 provides an input for the control system (see Fig. 3). In principle, the proposed control law (31) differs from the target impedance law (30). However, as Theorem 1 shows, the target impedance behaviour (30) can be designed for (31) with $\mathbf{D}_d$ and $\mathbf{K}_d$ by using Condition 1.

Theorem 1 satisfies the first objective above: realization of the target impedance behaviour for the required Cartesian velocity vector $\dot{\boldsymbol{\chi}}_r$ in (19). The realization of the second objective (Object 2 qualifies as *virtually stable* in the sense of Definition 6) using the designed control laws (31)–(33) is analyzed next in Section V-A.

V. Stability Analysis

The conceptual VPFs (see Definition 5) are a unique feature of VDC and they are used to address the dynamic interaction between subsystems. The *virtual stability* (see Definition 6) of every subsystem ensures that, at every placed VCP, a negative VPF (at a driving VCP of a subsystem) is connected to its corresponding positive VPF (at a driven VCP of the adjacent subsystem). Thus, VPFs act as "stability connectors" between subsystems; eventually, they cancel each other out at every VCP [8]. Finally, as addressed in Theorem 2.1 in [8], the *virtual stability* of every subsystem ensures the L_2 and L_∞ stability (see Lemma 1) of the entire system.

As can be seen from Fig. 2, only one VCP (having a VPF $p_{\mathbf{T}_{O2}}$; see (28)) is specified for Object 2. However, in (28), there also exists another VPF $p_{\mathbf{G}}$ (characterizing the dynamic interaction between the manipulator and the environment), which has no "stabilizing counterpart". Consequently, it is control designer's obligation to ensure that a control is designed for the system such that Object 2 qualifies to be *virtually stable*. Next, in Section V-A, the VPF $p_{\mathbf{G}}$ between the manipulator and the environment is analyzed using Definitions 5–6, eventually leading to the stabilizing solution for $p_{\mathbf{G}}$ and *virtual stability* of Object 2. Finally, the stability of the entire system is proven in Section V-B.

A. Virtual Stability of Object 2

Using the designed control law (31), the following Lemma 5 can be derived.

Lemma 5: Definition 5, (14), (16), (19), (21), (30) and (31) yields

$$\begin{aligned} p_{\mathbf{G}} = {} & (\dot{\boldsymbol{\chi}}_d - \dot{\boldsymbol{\chi}})^T(\mathbf{D}_d\boldsymbol{\Lambda}_f\mathbf{D}_d - \mathbf{D}_d)(\dot{\boldsymbol{\chi}}_d - \dot{\boldsymbol{\chi}}) \\ & + (\boldsymbol{\chi}_d - \boldsymbol{\chi})^T(\mathbf{K}_d\boldsymbol{\Lambda}_f\mathbf{K}_d - \boldsymbol{\Lambda}_\chi\mathbf{K}_d)(\boldsymbol{\chi}_d - \boldsymbol{\chi}) \\ & + (\boldsymbol{\chi}_d - \boldsymbol{\chi})^T(2\mathbf{D}_d\boldsymbol{\Lambda}_f\mathbf{K}_d - \boldsymbol{\Lambda}_\chi\mathbf{D}_d - \mathbf{K}_d)(\dot{\boldsymbol{\chi}}_d - \dot{\boldsymbol{\chi}}). \end{aligned} \tag{34}$$

Proof: See Appendix B. ∎

Then, the following Lemma 6 is defined for $p_{\mathbf{G}}$ to provide sufficient conditions for the *virtual stability* of Object 2.

Lemma 6: Let the following constraints hold for the diagonal positive-definite matrices $\boldsymbol{\Lambda}_f$ and $\boldsymbol{\Lambda}_\chi$:

$$\boldsymbol{\Lambda}_f \geqslant \mathbf{D}_d^{-1} \tag{35}$$

$$\boldsymbol{\Lambda}_\chi \leqslant \mathbf{K}_d\boldsymbol{\Lambda}_f. \tag{36}$$

Then, it follows from Lemma 5 that

$$\int_0^t p_{\mathbf{G}}(\tau)d\tau \geqslant -\gamma_{\mathbf{G}} \tag{37}$$

holds with $0 \leqslant \gamma_{\mathbf{G}} < \infty$.

Proof: See Appendix C. ∎

Finally, the following Theorem 2 ensures that Object 2 qualifies as *virtually stable* in the sense of Definition 6.

Theorem 2: Let Condition 1 hold. Then, using Lemma 4, Lemma 5 and Lemma 6, Object 2 qualifies as *virtually stable* in the sense of Definition 6.

Proof: Let Condition 1 hold. Substituting $\mathbf{\Lambda}_f$ and $\mathbf{\Lambda}_\chi$ (in Condition 1) into Lemma 5 yields $p_{\mathbf{G}} = 0 \rightarrow \int_0^t p_{\mathbf{G}}(\tau)d\tau = 0$, which satisfies (37) in Lemma 6 (note that Condition 1 satisfies the constraints in (35) and (36) in Lemma 6). Consider the fact that Object 2 has one driven VCP associated with frame $\{\mathbf{T}_{\mathrm{O2}}\}$. Then, using Lemma 4 and (37), Object 2 qualifies as *virtually stable* in the sense of Definition 6. ∎

Remark 4: The design process for the proposed impedance control laws (31)–(33) is iterative. The *virtual stability*, i.e, Definition 6, of Object 2 determines the general constraints for this process. In addition, the designed control input should be written in the form of required velocity (see the footnote in Section IV-B2), constraining the design of (31). Then, given the target impedance law (30), Definition 5 is used to design the control laws (31)–(33), which realizes the Cartesian impedance behavior for the system (see Theorem 1) and provides *virtual stability* for Object 2 (see Theorem 2).

Remark 5: Assumption 1, Condition 1 and Theorem 1 define that $\mathbf{\Lambda}_f$ and $\mathbf{\Lambda}_\chi$ in (31) are not subject to unstable system behaviour. As the constraints (35) and (36) in Lemma 6 suggest, in addition to Condition 1, other stable solutions for $\mathbf{\Lambda}_f$ and $\mathbf{\Lambda}_\chi$ can also exist. This is true; a Z-width [41] can be determined for the impedance-controlled systems [42]. Note that selecting $\mathbf{\Lambda}_f$ and $\mathbf{\Lambda}_\chi$ with (35) and (36) (excluding solution in Condition 1) will result to different impedance behaviour in relation to the specified $\mathbf{D}_{\mathrm{d}}$ and $\mathbf{K}_{\mathrm{d}}$.

B. Stability of the Entire System

In relation to [23], only the control laws for Object 2 have been changed in this paper. Thus, in view of [23], the non-negative accompanying function and its time-derivative for the remaining subsystem, shown with dashed lines in Fig. 1(b)–(c), can be written as

$$v_{\mathbf{R}} \geqslant 0 \tag{38}$$

$$\dot{v}_{\mathbf{R}} \leqslant -p_{\mathbf{T}_{\mathrm{O2}}} \tag{39}$$

where $p_{\mathbf{T}_{\mathrm{O2}}}$ is the VPF at the driving VCP of this subsystem.

The following Theorem 3 guarantees the stability of the entire system, in view of Lemma 1.

Theorem 3: Consider Object 2, shown in Fig. 2 and described by Lemma 5. Furthermore, let the remaining subsystem be addressed with (38) and (39), and let Assumption 1 and Condition 1 hold. Then, using (27), (28), (38), (39) and Lemma 6, it can be shown that ${}^{\mathbf{O}_2}V_{\mathrm{r}} - {}^{\mathbf{O}_2}V \in L_2 \bigcap L_\infty$ holds, in view of Lemma 1. Consequently, this yields that $\mathbf{\Lambda}_f^{-1}(\dot{\boldsymbol{\chi}}_{\mathrm{d}} - \dot{\boldsymbol{\chi}}) + \mathbf{\Lambda}_f^{-1}\mathbf{\Lambda}_\chi(\boldsymbol{\chi}_{\mathrm{d}} - \boldsymbol{\chi}) + ({}^{\mathbf{G}}\boldsymbol{f}_{\mathrm{d}} - {}^{\mathbf{G}}\boldsymbol{f}) \in L_2 \bigcap L_\infty$ holds.

In the special case $({}^{\mathbf{G}}\boldsymbol{f}_{\mathrm{d}} - {}^{\mathbf{G}}\boldsymbol{f}) = 0$, it follows from Lemma 2 that $\dot{\boldsymbol{\chi}}_{\mathrm{d}} - \dot{\boldsymbol{\chi}} \in L_2 \bigcap L_\infty$ and $\boldsymbol{\chi}_{\mathrm{d}} - \boldsymbol{\chi} \in L_2 \bigcap L_\infty$ hold, with an asymptotic convergence for $\boldsymbol{\chi}_{\mathrm{d}} - \boldsymbol{\chi}$ (in the sense of Lemma 3).

Proof: See Appendix D. ∎

Remark 6: In Theorem 3, $({}^{\mathbf{G}}\boldsymbol{f}_{\mathrm{d}} - {}^{\mathbf{G}}\boldsymbol{f}) \neq 0$ denotes constrained motion and $({}^{\mathbf{G}}\boldsymbol{f}_{\mathrm{d}} - {}^{\mathbf{G}}\boldsymbol{f}) = 0$, with ${}^{\mathbf{G}}\boldsymbol{f}_{\mathrm{d}} = [0\ 0]^T$, denotes free-space motions.

VI. Experiments

This section demonstrates the contact control performance of the proposed controller. System set-up and implementation issues are outlined in Section VI-A. Section VI-B demonstrates the controller's ability to prevent excessive contact forces when the manipulator collides with an object. The main results of this study are presented in Section VI-C, where the proposed control method is verified and the accuracy of Theorem 1 is shown in practice.

A. Experimental Set-up and Implementation Issues

The experimental set-up for the contact experiments is shown in Fig. 4. For the environmental contact, a set of wooden pallets was placed on a rubber mat. The set-up consisted of the following hardware components:

- dSpace DS1103 system, with 3 ms sample time
- 475 kg payload, denoted as M in Fig. 1(a)
- Bosch 4WRPEH10 proportional valve (100 dm^3/min @ Δp = 3.5 MPa per notch) for cylinders
- Heidenhain ROD 456 incremental encoder (5000 inc/rev) with IVB interpolation units for joints 1 and 2, providing a theoretical piston position resolution $< 1.2 \times 10^{-3}$ mm
- Druck PTX1400 pressure transmitters (range of 25 MPa)

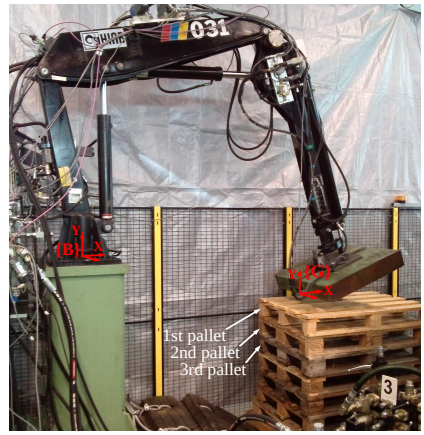

Fig. 4. The experimental set-up. Manipulator's base frame $\{\mathbf{B}\}$ and end-effector target frame $\{\mathbf{G}\}$ are shown in red. The manipulator's position in this figure shows the starting point of the driven motion trajectories.

In the experiments, the manipulator should be stiff along the frame $\{\mathbf{G}\}$ X-axis (the direction of unconstrained motion) and compliant along the frame $\{\mathbf{G}\}$ Y-axis (the direction of constrained motion). For this reason, in $\mathbf{D}_{\mathrm{d}}$ and $\mathbf{K}_{\mathrm{d}}$, high gains were imposed along the X-axis and minor gains were imposed along the Y-axis. Table I shows $\mathbf{\Lambda}_f$ and $\mathbf{\Lambda}_\chi$ based on the determined $\mathbf{D}_{\mathrm{d}}$ and $\mathbf{K}_{\mathrm{d}}$.

TABLE I
GAINS FOR THE CARTESIAN CONTROL; SEE (31)

Specified $\mathbf{D}_{\mathrm{d}}$ and $\mathbf{K}_{\mathrm{d}}$ for the manipulator
$\mathbf{D}_{\mathrm{d}} = \mathrm{diag}(1 \cdot 10^5,\ 2.2 \cdot 10^3)$
$\mathbf{K}_{\mathrm{d}} = \mathrm{diag}(1 \cdot 10^6,\ 1.1 \cdot 10^4)$
$\Downarrow$
Condition 1
$\mathbf{\Lambda}_f = \mathrm{diag}(1.0 \cdot 10^{-5},\ 4.545 \cdot 10^{-4})$
$\mathbf{\Lambda}_\chi = \mathrm{diag}(10,\ 5)$

As Fig. 4 shows, a force sensor that measures the exact six-dimensional contact forces/moments at the end-effector was not used. The contact forces (applied by the manipulator on the environment) were estimated from the cylinder chamber pressures by removing the gravitational forces. This methodology to estimate the contact forces is discussed in more detail in [23]. Even though this method has some limitations, e.g., in force estimation accuracy, it may provide a practical solution for many heavy-duty operations where a fragile six-DOF force/moment sensor cannot be placed at the end-effector.

B. Collision Experiment

To test the proposed controller interaction dynamics behaviour, in the first set of experiments, a collision between the manipulator end-effector and an obstacle was arranged with three different Cartesian velocities. The manipulator position in Fig. 4 shows the starting point for the test trajectories. Then, a set of wooden pallets was placed in the way of the driven trajectories, so that the end-effector collided with the surface of the second pallet (when pallet 1 was removed); see Fig. 4. In the first trajectory, the end-effector was instructed to travel from -0.5 m to -1.0 m along the Y-axis of the system base frame $\{\mathbf{B}\}$ in one second. Then, the same path was driven over three seconds and, finally, over five seconds.

The plots in the first row of Fig. 5 show the manipulator position paths in blue, red and green, using a one-second trajectory, three-second trajectory and five-second trajectory, respectively. In these plots, the desired path is shown in black and the surface of the second pallet is depicted with a dashed line. As these plots show, the proposed controller limits the end-effector path when contact with the environment is established. The collision velocities between the end-effector and the environment were -0.52 m/s, -0.26 m/s and -0.18 m/s for the one-second trajectory, three-second trajectory and five-second trajectory, respectively. Note that the X-axes of the plots are scaled significantly smaller compared to the Y-axes.

The plot in the second row of Fig. 5 shows the measured end-effector contact forces in blue, red and green, using the one-second trajectory, three-second trajectory and five-second trajectory, respectively. The contact points are shown by blue circles. As this plot shows, the proposed controller efficiently limits the contact force (applied by the manipulator on the environment along the frame $\{\mathbf{G}\}$ Y-axis) to approximately -2800 N when contact with the environment is established. Because contact forces were estimated from the cylinder chamber pressures, inaccuracies exist in the estimates; therefore, the measured end-effector force before contact is not zero. This is due to the fact that system inertia and piston friction were not considered in the contact force estimation. Thus, the smaller velocity yields a better contact force estimation in free space. One practical method to estimate link accelerations (and to address the system inertia in the contact force estimation proposed in [23]) can be found in [43].

C. Target Impedance Behaviour

In the second set of experiments, three test cases were chosen to evaluate the ability of the proposed controller to perform the target impedance behaviour. In test case 1, contact occurred on the surface of pallet 1. In test case 2, contact occurred on the surface of pallet 2 (after removing pallet 1). In test case 3, contact occurred on the surface of pallet 3 (after removing pallets 1 and 2). The manipulator position in Fig. 4 shows the starting point for the test trajectories.

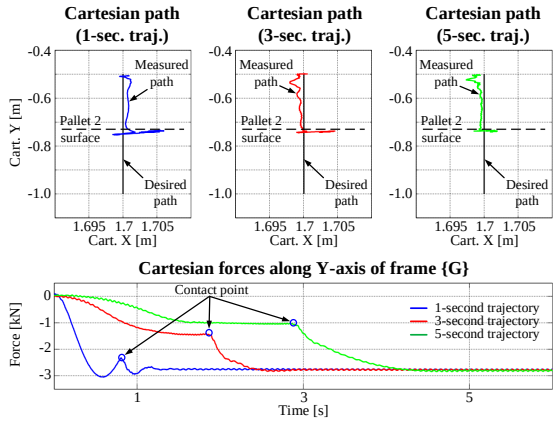

Fig. 5. The collision experiments. The plots in the first row show the measured end-effector paths in color, the desired paths in black and the surface of the environment with the dashed line. The test cases in the first row are driven using 1-second, 3-second and 5-second trajectories. The plot in the second row shows the measured contact forces in the test trajectories.

Fig. 6 shows the test trajectory in the Cartesian coordinates (along the Y- and X-axes of the system base frame $\{\mathbf{B}\}$). The surfaces of wooden pallets 1–3 are marked in the first plot (see relation to Fig. 4). As Fig. 6 shows, the end-effector was first instructed to travel a distance of -0.5 m along the Y-axis in three seconds (see time interval 0–3 s from the first plot). Then, the end-effector was instructed to travel a distance of 0.5 m along the X-axis in three seconds (see time interval 3–6 s from the second plot). Finally, the end-effector was instructed to travel a distance of 0.5 m along the Y-axis in three seconds (see time interval 6–9 s from the first plot).

The main results of this paper are shown in Figs. 7–9. The first plots in Figs. 7–9 show the desired Cartesian paths in black and the measured Cartesian paths in red. The contact point is shown by a blue circle in these plots. As all these plots show, the proposed controller delimits the end-effector position when contact with the environment occurs, thus preventing excessive contact forces from being applied to the environment.

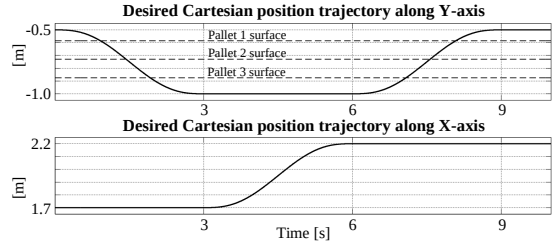

Fig. 6. Desired Cartesian position trajectories. The first plot shows the desired Cartesian position trajectory along the Y-axis, and the second plot shows the the desired Cartesian position trajectory along the X-axis. The surfaces of wooden pallets 1–3 are marked in the first plot (see the pallets in Fig. 4).

The second plots in Figs. 7–9 show the position tracking error along the X-axis of frame $\{\mathbf{G}\}$, in which direction the manipulator was made stiff. The contact point is shown by a blue circle in these plots. As these plots show, the maximum position tracking errors are all below 4 mm for the test trajectory. This can be considered a significant result in light of the manipulator scale, which has a reach of about 3.2 meters.

The last plots in Figs. 7–9 show the measured contact force exerted by the manipulator on the environment (shown in black) along the Y-axis of frame $\{\mathbf{G}\}$, in direction which the manipulator was made compliant. The contact point is shown by a blue circle in these plots. As addressed in Theorem 1, the target impedance behavior (30) should be achieved for the manipulator when the diagonal positive-definite matrices $\mathbf{\Lambda}_f$ and $\mathbf{\Lambda}_\chi$ in (31) are defined according to Condition 1. Consequently, the measured contact force should correspond to the contact force ${}^{\mathbf{G}}f_y$ solved from (30), i.e,[2]

$$ {}^{\mathbf{G}}f_y = \boldsymbol{y}_f[\mathbf{D}_\mathrm{d}(\dot{\boldsymbol{\chi}}_\mathrm{d} - \dot{\boldsymbol{\chi}}) + \mathbf{K}_\mathrm{d}(\boldsymbol{\chi}_\mathrm{d} - \boldsymbol{\chi}) + {}^{\mathbf{G}}\boldsymbol{f}_\mathrm{d}] \qquad (40) $$

where $\boldsymbol{y}_f = [0\ 1]$, ${}^{\mathbf{G}}\boldsymbol{f}_\mathrm{d} = [0\ 0]^T$, and $(\dot{\boldsymbol{\chi}}_\mathrm{d} - \dot{\boldsymbol{\chi}})$ and $(\boldsymbol{\chi}_\mathrm{d} - \boldsymbol{\chi})$ are variables from the driven test cases. As the last plots in Figs. 7–9 show, the measured contact force (shown in black) corresponds accurately to the contact force suggested by (40) (shown in green). The nearly perfect matching of the two lines in these plots demonstrates the accuracy of Theorem 1. The maximum deviations between the measured contact force and (40) are 136 N, 170 N and 146 N in Figs. 7–9, respectively.

VII. Conclusions

In this paper, a novel impedance control method in the Cartesian space was developed for hydraulic manipulators. To acquire high-bandwidth closed-loop performance for the system, the internal control for the manipulator was designed according to the subsystem-dynamics-based virtual decomposition control (VDC) approach. Interaction dynamics between the hydraulic manipulator end-effector and the environment were analyzed in a novel manner, using the *virtual power flow*, which is a unique feature of VDC. From the analysis, an explicit method (see Condition 1) was developed to define parameters for the proposed impedance control law (external control for the manipulator), so that target impedance behavior can be designed for the hydraulic manipulator. The L_2 and L_∞ stability was guaranteed for both free-space and constrained motion control. The experimental results support the mathematical theorems on the stability-guaranteed (see Theorem 3) target impedance behaviour (see Theorem 1).

Even though a two-DOF system was studied in this paper, the developed approach is extendable to systems with any number of actuators. The results of this study can be used to realize compliant behaviour for complex and nonlinear systems, not limited only to hydraulic manipulators. The control method, which rigorously addresses the nonlinear dynamic behaviour of the system, can be applied to many dynamically challenging (robotic) tasks, such as legged locomotion.

[2]Note that (40) is solved from the target impedance law (30) by Hogan [25], which is not directly involved in the control laws; rather it is used to define $\mathbf{\Lambda}_f$ and $\mathbf{\Lambda}_\chi$ in control law (31); see Condition 1 and Remark 3.

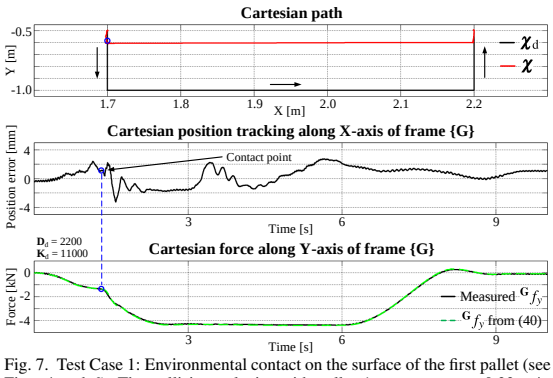

Fig. 7. Test Case 1: Environmental contact on the surface of the first pallet (see Figs. 4 and 6). The collision velocity with pallet 1 was approx. -0.22 m/s. The first plot shows the desired Cartesian position path in black and the measured Cartesian path in red. The second plot shows the Cartesian position tracking along the frame $\{\mathbf{G}\}$ X-axis. The last plot shows the measured Cartesian contact force (along the frame $\{\mathbf{G}\}$ Y-axis) in black. The contact force suggested by the target impedance law (40) is shown in green.

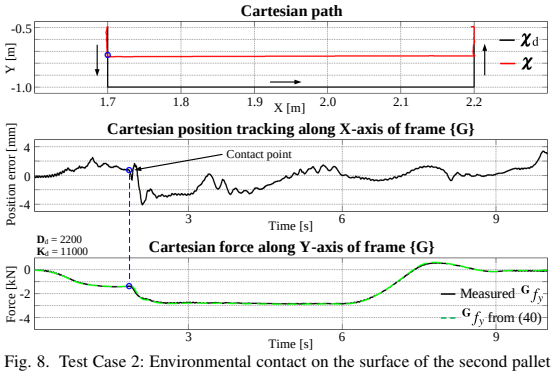

Fig. 8. Test Case 2: Environmental contact on the surface of the second pallet (see Figs. 4 and 6). The collision velocity with pallet 2 was approx. -0.27 m/s. The first plot shows the desired Cartesian position path in black and the measured Cartesian path in red. The second plot shows the Cartesian position tracking along the frame $\{\mathbf{G}\}$ X-axis. The last plot shows the measured Cartesian contact force (along the frame $\{\mathbf{G}\}$ Y-axis) in black. The contact force suggested by the target impedance law (40) is shown in green.

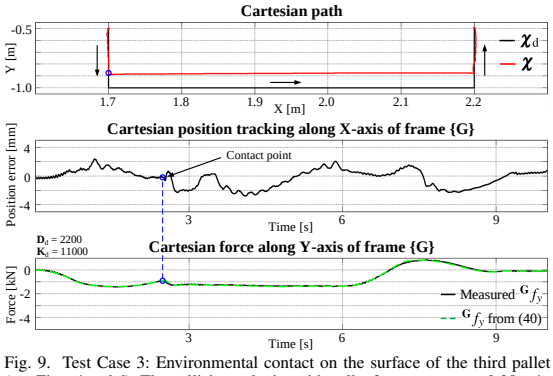

Fig. 9. Test Case 3: Environmental contact on the surface of the third pallet (see Figs. 4 and 6). The collision velocity with pallet 3 was approx. -0.28 m/s. The first plot shows the desired Cartesian position path in black and the measured Cartesian path in red. The second plot shows the Cartesian position tracking along the frame $\{\mathbf{G}\}$ X-axis. The last plot shows the measured Cartesian contact force (along the frame $\{\mathbf{G}\}$ Y-axis) in black. The contact force suggested by the target impedance law (40) is shown in green.

APPENDIX A
PROOF FOR THEOREM 1

Define $\mathbf{\Lambda}_f = \mathbf{D}_\mathrm{d}^{-1}$ and $\mathbf{\Lambda}_\chi = \mathbf{K}_\mathrm{d}\mathbf{\Lambda}_f$, as proposed in Condition 1. Then, it follows from the diagonal positive-definite property of $\mathbf{D}_\mathrm{d}$, $\mathbf{K}_\mathrm{d}$ and $\mathbf{\Lambda}_\chi$ that

$$\mathbf{D}_\mathrm{d}^{-1}\mathbf{\Lambda}_\chi\mathbf{D}_\mathrm{d} = \mathbf{\Lambda}_\chi \tag{41}$$
$$\mathbf{D}_\mathrm{d}\mathbf{K}_\mathrm{d}\mathbf{D}_\mathrm{d}^{-1} = \mathbf{K}_\mathrm{d} \tag{42}$$

hold. Substituting (30) into (31) and using Condition 1 and (41) yields

$$\begin{aligned}\dot{\boldsymbol{\chi}}_\mathrm{r} &= \dot{\boldsymbol{\chi}}_\mathrm{d} + \mathbf{\Lambda}_\chi(\boldsymbol{\chi}_\mathrm{d} - \boldsymbol{\chi}) - \mathbf{\Lambda}_f[\mathbf{D}_\mathrm{d}(\dot{\boldsymbol{\chi}}_\mathrm{d} - \dot{\boldsymbol{\chi}}) + \mathbf{K}_\mathrm{d}(\boldsymbol{\chi}_\mathrm{d} - \boldsymbol{\chi})] \\ &= \dot{\boldsymbol{\chi}}_\mathrm{d} + \mathbf{\Lambda}_\chi(\boldsymbol{\chi}_\mathrm{d} - \boldsymbol{\chi}) - \mathbf{D}_\mathrm{d}^{-1}\mathbf{D}_\mathrm{d}(\dot{\boldsymbol{\chi}}_\mathrm{d} - \dot{\boldsymbol{\chi}}) \\ &\quad -\mathbf{D}_\mathrm{d}^{-1}\mathbf{\Lambda}_\chi\mathbf{D}_\mathrm{d}(\boldsymbol{\chi}_\mathrm{d} - \boldsymbol{\chi}) \\ &= \dot{\boldsymbol{\chi}}_\mathrm{d} + \mathbf{\Lambda}_\chi(\boldsymbol{\chi}_\mathrm{d} - \boldsymbol{\chi}) - \dot{\boldsymbol{\chi}}_\mathrm{d} + \dot{\boldsymbol{\chi}} - \mathbf{\Lambda}_\chi(\boldsymbol{\chi}_\mathrm{d} - \boldsymbol{\chi}) \\ &= \dot{\boldsymbol{\chi}}. \end{aligned} \tag{43}$$

Then, using Condition 1, (42) and (43) yields

$$\begin{aligned}&\dot{\boldsymbol{\chi}}_\mathrm{r} = \dot{\boldsymbol{\chi}}_\mathrm{d} + \mathbf{\Lambda}_\chi(\boldsymbol{\chi}_\mathrm{d} - \boldsymbol{\chi}) + \mathbf{\Lambda}_f({}^{\mathbf{G}}\boldsymbol{f}_\mathrm{d} - {}^{\mathbf{G}}\boldsymbol{f}) \\ \Leftrightarrow\ & {}^{\mathbf{G}}\boldsymbol{f}_\mathrm{d} - {}^{\mathbf{G}}\boldsymbol{f} = -\mathbf{\Lambda}_f^{-1}(\dot{\boldsymbol{\chi}}_\mathrm{d} - \dot{\boldsymbol{\chi}}_\mathrm{r}) - \mathbf{\Lambda}_f^{-1}\mathbf{\Lambda}_\chi(\boldsymbol{\chi}_\mathrm{d} - \boldsymbol{\chi}) \\ \Leftrightarrow\ & {}^{\mathbf{G}}\boldsymbol{f}_\mathrm{d} - {}^{\mathbf{G}}\boldsymbol{f} = -\mathbf{D}_\mathrm{d}(\dot{\boldsymbol{\chi}}_\mathrm{d} - \dot{\boldsymbol{\chi}}) - \mathbf{D}_\mathrm{d}\mathbf{K}_\mathrm{d}\mathbf{D}_\mathrm{d}^{-1}(\boldsymbol{\chi}_\mathrm{d} - \boldsymbol{\chi}) \\ \Leftrightarrow\ & {}^{\mathbf{G}}\boldsymbol{f}_\mathrm{d} - {}^{\mathbf{G}}\boldsymbol{f} = -\mathbf{D}_\mathrm{d}(\dot{\boldsymbol{\chi}}_\mathrm{d} - \dot{\boldsymbol{\chi}}) - \mathbf{K}_\mathrm{d}(\boldsymbol{\chi}_\mathrm{d} - \boldsymbol{\chi}). \end{aligned} \tag{44}$$

Note that the first row in (44) is equal to (31), whereas the last row is equal to (30). This completes the proof for Theorem 1. ■

APPENDIX B
PROOF FOR LEMMA 5

It follows from Definition 5, (14), (16), (19), (21), (30), (31), $\mathbf{N}_\mathrm{c}^T\mathbf{N}_\mathrm{c} = \mathbf{I}_{2\times 2}$ and the diagonal positive-definite property[3] of matrices $\mathbf{\Lambda}_\chi$, $\mathbf{\Lambda}_f$, $\mathbf{D}_\mathrm{d}$ and $\mathbf{K}_\mathrm{d}$ that

$$\begin{aligned}p_\mathbf{G} &= ({}^{\mathbf{G}}V_\mathrm{r} - {}^{\mathbf{G}}V)^T({}^{\mathbf{G}}F_\mathrm{r} - {}^{\mathbf{G}}F) \\ &= [(\dot{\boldsymbol{\chi}}_\mathrm{d} - \dot{\boldsymbol{\chi}}) + \mathbf{\Lambda}_\chi(\boldsymbol{\chi}_\mathrm{d} - \boldsymbol{\chi}) + \mathbf{\Lambda}_f({}^{\mathbf{G}}\boldsymbol{f}_\mathrm{d} - {}^{\mathbf{G}}\boldsymbol{f})]^T\mathbf{N}_\mathrm{c}^T \\ &\quad \times \mathbf{N}_\mathrm{c}({}^{\mathbf{G}}\boldsymbol{f}_\mathrm{d} - {}^{\mathbf{G}}\boldsymbol{f}) \\ &= (\dot{\boldsymbol{\chi}}_\mathrm{d} - \dot{\boldsymbol{\chi}})^T({}^{\mathbf{G}}\boldsymbol{f}_\mathrm{d} - {}^{\mathbf{G}}\boldsymbol{f}) + (\boldsymbol{\chi}_\mathrm{d} - \boldsymbol{\chi})^T\mathbf{\Lambda}_\chi^T({}^{\mathbf{G}}\boldsymbol{f}_\mathrm{d} - {}^{\mathbf{G}}\boldsymbol{f}) \\ &\quad + ({}^{\mathbf{G}}\boldsymbol{f}_\mathrm{d} - {}^{\mathbf{G}}\boldsymbol{f})^T\mathbf{\Lambda}_f^T({}^{\mathbf{G}}\boldsymbol{f}_\mathrm{d} - {}^{\mathbf{G}}\boldsymbol{f}) \\ &= -(\dot{\boldsymbol{\chi}}_\mathrm{d} - \dot{\boldsymbol{\chi}})^T[\mathbf{D}_\mathrm{d}(\dot{\boldsymbol{\chi}}_\mathrm{d} - \dot{\boldsymbol{\chi}}) + \mathbf{K}_\mathrm{d}(\boldsymbol{\chi}_\mathrm{d} - \boldsymbol{\chi})] \\ &\quad - (\boldsymbol{\chi}_\mathrm{d} - \boldsymbol{\chi})^T\mathbf{\Lambda}_\chi^T[\mathbf{D}_\mathrm{d}(\dot{\boldsymbol{\chi}}_\mathrm{d} - \dot{\boldsymbol{\chi}}) + \mathbf{K}_\mathrm{d}(\boldsymbol{\chi}_\mathrm{d} - \boldsymbol{\chi})] \\ &\quad + [\mathbf{D}_\mathrm{d}(\dot{\boldsymbol{\chi}}_\mathrm{d} - \dot{\boldsymbol{\chi}}) + \mathbf{K}_\mathrm{d}(\boldsymbol{\chi}_\mathrm{d} - \boldsymbol{\chi})]^T\mathbf{\Lambda}_f^T \\ &\quad \times [\mathbf{D}_\mathrm{d}(\dot{\boldsymbol{\chi}}_\mathrm{d} - \dot{\boldsymbol{\chi}}) + \mathbf{K}_\mathrm{d}(\boldsymbol{\chi}_\mathrm{d} - \boldsymbol{\chi})] \\ &= (\dot{\boldsymbol{\chi}}_\mathrm{d} - \dot{\boldsymbol{\chi}})^T(\mathbf{D}_\mathrm{d}\mathbf{\Lambda}_f\mathbf{D}_\mathrm{d} - \mathbf{D}_\mathrm{d})(\dot{\boldsymbol{\chi}}_\mathrm{d} - \dot{\boldsymbol{\chi}}) \\ &\quad + (\boldsymbol{\chi}_\mathrm{d} - \boldsymbol{\chi})^T(\mathbf{K}_\mathrm{d}\mathbf{\Lambda}_f\mathbf{K}_\mathrm{d} - \mathbf{\Lambda}_\chi\mathbf{K}_\mathrm{d})(\boldsymbol{\chi}_\mathrm{d} - \boldsymbol{\chi}) \\ &\quad + (\boldsymbol{\chi}_\mathrm{d} - \boldsymbol{\chi})^T(2\mathbf{D}_\mathrm{d}\mathbf{\Lambda}_f\mathbf{K}_\mathrm{d} - \mathbf{\Lambda}_\chi\mathbf{D}_\mathrm{d} - \mathbf{K}_\mathrm{d})(\dot{\boldsymbol{\chi}}_\mathrm{d} - \dot{\boldsymbol{\chi}}) \end{aligned} \tag{45}$$

holds, which validates Lemma 5. ■

[3]The diagonal property of matrices $\mathbf{\Lambda}_\chi$, $\mathbf{\Lambda}_f$, $\mathbf{D}_\mathrm{d}$ and $\mathbf{K}_\mathrm{d}$ yields $\mathbf{\Lambda}_\chi^T = \mathbf{\Lambda}_\chi$, $\mathbf{\Lambda}_f^T = \mathbf{\Lambda}_f$, $\mathbf{D}_\mathrm{d}^T = \mathbf{D}_\mathrm{d}$ and $\mathbf{K}_\mathrm{d}^T = \mathbf{K}_\mathrm{d}$.

APPENDIX C
PROOF FOR LEMMA 6

Let $\mathbf{\Lambda}_f \geqslant \mathbf{D}_\mathrm{d}^{-1}$ and $\mathbf{\Lambda}_\chi \leqslant \mathbf{K}_\mathrm{d}\mathbf{\Lambda}_f$ hold, as defined in (35) and (36). Then, it follows from (45) that

$$p_\mathbf{G} \geqslant (\boldsymbol{\chi}_\mathrm{d} - \boldsymbol{\chi})^T\mathbf{A}_1(\dot{\boldsymbol{\chi}}_\mathrm{d} - \dot{\boldsymbol{\chi}}) \tag{46}$$

holds, where $\mathbf{A}_1 = (2\mathbf{D}_\mathrm{d}\mathbf{\Lambda}_f\mathbf{K}_\mathrm{d} - \mathbf{\Lambda}_\chi\mathbf{D}_\mathrm{d} - \mathbf{K}_\mathrm{d}) \geqslant 0$ holds, in view of (35) and (36).

Integrating (46) over time yields that

$$\begin{aligned}\int_0^t p_\mathbf{G}(\tau)d\tau &\geqslant \frac{1}{2}(\boldsymbol{\chi}_\mathrm{d}(t) - \boldsymbol{\chi}(t))^T\mathbf{A}_1(\boldsymbol{\chi}_\mathrm{d}(t) - \boldsymbol{\chi}(t)) \\ &\quad -\frac{1}{2}(\boldsymbol{\chi}_\mathrm{d}(0) - \boldsymbol{\chi}(0))^T\mathbf{A}_1(\boldsymbol{\chi}_\mathrm{d}(0) - \boldsymbol{\chi}(0)) \\ &\geqslant -\frac{1}{2}(\boldsymbol{\chi}_\mathrm{d}(0) - \boldsymbol{\chi}(0))^T\mathbf{A}_1(\boldsymbol{\chi}_\mathrm{d}(0) - \boldsymbol{\chi}(0)) \\ &= -\gamma_\mathbf{G} \end{aligned} \tag{47}$$

holds with $0 \leqslant \gamma_\mathbf{G} < \infty$, which validates Lemma 6. ■

APPENDIX D
PROOF FOR THEOREM 3

Let the remaining subsystem, shown with dashed lines in Fig. 1(b)–(c), be addressed with (38) and (39), and let Assumption 1 and Condition 1 hold. Then, in view of (27) and (38), the non-negative accompanying function v_tot for the entire manipulator can be chosen as

$$\begin{aligned}v_\mathrm{tot} &= v_\mathbf{R} + v_{\mathbf{O}_2} \\ &\geqslant \frac{1}{2}({}^{\mathbf{O}_2}V_\mathrm{r} - {}^{\mathbf{O}_2}V)^T\mathbf{M}_{\mathbf{O}_2}({}^{\mathbf{O}_2}V_\mathrm{r} - {}^{\mathbf{O}_2}V) \\ &\quad + \frac{1}{2}\sum_{i=1}^{13}\frac{(\theta_{\mathbf{O}_2 i} - \widehat{\theta}_{\mathbf{O}_2 i})^2}{\rho_{\mathbf{O}_2 i}}. \end{aligned} \tag{48}$$

Then, in view of (28) and (39), the time derivative of (48) can be written as

$$\begin{aligned}\dot{v}_\mathrm{tot} &\leqslant -({}^{\mathbf{O}_2}V_\mathrm{r} - {}^{\mathbf{O}_2}V)^T\mathbf{K}_{\mathbf{O}_2}({}^{\mathbf{O}_2}V_\mathrm{r} - {}^{\mathbf{O}_2}V) - p_{\mathbf{T}_{\mathrm{O}2}} + p_{\mathbf{T}_{\mathrm{O}2}} - p_\mathbf{G} \\ &= -({}^{\mathbf{O}_2}V_\mathrm{r} - {}^{\mathbf{O}_2}V)^T\mathbf{K}_{\mathbf{O}_2}({}^{\mathbf{O}_2}V_\mathrm{r} - {}^{\mathbf{O}_2}V) - p_\mathbf{G} \end{aligned} \tag{49}$$

where, in view of Lemma 6,

$$\int_0^t p_\mathbf{G}(\tau)d\tau \geqslant -\gamma_\mathbf{G} \tag{50}$$

holds with $0 \leqslant \gamma_\mathbf{G} < \infty$.

It follows directly from Lemma 1 and (48)–(50) that

$${}^{\mathbf{O}_2}V_\mathrm{r} - {}^{\mathbf{O}_2}V \in L_2 \bigcap L_\infty \tag{51}$$

holds. Using (14), (15), (19), (20) and (51) yields

$$\dot{\boldsymbol{\chi}}_\mathrm{r} - \dot{\boldsymbol{\chi}} \in L_2 \bigcap L_\infty. \tag{52}$$

Then, subtracting $\dot{\boldsymbol{\chi}}$ from both sides of (31) and using (52) yields

$$\mathbf{\Lambda}_f^{-1}(\dot{\boldsymbol{\chi}}_\mathrm{d} - \dot{\boldsymbol{\chi}}) + \mathbf{\Lambda}_f^{-1}\mathbf{\Lambda}_\chi(\boldsymbol{\chi}_\mathrm{d} - \boldsymbol{\chi}) + ({}^{\mathbf{G}}\boldsymbol{f}_\mathrm{d} - {}^{\mathbf{G}}\boldsymbol{f}) \in L_2 \bigcap L_\infty. \tag{53}$$

Let $({}^{\mathbf{G}}\boldsymbol{f}_\mathrm{d} - {}^{\mathbf{G}}\boldsymbol{f}) = 0$ hold. Subtracting $\dot{\boldsymbol{\chi}}$ from both sides of (31) yields

$$\dot{\boldsymbol{\chi}}_\mathrm{r} - \dot{\boldsymbol{\chi}} = (\dot{\boldsymbol{\chi}}_\mathrm{d} - \dot{\boldsymbol{\chi}}) + \mathbf{\Lambda}_\chi(\boldsymbol{\chi}_\mathrm{d} - \boldsymbol{\chi}). \tag{54}$$

Then, it follows directly from Lemma 2, (52) and (54) that

$$\dot{\boldsymbol{\chi}}_{\mathrm{d}} - \dot{\boldsymbol{\chi}} \in L_2 \bigcap L_\infty \tag{55}$$

$$\boldsymbol{\chi}_{\mathrm{d}} - \boldsymbol{\chi} \in L_2 \bigcap L_\infty \tag{56}$$

hold. Then, Lemma 3 yields $\lim_{t\to\infty} \left[\boldsymbol{\chi}_{\mathrm{d}}(t) - \boldsymbol{\chi}(t)\right] = 0$. ■

REFERENCES

[1] A. Alleyne and R. Liu, "On the limitations of force tracking control for hydraulic servosystems," *J. Dyn. Syst.–T. ASME*, vol. 121, no. 2, pp. 184–190, 1999.

[2] C. An and J. Hollerbach, "Dynamic stability issues in force control of manipulators," in *Proc. American Control Conf.*, 1987, pp. 821–827.

[3] ——, "Kinematic stability issues in force control of manipulators," in *Proc. IEEE Int. Conf. Robotics and Autom.*, vol. 4, 1987, pp. 897–903.

[4] ——, "The role of dynamic models in cartesian force control of manipulators," *Int. J. Robot. Res.*, vol. 8, no. 4, pp. 51–72, 1989.

[5] S. Eppinger and W. Seering, "Understanding bandwidth limitations in robot force control," in *Proc. IEEE Int. Conf. Robotics and Autom.*, vol. 4, 1987, pp. 904–909.

[6] ——, "Three dynamic problems in robot force control," in *Proc. IEEE Int. Conf. Robotics and Autom.*, 1989, pp. 392–397.

[7] T. Yoshikawa, "Force control of robot manipulators," in *Proc. IEEE Int. Conf. Robotics and Autom.*, vol. 1, Apr. 2000, pp. 220–226.

[8] W.-H. Zhu, *Virtual Decomposition Control - Toward Hyper Degrees of Freedom Robots*. Springer-Verlag, 2010.

[9] C. An, C. Atkeson, and J. Hollerbach, *Model-based control of a robot manipulator*. MIT press Cambridge, MA, 1988, vol. 214.

[10] L. Sciavicco and B. Siciliano, *Modeling and Control of Robot Manipulators*. London: Springer, 2000.

[11] R. N. Jazar, *Theory of applied robotics: kinematics, dynamics, and control*. Springer Science & Business Media, 2010.

[12] W.-H. Zhu *et al.*, "Virtual decomposition based control for generalized high dimensional robotic systems with complicated structure," *IEEE Trans. Robot. Autom.*, vol. 13, no. 3, pp. 411–436, 1997.

[13] W.-H. Zhu, Z. Bien, and J. De Schutter, "Adaptive motion/force control of multiple manipulators with joint flexibility based on virtual decomposition," *IEEE Trans. Autom. Control*, vol. 43, no. 1, pp. 46–60, 1998.

[14] W.-H. Zhu and J. De Schutter, "Adaptive control of mixed rigid/flexible joint robot manipulators based on virtual decomposition," *IEEE Trans. Robot. Autom.*, vol. 15, no. 2, pp. 310–317, 1999.

[15] ——, "Control of two industrial manipulators rigidly holding an egg," *IEEE Control Systems*, vol. 19, no. 2, pp. 24–30, 1999.

[16] ——, "Experimental verifications of virtual-decomposition-based motion/force control," *IEEE Trans. Robot. Autom.*, vol. 18, no. 3, pp. 379–386, 2002.

[17] W.-H. Zhu and G. Vukovich, "Virtual decomposition control for modular robot manipulators," in *Proc. IFAC World Congress*, Sep. 2011, pp. 13 486–13 491.

[18] W.-H. Zhu *et al.*, "Precision control of modular robot manipulators: The VDC approach with embedded FPGA," *IEEE Trans. Robot.*, vol. 29, no. 5, pp. 1162–1179, 2013.

[19] W.-H. Zhu and J. Piedboeuf, "Adaptive output force tracking control of hydraulic cylinders with applications to robot manipulators," *J. Dynamic Syst., Meas. Control*, vol. 127, no. 2, pp. 206–217, Jun. 2005.

[20] J. Koivumäki and J. Mattila, "The automation of multi degree of freedom hydraulic crane by using virtual decomposition control," in *Proc. IEEE/ASME Int. Conf. Adv. Intell. Mechatr.*, 2013, pp. 912–919.

[21] ——, "An energy-efficient high performance motion control of a hydraulic crane applying virtual decomposition control," in *Proc. IEEE/RJS Int. Conf. Intell. Robots Syst.*, 2013, pp. 4426–4433.

[22] ——, "High performance non-linear motion/force controller design for redundant hydraulic construction crane automation," *Automation in Construction*, vol. 51, pp. 59–77, 2015.

[23] ——, "Stability-guaranteed force-sensorless contact force/motion control of heavy-duty hydraulic manipulators," *IEEE Trans. Robot.*, vol. 31, no. 4, 2015.

[24] M. Raibert and J. Craig, "Hybrid position/force control of manipulators," *J. Dyn. Syst.–T. ASME*, vol. 103, no. 2, pp. 126–133, 1981.

[25] N. Hogan, "Impedance control: An approach to manipulation: Parts I-III," *J. Dyn. Syst.–T. ASME*, vol. 107, no. 1, pp. 1–24, 1985.

[26] D. Whitney, "Historical perspective and state of the art in robot force control," in *Proc. IEEE Int. Conf. Robotics and Autom.*, vol. 2, 1985, pp. 262–268.

[27] M. Vukobratović and A. Tuneski, "Contact control concepts in manipulation robotics – an overview," *IEEE Trans. Ind. Electron.*, vol. 41, no. 1, pp. 12–24, Feb. 1994.

[28] O. Khatib, "A unified approach for motion and force control of robot manipulators: The operational space formulation," *IEEE Trans. Robot. Autom.*, vol. 3, no. 1, pp. 43–53, 1987.

[29] J. De Schutter and H. Van Brussel, "Compliant robot motion: Parts I-II," *Int. J. Robot. Res.*, vol. 7, no. 4, pp. 3–17, 1988.

[30] N. McClamroch and D. Wang, "Feedback stabilization and tracking of constrained robots," *IEEE Trans. Autom. Control*, vol. 33, no. 5, pp. 419–426, 1988.

[31] S. Chiaverini and L. Sciavicco, "The parallel approach to force/position control of robotic manipulators," *IEEE Trans. Robot. Autom.*, vol. 9, no. 4, pp. 361–373, 1993.

[32] J. Pratt *et al.*, "Virtual model control: An intuitive approach for bipedal locomotion," *Int. J. Robot. Res.*, vol. 20, no. 2, pp. 129–143, 2001.

[33] B. Heinrichs, N. Sepehri, and A. Thornton-Trump, "Position-based impedance control of an industrial hydraulic manipulator," *IEEE Control Systems*, vol. 17, no. 1, pp. 46–52, 1997.

[34] S. Tafazoli *et al.*, "Impedance control of a teleoperated excavator," *IEEE Trans. Control Syst. Technol.*, vol. 10, no. 3, pp. 355–367, 2002.

[35] S. Salcudean, S. Tafazoli, P. Lawrence, and I. Chau, "Impedance control of a teleoperated mini excavator," in *Proc. 8th Int. IEEE Conf. on Advanced Robotics*, 1997, pp. 19–25.

[36] S. Salcudean *et al.*, "Bilateral matched-impedance teleoperation with application to excavator control," *IEEE Control Systems*, vol. 19, no. 6, pp. 29–37, 1999.

[37] H. Zeng and N. Sepehri, "On tracking control of cooperative hydraulic manipulators," *Int. J. Control*, vol. 80, no. 3, pp. 454–469, 2007.

[38] H. Zeng, "Nonlinear control of co-operating hydraulic manipulators," Ph.D. dissertation, University of Manitoba, 2007.

[39] C. Semini *et al.*, "Towards versatile legged robots through active impedance control," *Int. J. Robot. Res.*, vol. 34, no. 7, pp. 1003–1020, 2015.

[40] G. Tao, "A simple alternative to the barbalat lemma," *IEEE Trans. Autom. Control*, vol. 42, no. 5, p. 698, may 1997.

[41] J. Colgate and J. Brown, "Factors affecting the z-width of a haptic display," in *Proc. IEEE Int. Conf. Robotics and Automation*, 1994, pp. 3205–3210.

[42] T. Boaventura *et al.*, "Stability and performance of the compliance controller of the quadruped robot HyQ," in *Proc. of IEEE/RSJ Int. Conf. on Intel. Robots and Syst.*, 2013, pp. 1458–1464.

[43] J. Vihonen, J. Honkakorpi, J. Tuominen, J. Mattila, and A. Visa, "Linear accelerometers and rate gyros for rotary joint angle estimation of heavy-duty mobile manipulators using forward kinematic modeling," *IEEE/ASME Trans. Mechatronics*, vol. 21, no. 3, pp. 1765–1774, 2016.

Janne Koivumäki received his M.Sc. degree in Automation Engineering from the Tampere University of Technology (TUT), Finland, in 2012. He has worked at IHA, TUT, since 2011 and is currently pursuing a doctoral degree in Machine Automation. From 1/2015 his work has been supported by the Academy of Finland under the project "Cooperative heavy-duty hydraulic manipulators for sustainable subsea infrastructure installation and dismantling". His research interests include a control of electro-hydraulic systems and hydraulic robotic manipulators, nonlinear model-based control, contact force/motion control and energy-efficiency of fluid power systems.

Jouni Mattila received his M.Sc. (Eng.) in 1995 and Dr. Tech. in 2000, both from the Tampere University of Technology (TUT), Finland. He has been involved in numerous industrial research projects, including the Sandvik AutoMine® with Hermia Group Ltd. He is currently a Professor in Machine Automation in the Dept. of Intelligent Hydraulics and Automation (IHA), TUT. For the past ten years, he has been a program manager on ITER fusion reactor maintenance projects involving research on heavy-duty hydraulic robotic manipulators. His research interests include machine automation, nonlinear model-based control of hydraulic robotic manipulators and energy-efficiency of fluid power systems.

Publication P.IV

Janne Koivumäki and Jouni Mattila, "Stability-Guaranteed Multiple Cartesian Degrees of Freedom Variable Impedance Control of Hydraulic Manipulators," in *Proc. FPNI Ph.D. Symposium on Fluid Power*, Florianopolis, SC, Brazil, October 2016.

Errata:

• In page 2 in Definition 1, the item **(b)** should be written as "*A Lebesgue measurable function $f(t)$ belongs to L_∞ if and only if* $\max_{t\in[0,\infty)} |f(t)| < +\infty$."
• In page 4, Object 0 should be represented as *source node* and Object 2 should be represented as *sink node*.
• The proof for Lemma 3 (in page 5) should be written as "*The proof for Lemma 3 is similar to Appendix B in [12].*"
• The proof for Theorem 1 (in page 6) should be written as "*The proof for Theorem 1 is similar to the proof for Theorem 1 in [13] (see Appendix A in [13]) but...*".
• The proof for Lemma 4 (in page 7) should be written as "*The proof for (37) is similar to the proof for Lemma 5 in [13] (see Appendix B in [13]) but...*".

The original print of this publication is available online (DOI: 10.1115/FPNI2016-1565)

Unpublished Manuscript P.V

Janne Koivumäki and Jouni Mattila, "Adaptive and Nonlinear Control of Discharge Pressure for Variable Displacement Axial Piston Pumps", 2016.

Adaptive and Nonlinear Control of Discharge Pressure for Variable Displacement Axial Piston Pumps

Janne Koivumäki* **and Jouni Mattila**
Department of Intelligent Hydraulics and Automation (IHA)
Tampere University of Technology
Korkeakoulunkatu 6, 33720 Tampere, Finland.
Emails: janne.koivumaki@tut.fi, jouni.mattila@tut.fi

This paper proposes, for the first time without using any linearization or order-reduction, an adaptive and model-based discharge pressure control design for the variable displacement axial piston pumps (VDAPPs), whose dynamical behaviours are highly nonlinear and can be described by a fourth-order differential equation. The rigorous stability proof, with an asymptotic convergence, is given for the entire system. In the proposed novel controller design method, the specifically designed stabilizing terms constitute an essential core to cancel out all the stability-preventing terms. In the experiments, an adaptive controller design demonstrates superior control performance with accurate discharge pressure tracking, enabling energy efficiency improvement for the hydraulic systems driven with VDAPP. The experimental results also reveal that rapid parameter adaptation significantly improves the feedback signal tracking precision compared to a known-parameter controller design.

1 Introduction

Hydraulic power transfer systems are widely utilized in many industries, such as forestry, mining, offshore and agriculture, where heavy-duty operations are needed. In these industries, the hydraulic systems have edge over electric systems for their significantly higher power-to-weight ratio. However, as a significant drawback, conventional hydraulic systems lack of energy efficiency. The hydraulic power transferred into the system is a product of the supplied fluid flow rate and a prevailing system supply pressure level. In conventional hydraulic systems, a constant amount of fluid is discharged into the system (using a constant displacement pump) regardless of the actual system demands. An excessive amount of fluid is then discharged back to the reservoir through a pressure relief valve, which simultaneously determines a constant supply pressure level for the system. Thus, a significant amount of energy is typically wasted across the pressure relief valve. Energy is also wasted across the load pressure control valve(s), if there exists any in the system, when the load pressure is significantly smaller than the system supply pressure.

Contrary to the conventional hydraulic systems, Variable Displacement Pumps (VDPs) are devices which enable one to regulate the hydraulic power delivered into the system. Among the VDPs, a Variable Displacement Axial Piston Pump (VDAPP) is the best known and most widely used VDP, and during the past decades, it has attracted a significant interest in research (see e.g., [1–8]). The amount of fluid discharged into the system per VDAPP's input shaft revolution can be adjusted by varying pump's swash plate angle, which is done by driving a swash plate mounted control piston through a specific control valve (see Figs. 1–2). In these systems, the discharge pressure is a build-up function of the system resistance to the discharged fluid flow, and the pressure relief valve is used only as a safety valve (not to define the system discharge pressure level). Thus, from the control point of view, an optimized energy consumption can be achieved, if the discharge pressure remains a bit higher than the required load pressure. The Load Sensing (LS) systems (see [9–13] for the traditional LS systems and [14–16] for the electric LS systems) are built on this idea and are considered to be one of the key technologies to improve the energy efficiency of hydraulic systems. However, in LS systems the load dynamics and the pump dynamics become heavily coupled through a specific LS mechanism. Consequently, the LS systems are well-known for their oscillatory or even unstable behaviour (see [9, 10, 12]), which is caused by the highly complex nature of pressure dynamics and the interaction between the LS mechanism and the load.

An alternative method for controlling the LS systems is to design a discharge pressure controller with the electro-hydraulically controlled VDAPP (see Fig. 1). In this method, the control objective is to make a system's discharge pressure track a prespecified desired discharge pressure trajectory (settled). However, the design for such a pressure tracking controller is not straightforward. The mapping between the discharge pressure and the control valve input is evidently very complex, governed by a highly nonlinear fourth-

*Address all correspondence related to this paper to this author.

order differential equation, making the control design task extremely challenging. This difficulty in control design prevents many previous researchers from adopting full-model-based nonlinear control, forcing them to use either linearization or model-reduction methods, at the expense of control performance.

Research on reducing the VDAPP's fourth-order dynamics to second-order can be found in [2, 3, 6]. Lin and Akers presented in [17] one of the early works on electro-hydraulically controlled VDAPPs, employing linear control method. More linear and reduced order control strategies for electro-hydraulically controlled VDAPPs can be found, e.g., in [18–20]. A significant step forward was taken in [21], where Kemmetmüller et al. proposed a model-based nonlinear control strategy with a load estimator. Based on the singular perturbation theory, the reduced order dynamical models, e.g., neglecting the second-order swash plate motion model, were used in the controller design. The stability of the controller design with load estimation was provided. Guo and Wei [22] proposed a Adaptive Robust Control (ARC) design, where a parameter adaptation was incorporated for three system parameters. As a demerit, a swivel torque was approximated with a reduced order polynomial function and the controller performance was evaluated with simulations only. Wei et al. [23] proposed a nonlinear discharge pressure control for a VDAPP with disturbance observer for the varying load. Simplified second-order dynamic model was used. Both state-of-the-art studies [21] and [23] applied in their experiments a narrow discharge pressure range (with range of $\leqslant 60$ bars). In summary, current methods for the discharge pressure control of VDAPPs use linearization and/or reduced order methods, without accommodating parametric uncertain dynamics and without extensively covering a VDAPP's highly nonlinear operation space. Thus, full-model-based tracking control of VDAPPs incorporating parametric uncertainty still remains an open problem.

In this paper, it is shown for the first time, without using any linearization or order-reduction, that it is possible to design full-model-based adaptive and nonlinear control for VDAPPs described with fourth-order nonlinear dynamics. This very design has the following features: 1) It is a full-model-based nonlinear discharge pressure controller. 2) The control does not use any linearization or order-reduction in the controller design. 3) The parametric uncertainties in the subsystems dynamics can be rigorously addressed in a natural manner. 4) The stability of the designed controller is rigorously guaranteed. The proposed novel solution can be considered as a Virtual Decomposition Control (VDC) (see [24, 25]) inspired approach. It uses VDC principles, but is developed in a novel manner. Similar to VDC, the control design is based on the use of subsystems' dynamics, rather than the centralized system dynamics, while rigorously guaranteeing the stability of the entire system by canceling out all the stability-preventing terms. The experiment demonstrates, by extensively covering the VDAPP's highly nonlinear operation space, that the proposed adaptive control design, with rapid parameter adaptation, results in a superior discharge pressure tracking performance for the studied VDAPP.

This paper is organized as follows. Section 2 provides the essential foundations for this paper. The detailed mathematical models for the studied system including kinematics and dynamics are introduced in Section 3. In Section 4, the detailed control laws are given for the known-parameter control design first and then the adaptive control design follows, with rigorous stability proofs. Furthermore, asymptotic convergence is discussed in detail. Section 5 discusses the controller implementation issues followed by experimental results. Finally, conclusions are outlined in Section 6.

2 Mathematical Preliminaries

This section provides essential preliminaries for the proposed control design method.

2.1 L_2 and L_∞ Stability

Definition 1 ([25]). *Lebesgue space, denoted as L_p with p being a positive integer, contains all Lebesgue measurable and integrable functions $f(t)$ subject to*

$$\|f\|_p = \lim_{T\to\infty}\left[\int_0^T |f(t)|^p d\tau\right]^{\frac{1}{p}} < +\infty. \tag{1}$$

Two particular cases are considered:

(a) *A Lebesgue measurable function $f(t)$ belongs to L_2 if and only if $\lim_{T\to\infty}\int_0^T |f(t)|^2 d\tau < +\infty$.*
(b) *A Lebesgue measurable function $f(t)$ belongs to L_∞ if and only if $\max_{t\in[0,\infty)}|f(t)| < +\infty$.*

Derived from the Lemma 2.3 in [25], the following lemma provides that a system is stable with its affiliated variable $x_i(t), \forall i \in \{1,n\}$, being a function in L_∞ and its affiliated variable $y_j(t), \forall j \in \{1,m\}$, being a function in L_2.

Lemma 1. *Consider a non-negative differentiable function $\xi(t)$ defined as*

$$\xi(t) \geqslant \sum_{i=1}^{n} \frac{a_i}{2} x_i(t)^2 \tag{2}$$

with $a_i > 0$ and $n \geqslant 1$. If the time derivative of $\xi(t)$ is Lebesgue integrable and governed by

$$\dot{\xi}(t) \leqslant -\sum_{j=1}^{m} b_j y_j(t)^2 \tag{3}$$

with $b_j > 0$ and $m \geqslant 1$, then it follows that $\xi(t) \in L_\infty$, $x_i(t) \in L_\infty$ and $y_j(t) \in L_2$ hold $\forall i \in \{1,n\}$ and $\forall j \in \{1,m\}$.

Proof. See Appendix A.

The following Lemma 2 provides that L_2 and L_∞ signal retains its properties after passing through a first-order filter.

Lemma 2 ([25]). *Consider a first-order system described by*

$$\dot{x}(t) + cx(t) = u(t) \tag{4}$$

with $c > 0$. If $u(t) \in L_p$ holds, then $x(t) \in L_p$ and $\dot{x}(t) \in L_p$ hold for $p = 2, \infty$.

If *asymptotic stability* is demanded for the control system, then a well-known Barbalat's lemma is typically used [26]. The following Lemma 3 provides an alternative to the Barbalat's lemma.

Lemma 3 ([27]). *If $e(t) \in L_2$ and $\dot{e}(t) \in L_\infty$, then $\lim_{t\to\infty} e(t) = 0$.*

Remark 1. *As a distinction to Lyapunov approaches, Lemma 1 allows different appearances of variables in the non-negative function itself and in its time-derivative. When all error signals are first proven to belong to L_2 and L_∞ in the sense of Lemma 1, then asymptotic stability can be proven with Lemma 3, if the time-derivatives of all error signals belong to L_∞.*

2.2 Parameter Adaptation

The following projection function is used for parameter adaptation[1]:

Definition 2 ([25,28,29]). *A projection function $\mathscr{P}_2(s(t),k,a(t),b(t),d,t) \in \mathbb{R}$ is a second-order differentiable scalar function defined for $t \geqslant 0$ such that its time derivative is governed by*

$$\dot{\mathscr{P}}_2 = k\,(s(t) + d\kappa_2) \tag{5}$$

with

$$\kappa_2 = \begin{cases} a(t) - \mathscr{P}_2, & \text{if } \mathscr{P}_2 \leqslant a(t) \\ b(t) - \mathscr{P}_2, & \text{if } \mathscr{P}_2 \geqslant b(t) \\ 0, & \text{otherwise} \end{cases}$$

where $s(t) \in \mathbb{R}$ is a scalar variable, $k > 0$ and $d > 0$ are two constants, and $a(t) \leqslant b(t)$ holds.

The projection function in (5) has the following property [25]:

Lemma 4. *For any constant $\mathscr{P}_{c2}$ subject to $a(t) \leqslant \mathscr{P}_{c2} \leqslant b(t)$, it yields*

$$(\mathscr{P}_{c2} - \mathscr{P}_2)\left(s(t) - \frac{1}{k}\dot{\mathscr{P}}_2\right) \leqslant -d\kappa_2^2 \leqslant 0. \tag{6}$$

Remark 2. *As a distinction to all other indirect adaptive control approaches, with $\mathscr{P}_2$ in (5), state convergence does not require parameter convergence. However, bounded parameter errors are guaranteed. For a known parameter, its lower bound $a(t)$ and upper bound $b(t)$ can be set to its true value.*

[1] It can be seen later, the $\mathscr{P}_2$ is necessarily needed to update $\widehat{\boldsymbol{\theta}}_\mathrm{p}$, since its second-order time derivative is used in the control law. For other system parameter adaptations ($\widehat{\boldsymbol{\theta}}_\mathrm{s}$, $\widehat{\boldsymbol{\theta}}_\mathrm{c}$ and $\widehat{\boldsymbol{\theta}}_\mathrm{v}$), a first-order differentiable projection function $\mathscr{P}$, defined in [25,28], can also be used alternatively.

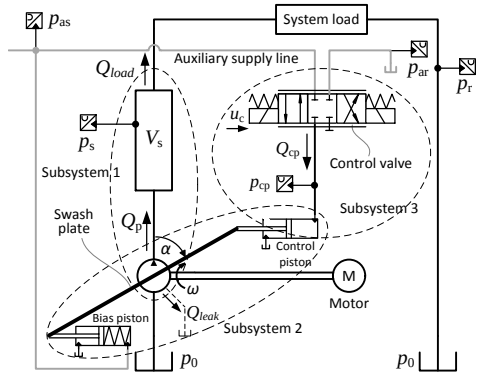

Fig. 1. Decomposed subsystems and system control set-up.

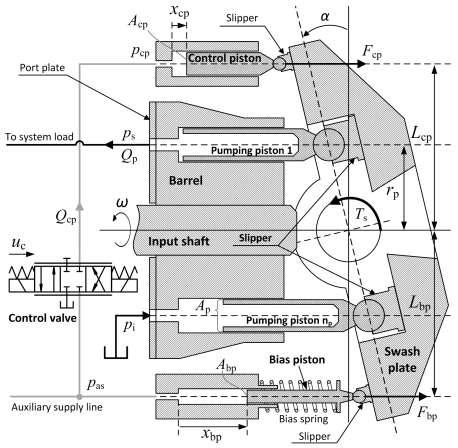

Fig. 2. Operating principle of the variable displacement axial piston pump.

3 System Modeling

Fig. 1 shows the electro-hydraulically controlled VDAPP. The operating principle of the VDAPP can be seen from Fig. 2. There are totally n_p pumping pistons which are nested into the barrel and are able to slide on the swash plate surface. When the barrel is driven (from the input shaft connected to the motor) with an angular velocity ω, each pumping piston produces a periodic oscillatory stroke, whose amplitude is depending on the swash plate angle α. The period of a pumping piston is divided into the suction phase (where the piston takes fluid from the system's reservoir) and the discharge phase (where the piston pumps fluid into the system). This process is synchronized mechanically with the port plate. Thus, the amount of fluid supplied into the system per the pump's input shaft revolution can be adjusted in operations by changing the pumping pistons' geometrical displacement volume, which in turn is done by varying the pump's swash plate angle α. The swash plate angle is adjusted by the control piston through the electro-hydraulic control valve. More detailed operational descriptions for the VDAPP can be found in many pioneering studies (e.g., [2–4, 6]).

The VDAPP system, with the discharge pressure p_s being the variable to be controlled and the control valve voltage u_c being the control variable, is complex and highly nonlinear and can be described by a fourth-order differential equation. As shown in Fig. 1, three subsystems are identified in the studied system. The first subsystem denotes the volume of the pump's discharge line and can be described with a first-order fluid continuity differential equation; see (13). The second subsystem denotes the pump itself and can be described with a second-order swash plate motion differential equation; see (17). The third subsystem denotes the volume of the control piston and can be described with a first-order fluid continuity differential equation; see (27).

Next, in Section 3.1, the kinematics between the swash plate and its related pistons (control piston and bias piston) are given. Then, the dynamical models for the three subsystems are specified in Section 3.2.

3.1 Kinematics

In view of Fig. 2, the relation between the swash plate angle and the control piston position can be written as

$$x_{cp}(\alpha) = x_{cp0} - L_{cp}\tan(\alpha) \tag{7}$$

where α is a swash plate angle, x_{cp0} denotes a control piston position at $\alpha = 0$ and L_{cp} denotes the distance between the barrel pivot and the control piston center line.

Then, by taking time derivatives of (7), the control piston velocity and acceleration can be written as

$$\dot{x}_{cp}(\dot{\alpha},\alpha) = -\frac{L_{cp}}{\cos^2(\alpha)}\dot{\alpha} \tag{8}$$

$$\ddot{x}_{cp}(\ddot{\alpha},\dot{\alpha},\alpha) = -\frac{2L_{cp}\sin(\alpha)}{\cos^3(\alpha)}\dot{\alpha}^2 - \frac{L_{cp}}{\cos^2(\alpha)}\ddot{\alpha}. \tag{9}$$

Similar to (7)–(9), the motion relations between the swash plate and the bias piston can be written as

$$x_{bp}(\alpha) = x_{bp0} + L_{bp}\tan(\alpha) \tag{10}$$

$$\dot{x}_{bp}(\dot{\alpha},\alpha) = \frac{L_{bp}}{\cos^2(\alpha)}\dot{\alpha} \tag{11}$$

$$\ddot{x}_{bp}(\ddot{\alpha},\dot{\alpha},\alpha) = \frac{2L_{bp}\sin(\alpha)}{\cos^3(\alpha)}\dot{\alpha}^2 + \frac{L_{bp}}{\cos^2(\alpha)}\ddot{\alpha} \tag{12}$$

where x_{bp0} denotes a bias piston position at $\alpha = 0$ and L_{bp} denotes the distance between barrel pivot and the bias piston center line.

The following condition, making (7)–(12) executable, holds.

Condition 1. *The following relationship holds for the swash plate angle*

$$-\frac{\pi}{2} < \alpha < \frac{\pi}{2}.$$

3.2 Dynamics

The complete VDAPP system can be virtually decomposed into three cascaded subsystems that control the discharging pressure p_s by using the control valve voltage u_c (see Fig 3). Specifically, subsystem 1 controls the discharging pressure p_s using the swash plate angle α; subsystem 2 controls the swash plate angle α using the control piston pressure p_{cp}; and subsystem 3 controls the control piston pressure p_{cp} using the control valve voltage u_c. Next, Sections 3.2.1–3.2.3 establish the dynamic relations for the subsystems 1–3.

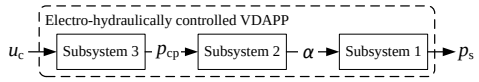

Fig. 3. The mapping between the controlling variable u_c and the controlled variable p_s.

3.2.1 Subsystem 1 – Discharge line fluid dynamics

The fluid continuity equation for the pressurized fluid in the system discharge line, denoted as subsystem 1 in Fig. 1, can be written as

$$\dot{p}_s = \frac{\beta_{eff}}{V_s}(Q_p - Q_{load} - Q_{leak}) \tag{13}$$

where β_{eff} denotes the effective bulk modulus, V_s denotes the volume of the pressurized fluid in discharge line, and Q_{load} is the measurable fluid flow rate taken by the system load. The, similar to [21–23], the remaining fluid flows in (13) can be written as

$$Q_p = \frac{V_{max}\omega(t)}{2\pi\alpha_{max}}\alpha \tag{14}$$

$$Q_{leak} = k_{leak}p_s \tag{15}$$

where Q_p is the fluid flow rate produced by the pump and Q_{leak} is the pump leakage flow rate. Moreover, in (14) and (15), V_{max} is the maximum geometric displacement (volume) of the pumping pistons per revolution, $\omega(t)$ is the pump input shaft angular velocity, α_{max} is the maximum swash plate angle, and k_{leak} is the leakage coefficient.

Substituting (14) and (15) into (13), taking the time derivative from (13) and rearranging terms yields

$$\frac{V_{max}}{2\pi\alpha_{max}}\omega(t)\dot{\alpha} = \frac{V_s}{\beta_{eff}}\ddot{p}_s - \frac{V_{max}}{2\pi\alpha_{max}}\dot{\omega}(t)\alpha + \dot{Q}_{load} + k_{leak}\dot{p}_s. \tag{16}$$

3.2.2 Subsystem 2 – Swash plate dynamics

The equation of motion for the swash plate can be written as

$$I_s\ddot{\alpha} = F_{bp}L_{bp} - F_{cp}L_{cp} + T_s \tag{17}$$

where I_s is the swash plate mass moment of inertia, F_{bp} is the force exerted from the bias piston to the swash plate, F_{cp} is the force exerted from the control piston to the swash plate, and T_s is the swash plate swivel torque. The detailed equations of F_{bp}, F_{cp} and T_s can be written as

$$F_{bp} = -m_{bp}\ddot{x}_{bp} - C_{bp}\dot{x}_{bp} + A_{bp}p_{as} + \overbrace{f_{s0} - k_b L_{bp}\tan(\alpha)}^{\text{spring force}} \quad (18)$$

$$F_{cp} = -m_{cp}\ddot{x}_{cp} - C_{cp}\dot{x}_{cp} + A_{cp}p_{cp} \quad (19)$$

$$T_s = \frac{n_p}{2}\left[-\frac{m_p r_p^2}{\cos^4(\alpha)}\ddot{\alpha} - \frac{2m_p r_p^2 \sin(\alpha)}{\cos^5(\alpha)}\dot{\alpha}^2 - \frac{C_p r_p^2}{\cos^4(\alpha)}\dot{\alpha} + \frac{m_p r_p^2 \tan(\alpha)}{\cos^2(\alpha)}\omega(t)^2 - \frac{A_p r_p \phi}{\pi\cos^2(\alpha)}(p_s - p_i)\right] \quad (20)$$

where p_{as} is a pressure of the auxiliary supply line (see Fig. 1); p_{cp} is the control piston chamber pressure; m_{bp}, m_{cp} and m_p are the masses of the bias piston, control piston and pumping piston, respectively; C_{bp}, C_{cp} and C_p are the damping coefficients of the bias piston, control piston and pumping piston, respectively; A_{bp}, A_{cp} and A_p are the effective areas of the bias piston, control piston and pumping piston, respectively; f_{s0} is the bias-spring force at $\alpha = 0$; k_b is the bias-spring constant; n_p is the number of the pumping pistons; r_p is the pumping pistons' pitch radius; ϕ is the pressure carry-over angle on the port plate; and p_i denotes the pump inlet (suction) port pressure. For more detailed information, see [6].

Then, substituting (8), (9), (11), (12) and (18)–(20) into (17) and rearranging terms yields

$$A_{cp}L_{cp}g_1(\alpha)p_{cp} = -\ddot{\alpha} + g(\dot{\alpha}, \alpha, \omega(t), p_{as}, p_s, p_i) \quad (21)$$

with

$$\begin{aligned} &g(\dot{\alpha}, \alpha, \omega(t), p_{as}, p_s, p_i) \\ &= g_1(\alpha)\left[-\frac{2m_{bp}L_{bp}^2\sin(\alpha)}{\cos^3(\alpha)}\dot{\alpha}^2 - \frac{C_{bp}L_{bp}^2}{\cos^2(\alpha)}\dot{\alpha} + A_{bp}L_{bp}p_{as} \right. \\ &\quad + f_{s0}L_{bp} - k_b L_{bp}^2\tan(\alpha) - \frac{2m_{cp}L_{cp}^2\sin(\alpha)}{\cos^3(\alpha)}\dot{\alpha}^2 \\ &\quad - \frac{C_{cp}L_{cp}^2}{\cos^2(\alpha)}\dot{\alpha} - \frac{n_p m_p r_p^2 \sin(\alpha)}{\cos^5(\alpha)}\dot{\alpha}^2 - \frac{n_p C_p r_p^2}{2\cos^4(\alpha)}\dot{\alpha} \\ &\quad \left. + \frac{n_p m_p r_p^2 \tan(\alpha)}{2\cos^2(\alpha)}\omega(t)^2 - \frac{n_p A_p r_p \phi(p_s - p_i)}{2\pi\cos^2(\alpha)}\right] \end{aligned} \quad (22)$$

$$g_1(\alpha) = \left(I_s + \frac{m_{bp}L_{bp}^2}{\cos^2(\alpha)} + \frac{m_{cp}L_{cp}^2}{\cos^2(\alpha)} + \frac{n_p m_p r_p^2}{2\cos^4(\alpha)}\right)^{-1}. \quad (23)$$

Note that Condition 1 makes (21)–(23) executable.

3.2.3 Subsystem 3 – Control piston fluid dynamics

The fluid flow rate Q_{cp} entering the control piston can be written as

$$Q_{cp} = c_p\upsilon(p_{as} - p_{cp})u_c S(u_c) + c_n\upsilon(p_{cp} - p_{ar})u_c S(-u_c) \quad (24)$$

where $c_p > 0$ and $c_n > 0$ are two flow coefficients and p_{ar} is the pressure of the auxiliary return line (see Fig. 1). Similar to [25], a pressure-related function $\upsilon(\Delta p)$ is defined as

$$\upsilon(\Delta p) = \text{sign}(\Delta p)\sqrt{|\Delta p|} \quad (25)$$

and a selective function $S(u)$ is defined as

$$S(u) \stackrel{\text{def}}{=} \begin{cases} 1, & \text{if } u > 0 \\ 0, & \text{if } u \le 0 \end{cases}. \quad (26)$$

The fluid continuity equation in the control piston chamber can be written as

$$\begin{aligned} \dot{p}_{cp} &= \frac{\beta_f}{A_{cp}x_{cp}(\alpha)}(Q_{cp} - A_{cp}\dot{x}_{cp}(\dot{\alpha}, \alpha)) \\ &= \frac{\beta_f}{A_{cp}}\left(u_v - \frac{A_{cp}\dot{x}_{cp}(\dot{\alpha}, \alpha)}{x_{cp}(\alpha)}\right) \end{aligned} \quad (27)$$

where β_f is the bulk modulus of the hydraulic fluid and the control valve voltage related term u_v can be written as

$$\begin{aligned} u_v &= \frac{c_p\upsilon(p_{as} - p_{cp})}{x_{cp}(\alpha)}u_c S(u_c) + \frac{c_n\upsilon(p_{cp} - p_{ar})}{x_{cp}(\alpha)}u_c S(-u_c) \\ &= -\mathbf{Y}_v\boldsymbol{\theta}_v. \end{aligned} \quad (28)$$

The detailed expressions for the regressor vector $\mathbf{Y}_v \in \mathbb{R}^{1\times 2}$ and the parameter vector $\boldsymbol{\theta}_v \in \mathbb{R}^2$ are given in Appendix B.

The following two conditions are defined.

Condition 2. *The control piston never reaches a zero stroke, i.e.,*

$$x_{cp}(\alpha) > 0.$$

Condition 3. *The following pressure relationship holds for the system pressures*

$$p_{as} > p_{cp} > p_{ar} \geqslant 0.$$

In view of (28) and Conditions 2–3, the univalence between u_c and u_v exists.[2] Thus, for a given u_v, a unique valve control voltage u_c can be found as

$$u_c = \frac{x_{cp}(\alpha)}{c_p\upsilon(p_{as} - p_{cp})}u_v S(u_v) + \frac{x_{cp}(\alpha)}{c_n\upsilon(p_{cp} - p_{ar})}u_v S(-u_v) \quad (29)$$

Remark 3. *In this study, the main emphasis is on the highly nonlinear dynamic behaviour of a VDAPP itself. Thus, similar to [21, 23, 30–32], the control valve dynamics are neglected in this study. If a high-bandwidth control valve is used, this is reasonable due to its significantly faster dynamics in relation to VDAPPs dynamics.*

[2] When Conditions 2–3 hold, $x_{cp}(\alpha) > 0$, $\upsilon(p_{as} - p_{cp}) > 0$ and $\upsilon(p_{cp} - p_{ar}) > 0$ hold, which ensure non-singular solutions for (28) and (29).

4 Control Design

The control design method used in this paper originates from the VDC approach[3] (see [24,25]), as it uses VDC principles, but is developed in a novel manner. Similar to the VDC, the control design in this paper is based on the subsystems' dynamics, rather than the centralized system dynamics. In the VDC, the unique *virtual power flows*[4] define the dynamic interaction among subsystems and play a vital role in proving the L_2 and L_∞ stability of the entire system. However, when VDC principles are applied beyond the robotic systems, cross couplings among subsystems cannot be necessarily described in the form of virtual power flows. Thus, alternative methods must be provided to address the dynamic interactions among the subsystems.

In the studied system, a *stability-preventing term* (created by a subsystem local control) can appear in the time derivative of the non-negative accompanying function of the nth subsystem, $\forall n \in \{1,2\}$. Thus, a specific *stabilizing term* is designed for the time derivative of the non-negative accompanying function of the subsequent $(n+1)$th subsystem, $\forall n \in \{1,2\}$. The stabilizing term is designed by placing a specific stabilizing feedback in the control law of the $(n+1)$th subsystem. As Theorems 1–2 show later, the stability of the entire system is obtained (in the sense of Lemma 1), as these designed stabilizing terms eventually cancel out all the stability-preventing terms. Similar to the VDC, the stability is rigorously based on Lemma 1. As a distinction to Lyapunov approaches, Lemma 1 allows different appearance of variables in the non-negative function itself and in its time-derivative, providing a more flexible tool for control system design. When all error signals are first proved to belonging to L_2 and L_∞, then asymptotic stability can be proved with Lemma 3, if the time-derivatives of all error signals belong to L_∞.

As an advantage of the proposed control design method, it enables an adaptive control for complex systems, without employing any linearization or order-reduction, while rigorously guaranteeing the stability of the entire system. Existing nonlinear control methods (see [21–23] for the discharge pressure controlled VDAPP) have employed linearization and/or order-reduction. In addition, any of the state-of-the-art studies [21–23] did not rigorously address the parametric uncertainties in the system dynamics. As will be shown later (in Section 4.2), the proposed method is able to rigorously handle parametric uncertainties of each subsystem in a natural manner, permitting an even broader applicability to complex nonlinear systems with parametric uncertainties.

Next, Section 4.1 addresses the control design using known parameters. Then, the unknown-parameter (adaptive) control that accommodates parameter uncertainties is developed in Section 4.2. Finally, asymptotic convergence of the feedback signals is presented in Section 4.3.

[3] A unique subsystem-dynamics-based (nonlinear model-based) control method, developed especially for controlling complex robotic systems.

[4] In short, the *virtual power flow*, having unit in power [W], is the product of two error signals.

4.1 Known-Parameter Control Design

In Sections 4.1.1–4.1.3, the control laws for the subsystems 1–3 are designed using known-parameter values. The stability of the designed control system is addressed in Section 4.1.4.

4.1.1 Subsystem 1

For the control of subsystem 1, the following assumption is made.

Assumption 1. *The pump input shaft angular velocity $\omega(t)$ is a lower bounded function such that*

$$\omega(t) \geqslant \omega^* > 0$$

holds with a constant ω^*.

The ultimate control objective is to make the discharge pressure p_s track its desired pressure p_{sd}. Similar to VDC approach, the required reference trajectory is used in the control instead of typically used desired reference trajectory. Thus, the discharge pressure control can be performed using the required first-order discharge pressure dynamics $\dot{p}_{sr}$, which is defined as

$$\dot{p}_{sr} = \dot{p}_{sd} + \lambda_p (p_{sd} - p_s) \tag{30}$$

where $\lambda_p > 0$ is a gain for the discharge pressure feedback.

Based on (16), the control law for the subsystem 1 with known-parameters is designed as

$$\begin{aligned} \frac{V_{max}}{2\pi\alpha_{max}}\omega(t)\dot{\alpha}_d &= \frac{V_s}{\beta_{eff}}\ddot{p}_{sr} - \frac{V_{max}}{2\pi\alpha_{max}}\dot{\omega}(t)\alpha + \dot{Q}_{load} \\ &\quad + k_{leak}\dot{p}_s + k_{p1}(\dot{p}_{sr} - \dot{p}_s) \\ &= \mathbf{Y}_p\boldsymbol{\theta}_p + k_{p1}(\dot{p}_{sr} - \dot{p}_s) \end{aligned} \tag{31}$$

where $\dot{\alpha}_d$ is the desired swash plate velocity; $\mathbf{Y}_p\boldsymbol{\theta}_p$ is a model-based feedforward compensation term by using $\ddot{p}_{sr}$; and $k_{p1} > 0$ is a gain for the local feedback signal. The detailed expressions of the regressor vector $\mathbf{Y}_p \in \mathbb{R}^{1\times 4}$ and parameter vector $\boldsymbol{\theta}_p \in \mathbb{R}^4$ are given in Appendix B.

Note that Assumption 1 makes (31) executable. Then, equation (31) computes $\dot{\alpha}_d$ from $\ddot{p}_{sr}$, the time derivative of $\dot{p}_{sr}$ specified by (30).

Remark 4. *Note that, in view of* (13) *and* (14)*, an option to control the discharge pressure p_s directly using the pump's input shaft angular velocity $\omega(t)$ with a constant α does exist. Although this solution can substantially simplify system dynamics and control, the control of the input shaft angular velocity might not always be feasible. For instance, most internal combustion engines need certain angular rates to provide optimized power outputs. Asynchronous electric motors have a very narrow band in speed regulation. On the other hand, the use of DC motors or brushless DC motors may make this solution feasible, see, e.g., [33].*

Remark 5. *If the input shaft (see Figs. 1–2) is driven with a constant angular velocity ω_c, e.g., with an asynchronous electric motor, then $\omega(t) = \omega_c$ and $\dot{\omega}(t) = 0$ can be used for* (31) *and later for* (49).

The following lemma holds for the subsystem 1 subject to the control equation (31) with known-parameters.

Lemma 5. *Consider the decomposed subsystem 1, given in Fig. 1, described by* (16) *and combined with its respective control equation* (31). *Let the non-negative accompanying function v_1 for the subsystem 1 be*

$$v_1 = \frac{V_s}{2\beta_{eff}}(\dot{p}_{sr} - \dot{p}_s)^2. \tag{32}$$

Then, the time derivative of (32) *can be expressed by*

$$\dot{v}_1 = \underbrace{\frac{V_{max}}{2\pi\alpha_{max}}\omega(t)(\dot{\alpha}_d - \dot{\alpha})(\dot{p}_{sr} - \dot{p}_s)}_{\textit{Stability-preventing term 1}} - k_{p1}(\dot{p}_{sr} - \dot{p}_s)^2. \tag{33}$$

Proof. See Appendix C.

The designed subsystem 1 control equation (31) creates the stability-preventing term 1 in the right-hand side of (33). This term is addressed next in the control design for the subsystem 2.

4.1.2 Subsystem 2

Based on (21), the control law for the subsystem 2 with known-parameters is designed as

$$\begin{aligned} A_{cp}L_{cp}g_1(\alpha)p_{cpd} &= -\ddot{\alpha}_d + g(\dot{\alpha}, \alpha, \omega(t), p_{as}, p_s, p_i) \\ &\quad - k_{\alpha 1}(\dot{\alpha}_d - \dot{\alpha}) - \omega(t)k_{p2}(\dot{p}_{sr} - \dot{p}_s) \\ &= -\mathbf{Y}_s\boldsymbol{\theta}_s - k_{\alpha 1}(\dot{\alpha}_d - \dot{\alpha}) \\ &\quad - \underbrace{\omega(t)k_{p2}(\dot{p}_{sr} - \dot{p}_s)}_{\text{Stabilizing FB 1}} \end{aligned} \tag{34}$$

where p_{cpd} is the desired control piston chamber pressure; $\mathbf{Y}_s\boldsymbol{\theta}_s$ is a model-based feedforward compensation term by using $\ddot{\alpha}_d$; and $k_{p2} > 0$ and $k_{\alpha 1} > 0$ are gains for the stabilizing feedback and the local feedback signals, respectively. The detailed expressions of the regressor vector $\mathbf{Y}_s \in \mathbb{R}^{1\times 12}$ and parameter vector $\boldsymbol{\theta}_s \in \mathbb{R}^{12}$ are given in Appendix B.

Equation (34) computes p_{cpd} from $\ddot{\alpha}_d$, the time derivative of $\dot{\alpha}_d$ obtained in (31). The validity of the computation requires $g_1(\alpha) \neq 0$, which is satisfied by Condition 1 and (23).

The following lemma holds for the subsystem 2 subject to control equation (34) with known-parameters.

Lemma 6. *Consider the decomposed subsystem 2, given in Fig. 1, described by* (21)*, and combined with its respective control equation* (34). *Let the non-negative accompanying function v_2 for the subsystem 2 be*

$$v_2 = \frac{1}{2}(\dot{\alpha}_d - \dot{\alpha})^2. \tag{35}$$

Then, the time derivative of (35) *can be expressed by*

$$\begin{aligned} \dot{v}_2 = &\overbrace{-L_{cp}A_{cp}g_1(\alpha)(p_{cpd} - p_{cp})(\dot{\alpha}_d - \dot{\alpha})}^{\textit{Stability-preventing term 2}} \\ &\underbrace{-\omega(t)k_{p2}(\dot{\alpha}_d - \dot{\alpha})(\dot{p}_{sr} - \dot{p}_s)}_{\textit{Stabilizing term 1}} - k_{\alpha 1}(\dot{\alpha}_d - \dot{\alpha})^2. \end{aligned} \tag{36}$$

Proof. See Appendix D.

In (36), the stabilizing term 1 is a designed stabilizing counterpart for the stability-preventing term 1 in (33). However, the designed subsystem 2 control equation (34) creates another stability-preventing term 2 in (36). This term is addressed next in the control design for the subsystem 3.

4.1.3 Subsystem 3

Based on (27), the control law for the subsystem 3 with known-parameters is designed as

$$\begin{aligned} u_{vd} &= \frac{A_{cp}}{\beta_f}\dot{p}_{cpd} + A_{cp}\frac{\dot{x}_{cp}(\dot{\alpha}, \alpha)}{x_{cp}(\alpha)} - g_1(\alpha)k_{\alpha 2}(\dot{\alpha}_d - \dot{\alpha}) \\ &\quad + k_{p3}(p_{cpd} - p_{cp}) \\ &= \mathbf{Y}_c\boldsymbol{\theta}_c - \underbrace{g_1(\alpha)k_{\alpha 2}(\dot{\alpha}_d - \dot{\alpha})}_{\text{Stabilizing FB 2}} + k_{p3}(p_{cpd} - p_{cp}) \end{aligned} \tag{37}$$

where $\mathbf{Y}_c\boldsymbol{\theta}_c$ is a model-based feedforward compensation term by using $\dot{p}_{cpd}$; and $k_{\alpha 2} > 0$ and $k_{p3} > 0$ are gains for the stabilizing feedback and the local feedback signals, respectively. The detailed expressions of the regressor vector $\mathbf{Y}_c \in \mathbb{R}^{1\times 2}$ and parameter vector $\boldsymbol{\theta}_c \in \mathbb{R}^2$ are given in Appendix B.

Equation (37) computes u_{vd} from $\dot{p}_{cpd}$, the time derivative of p_{cpd} obtained in (34).

When Condition 3 holds, using (37), the control valve voltage can be obtained, in view of (29), as

$$\begin{aligned} u_c = &\frac{x_{cp}(\alpha)}{c_p w(p_{as} - p_{cp})}u_{vd}S(u_{vd}) \\ &+ \frac{x_{cp}(\alpha)}{c_n w(p_{cp} - p_{ar})}u_{vd}S(-u_{vd}). \end{aligned} \tag{38}$$

When Condition 2 holds, (38) can be written inversely as

$$u_{vd} = -\mathbf{Y}_v\boldsymbol{\theta}_v \tag{39}$$

in view of (28).

The following lemma holds for the subsystem 3 subject to control equation (37) with known-parameters.

Lemma 7. *Consider the decomposed subsystem 3, given in Fig. 1, described by* (27) *and* (29)*, and combined with its respective control equations* (37) *and* (38). *Let the non-negative accompanying function v_3 for the subsystem 3 be*

$$v_3 = \frac{A_{cp}}{2\beta_f}(p_{cpd} - p_{cp})^2. \tag{40}$$

Then, the time derivative of (40) *can be expressed by*

$$\dot{v}_3 = \underbrace{g_1(\alpha)k_{\alpha 2}(p_{\mathrm{cp}d} - p_{\mathrm{cp}})(\dot{\alpha}_d - \dot{\alpha})}_{\textit{Stabilizing term 2}} - k_{\mathrm{p}3}(p_{\mathrm{cp}d} - p_{\mathrm{cp}})^2. \quad (41)$$

Proof. See Appendix E.

In (41), the stabilizing term 2 is a designed stabilizing counterpart for the stability-preventing term 2 in (36).

4.1.4 Stability of the Known-Parameter Control Design

The following Theorem 1 guarantees, in the sense of Lemma 1, the stability of the entire system with the known-parameter control design.

Theorem 1. *Consider the discharge pressure controlled VDAPP, decomposed into subsystems 1–3, given in Fig. 1, described by* (16)*,* (21)*,* (27) *and* (29) *and combined with the control equations* (30)*,* (31)*,* (34)*,* (37) *and* (38)*. Then, it follows that*

$$\dot{p}_{sr} - \dot{p}_{\mathrm{s}} \in L_2 \bigcap L_\infty \quad (42)$$

$$\dot{\alpha}_d - \dot{\alpha} \in L_2 \bigcap L_\infty \quad (43)$$

$$p_{\mathrm{cp}d} - p_{\mathrm{cp}} \in L_2 \bigcap L_\infty \quad (44)$$

are guaranteed, leading to

$$\dot{p}_{sd} - \dot{p}_{\mathrm{s}} \in L_2 \bigcap L_\infty \quad (45)$$

$$p_{sd} - p_{\mathrm{s}} \in L_2 \bigcap L_\infty \quad (46)$$

in view of (30)*,* (42) *and Lemma 2.*

Proof. The proof for Theorem 1 follows directly from Lemmas 5–7. Using (32), (35) and (40), let the non-negative accompanying function for the discharge pressure controlled VDAPP be

$$\begin{aligned} v &= \frac{2\pi\alpha_{max}}{V_{max}}v_1 + \frac{1}{k_{\mathrm{p}2}}v_2 + \frac{L_{\mathrm{cp}}A_{\mathrm{cp}}}{k_{\mathrm{p}2}k_{\alpha 2}}v_3 \\ &= \frac{\pi\alpha_{max}V_s}{V_{max}\beta_{eff}}(\dot{p}_{sr} - \dot{p}_{\mathrm{s}})^2 + \frac{1}{2k_{\mathrm{p}2}}(\dot{\alpha}_d - \dot{\alpha})^2 \\ &\quad + \frac{L_{\mathrm{cp}}A_{\mathrm{cp}}^2}{2k_{\mathrm{p}2}k_{\alpha 2}\beta_{\mathrm{f}}}(p_{\mathrm{cp}d} - p_{\mathrm{cp}})^2 \\ &= a_1(\dot{p}_{sr} - \dot{p}_{\mathrm{s}})^2 + a_2(\dot{\alpha}_d - \dot{\alpha})^2 + a_3(p_{\mathrm{cp}d} - p_{\mathrm{cp}})^2 \quad (47) \end{aligned}$$

where $a_1 > 0$, $a_2 > 0$ and $a_3 > 0$. Then, it follows from (33), (36) and (41) that

$$\begin{aligned} \dot{v} &= \frac{2\pi\alpha_{max}}{V_{max}}\dot{v}_1 + \frac{1}{k_{\mathrm{p}2}}\dot{v}_2 + \frac{L_{\mathrm{cp}}A_{\mathrm{cp}}}{k_{\mathrm{p}2}k_{\alpha 2}}\dot{v}_3 \\ &= \omega(t)(\dot{\alpha}_d - \dot{\alpha})(\dot{p}_{sr} - \dot{p}_{\mathrm{s}}) - \omega(t)(\dot{\alpha}_d - \dot{\alpha})(\dot{p}_{sr} - \dot{p}_{\mathrm{s}}) \\ &\quad - \frac{L_{\mathrm{cp}}A_{\mathrm{cp}}}{k_{\mathrm{p}2}}g_1(\alpha)(p_{\mathrm{cp}d} - p_{\mathrm{cp}})(\dot{\alpha}_d - \dot{\alpha}) \\ &\quad + \frac{L_{\mathrm{cp}}A_{\mathrm{cp}}}{k_{\mathrm{p}2}}g_1(\alpha)(p_{\mathrm{cp}d} - p_{\mathrm{cp}})(\dot{\alpha}_d - \dot{\alpha}) \\ &\quad - \frac{2\pi\alpha_{max}k_{\mathrm{p}1}}{V_{max}}(\dot{p}_{sr} - \dot{p}_{\mathrm{s}})^2 - \frac{k_{\alpha 1}}{k_{\mathrm{p}2}}(\dot{\alpha}_d - \dot{\alpha})^2 \\ &\quad - \frac{L_{\mathrm{cp}}A_{\mathrm{cp}}k_{\mathrm{p}3}}{k_{\mathrm{p}2}k_{\alpha 2}}(p_{\mathrm{cp}d} - p_{\mathrm{cp}})^2 \\ &= -b_1(\dot{p}_{sr} - \dot{p}_{\mathrm{s}})^2 - b_2(\dot{\alpha}_d - \dot{\alpha})^2 - b_3(p_{\mathrm{cp}d} - p_{\mathrm{cp}})^2 \quad (48) \end{aligned}$$

holds, with $b_1 > 0$, $b_2 > 0$ and $b_3 > 0$.

Consequently, in view of Lemma 1, it follows from (47) and (48) that (42)–(46) hold for the designed known-parameter control system.

4.2 Adaptive Control Design

In the last subsection, subsystem-dynamics-based control with known-parameters is presented to demonstrate the main control concept. In this subsection, the control is extended to accommodate parametric uncertainty.

4.2.1 Subsystem 1

The required first-order discharge pressure dynamics $\dot{p}_{sr}$ can be obtained from (30). When parameters in (31) are unknown, the control law for the subsystem 1 is changed to

$$\frac{V_{max}}{2\pi\alpha_{max}}\omega(t)\dot{\alpha}_d = \mathbf{Y}_{\mathrm{p}}\widehat{\boldsymbol{\theta}}_{\mathrm{p}} + k_{\mathrm{p}1}(\dot{p}_{sr} - \dot{p}_{\mathrm{s}}) \quad (49)$$

where $\mathbf{Y}_{\mathrm{p}}\widehat{\boldsymbol{\theta}}_{\mathrm{p}}$ is a model-based feedforward compensation term by using the estimated parameters for $\boldsymbol{\theta}_{\mathrm{p}}$.

The estimated parameter vector $\widehat{\boldsymbol{\theta}}_{\mathrm{p}}$ in (49) needs to be updated. Define

$$\mathbf{s}_{\mathrm{p}} = (\dot{p}_{sr} - \dot{p}_{\mathrm{s}})\mathbf{Y}_{\mathrm{p}}^T. \quad (50)$$

The γth element of $\widehat{\boldsymbol{\theta}}_{\mathrm{p}}$ is updated by using the $\mathscr{P}_2$ function defined by (5) as

$$\widehat{\theta}_{\mathrm{p}\gamma} = \mathscr{P}_2(\mathrm{s}_{\mathrm{p}\gamma}, \rho_{\mathrm{p}\gamma}, \underline{\theta}_{\mathrm{p}\gamma}, \overline{\theta}_{\mathrm{p}\gamma}, \sigma_{\mathrm{p}\gamma}, t), \forall\gamma \in \{1,2,...,4\} \quad (51)$$

where $\widehat{\theta}_{\mathrm{p}\gamma}$ denotes the γth element of $\widehat{\boldsymbol{\theta}}_{\mathrm{p}}$, $\mathrm{s}_{\mathrm{p}\gamma}$ denotes the γth element of $\mathbf{s}_{\mathrm{p}}$, $\rho_{\mathrm{p}\gamma}$ is an update gain, $\sigma_{\mathrm{p}\gamma}$ is a correction gain, $\underline{\theta}_{\mathrm{p}\gamma}$ denotes the lower bound of $\theta_{\mathrm{p}\gamma}$ and $\overline{\theta}_{\mathrm{p}\gamma}$ denotes the upper bound of $\theta_{\mathrm{p}\gamma}$.

The following lemma holds for the subsystem 1 subject to (49) with the parameter adaptation laws (50) and (51).

Lemma 8. *Consider the decomposed subsystem 1, given in Fig. 1, described by* (16) *and combined with its respective control equation* (49) *and with the parameter adaptation* (50) *and* (51)*. Let the non-negative accompanying function* $v_{1\mathrm{a}}$ *for the subsystem 1 be*

$$v_{1\mathrm{a}} = \frac{V_s}{2\beta_{eff}}(\dot{p}_{sr} - \dot{p}_{\mathrm{s}})^2 + \frac{1}{2}\sum_{\gamma=1}^{4}\frac{(\theta_{\mathrm{p}\gamma} - \widehat{\theta}_{\mathrm{p}\gamma})^2}{\rho_{\mathrm{p}\gamma}}. \quad (52)$$

Then, the time derivative of (52) *can be expressed by*

$$\dot{v}_{1\mathrm{a}} \leqslant \frac{V_{max}}{2\pi\alpha_{max}}\omega(t)(\dot{\alpha}_d - \dot{\alpha})(\dot{p}_{sr} - \dot{p}_{\mathrm{s}}) - k_{\mathrm{p}1}(\dot{p}_{sr} - \dot{p}_{\mathrm{s}})^2. \quad (53)$$

Proof. See Appendix F.

The terms in the right-hand side of (53) are the same terms in the right-hand side of (33).

4.2.2 Subsystem 2

When parameters in (34) are unknown, the control law for the subsystem 2 is changed to

$$A_{\rm cp}L_{\rm cp}g_1(\alpha)p_{\rm cpd} = -\mathbf{Y}_{\rm s}\widehat{\boldsymbol{\theta}}_{\rm s} - \omega(t)k_{\rm p2}(\dot{p}_{sr}-\dot{p}_{\rm s}) - k_{\alpha 1}(\dot{\alpha}_d-\dot{\alpha}) \quad (54)$$

where $\mathbf{Y}_{\rm s}\widehat{\boldsymbol{\theta}}_{\rm s}$ is a model-based feedforward compensation term by using the estimated parameters for $\boldsymbol{\theta}_{\rm s}$.

The estimated parameter vector $\widehat{\boldsymbol{\theta}}_{\rm s}$ in (54) needs to be updated. Define

$$\mathbf{s}_{\rm s} = (\dot{\alpha}_d-\dot{\alpha})\mathbf{Y}_{\rm s}^T. \quad (55)$$

The γth element of $\widehat{\boldsymbol{\theta}}_{\rm s}$ is updated by using the $\mathscr{P}_2$ function defined by (5) as

$$\widehat{\theta}_{{\rm s}\gamma} = \mathscr{P}_2({\rm s}_{\rm s}\gamma, \rho_{{\rm s}\gamma}, \underline{\theta}_{{\rm s}\gamma}, \overline{\theta}_{{\rm s}\gamma}, \sigma_{{\rm s}\gamma}, t), \forall \gamma \in \{1,2,...,12\} \quad (56)$$

where $\widehat{\theta}_{{\rm s}\gamma}$ denotes the γth element of $\widehat{\boldsymbol{\theta}}_{\rm s}$, ${\rm s}_{{\rm s}\gamma}$ denotes the γth element of $\mathbf{s}_{\rm s}$, $\rho_{{\rm s}\gamma}$ is an update gain, $\sigma_{{\rm s}\gamma}$ is a correction gain, $\underline{\theta}_{{\rm s}\gamma}$ denotes the lower bound of $\theta_{{\rm s}\gamma}$ and $\overline{\theta}_{{\rm s}\gamma}$ denotes the upper bound of $\theta_{{\rm s}\gamma}$.

The following lemma holds for the subsystem 2 subject to control equation (54) with the parameter adaptation laws (55) and (56).

Lemma 9. *Consider the decomposed subsystem 2, given in Fig. 1, described by* (21) *and combined with its respective control equation* (54) *and with the parameter adaptation* (55) *and* (56)*. Let the non-negative accompanying function* v_{2a} *for the subsystem 2 be*

$$v_{2a} = \frac{1}{2}(\dot{\alpha}_d-\dot{\alpha})^2 + \frac{1}{2}\sum_{\gamma=1}^{12}\frac{(\theta_{{\rm s}\gamma}-\widehat{\theta}_{{\rm s}\gamma})^2}{\rho_{{\rm s}\gamma}}. \quad (57)$$

Then, the time derivative of (57) *can be expressed by*

$$\dot{v}_{2a} \leqslant -L_{\rm cp}A_{\rm cp}g_1(\alpha)(p_{\rm cpd}-p_{\rm cp})(\dot{\alpha}_d-\dot{\alpha}) - \omega(t)k_{\rm p2}(\dot{\alpha}_d-\dot{\alpha})(\dot{p}_{sr}-\dot{p}_{\rm s}) - k_{\alpha 1}(\dot{\alpha}_d-\dot{\alpha})^2. \quad (58)$$

Proof. See Appendix G.

The terms in the right-hand side of (58) are the same terms in the right-hand side of (36).

4.2.3 Subsystem 3

When parameters in (37) are unknown, the control law for the subsystem 3 is changed to

$$u_{vd} = \mathbf{Y}_{\rm c}\widehat{\boldsymbol{\theta}}_{\rm c} - g_1(\alpha)k_{\alpha 2}(\dot{\alpha}_d-\dot{\alpha}) + k_{\rm p3}(p_{\rm cpd}-p_{\rm cp}) \quad (59)$$

where $\mathbf{Y}_{\rm c}\widehat{\boldsymbol{\theta}}_{\rm c}$ is a model-based feedforward compensation term by using the estimated parameters for $\boldsymbol{\theta}_{\rm c}$.

When Condition 3 holds, using (59), the control valve voltage can be obtained, in view of (29), as

$$u_{\rm c} = \frac{x_{\rm cp}(\alpha)}{\widehat{c}_{\rm p}\upsilon(p_{\rm as}-p_{\rm cp})}u_{vd}S(u_{vd}) + \frac{x_{\rm cp}(\alpha)}{\widehat{c}_{\rm n}\upsilon(p_{\rm cp}-p_{\rm ar})}u_{vd}S(-u_{vd}). \quad (60)$$

When Condition 2 holds, (60) can be written inversely as

$$u_{vd} = -\mathbf{Y}_{\rm v}\widehat{\boldsymbol{\theta}}_{\rm v} \quad (61)$$

in view of (28).

The estimated parameter vectors $\widehat{\boldsymbol{\theta}}_{\rm c}$ and $\widehat{\boldsymbol{\theta}}_{\rm v}$ in (59) and (61), respectively, need to be updated. Define

$$\mathbf{s}_{\rm c} = (p_{\rm cpd}-p_{\rm cp})\mathbf{Y}_{\rm c}^T \quad (62)$$

$$\mathbf{s}_{\rm v} = (p_{\rm cpd}-p_{\rm cp})\mathbf{Y}_{\rm v}^T. \quad (63)$$

The γth elements of $\widehat{\boldsymbol{\theta}}_{\rm c}$ and $\widehat{\boldsymbol{\theta}}_{\rm v}$ are updated by using the $\mathscr{P}_2$ function defined by (5) as

$$\widehat{\theta}_{{\rm c}\gamma} = \mathscr{P}_2({\rm s}_{{\rm c}\gamma}, \rho_{{\rm c}\gamma}, \underline{\theta}_{{\rm c}\gamma}, \overline{\theta}_{{\rm c}\gamma}, \sigma_{{\rm c}\gamma}, t), \forall \gamma \in \{1,2\} \quad (64)$$

$$\widehat{\theta}_{{\rm v}\gamma} = \mathscr{P}_2({\rm s}_{{\rm v}\gamma}, \rho_{{\rm v}\gamma}, \underline{\theta}_{{\rm v}\gamma}, \overline{\theta}_{{\rm v}\gamma}, \sigma_{{\rm v}\gamma}, t), \forall \gamma \in \{1,2\} \quad (65)$$

where $\widehat{\theta}_{{\rm c}\gamma}$ and $\widehat{\theta}_{{\rm v}\gamma}$ denote the γth element of $\widehat{\boldsymbol{\theta}}_{\rm c}$ and $\widehat{\boldsymbol{\theta}}_{\rm v}$, respectively; ${\rm s}_{{\rm c}\gamma}$ and ${\rm s}_{{\rm v}\gamma}$ denote the γth element of $\mathbf{s}_{\rm c}$ and $\mathbf{s}_{\rm v}$, respectively; $\rho_{{\rm c}\gamma}$ and $\rho_{{\rm v}\gamma}$ are update gains; $\sigma_{{\rm c}\gamma}$ and $\sigma_{{\rm v}\gamma}$ are correction gains; $\underline{\theta}_{{\rm c}\gamma}$ and $\underline{\theta}_{{\rm v}\gamma}$ denote the lower bounds of $\theta_{{\rm c}\gamma}$ and $\theta_{{\rm v}\gamma}$, respectively; and $\overline{\theta}_{{\rm c}\gamma}$ and $\overline{\theta}_{{\rm v}\gamma}$ denote the upper bounds of $\theta_{{\rm c}\gamma}$ and $\theta_{{\rm v}\gamma}$, respectively.

The following lemma holds for the subsystem 3 subject to control equation (59) with the parameter adaptation laws (62)–(65).

Lemma 10. *Consider the decomposed subsystem 3, given in Fig. 1, described by* (27) *and* (29)*, combined with its respective control equations* (59) *and* (60) *and with the parameter adaptation* (62)–(65)*. Let the non-negative accompanying function* v_{3a} *for the subsystem 3 be*

$$v_{3a} = \frac{A_{\rm cp}}{2\beta_{\rm f}}(p_{\rm cpd}-p_{\rm cp})^2 + \frac{1}{2}\sum_{\gamma=1}^{2}\frac{(\theta_{{\rm c}\gamma}-\widehat{\theta}_{{\rm c}\gamma})^2}{\rho_{{\rm c}\gamma}} + \frac{1}{2}\sum_{\gamma=1}^{2}\frac{(\theta_{{\rm v}\gamma}-\widehat{\theta}_{{\rm v}\gamma})^2}{\rho_{{\rm v}\gamma}}. \quad (66)$$

Then, the time derivative of (66) *can be expressed by*

$$\dot{v}_{3a} \leqslant g_1(\alpha)k_{\alpha 2}(p_{\rm cpd}-p_{\rm cp})(\dot{\alpha}_d-\dot{\alpha}) - k_{\rm p3}(p_{\rm cpd}-p_{\rm cp})^2. \quad (67)$$

Proof. See Appendix H.

The terms in the right-hand side of (67) are the same terms in the right-hand side of (41).

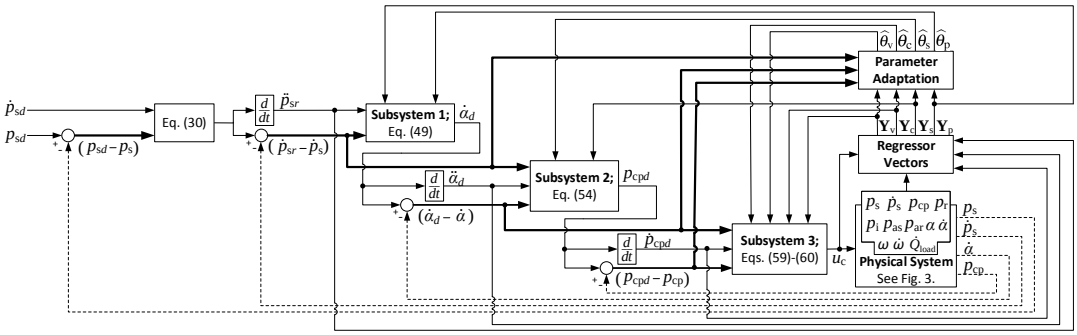

Fig. 4. The diagram of the designed adaptive control system for the VDAPP controlling the discharge pressure. The error signals are highlighted in bold and the feedback variables are highlighted with the dashed line.

The detailed diagram for the adaptive control design is given in Fig. 4. As shown in Fig. 3, the system discharge pressure p_s is controlled using the control valve voltage u_c. In the adaptive control design, such a control valve voltage u_c is solved inversely (based on the designed adaptive feedforward compensation terms and the feedback signals), which yields an accurate discharge pressure tracking performance for the system.

4.2.4 Stability of the Adaptive Control Design

The following Theorem 2 guarantees, in the sense of Lemma 1, the stability of the entire system with the adaptive control design.

Theorem 2. *Consider the discharge pressure controlled VDAPP, decomposed into subsystems 1–3, given in Fig. 1, described by* (16)*,* (21)*,* (27) *and* (29) *and combined with the control equations* (30)*,* (49)*,* (54)*,* (59) *and* (60) *and with the parameter adaptation* (50)*,* (51)*,* (55)*,* (56) *and* (62)–(65)*. Then, it follows that* (42)–(46) *are guaranteed for the adaptive control design.*

Proof. The proof for Theorem 2 follows directly from the Lemmas 8–10. Using (52), (57) and (66), let the non-negative accompanying function for the discharge pressure controlled VDAPP be

$$v_a = \frac{2\pi\alpha_{max}}{V_{max}} v_{1a} + \frac{1}{k_{p2}} v_{2a} + \frac{L_{cp}A_{cp}}{k_{p2}k_{\alpha 2}} v_{3a} \geqslant a_1(\dot{p}_{sr} - \dot{p}_s)^2 + a_2(\dot{\alpha}_d - \dot{\alpha})^2 + a_3(p_{cpd} - p_{cp})^2 \quad (68)$$

where $a_1 > 0$, $a_2 > 0$ and $a_3 > 0$. Then, it follows from (53), (58) and (67) that

$$\dot{v}_a = \frac{2\pi\alpha_{max}}{V_{max}} \dot{v}_{1a} + \frac{1}{k_{p2}} \dot{v}_{2a} + \frac{L_{cp}A_{cp}}{k_{p2}k_{\alpha 2}} \dot{v}_{3a} \leqslant -b_1(\dot{p}_{sr} - \dot{p}_s)^2 - b_2(\dot{\alpha}_d - \dot{\alpha})^2 - b_3(p_{cpd} - p_{cp})^2 \quad (69)$$

holds, with $b_1 > 0$, $b_2 > 0$ and $b_3 > 0$.

Consequently, in view of Lemma 1, it follows from Lemma 2, (30), (68) and (69) that (42)–(46) hold for the adaptive control design.

4.3 Asymptotic Convergence

For the asymptotic convergence, the following assumption is made for Q_{load}, $\omega(t)$ and p_{as}.

Assumption 2. *The load fluid flow rate Q_{load}, the VDAPP input shaft angular velocity $\omega(t)$ and the auxiliary supply line pressure p_{as} are continuously differentiable functions in C^2, C^2 and C^0, respectively.*

Theorem 3. *When the desired discharge pressure p_{sd} is a continuously differentiable function in C^3 and Assumptions 1–2 hold, it follows from Lemma 1, Definition 2, Condition 3,* (13)–(16)*,* (21)*,* (27)*,* (28)*,* (30)*,* (42)–(46)*,* (49)–(52)*,* (54)–(57)*,* (59)*,* (60)*,* (66)*,* (68)*,* (69) *and* (86)–(87) *that for the adaptive control design the following properties*

$$p_{sd} - p_s \in L_2 \wedge \dot{p}_{sd} - \dot{p}_s \in L_\infty \quad (70)$$

$$\dot{p}_{sr} - \dot{p}_s \in L_2 \wedge \ddot{p}_{sr} - \ddot{p}_s \in L_\infty \quad (71)$$

$$\dot{\alpha}_d - \dot{\alpha} \in L_2 \wedge \ddot{\alpha}_d - \ddot{\alpha} \in L_\infty \quad (72)$$

$$p_{cpd} - p_{cp} \in L_2 \wedge \dot{p}_{cpd} - \dot{p}_{cp} \in L_\infty \quad (73)$$

hold, which directly lead to $(p_{sd} - p_s) \to 0$, $(\dot{p}_{sr} - \dot{p}_s) \to 0$, $(\dot{\alpha}_d - \dot{\alpha}) \to 0$ and $(p_{cpd} - p_{cp}) \to 0$, in view of Lemma 3.

Proof. See Appendix I.

5 Experiments

Experiments have been conducted to validate the proposed control approach. First, in Section 5.1, the system set-up and the controller implementation issues are discussed. Then, the experimental results for both the known-parameter control design and the adaptive control design are presented in Section 5.2.

5.1 System Set-up and Implementation Issues

The experimental set-up (see Fig. 5) consisted of the following hardware components:

- dSpace DS1103 system
- Bosch Rexroth A10VS/45 variable displacement axial piston pump

- ABB 22kW asynchronous electric motor, with constant angular velocity ($\omega(t) = 1470$ rpm), to drive pump's input shaft
- Bosch Rexroth 4WRPEH6 proportional valve (40 dm^3/min @ Δp = 3.5 MPa per notch), with a bandwidth of 100 Hz @ $\pm$5% signals, for the control valve
- Bosch Rexroth 4WRPEH6 proportional valve (4 dm^3/min @ Δp = 3.5 MPa per notch), with a bandwidth of 100 Hz @ $\pm$5% signals, for the valve for Q_{add}
- Two series-connected turbulent flow orifices as the load
- Druck PTX1400 pressure transmitters with an operating pressure range of 25 MPa

With the VDAPP, the bias piston is connected internally to the pump discharge line. To emulate the independent-feeding system, given in Fig. 1, an additional fluid flow rate Q_{add} was added (in open-loop manner) to the system discharge line (see Fig. 5) to counterbalance the fluid flow rate Q_{bp}, so that $Q_{add} + Q_{\mathrm{bp}} = 0$. For the bias piston chamber pressure, p_{s} was used instead of p_{as} (note that the pressure for the bias piston is an isolated local issue that can be addressed locally and does not invalidate the system stability or convergence).

In the experiments, two series-connected turbulent orifices were used as the system load. Thus, Q_{load} was estimated as

$$Q_{load} = c_{\mathrm{lo}}\sqrt{p_{\mathrm{s}} - p_{\mathrm{lo}}} \tag{74}$$

where c_{lo} is a constant and p_{lo} is the pressure between the orifices. If a fluid flow rate sensor is available, it can also be used to measure Q_{load}.

Table 1 shows applied parameter values for the known-parameter control design in the fourth column ($\theta_{\mathrm{p}\gamma}$, $\theta_{\mathrm{s}\gamma}$, $\theta_{\mathrm{c}\gamma}$ and $\theta_{\mathrm{v}\gamma}$). For the adaptive control design, the parameter update gains ($\rho_{\mathrm{p}\gamma}$, $\rho_{\mathrm{s}\gamma}$, $\rho_{\mathrm{c}\gamma}$ and $\rho_{\mathrm{v}\gamma}$), upper bounds ($\overline{\theta}_{\mathrm{p}\gamma}$, $\overline{\theta}_{\mathrm{s}\gamma}$, $\overline{\theta}_{\mathrm{c}\gamma}$ and $\overline{\theta}_{\mathrm{v}\gamma}$) and lower bounds ($\underline{\theta}_{\mathrm{p}\gamma}$, $\underline{\theta}_{\mathrm{s}\gamma}$, $\underline{\theta}_{\mathrm{c}\gamma}$ and $\underline{\theta}_{\mathrm{v}\gamma}$) are given in the second, third and last columns, respectively. The

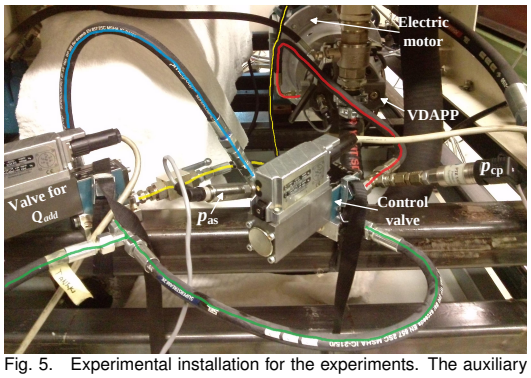

Fig. 5. Experimental installation for the experiments. The auxiliary supply line is highlighted in blue, the fluid return line is highlighted in green, the line between the control valve and the VDAPP is highlighted in red and the line for an additional fluid flow rate Q_{add} is highlighted in yellow.

Table 1. Values used for the known-parameters θ, parameter update gains ρ, upper bounds $\overline{\theta}$ and lower bounds $\underline{\theta}$

γ	$\rho_{\mathrm{p}\gamma}$	$\overline{\theta}_{\mathrm{p}\gamma}$	$\theta_{\mathrm{p}\gamma}$	$\underline{\theta}_{\mathrm{p}\gamma}$
1	$4\cdot10^{-24}$	$1.2\cdot10^{-9}$	$1.0\cdot10^{-10}$	$1.0\cdot10^{-14}$
2	$1\cdot10^{-20}$	$2.3\cdot10^{-3}$	$2.3\cdot10^{-3}$	$2.3\cdot10^{-3}$
3	$1\cdot10^{-3}$	3.0	1.0	0.5
4	$4\cdot10^{-22}$	$1.0\cdot10^{-8}$	$1.0\cdot10^{-12}$	$1.0\cdot10^{-13}$
γ	$\rho_{\mathrm{s}\gamma}$	$\overline{\theta}_{\mathrm{s}\gamma}$	$\theta_{\mathrm{s}\gamma}$	$\underline{\theta}_{\mathrm{s}\gamma}$
1	50	2.0	1.0	0.01
2	$1\cdot10^{-20}$	$1.3\cdot10^{-3}$	$1.3\cdot10^{-3}$	$1.3\cdot10^{-3}$
3	$1\cdot10^{-20}$	$4.4\cdot10^{-3}$	$4.4\cdot10^{-3}$	$4.4\cdot10^{-3}$
4	$1\cdot10^{-14}$	$1.0\cdot10^{-5}$	$7.5\cdot10^{-6}$	$1.0\cdot10^{-6}$
5	10	40	16.5	1.0
6	6	40	8.7	1.0
7	$1\cdot10^{-20}$	$1.7\cdot10^{-3}$	$1.7\cdot10^{-3}$	$1.7\cdot10^{-3}$
8	$1\cdot10^{-20}$	$4.4\cdot10^{-3}$	$4.4\cdot10^{-3}$	$4.4\cdot10^{-3}$
9	$1\cdot10^{-20}$	$6.4\cdot10^{-4}$	$6.4\cdot10^{-4}$	$6.4\cdot10^{-4}$
10	$1\cdot10^{-20}$	$4.9\cdot10^{-3}$	$4.9\cdot10^{-3}$	$4.9\cdot10^{-3}$
11	$1\cdot10^{-8}$	$1.0\cdot10^{-3}$	$3.2\cdot10^{-4}$	$1.0\cdot10^{-5}$
12	$1\cdot10^{-20}$	$1.9\cdot10^{-6}$	$1.9\cdot10^{-6}$	$1.9\cdot10^{-6}$
γ	$\rho_{\mathrm{c}\gamma}$	$\overline{\theta}_{\mathrm{c}\gamma}$	$\theta_{\mathrm{c}\gamma}$	$\underline{\theta}_{\mathrm{c}\gamma}$
1	$1\cdot10^{-24}$	$1\cdot10^{-12}$	$4.8\cdot10^{-13}$	$5.0\cdot10^{-14}$
2	$1\cdot10^{-10}$	$1\cdot10^{-3}$	$4.8\cdot10^{-4}$	$1.0\cdot10^{-4}$
γ	$\rho_{\mathrm{v}\gamma}$	$\overline{\theta}_{\mathrm{v}\gamma}$	$\theta_{\mathrm{v}\gamma}$	$\underline{\theta}_{\mathrm{v}\gamma}$
1	$1\cdot10^{-20}$	$6.0\cdot10^{-9}$	$3.6\cdot10^{-9}$	$2.0\cdot10^{-9}$
2	$1\cdot10^{-18}$	$6.0\cdot10^{-9}$	$3.6\cdot10^{-9}$	$2.0\cdot10^{-9}$

value for the parameter correction gain $\sigma_{\mathrm{x}\gamma}$ (i.e., $\sigma_{\mathrm{p}\gamma}$, $\sigma_{\mathrm{s}\gamma}$, $\sigma_{\mathrm{c}\gamma}$ and $\sigma_{\mathrm{v}\gamma}$) was computed from the respective $\rho_{\mathrm{x}\gamma}$ (i.e., $\rho_{\mathrm{p}\gamma}$, $\rho_{\mathrm{s}\gamma}$, $\rho_{\mathrm{c}\gamma}$ and $\rho_{\mathrm{v}\gamma}$) as

$$\sigma_{\mathrm{x}\gamma} = \frac{1000}{\rho_{\mathrm{x}\gamma}}. \tag{75}$$

Despite a relatively high number of tuning parameters in Table 1, the tuning of the adaptive controller is rather simple. This originates from the subsystem-dynamics-based control design principle of the proposed control design method. First, the controller is tuned with the known-parameter values (θ). Then, the adaptive control is enabled. The choice of upper and lower bounds ($\overline{\theta}$ and $\underline{\theta}$) for a parameter can be performed rather intuitively. Then, the parameter update gains (ρ) for a specific subsystem are gradually increased until the tracking performance of the controlled signal of this subsystem (see Fig. 3 for the controlled signals of the system) is improved sufficiently. This procedure is repeated subsystem by subsystem.

Table 2 shows the controller feedback gains for both the known-parameter and the adaptive control designs. The controller sample time was $t_s = 1$ ms. In the control designs, SI-units were used for all variables and parameters.

As can be seen from Fig. 4, many variables with their time derivatives are used in the control design. It is well-

Table 2. Controller feedback gains used in the experiments

λ_{p}	k_{p1}	k_{p2}	$k_{\alpha 1}$	$k_{\alpha 2}$	k_{p3}
15 $\left[\frac{1}{\mathrm{s}}\right]$	$1\cdot10^{-8}$ $\left[\frac{\mathrm{m}^3}{\mathrm{Pa\cdot s}}\right]$	$4\cdot10^{-5}$ $\left[\frac{1}{\mathrm{Pa}}\right]$	0.2 $\left[\frac{1}{\mathrm{s}}\right]$	$4\cdot10^{-5}$ $\left[\frac{\mathrm{m}^4\cdot\mathrm{kg}}{\mathrm{rad}}\right]$	$4\cdot10^{-9}$ $\left[\frac{\mathrm{m}^2}{\mathrm{Pa\cdot s}}\right]$

known that commonly used computations for the derivative, e.g., the backward difference, often lead to noisy differentiation signals, especially with small step increments and high sampling rates. As discussed and experimentally verified in our previous study [34], a finite difference method [35], defined as

$$\dot{y}(t) \approx \frac{1}{t_s}\sum_{k=0}^{n-1} C_k y(t-kt_s) \tag{76}$$

enhanced with a Geometric Moving Average (GMA) filter [36], defined as

$$y(k) = (1-\delta)y(k-1) + \delta u(k) \tag{77}$$

provides an effective method to produce noise-suppressed differentiated signals. In the control implementation, all time derivative signals were estimated with (76) and (77). In (76), $C_k = [5\ 3\ 1\ -1\ -3\ -5]/35$ was used. In (77), the most recent input $u(k)$ is weighted by δ and the past values are weighted by $(1-\delta)$. The value $\delta = 0.04$ was used to compromise between disturbance attenuation and low phase lag. The choice of the filter is to make sure that considerable phase lags only happen at frequencies beyond the range determined by the swash plate dynamics.

Fig. 6 shows samples of the measured system discharge pressure p_{s} (the first plot) and the measured control piston chamber pressure p_{cp} (the second plot) in open-loop control. As this figure shows, the nature of both pressures is inherently oscillatory with high frequencies. Oscillatory pressure behaviours originate from the VDAPP's pumping pistons' high-frequency transitions (in the experiment $\omega(t) =$ 1470 rpm) between the suction and the discharge phases (see Fig. 2). Evidently, it is not practical to input these perturbed pressure signals to the controller without signal processing. Thus, before using these pressure signals in control, they were filtered (and averaged) with the GMA filter, given in (77). The p_{s} and p_{cp}, shown in Figs. 7–10, are GMA-filtered pressures.

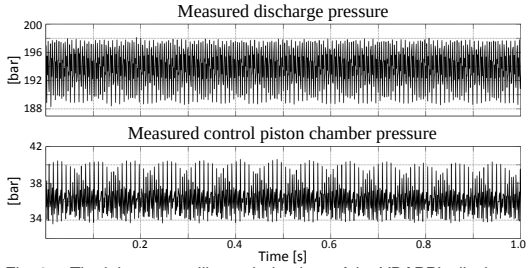

Fig. 6. The inherent oscillatory behaviour of the VDAPP's discharge pressure and control piston chamber pressure.

5.2 Discharge Pressure Control Experiments

In the experiments, the system discharge pressure was first driven to its desired pressure level $p_{\mathrm{s}d0} = 190$ bar. Then, the following desired discharge pressure trajectory $p_{\mathrm{s}d}(t)$ was used

$$p_{\mathrm{s}d}(t) = p_{\mathrm{s}d0} + 85\,[\cos(0.8\pi t) - 1]\,\mathrm{bar}. \tag{78}$$

Note that, equation (78) is a continuously differentiable function in C^3, and no additional closed-loop control is employed for Q_{load}, $\omega(t)$ or p_{as} (Assumption 2 is valid). Thus, an asymptotic convergence is anticipated for the adaptive control design, in the sense of Theorem 3.

5.2.1 Results with the Known-Parameter Control

In Fig. 7, the first plot shows the desired discharge pressure in black and the measured discharge pressure in red. The second plot shows a detailed discharge pressure tracking error. The absolute maximum discharge pressure tracking error for the test trajectory is approximately 10.13 bar (5.9 percent of the test trajectory's peak-to-peak amplitude). The last plot shows the (normalized) measured swash plate angle (with α_{max} = 0.3163 [rad] = 18.1 [deg]) during the experiment. As this plot shows, a smooth swash plate angle behaviour is achieved and a wide range of the VDAPP's operating space was covered in the experiment.

Fig. 8 shows the tracking performances for the subsidiary feedback variables ($\dot{p}_{\mathrm{s}}$, $\dot{\alpha}$ and p_{cp}) with the known-parameter control design. The first plot shows the required first-order discharge pressure dynamics $\dot{p}_{\mathrm{s}r}$ in black and its controlled variable $\dot{p}_{\mathrm{s}}$ in red. The second plot shows the desired swash plate angular velocity $\dot{\alpha}_d$ in black and its controlled variable $\dot{\alpha}$ in red. The last plot shows the desired control piston chamber pressure $p_{\mathrm{cp}d}$ in black and its controlled variable p_{cp} in red.

5.2.2 Results with the Adaptive Control

Figs. 9–10 show the main results of this paper. In Fig. 9, the first plot shows the desired discharge pressure trajectory in black and the measured discharge pressure in red. The second plot shows a detailed discharge pressure tracking error. The absolute maximum discharge pressure tracking error for the test trajectory is 1.36 bar (0.8 percent of the test trajectory's peak-to-peak amplitude). This is approximately seven times improvement compared to the results with the known-parameter control design. The last plot in Fig. 9 shows the (normalized) measured swash plate angle. As this plot shows, a smooth swash plate angle behaviour is achieved and a wide range of the VDAPP's operating space was covered in the experiment.

Fig. 10 shows the tracking performances for the subsidiary feedback variables ($\dot{p}_{\mathrm{s}}$, $\dot{\alpha}$ and p_{cp}) with the adaptive control design. The first plot shows the required first-order discharge pressure dynamics $\dot{p}_{\mathrm{s}r}$ in black and its controlled variable $\dot{p}_{\mathrm{s}}$ in red. The second plot shows the desired swash plate angular velocity $\dot{\alpha}_d$ in black and its controlled variable $\dot{\alpha}$ in red. The last plot shows the desired control piston cham-

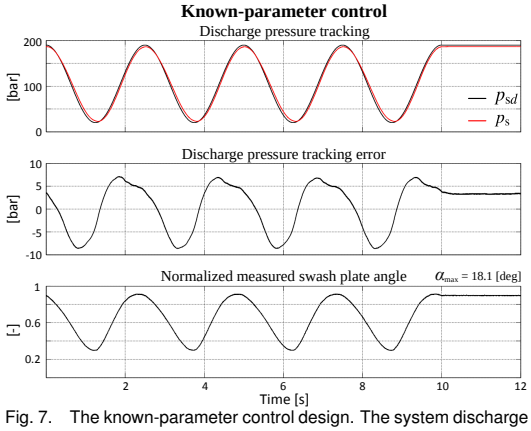

Fig. 7. The known-parameter control design. The system discharge pressure tracking performance is described in plots 1–2 and the measured (normalized) swash plate angle is given in plot 3.

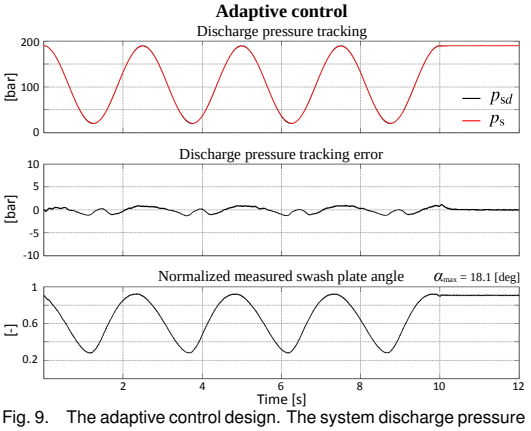

Fig. 9. The adaptive control design. The system discharge pressure tracking performance is described in plots 1–2 and the measured (normalized) swash plate angle is given in plot 3.

ber pressure p_{cpd} in black and its controlled variable p_{cp} in red. As Fig. 10 shows, very accurate trajectory tracking performance is achieved for all subsidiary feedback variables.

As Figs. 7–10 demonstrate, the adaptive control design, with the rapid parameter adaptation law (5), is superior to the known-parameter control. In [32] and [37], corresponding results were obtained in the control of the hydraulic manipulator, where the results using rapid parameter adaptation law were superior compared to the known-parameter control design (in [32] and [37], a first-order differentiable projection function was used instead of the second-order differentiable version used in the present paper). Thus, it can be concluded that the rapid parameter adaptation law 1) provides an efficient method to compensate model parameter uncertainties and 2) significantly improves the control performance of complex nonlinear systems, such as hydraulic systems.

In [23], a desired discharge pressure was varied between 50–100 bars using a sinusoidal desired pressure trajectory. To promote the scientific cornerstones of reproducible and measurable research (see [38]), the following unifying performance indicator φ (originating from the performance indicator ρ in [32, 39, 40]) is proposed

$$\varphi = \frac{\max\{|p_{sd} - p_s|\}}{\max\{|\dot{p}_s|\}}. \tag{79}$$

This novel indicator evaluates the discharge pressure tracking error with respect to the rate of applied dynamics and can be used to compare the control performances between the proposed method and the results in [23]. The smaller the φ, the better the control performance. Using the data in Figs. 9–10, for the proposed method, $\varphi = \frac{1.36 \text{ bar}}{213 \text{ bar/s}} \approx 0.00064$ (s) can be measured. Surprisingly, for the results in [23] (see Fig. 11a in [23]), the same value $\varphi = \frac{1 \text{ bar}}{157 \text{ bar/s}} \approx 0.00064$ (s) is obtained ($\dot{p}_s$ was not reported in [23]; thus, $\max\{|\dot{p}_s|\}$ in φ was estimated from the used pressure profile $p_{sd}(t) = [75 - 25\cos(2\pi t)]$ bar). However, it is evident that the dis-

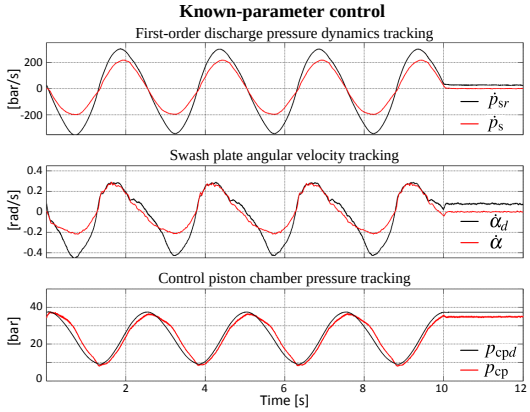

Fig. 8. The tracking performance of the system's subsidiary feedback variables $\dot{p}_s$, $\dot{\alpha}$ and p_{cp} with the known-parameter control design. The reference trajectories are given in black (—) and their feedback variables are given in red (—).

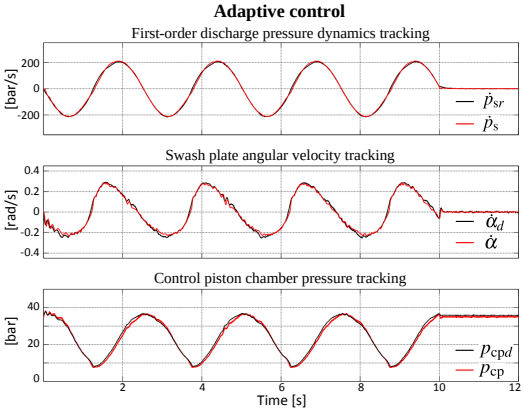

Fig. 10. The tracking performance of the system's subsidiary feedback variables $\dot{p}_s$, $\dot{\alpha}$ and p_{cp} with the adaptive control design. The reference trajectories are given in black (—) and their feedback variables are given in red (—).

charge pressure range of 170 bars with the minimum pressure of 20 bars (the test trajectory in this study) is much more challenging than the discharge pressure range of 50 bars with the minimum pressure of 50 bars (the test trajectory in [23]). This is due to the highly nonlinear operation space of VDAPPs. The absolute maximum discharge pressure tracking error with the proposed method is only 0.8 percent of the test trajectory's peak-to-peak amplitude. In [23] this same value is 2 percent. This was expected due to the proposed controller's proper handling of swash plate dynamics. Thus, it can be concluded that the proposed controller has a comparative ratio to [23], in view of (79), but tested in a larger operation range.

The main emphasis in this study was to design a high-performance discharge pressure tracking controller for VDAPPs, whose dynamical behaviours are highly nonlinear and can be described by a fourth-order differential equation. As the results in Figs. 9–10 indisputably verify, the proposed control method is capable of rigorously addressing the highly nonlinear dynamic behaviours of the truly complex VDAPP in a very large operational range.

6 Conclusions

This paper proposed for the first time, without any linearization or order-reduction, an adaptive and model-based nonlinear control method for the discharge pressure controlled variable displacement axial piston pump, whose dynamical behaviour is highly nonlinear and can be described by a fourth-order nonlinear differential equation. Similar to the Virtual Decomposition Control (VDC) approach, the control design was based on the use of subsystems' dynamics, rather than the centralized system dynamics, while rigorously guaranteeing the stability of the entire system. In the proposed control design method, the designed stabilizing terms constitute an essential core for the method, by canceling out all the stability-preventing terms. The experiments with the rapid parameter adaptation law demonstrated superior control performance to the known-parameter control design. When the desired discharge pressure was varied between 20–190 bars, as small as 1.36 bar maximum tracking error was achieved with the adaptive control design. The experiments of this study indisputably verified that the proposed control design method is capable of rigorously addressing the highly nonlinear dynamic behaviours of truly complex systems (in this study a VDAPP) in a very large operational range. With an accurate discharge pressure tracking ability, the possibility for energy consumption optimization exists, as the desired discharge pressure can be designed slightly higher than the required load pressure.

A Proof for Lemma 1

The proof for Lemma 1 is derived directly from proofs for Lemmas 2.1 and 2.2 in [25].

Consider a non-negative piecewise continuous function

$$\xi(t) \geqslant \sum_{i=1}^{n} \frac{a_i}{2} x_i(t)^2 \geqslant 0 \tag{80}$$

such that

$$\dot{\xi}(t) \leqslant -\sum_{j=1}^{m} b_j y_j(t)^2 \leqslant 0 \tag{81}$$

holds $\forall i \in \{1,n\}$, $\forall j \in \{1,m\}$, and with $a_i > 0$ and $b_j > 0$.

Integrating (81) over time yields

$$\xi(t) \leqslant -\int_0^{\infty} \sum_{j=1}^{m} b_j y_j(t)^2 dt \leqslant \xi(0),\ \forall t > 0 \tag{82}$$

which implies $\xi(t) \in L_\infty$, in the sense of Definition 1.

As $\xi(t) \in L_\infty$, it follows from (80) that

$$\sum_{i=1}^{n} \frac{a_i}{2} x_i(t)^2 \leqslant \xi(t) < \infty \tag{83}$$

holds $\forall t > 0$, leading to $x_i(t) \in L_\infty, \forall i \in \{1,n\}$.

Re-writing (81) as

$$\sum_{j=1}^{m} b_j y_j(t)^2 \leqslant -\dot{\xi}(t) \tag{84}$$

and integrating both sides over time yields

$$\begin{aligned} \int_0^{\infty} \sum_{j=1}^{m} b_j y_j(t)^2 dt &\leqslant -\int_0^{\infty} \dot{\xi}(t) dt \\ &\leqslant \xi(0) - \xi(\infty) \\ &\leqslant \xi(0) \end{aligned} \tag{85}$$

which implies $y_j(t) \in L_2, \forall j \in \{1,m\}$, in the sense of Definition 1. ■

B Regressor Vectors $\mathbf{Y}_\mathrm{p}$, $\mathbf{Y}_\mathrm{s}$, $\mathbf{Y}_\mathrm{c}$ and $\mathbf{Y}_\mathrm{v}$, and Parameter Vectors $\boldsymbol{\theta}_\mathrm{p}$, $\boldsymbol{\theta}_\mathrm{s}$, $\boldsymbol{\theta}_\mathrm{c}$ and $\boldsymbol{\theta}_\mathrm{v}$

The detailed expressions for the regressor vector $\mathbf{Y}_\mathrm{p} \in \mathbb{R}^{1\times 4}$ and parameter vector $\boldsymbol{\theta}_\mathrm{p} \in \mathbb{R}^4$ are written as

$$\mathbf{Y}_\mathrm{p} = \begin{bmatrix} \ddot{p}_{sr} \\ -\dot{\omega}(t)\alpha \\ \dot{Q}_{load} \\ \dot{p}_\mathrm{s} \end{bmatrix}^T, \quad \boldsymbol{\theta}_\mathrm{p} = \begin{bmatrix} \frac{V_\mathrm{s}}{\beta_{eff}} \\ \frac{V_{max}}{2\pi\alpha_{max}} \\ 1 \\ k_{leak} \end{bmatrix}. \tag{86}$$

The detailed expressions for the regressor vector $\mathbf{Y}_\mathrm{c} \in \mathbb{R}^{1\times 2}$ and the parameter vector $\boldsymbol{\theta}_\mathrm{c} \in \mathbb{R}^2$ are written as

$$\mathbf{Y}_\mathrm{c} = \begin{bmatrix} \dot{p}_{\mathrm{cp}d} & \dfrac{\dot{x}_\mathrm{cp}(\dot{\alpha},\alpha)}{x_\mathrm{cp}(\alpha)} \end{bmatrix}, \ \boldsymbol{\theta}_\mathrm{c} = \begin{bmatrix} \dfrac{A_\mathrm{cp}}{\beta_\mathrm{f}} & A_\mathrm{cp} \end{bmatrix}^T. \tag{87}$$

The detailed expressions for the regressor vector $\mathbf{Y}_\mathrm{v} \in$

$\mathbb{R}^{1\times 2}$ and the parameter vector $\boldsymbol{\theta}_{\rm v}\in\mathbb{R}^2$ are written as

$$\mathbf{Y}_{\rm v}=\begin{bmatrix}-\frac{\upsilon(p_{\rm as}-p_{\rm cp})}{x_{\rm cp}(\alpha)}u_{\rm c}S(u_{\rm c})\\ -\frac{\upsilon(p_{\rm cp}-p_{\rm ar})}{x_{\rm cp}(\alpha)}u_{\rm c}S(-u_{\rm c})\end{bmatrix}^T,\ \boldsymbol{\theta}_{\rm v}=\begin{bmatrix}c_{\rm p}\\ c_{\rm n}\end{bmatrix}. \tag{88}$$

The detailed expressions for the regressor vector $\mathbf{Y}_{\rm s}\in\mathbb{R}^{1\times 12}$ and parameter vector $\boldsymbol{\theta}_{\rm s}\in\mathbb{R}^{12}$ are written as

$$\mathbf{Y}_{\rm s}=\begin{bmatrix}\ddot{\alpha}_d\\ \frac{g_1(\alpha)\sin(\alpha)}{\cos^3(\alpha)}\dot{\alpha}^2\\ \frac{g_1(\alpha)}{\cos^2(\alpha)}\dot{\alpha}\\ -g_1(\alpha)p_{\rm as}\\ -g_1(\alpha)\\ g_1(\alpha)\tan(\alpha)\\ \frac{g_1(\alpha)\sin(\alpha)}{\cos^3(\alpha)}\dot{\alpha}^2\\ \frac{g_1(\alpha)}{\cos^2(\alpha)}\dot{\alpha}\\ \frac{g_1(\alpha)\sin(\alpha)}{\cos^5(\alpha)}\dot{\alpha}^2\\ \frac{g_1(\alpha)}{\cos^4(\alpha)}\dot{\alpha}\\ -\frac{g_1(\alpha)\tan(\alpha)}{\cos^2(\alpha)}\omega(t)^2\\ \frac{g_1(\alpha)(p_{\rm s}-p_{\rm i})}{\cos^2(\alpha)}\end{bmatrix}^T,\ \boldsymbol{\theta}_{\rm s}=\begin{bmatrix}1\\ 2m_{\rm bp}L_{\rm bp}^2\\ C_{\rm bp}L_{\rm bp}^2\\ A_{\rm bp}L_{\rm bp}\\ f_{\rm s0}L_{\rm bp}\\ k_{\rm b}L_{\rm bp}^2\\ 2m_{\rm cp}L_{\rm cp}^2\\ C_{\rm cp}L_{\rm cp}^2\\ n_{\rm p}m_{\rm p}r_{\rm p}^2\\ \frac{n_{\rm p}C_{\rm p}r_{\rm p}^2}{2}\\ \frac{n_{\rm p}m_{\rm p}r_{\rm p}^2}{2}\\ \frac{n_{\rm p}A_{\rm p}r_{\rm p}\phi}{2\pi}\end{bmatrix}. \tag{89}$$

C Proof for Lemma 5

Subtracting (16) from (31) yields

$$\frac{V_s}{\beta_{eff}}(\ddot{p}_{sr}-\ddot{p}_{\rm s})=\frac{V_{max}}{2\pi\alpha_{max}}\omega(t)(\dot{\alpha}_d-\dot{\alpha})-k_{\rm p1}(\dot{p}_{sr}-\dot{p}_{\rm s}). \tag{90}$$

Then, differentiating (32) with respect to time and using (90) yields

$$\begin{aligned}\dot{\nu}_1&=(\dot{p}_{sr}-\dot{p}_{\rm s})\frac{V_s}{\beta_{eff}}(\ddot{p}_{sr}-\ddot{p}_{\rm s})\\ &=\frac{V_{max}}{2\pi\alpha_{max}}\omega(t)(\dot{\alpha}_d-\dot{\alpha})(\dot{p}_{sr}-\dot{p}_{\rm s})-k_{\rm p1}(\dot{p}_{sr}-\dot{p}_{\rm s})^2.\end{aligned} \tag{91}$$

■

D Proof for Lemma 6

Subtracting (21) from (34) yields

$$\begin{aligned}(\ddot{\alpha}_d-\ddot{\alpha})=&-L_{\rm cp}A_{\rm cp}g_1(\alpha)(p_{{\rm cp}d}-p_{\rm cp})\\ &-\omega(t)k_{\rm p2}(\dot{p}_{sr}-\dot{p}_{\rm s})-k_{\alpha 1}(\dot{\alpha}_d-\dot{\alpha}).\end{aligned} \tag{92}$$

Then, differentiating (35) with respect to time and using (92) yields

$$\begin{aligned}\dot{\nu}_2&=(\dot{\alpha}_d-\dot{\alpha})(\ddot{\alpha}_d-\ddot{\alpha})\\ &=-L_{\rm cp}A_{\rm cp}g_1(\alpha)(p_{{\rm cp}d}-p_{\rm cp})(\dot{\alpha}_d-\dot{\alpha})\\ &\quad-\omega(t)k_{\rm p2}(\dot{\alpha}_d-\dot{\alpha})(\dot{p}_{sr}-\dot{p}_{\rm s})-k_{\alpha 1}(\dot{\alpha}_d-\dot{\alpha})^2.\end{aligned} \tag{93}$$

■

E Proof for Lemma 7

Subtracting (27) from (37) and using (28) and (39) yields

$$\begin{aligned}\frac{A_{\rm cp}}{\beta_{\rm f}}(\dot{p}_{{\rm cp}d}-\dot{p}_{\rm cp})&=(u_{{\rm v}d}-u_{\rm v})+g_1(\alpha)k_{\alpha 2}(\dot{\alpha}_d-\dot{\alpha})\\ &\quad-k_{\rm p3}(p_{{\rm cp}d}-p_{\rm cp})\\ &=g_1(\alpha)k_{\alpha 2}(\dot{\alpha}_d-\dot{\alpha})-k_{\rm p3}(p_{{\rm cp}d}-p_{\rm cp}).\end{aligned} \tag{94}$$

Then, differentiating (40) with respect to time and using (94) yields

$$\begin{aligned}\dot{\nu}_3&=(p_{{\rm cp}d}-p_{\rm cp})\frac{A_{\rm cp}}{\beta_{\rm f}}(\dot{p}_{{\rm cp}d}-\dot{p}_{\rm cp})\\ &=g_1(\alpha)k_{\alpha 2}(p_{{\rm cp}d}-p_{\rm cp})(\dot{\alpha}_d-\dot{\alpha})-k_{\rm p3}(p_{{\rm cp}d}-p_{\rm cp})^2.\end{aligned} \tag{95}$$

■

F Proof for Lemma 8

Subtracting (16) from (49) and using (86) yields

$$\begin{aligned}\frac{V_s}{\beta_{eff}}(\ddot{p}_{sr}-\ddot{p}_{\rm s})=&\frac{V_{max}}{2\pi\alpha_{max}}\omega(t)(\dot{\alpha}_d-\dot{\alpha})\\ &+\mathbf{Y}_{\rm p}(\boldsymbol{\theta}_{\rm p}-\widehat{\boldsymbol{\theta}}_{\rm p})-k_{\rm p1}(\dot{p}_{sr}-\dot{p}_{\rm s}).\end{aligned} \tag{96}$$

Then, differentiating (52) with respect to time and using (50), (51), (91), (96) and Lemma 4 yields

$$\begin{aligned}\dot{\nu}_{1a}&=(\dot{p}_{sr}-\dot{p}_{\rm s})\frac{V_s}{\beta_{eff}}(\ddot{p}_{sr}-\ddot{p}_{\rm s})-\sum_{\gamma=1}^{4}(\theta_{{\rm p}\gamma}-\widehat{\theta}_{{\rm p}\gamma})\frac{\dot{\hat{\theta}}_{{\rm p}\gamma}}{\rho_{{\rm p}\gamma}}\\ &=\dot{\nu}_1+(\dot{p}_{sr}-\dot{p}_{\rm s})\mathbf{Y}_{\rm p}(\boldsymbol{\theta}_{\rm p}-\widehat{\boldsymbol{\theta}}_{\rm p})-\sum_{\gamma=1}^{4}(\theta_{{\rm p}\gamma}-\widehat{\theta}_{{\rm p}\gamma})\frac{\dot{\hat{\theta}}_{{\rm p}\gamma}}{\rho_{{\rm p}\gamma}}\\ &=\dot{\nu}_1+\sum_{\gamma=1}^{4}(\theta_{{\rm p}\gamma}-\widehat{\theta}_{{\rm p}\gamma})\left(s_{{\rm p}\gamma}-\frac{\dot{\hat{\theta}}_{{\rm p}\gamma}}{\rho_{{\rm p}\gamma}}\right)\\ &\leqslant\dot{\nu}_1\end{aligned} \tag{97}$$

where $\dot{\nu}_1$ is defined in (91). ■

G Proof for Lemma 9

Subtracting (21) from (54) and using (89) yields

$$\begin{aligned}(\ddot{\alpha}_d-\ddot{\alpha})=&-L_{\rm cp}A_{\rm cp}g_1(\alpha)(p_{{\rm cp}d}-p_{\rm cp})+\mathbf{Y}_{\rm s}(\boldsymbol{\theta}_{\rm s}-\widehat{\boldsymbol{\theta}}_{\rm s})\\ &-\omega(t)k_{\rm p2}(\dot{p}_{sr}-\dot{p}_{\rm s})-k_{\alpha 1}(\dot{\alpha}_d-\dot{\alpha}).\end{aligned} \tag{98}$$

Then, differentiating (57) with respect to time and using (55), (56), (93), (98) and Lemma 4 yields

$$\begin{aligned}\dot{v}_{2\mathrm{a}} &= (\dot{\alpha}_d-\dot{\alpha})(\ddot{\alpha}_d-\ddot{\alpha})-\sum_{\gamma=1}^{12}(\theta_{\mathrm{s}\gamma}-\widehat{\theta}_{\mathrm{s}\gamma})\frac{\dot{\widehat{\theta}}_{\mathrm{s}\gamma}}{\rho_{\mathrm{s}\gamma}}\\ &= \dot{v}_2+(\dot{\alpha}_d-\dot{\alpha})\mathbf{Y}_{\mathrm{s}}(\boldsymbol{\theta}_{\mathrm{s}}-\widehat{\boldsymbol{\theta}}_{\mathrm{s}})-\sum_{\gamma=1}^{12}(\theta_{\mathrm{s}\gamma}-\widehat{\theta}_{\mathrm{s}\gamma})\frac{\dot{\widehat{\theta}}_{\mathrm{s}\gamma}}{\rho_{\mathrm{s}\gamma}}\\ &= \dot{v}_2+\sum_{\gamma=1}^{12}(\theta_{\mathrm{s}\gamma}-\widehat{\theta}_{\mathrm{s}\gamma})\left(\mathrm{s}_{\mathrm{s}\gamma}-\frac{\dot{\widehat{\theta}}_{\mathrm{s}\gamma}}{\rho_{\mathrm{s}\gamma}}\right)\\ &\leqslant \dot{v}_2 \end{aligned} \tag{99}$$

where $\dot{v}_2$ is defined in (93). ■

H Proof for Lemma 10

Subtracting (27) from (59) and using (28), (61) and (87) yields

$$\begin{aligned}\frac{A_{\mathrm{cp}}}{\beta_{\mathrm{f}}}(\dot{p}_{\mathrm{cp}d}-\dot{p}_{\mathrm{cp}}) &= \mathbf{Y}_{\mathrm{v}}(\boldsymbol{\theta}_{\mathrm{v}}-\widehat{\boldsymbol{\theta}}_{\mathrm{v}})+\mathbf{Y}_{\mathrm{c}}(\boldsymbol{\theta}_{\mathrm{c}}-\widehat{\boldsymbol{\theta}}_{\mathrm{c}})\\ &\quad +g_1(\alpha)k_{\alpha 2}(\dot{\alpha}_d-\dot{\alpha})-k_{\mathrm{p}3}(p_{\mathrm{cp}d}-p_{\mathrm{cp}})\end{aligned} \tag{100}$$

Then, differentiating (66) with respect to time and using (62)–(65), (95), (100) and Lemma 4 yields

$$\begin{aligned}\dot{v}_{3\mathrm{a}} &= (p_{\mathrm{cp}d}-p_{\mathrm{cp}})\frac{A_{\mathrm{cp}}}{\beta_{\mathrm{f}}}(\dot{p}_{\mathrm{cp}d}-\dot{p}_{\mathrm{cp}})-\sum_{\gamma=1}^{2}(\theta_{\mathrm{c}\gamma}-\widehat{\theta}_{\mathrm{c}\gamma})\frac{\dot{\widehat{\theta}}_{\mathrm{c}\gamma}}{\rho_{\mathrm{c}\gamma}}\\ &\quad -\sum_{\gamma=1}^{2}(\theta_{\mathrm{v}\gamma}-\widehat{\theta}_{\mathrm{v}\gamma})\frac{\dot{\widehat{\theta}}_{\mathrm{v}\gamma}}{\rho_{\mathrm{v}\gamma}}\\ &= \dot{v}_3+(p_{\mathrm{cp}d}-p_{\mathrm{cp}})\mathbf{Y}_{\mathrm{c}}(\boldsymbol{\theta}_{\mathrm{c}}-\widehat{\boldsymbol{\theta}}_{\mathrm{c}})-\sum_{\gamma=1}^{2}(\theta_{\mathrm{c}\gamma}-\widehat{\theta}_{\mathrm{c}\gamma})\frac{\dot{\widehat{\theta}}_{\mathrm{c}\gamma}}{\rho_{\mathrm{c}\gamma}}\\ &\quad +(p_{\mathrm{cp}d}-p_{\mathrm{cp}})\mathbf{Y}_{\mathrm{v}}(\boldsymbol{\theta}_{\mathrm{v}}-\widehat{\boldsymbol{\theta}}_{\mathrm{v}})-\sum_{\gamma=1}^{2}(\theta_{\mathrm{v}\gamma}-\widehat{\theta}_{\mathrm{v}\gamma})\frac{\dot{\widehat{\theta}}_{\mathrm{v}\gamma}}{\rho_{\mathrm{v}\gamma}}\\ &= \dot{v}_3+\sum_{\gamma=1}^{2}(\theta_{\mathrm{c}\gamma}-\widehat{\theta}_{\mathrm{c}\gamma})\left(\mathrm{s}_{\mathrm{c}\gamma}-\frac{\dot{\widehat{\theta}}_{\mathrm{c}\gamma}}{\rho_{\mathrm{c}\gamma}}\right)\\ &\quad +\sum_{\gamma=1}^{2}(\theta_{\mathrm{v}\gamma}-\widehat{\theta}_{\mathrm{v}\gamma})\left(\mathrm{s}_{\mathrm{v}\gamma}-\frac{\dot{\widehat{\theta}}_{\mathrm{v}\gamma}}{\rho_{\mathrm{v}\gamma}}\right)\\ &\leqslant \dot{v}_3\end{aligned} \tag{101}$$

where $\dot{v}_3$ is defined in (95). ■

I Proof for Theorem 3

Let the desired discharge pressure trajectory $p_{\mathrm{s}d}$ be a continuously differentiable function in C^3, i.e.,

$$\{p_{\mathrm{s}d},\dot{p}_{\mathrm{s}d},\ddot{p}_{\mathrm{s}d},p_{\mathrm{s}d}^{(3)},p_{\mathrm{s}d}^{(4)}\}\in L_\infty. \tag{102}$$

Then, let Assumptions 1–2 and Condition 3 hold, leading to

$$\{Q_{load},\dot{Q}_{load},\ddot{Q}_{load},Q_{load}^{(3)}\}\in L_\infty \tag{103}$$

$$\{\omega(t),\frac{1}{\omega(t)},\dot{\omega}(t),\ddot{\omega}(t),\omega^{(3)}(t)\}\in L_\infty \tag{104}$$

$$\{p_{\mathrm{as}},\dot{p}_{\mathrm{as}},p_{\mathrm{ar}}\}\in L_\infty. \tag{105}$$

Then, Lemma 1, (52), (57), (66), (68) and (69) yields

$$\{\widehat{\boldsymbol{\theta}}_{\mathrm{p}},\widehat{\boldsymbol{\theta}}_{\mathrm{s}},\widehat{\boldsymbol{\theta}}_{\mathrm{c}},\widehat{\boldsymbol{\theta}}_{\mathrm{v}}\}\in L_\infty. \tag{106}$$

Next, interconnections between the control system variables are depicted in (107)–(122). Then, these affine functions in (107)–(122) are used in Fig. 11 to prove the asymptotic convergence (in the sense of Lemma 3) of the designed control system.

Equation (30) can be expressed as

$$\dot{p}_{\mathrm{s}r}=f_{p1}(\dot{p}_{\mathrm{s}d},p_{\mathrm{s}d},p_{\mathrm{s}}). \tag{107}$$

Then, taking the time derivatives from (30) yields that $\ddot{p}_{\mathrm{s}r}$, $p_{\mathrm{s}r}^{(3)}$ and $p_{\mathrm{s}r}^{(4)}$ can be expressed as

$$\ddot{p}_{\mathrm{s}r}=f_{p2}(\ddot{p}_{\mathrm{s}d},\dot{p}_{\mathrm{s}d},\dot{p}_{\mathrm{s}}) \tag{108}$$

$$p_{\mathrm{s}r}^{(3)}=f_{p3}(p_{\mathrm{s}d}^{(3)},\ddot{p}_{\mathrm{s}d},\ddot{p}_{\mathrm{s}}) \tag{109}$$

$$p_{\mathrm{s}r}^{(4)}=f_{p4}(p_{\mathrm{s}d}^{(4)},p_{\mathrm{s}d}^{(3)},p_{\mathrm{s}}^{(3)}). \tag{110}$$

It follows from (49), see (86) for $\mathbf{Y}_{\mathrm{p}}$, that

$$\dot{\alpha}_d=f_{\alpha 1}\big(\ddot{p}_{\mathrm{s}r},\dot{p}_{\mathrm{s}r},\dot{p}_{\mathrm{s}},\alpha,\dot{\omega}(t),\frac{1}{\omega(t)},\dot{Q}_{load},\widehat{\boldsymbol{\theta}}_{\mathrm{p}}\big). \tag{111}$$

Taking the time derivative from (49) yields that $\ddot{\alpha}_d$ can be expressed as

$$\begin{aligned}\ddot{\alpha}_d=f_{\alpha 2}\big(&p_{\mathrm{s}r}^{(3)},\ddot{p}_{\mathrm{s}r},\ddot{p}_{\mathrm{s}},\dot{p}_{\mathrm{s}},\dot{\alpha}_d,\dot{\alpha},\alpha,\ddot{\omega}(t),\dot{\omega}(t),\frac{1}{\omega(t)},\\ &\ddot{Q}_{load},\dot{Q}_{load},\dot{\widehat{\boldsymbol{\theta}}}_{\mathrm{p}},\widehat{\boldsymbol{\theta}}_{\mathrm{p}}\big).\end{aligned} \tag{112}$$

Taking the second-order time derivative from (49) yields that $\alpha_d^{(3)}$ can be expressed as

$$\begin{aligned}\alpha_d^{(3)}=f_{\alpha 3}\big(&p_{\mathrm{s}r}^{(4)},p_{\mathrm{s}r}^{(3)},\ddot{p}_{\mathrm{s}r},p_{\mathrm{s}}^{(3)},\ddot{p}_{\mathrm{s}},\dot{p}_{\mathrm{s}},\ddot{\alpha}_d,\dot{\alpha}_d,\ddot{\alpha},\dot{\alpha},\alpha,\\ &\omega^{(3)}(t),\ddot{\omega}(t),\dot{\omega}(t),\frac{1}{\omega(t)},Q_{load}^{(3)},\ddot{Q}_{load},\\ &\dot{Q}_{load},\ddot{\widehat{\boldsymbol{\theta}}}_{\mathrm{p}},\dot{\widehat{\boldsymbol{\theta}}}_{\mathrm{p}},\widehat{\boldsymbol{\theta}}_{\mathrm{p}}\big).\end{aligned} \tag{113}$$

It follows from (54), see (89) for $\mathbf{Y}_{\mathrm{s}}$, that

$$p_{\mathrm{cp}d}=f_{p5}\big(\dot{p}_{\mathrm{s}r},\dot{p}_{\mathrm{s}},p_{\mathrm{s}},\ddot{\alpha}_d,\dot{\alpha}_d,\dot{\alpha},\alpha,\omega(t),p_{\mathrm{as}},p_{\mathrm{i}},\widehat{\boldsymbol{\theta}}_{\mathrm{s}}\big) \tag{114}$$

Taking the time derivative from (54) yields that $\dot{p}_{\mathrm{cp}d}$ can

be expressed as

$$\dot{p}_{\mathrm{cp}d} = f_{p6}\big(\ddot{p}_{\mathrm{s}r}, \dot{p}_{\mathrm{s}r}, \ddot{p}_{\mathrm{s}}, \dot{p}_{\mathrm{s}}, p_{\mathrm{s}}, \alpha_d^{(3)}, \ddot{\alpha}_d, \ddot{\alpha}, \dot{\alpha}, \alpha, \dot{\omega}(t), \omega(t), \dot{p}_{\mathrm{as}}, p_{\mathrm{as}}, \dot{p}_{\mathrm{i}}, p_{\mathrm{i}}, \hat{\dot{\boldsymbol{\theta}}}_{\mathrm{s}}, \hat{\boldsymbol{\theta}}_{\mathrm{s}}\big). \tag{115}$$

It follows from (59), see (87) for $\mathbf{Y}_{\mathrm{c}}$, that

$$u_{\mathrm{v}d} = f_{u1}\big(\dot{p}_{\mathrm{cp}d}, p_{\mathrm{cp}d}, p_{\mathrm{cp}}, \dot{\alpha}_d, \dot{\alpha}, \alpha, \hat{\boldsymbol{\theta}}_{\mathrm{c}}\big). \tag{116}$$

Then, it follows from (60) that

$$u_{\mathrm{c}} = f_{u2}\big(u_{\mathrm{v}d}, p_{\mathrm{as}}, p_{\mathrm{cp}}, p_{\mathrm{ar}}, \alpha, \hat{\boldsymbol{\theta}}_{\mathrm{v}}\big). \tag{117}$$

In view of Definition 2, (50), (51) and (86), $\hat{\dot{\boldsymbol{\theta}}}_{\mathrm{p}}$ can be written as

$$\hat{\dot{\boldsymbol{\theta}}}_{\mathrm{p}} = f_{\theta 1}\big(\ddot{p}_{\mathrm{s}r}, \dot{p}_{\mathrm{s}r}, \dot{p}_{\mathrm{s}}, \alpha, \dot{Q}_{load}, \dot{\omega}(t)\big). \tag{118}$$

The projection function $\mathscr{P}_2$ is a second-order differentiable function. In view of Definition 2, (51) and (86), $\hat{\ddot{\boldsymbol{\theta}}}_{\mathrm{p}}$ can be written as

$$\hat{\ddot{\boldsymbol{\theta}}}_{\mathrm{p}} = f_{\theta 2}\big(p_{sr}^{(3)}, \ddot{p}_{\mathrm{s}r}, \dot{p}_{\mathrm{s}r}, \ddot{p}_{\mathrm{s}}, \dot{p}_{\mathrm{s}}, \dot{\alpha}, \alpha, \ddot{Q}_{load}, \dot{Q}_{load}, \ddot{\omega}(t), \dot{\omega}(t)\big). \tag{119}$$

In view of Definition 2, (55), (56) and (89), $\hat{\dot{\boldsymbol{\theta}}}_{\mathrm{s}}$ can be written as

$$\hat{\dot{\boldsymbol{\theta}}}_{\mathrm{s}} = f_{\theta 3}\big(\ddot{\alpha}_d, \dot{\alpha}_d, \dot{\alpha}, \alpha, p_{\mathrm{s}}, p_{\mathrm{as}}, p_{\mathrm{i}}, \omega(t)\big). \tag{120}$$

For the asymptotic convergence $p_{\mathrm{i}} \in L_\infty$ and $\dot{p}_{\mathrm{i}} \in L_\infty$ must be provided (note that detailed models for these variables were not defined in the controller design). Assuming that the fluid flow in the system suction line is laminar, the suction pressure p_{i} can be expressed as[5]

$$p_{\mathrm{i}} = f_{p7}\big(p_{\mathrm{s}}, \alpha, \omega(t)\big) \tag{121}$$

and its time derivative $\dot{p}_{\mathrm{i}}$ can be expressed as

$$\dot{p}_{\mathrm{i}} = f_{p8}\big(\dot{p}_{\mathrm{s}}, \dot{\alpha}, \alpha, \dot{\omega}(t), \omega(t)\big). \tag{122}$$

It follows directly from (42)–(44) and (46) that $(\dot{p}_{\mathrm{s}r} - \dot{p}_{\mathrm{s}}) \in L_2$, $(\dot{\alpha}_d - \dot{\alpha}) \in L_2$, $(p_{\mathrm{cp}d} - p_{\mathrm{cp}}) \in L_2$ and $(p_{\mathrm{s}d} - p_{\mathrm{s}}) \in L_2$ hold. Then, as illustrated in the flow-map presentation in Fig. 11, using (13)–(16), (21), (27), (28), (43)–(46) and (102)–(122), it follows that $(\ddot{p}_{\mathrm{s}r} - \ddot{p}_{\mathrm{s}}) \in L_\infty$, $(\ddot{\alpha}_d - \ddot{\alpha}) \in L_\infty$, $(\dot{p}_{\mathrm{cp}d} - \dot{p}_{\mathrm{cp}}) \in L_\infty$, and $(\dot{p}_{\mathrm{s}d} - \dot{p}_{\mathrm{s}}) \in L_\infty$ hold. Then, Lemma 3 can be used to provide that $(p_{\mathrm{s}d} - p_{\mathrm{s}}) \to 0$, $(\dot{p}_{\mathrm{s}r} - \dot{p}_{\mathrm{s}}) \to 0$, $(\dot{\alpha}_d - \dot{\alpha}) \to 0$ and $(p_{\mathrm{cp}d} - p_{\mathrm{cp}}) \to 0$ hold. ■

[5] A laminar fluid flow is usually a design criteria for a hydraulic system's suction line. Thus, in view of Hagen-Poiseuille law, the (laminar) fluid flow rate Q_{suc} in the system suction line can be written as $Q_{suc} = c_{lam}(p_0 - p_{\mathrm{i}})$, where c_{lam} and p_0 are constants (typically a constant pressure applies for the pressure p_0 in the system reservoir). On the other hand, Q_{suc} can be written as $Q_{suc} = Q_{\mathrm{p}} + Q_{leak}$. Then, using the defined equations for Q_{suc}, (14) and (15), it yields $p_{\mathrm{i}} = -\frac{V_{max}}{2\pi\alpha_{max}c_{lam}}\omega(t)\alpha - \frac{k_{leak}}{c_{lam}}p_{\mathrm{s}} + p_0$, which yields (121). Eventually, taking the time derivative from the equation for p_{i} yields (122).

References

[1] Zeiger, G., and Akers, A., 1985. "Torque on the swashplate of an axial piston pump". *J. Dynamic Syst., Meas. Control,* **107**(3), pp. 220–226.

[2] Zeiger, G., and Akers, A., 1986. "Dynamic analysis of an axial piston pump swashplate control". *Proc. IMechE, Part C: J. Mechanical Engineering Science,* **200**(1), pp. 49–58.

[3] Kim, S., Cho, H., and Lee, C., 1987. "A parameter sensitivity analysis for the dynamic model of a variable displacement axial piston pump". *Proc. IMechE, Part C: J. Mechanical Engineering Science,* **201**(4), pp. 235–243.

[4] Schoenau, G., Burton, R., and Kavanagh, G., 1990. "Dynamic analysis of a variable displacement pump". *J. Dynamic Syst., Meas. Control,* **112**(1), pp. 122–132.

[5] Manring, N., and Johnson, R., 1994. "Swivel torque within a variable-displacement pump". In Proc. 46th National Conf. on Fluid Power, pp. 13–24.

[6] Manring, N., and Johnson, R., 1996. "Modeling and designing a variable-displacement open-loop pump". *J. Dynamic Syst., Meas. Control,* **118**(2), pp. 267–271.

[7] Manring, N., 1998. "The torque on the input shaft of an axial-piston swash-plate type hydrostatic pump". *J. Dynamic Syst., Meas. Control,* **120**(1), pp. 57–62.

[8] Manring, N., and Damtew, F., 2001. "The control torque on the swash plate of an axial-piston pump utilizing piston-bore springs". *J. Dynamic Syst., Meas. Control,* **123**(3), pp. 471–478.

[9] Kim, S., Cho, H., and Lee, C., 1988. "Stability analysis of a load-sensing hydraulic system". *Proc. IMechE, Part A: J. Power and Energy,* **202**(2), pp. 79–88.

[10] Krus, P., 1988. "On load sensing fluid power systems". PhD thesis, Linköping University, Sweden.

[11] Chiriboga, J., Thein, M.-W., and Misawa, E., 1995. "Input-output feedback linearization control of a load-sensing hydraulic servo system". In Proc. 4th IEEE Conf. on Control Applications, pp. 910–915.

[12] Sakurai, Y., Nakada, T., and Tanaka, K., 2002. "Design method of an intelligent oil-hydraulic system (load sensing oil-hydraulic system)". In Proc. IEEE Int. Symposium on Intelligent Control, pp. 626–630.

[13] Wu, D., Burton, R., Schoenau, G., and Bitner, D., 2002. "Establishing operating points for a linearized model of a load sensing system". *Int. J. Fluid Power,* **3**(2), pp. 47–54.

[14] Pedersen, H., Andersen, T., and Hansen, M., 2008. "Controlling a conventional LS-pump based on electrically measured LS-pressure". In Proc. Bath/ASME Symposium on Fluid Power & Motion Control.

[15] Jayaraman, G., and Lunzman, S., 2010. "Parameter estimation of an electronic load sensing pump using the

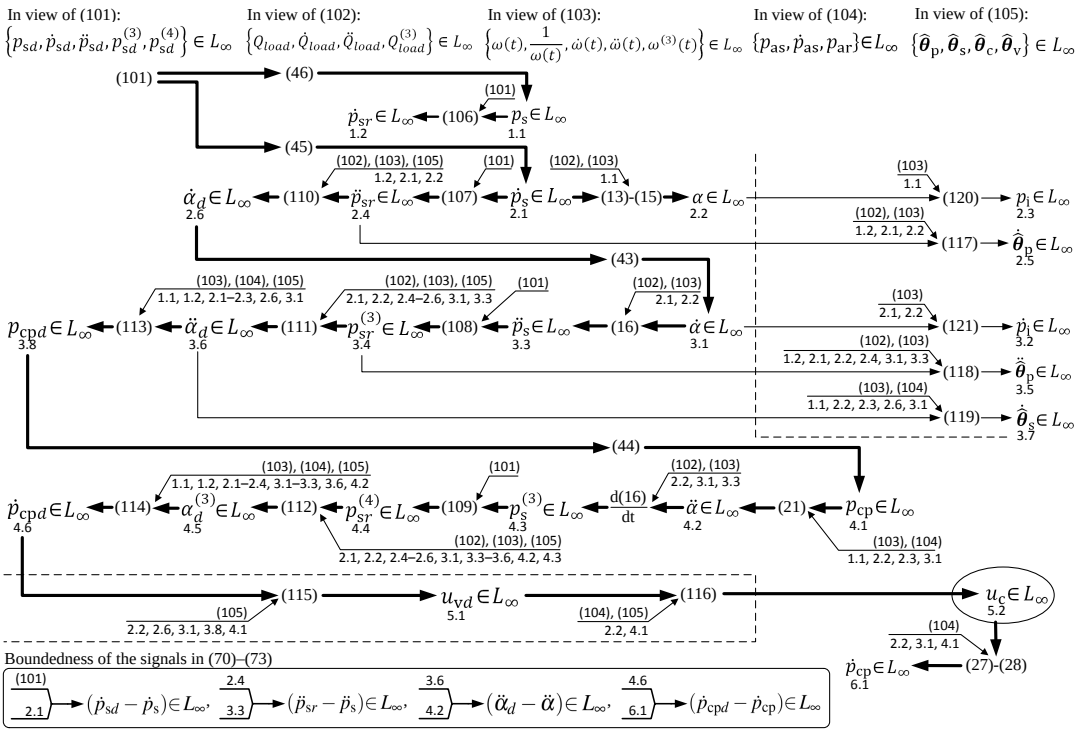

Fig. 11. The flow-map for the boundedness of the control system variables. Each bounded signal in the flow-map is named with a two-part number, where the first number denotes the row number and the second number is a signal identifier (for instance, $\dot{\alpha} \in L_\infty$ is named with 3.1, because it lies in the third line and is the first signal in it). The main flow is highlighted in bold. In the flow-map, the boundedness of a certain signal is formed from (102)–(106) and from the earlier bounded signals (see entries to the equations). The controller main signals are grouped with a column-based presentation (for instance, p_s, $\dot{p}_\mathrm{s}$, $\ddot{p}_\mathrm{s}$ and $p_\mathrm{s}^{(3)}$ lie in the same column), whereas subsidiary signals are delimited with a dashed line. Finally, the boundedness of $(\dot{p}_{sd} - \dot{p}_\mathrm{s})$, $(\ddot{p}_{sr} - \ddot{p}_\mathrm{s})$, $(\ddot{\alpha}_d - \ddot{\alpha})$ and $(\dot{p}_{\mathrm{cp}d} - \dot{p}_\mathrm{cp})$ in (70)–(73) is delimited with a rectangle. The boundedness of the system input ($u_\mathrm{c} \in L_\infty$) is highlighted with a circle.

recursive least squares algorithm". In Proc. 49th IEEE Conf. on Decision and Control, pp. 3445–3450.

[16] Jayaraman, G., and Lunzman, S., 2011. "Modeling and analysis of an electronic load sensing pump". In Proc. IEEE Int. Conf. on Control Applications, pp. 82–87.

[17] Lin, S., and Akers, A., 1990. "Optimal control theory applied to pressure-controlled axial piston pump design". *J. Dynamic Syst., Meas. Control,* **112**(3), pp. 475–481.

[18] Du, H., and Manring, N., 2001. "A single-actuator control design for hydraulic variable displacement pumps". In Proc. Am. Control Conf., Vol. 6, pp. 4484–4489.

[19] Grabbel, J., and Ivantysynova, M., 2005. "An investigation of swash plate control concepts for displacement controlled actuators". *Int. J. Fluid Power,* **6**(2), pp. 19–36.

[20] Dean, P., and Fales, R., 2007. "Modern control design for a variable displacement hydraulic pump". In Proc. Am. Control Conf., pp. 3535–3540.

[21] Kemmetmüller, W., Fuchshumer, F., and Kugi, A., 2010. "Nonlinear pressure control of self-supplied variable displacement axial piston pumps". *Control Engineering Practice,* **18**(1), pp. 84–93.

[22] Guo, K., and Wei, J., 2013. "Adaptive robust control of variable displacement pumps". In Proc. Am. Control Conf., pp. 1112–1117.

[23] Wei, J., Guo, K., Fang, J., and Tian, Q., 2015. "Nonlinear supply pressure control for a variable displacement axial piston pump". *Proc. IMechE, Part I: Journal of Systems and Control Engineering*, pp. 1–11.

[24] Zhu, W.-H., et al., 1997. "Virtual decomposition based control for generalized high dimensional robotic systems with complicated structure". *IEEE Trans. Robot. Autom.,* **13**(3), pp. 411–436.

[25] Zhu, W.-H., 2010. *Virtual Decomposition Control - Toward Hyper Degrees of Freedom Robots*. Springer-Verlag.

[26] Slotine, J.-J. E., and Li, W., 1991. *Applied Nonlinear Control*. Prentice-Hall Englewood Cliffs, NJ.

[27] Tao, G., 1997. "A simple alternative to the barbalat lemma". *IEEE Trans. Autom. Control,* **42**(5).

[28] Zhu, W.-H., and De Schutter, J., 1999. "Adaptive

control of mixed rigid/flexible joint robot manipulators based on virtual decomposition". *IEEE Trans. Robot. Autom.,* **15**(2), pp. 310–317.

[29] Zhu, W.-H., Bien, Z., and De Schutter, J., 1998. "Adaptive motion/force control of multiple manipulators with joint flexibility based on virtual decomposition". *IEEE Trans. Autom. Control,* **43**(1), pp. 46–60.

[30] Sohl, G. A., and Bobrow, J. E., 1999. "Experiments and simulations on the nonlinear control of a hydraulic servosystem". *IEEE Trans. Control Syst. Technol.,* **7**(2), pp. 238–247.

[31] Yao, B., Bu, F., Reedy, J., and Chiu, G. T.-C., 2000. "Adaptive robust control of single-rod hydraulic actuators: Theory and experiments". *IEEE/ASME Trans. on Mechatronics,* **5**(1), Mar., pp. 79–91.

[32] Zhu, W.-H., and Piedboeuf, J., 2005. "Adaptive output force tracking control of hydraulic cylinders with applications to robot manipulators". *J. Dynamic Syst., Meas. Control,* **127**(2), June, pp. 206–217.

[33] Lovrec, D., and Ulaga, S., 2007. "Pressure control in hydraulic systems with variable or constant pumps?". *Experimental Techniques,* **31**(2), pp. 33–41.

[34] Koivumäki, J., Honkakorpi, J., Vihonen, J., and Mattila, J., 2014. "Hydraulic manipulator virtual decomposition control with performance analysis using low-cost MEMS sensors". In Proc. IEEE/ASME Int. Conf. Adv. Intell. Mechatronics, pp. 910–917.

[35] Harrison, A., and Stoten, D., 1995. "Generalized finite difference method for optimal estimation of derivatives in real-time control problems". In Proc. Inst. of Mech. Eng., Vol. 209, pp. 67–78.

[36] Roberts, S., 1959. "Control charts based on geometric moving averages". *Technometrics,* **1**(3), pp. 239–250.

[37] Koivumäki, J., and Mattila, J., 2015. "Stability-guaranteed force-sensorless contact force/motion control of heavy-duty hydraulic manipulators". *IEEE Trans. Robot.,* **31**(4).

[38] Bonsignorio, F., and del Pobil, A., 2015. "Toward replicable and measurable robotics research [from the guest editors]". *IEEE Robotics & Automation Magazine,* **22**(3), pp. 32–32.

[39] Zhu, W.-H., and Vukovich, G., 2011. "Virtual decomposition control for modular robot manipulators". In Proc. IFAC World Congress, pp. 13486–13491.

[40] Zhu, W.-H., et al., 2013. "Precision control of modular robot manipulators: The VDC approach with embedded FPGA". *IEEE Trans. Robot.,* **29**(5), pp. 1162–1179.

Tampereen teknillinen yliopisto
PL 527
33101 Tampere

Tampere University of Technology
P.O.B. 527
FI-33101 Tampere, Finland

ISBN 978-952-15-3868-1
ISSN 1459-2045